UNIVERSITÀ DEGLI STUDI DI MILANO

DEPARTMENT OF PHYSICS

PHD SCHOOL IN
PHYSICS, ASTROPHYSICS AND APPLIED PHYSICS
CYCLE XXXII

Optomechanical Collective Effects using Cold Atoms in Free Space: Collective Atomic Recoil Lasing & Optical Binding

Disciplinary Scientific Sector FIS/03

PhD Thesis of:
Angel Tarramera Gisbert

Director of the School: Prof. Matteo Paris
Supervisor of the Thesis: Prof. Nicola Piovella

A.Y. 2020-2021

Referees of the thesis:
Prof. Francesco Saverio Cataliotti
Prof. Helmut Ritsch

Commission of the final examination:
Dr. Marco Genoni
Prof. Maurizio Artoni
Prof. Giovanna Morigi

Final examination:
11th December 2020 , Milan, Italy

Marie Skłodowska-Curie Actions

THIS PROJECT RECEIVES FUNDING FROM THE EUROPEAN UNION'S HORIZON 2020 RESEARCH AND INNOVATION PROGRAMME UNDER THE MARIE SKLODOWSKA-CURIE GRANT AGREEMENT NO. 721465

ColOpt

"More is different"

P. W. Anderson
1972

Dedication

I would like to dedicate this entire doctoral dissertation to my beloved soulmate, Ana Seixas Dias. She has been the inspiration and energy that has carried me through the most arduous and exhausting days of this journey. All the effort and work invested in this thesis have been possible thanks to the words of encouragement that I receive from her every day of my life. Thank you for always believing in me no matter the circumstances. *Amo-te muito.*

Amo como o amor ama.
Não sei razão pra amar-te mais que amar-te.
Que queres que te diga mais que te amo,
Se o que quero dizer-te é que te amo?
...

Fernando Pessoa

Additionally, I would like to devote a small share of this dedication to my family, who always believe that I can do whatever I set my mind to, and support me emotionally wherever the winds of the world take me. They are my mother, Carmen Gisbert Carro, my younger sister, Gemma Tarramera Gisbert, and my little brother, Jesús Gisbert Tarramera. *Moltes merces a tots tres.*

Acknowledgement

First and foremost I wish to express my greatest and most sincere appreciation to my Supervisor, Nicola Piovella, without whom this PhD thesis simply would not exist. There are so many reasons why I would like to thank him for all the contributions made throughout the entire period of my doctoral studies, that they are difficult to convey in a few lines. They range from his ability to explain the physics underlying in his most complex mathematical derivations, helping me with the comprehension of new collective phenomena and cooling mechanisms, to his personal calm nature, that made the learning process pleasant and rewarding. In addition, thank him for the time he has dedicated on reviewing this thesis dissertation and the different published reviews produced over this period of time.

I would like to extend my special thanks to the whole European ColOpt programme, which is the main framework of the project exposed in this dissertation and whose members have contributed richly to improve my knowledge in the field of optomechanical effects and to enlarge greatly my soft skills. Very special thanks to Gordon Robb, Robin Kaiser and Thorsten Ackemann, together with Nicola McRobbie. I would also like to thanks my distant fellow research students of the programme for all the discussion and presentation that helped me better understand other projects related to mine.

Apart from my Supervisor, I would also like to offer a great appreciation to Romain Bachelard for his enormous contribution in the composition of the majority of the published articles attached to this work. His insightful comments have always helped me to push forward in my research.

In addition, I am deeply grateful to Helmut Ritsch and Francesco Saverio Cataliotti for the careful revision of this thesis and whose comments have sparked a huge update and correction of this work

I won't forget to thank the good people from the Applied Quantum Mechanics Group, those who left and those who remain, that granted a friendly atmosphere in the physics department of the University of Milan.

Abstract

This theoretical doctoral thesis investigates the collective effects that emerge in cold atomic systems caused by light-scattering in free space. Two specific cases are investigated: the collective atomic recoil laser (CARL) effect in a cold gas, without optical cavity, and a novel cooperative cooling effect via optical binding (OB) with cold atoms.

As a main objective, this theoretical project investigates the spatial grating structures and the backward radiation that appears in a cold atomic cloud when it is irradiated by a single far-detuned laser beam, also known as CARL effect. While this effect has traditionally been described using a ring cavity, the study is performed here in free space, in the absence of such a cavity. Both 2D and 3D clouds show a transition from single-atom isotropic scattering to collective directional scattering. The effect is shown by the derivation and numerical solution of a set of multi-particle motion equations coupled by a self-consistent optical field, which is inspected with both a scalar model and a vectorial model. New original approaches are used to address the numerical study of the dynamics of the atomic system, such as molecular dynamics (MD) algorithms.

A second system emerged, from the attempt to understand the main objective, where a few atoms rearrange themselves into crystalline atomic structures, with a periodicity between particles close to the optical wavelength. The atomic system is initially confined into a 2D plane (or 1D string) using two (or four) counter-propagating laser beams. Due to the multiple scattering experienced by all the particles in the system, a dipole-dipole force arises among them, generating a non-trivial dynamical trapping potential landscape that compels the atoms, to self-organize at distances multiple of the light wavelength. When atoms are rearranged into an atomic crystal, the force acting on each particle depends on the position of the others, thus allowing to study the stability of such optically bound structures.

In addition, it turns out that a non-conservative force is generated from the dipole-dipole interaction, allowing the system to be cooled by controlling the value of certain parameters. This new phenomenon arises as a direct consequence of the use of cold atoms instead of dielectric nanoparticles in an OB system. Therefore, besides the atomic external motion, internal degrees of freedom (DOF) of the atoms are considered by treating each atom as a dipole. This latter aspect is investigated using the coupled dipole equations. When multiple atoms are set in line, the cooling mechanism is collectively enhanced, generating a novel cooperative cooling effect.

Synopsis

The objective of this thesis is to present collective optomechanical effects in free space, and these are described in two different systems. The thesis is organized as follows.

The thesis introduction, Chapter 1, begins by describing how atoms and electromagnetic waves (light) interact with each other. The chapter keeps digging into the light-matter interaction thought the scattering effects, which is presented with several important representatives. Detailed description of what cold atoms are and how cold or ultra-cold clouds are obtained is also provided. These atoms can be exploited to harness and amplify collective effects, such as the amplified scattering phenomenon, labelled as the collective light scattering effect, which are also introduced. Several main cooperative phenomena are discussed, resulting from the collective scattering produced by cold atomic ensembles when they are irradiated by light.

The body of the thesis has a couple of chapters dedicated to two collective effects. One the one hand, in Chapter 2, an effect presented in 1994 and regarded as collective atomic recoil lasing (CARL) [1] is introduced and extended into free space systems of two and three dimensions. The effect is also investigated taking into account the vectorial nature of an electromagnetic wave. On the other hand, in Chapter 3 a novel cooling effect is presented, linked to optical binding (OB) [2] and based in a one-dimension cold atomic system.

There are two chapters that complete the content of the main body of the thesis: Chapter 4, contains both the summary or conclusion and a short outlook for each of the two main topics presented throughout the body of the thesis, and a chapter, called Appendices, which includes a collection of addenda containing more details about the concept presented in the main body of the thesis. This last chapter is composed of three full analytical derivations and a couple of secondary numerical issues. Furthermore, in addition to the usual bibliography (Chapter References), the three published Physical Review A papers about the results presented in this thesis are included in Chapter 5.

Finally, assisting all readers of the digital version of the thesis: sections, equations, figures, chapter or section citations, references, allusions to certain page numbers, and entries of the table of contents, are defined as hyperlinks pointing to the quotation. Moreover, any page number jump back to the table of contents.

Contents

Chapter one

Introduction: basic concepts, elements and effects

The coming chapter serves as an introduction to the general concept of this PhD thesis: collective phenomena emerging from the light scattering in cold atoms. The chapter tries to level the knowledge of the reader in topics like: light-matter interaction, cold and ultracold atoms, atomic clouds, light scattering, and collective effects. The listed concepts may seem trivial for the trained mind, but they are not so common for the general public. In addition, the chapter introduces the progress achieve to this day, on light scattering, and lay the grounds for the understanding of the state-of-the-art collective effects emerging from the interaction between light and cold atoms presented in the two main chapters of this dissertation.

1.1 Light, matter and light scattering

Atoms are fundamental particles of matter elements, and their internal distribution is widely accepted, since a model of their structured was introduced by Bohr in 1913 [3]. They are composed of two fundamental parts: the central nucleus, including neutrons and protons, neutrally and positively charged, respectively; and the orbiting electrons, negatively charged and circling around this centre. The electrons constituting an atom are referred to as bounded electrons and they distribute themselves into different shells or energy levels. Only seven chemical atomic elements have their outer shell considered to be full, such elements are called noble gases and they are reckoned to be highly non-reactive. Conversely, the rest of the known elements have a semi filled outer shell, which makes them more susceptible to undergo variations of their electronic configuration. In particular, the electrons contained in the exterior energy level, the valence electrons, are more susceptible to be excited to a different stage, or even separated of the atom if the right amount of energy is provided; action that transforms the neutral atom in a positively charged ion. In addition, an electron can be absorbed by an atom if the valence band (shell) is not complete, converting the atoms in a negative ion.

Besides matter, there exist electromagnetic radiation, which is ordinarily described as light, and it extends from radio waves, passing through the infra-red and visible light, until the highly energetic gamma radiation. The electromagnetic waves are composed of elementary quantum particles called photons, which are discrete packets of electromagnetic energy that behave both as ballistic particles and as waves. Therefore, they possess wave-particle duality, and they can be accurately described using a quantum mechanical approach. The two simultaneous properties of light were linked through the theory developed in the doctoral thesis of de Broglie [4] in 1924, where the wavelength is obtained as the Planck constant divided by the relativistic momentum of the particle, $\lambda = h/p$.

A practical simplified model is generally adopted when considering an atom, in it the particle is considered as a two-level system. In such system, the atoms are featured to have two energy levels: a higher or excited state and a lower or ground state. This approximation is conceivable because in real atoms the energy levels are split into sub-levels, always leaving one of the bounded electrons less attached to the nucleus than the rest. Following this model, when an atom is irradiated by an electromagnetic field, and if the photons building the incoming field have an energy close to the energy difference between the ground and the excited state (see Sec.1.2), a photon will be absorbed from this optical field. Consequently, the action will allow to promote one of the outer electrons from its ground level to a higher energy level, leaving such atom in an excited state and generating an electric dipole in the atom itself. Eventually, the atom (i.e., the electron) will decay to its original ground state, emitting a photon with an energy equal to the energy of the electronic transition. The new photon will most likely be emitted with a different direction than the incident one, generating a new radiation mode.

Light-matter interaction: light scattering

The phenomenon is regarded as a primal light-matter interaction effect and it can be defined as the dispersion of radiation (light) into a range of directions as a result of physical collision or interactions with a particle of matter. Light scattering phenomena have been widely categorized throughout history into several interaction between light and matter. This type of light matter interactions can be distinguished attending different aspects [5], such as: the ratio between the particle dimensions and the light wavelength, which will determine the whether the collision is elastic or inelastic, the energy of the incident photon, and the initial bounding state of the scatterer (particle that absorbs and re-emit a photon). For instance, *Rayleigh scattering* [6], which is produced by particles that have a much smaller diameter than the incident light wavelength, less than one-tenth; represent the light scattering effects occurring throughout this dissertation.

Some of the main light scattering phenomenon are: *Mie scattering* [7] involves particles whose diameter is in the order of the wavelength of the incident electromagnetic field (good analysis found in [8]); *Raman scattering* or *Raman effect* [9], scattered photons can have higher or lower energy than the absorbed one (anti-Stokes or Stokes Raman scattering); *Compton scattering* [10], due to free charged particle, usually electrons. *Thomson scattering* [11], the incident photon's energy is smaller than the electron's mass energy, yet higher than its binding energy. *Brillouin scattering* [12], interaction between a photon and a phonon.[1]

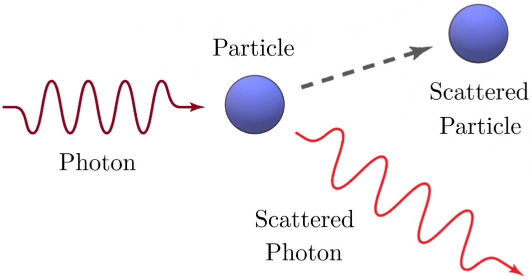

Figure 1.1: Schematic diagram of a scattering event, where a photon hits a particle, generating a scattered photon and the displacement of the particle. Such particle could represent an atom, an electron (free or bound), an ion or any other particle at the atomic scale.

There exist other more specific light scattering effects like: *Rutherford's*, charged particles mediated by Coulomb interaction; *Mott's*, relativistic electrons; *Deep inelastic*, represent Rutherford extension to higher energies; *Møller's*, electron-electron in quantum field theory; *Bhabha's*, electron-positron; *Tyndall's*, sunlight beams visible due to presence of dust particle; among others.

---

[1] A phonon is considered to be a discrete unit of vibrational mechanical energy that arises when atoms inside a crystal oscillate, as the photon is a discrete unit of electromagnetic energy.

1.2 Cold atoms

The idea that all physical elements are formed by sets of atoms, is nowadays trivial for most people. Nonetheless, there are two not-so-well-known subcategories that have emerged in recent decades: cold and ultra-cold atoms. These specific subsets of matter are vaguely familiar to the general scientific community and truly trendy within the circle of atomic, molecular, and optical (AMO) physics. Atoms are said to be cold or ultracold when their temparature has been reduced to very few millikelvins ($T \lesssim mK$) or to few tens of microkelvins ($T \lesssim \mu K$) and beyond, respectively. The topic has become rather interdisciplinary, besides the awaken interest among scientists from atomic physics, the topic has also gained attention in nuclear, condensed matter, solid state and high energy physics, along with the fields of quantum information, quantum computing and quantum optics, among others (check Fig. 1.2 for a quick overview).

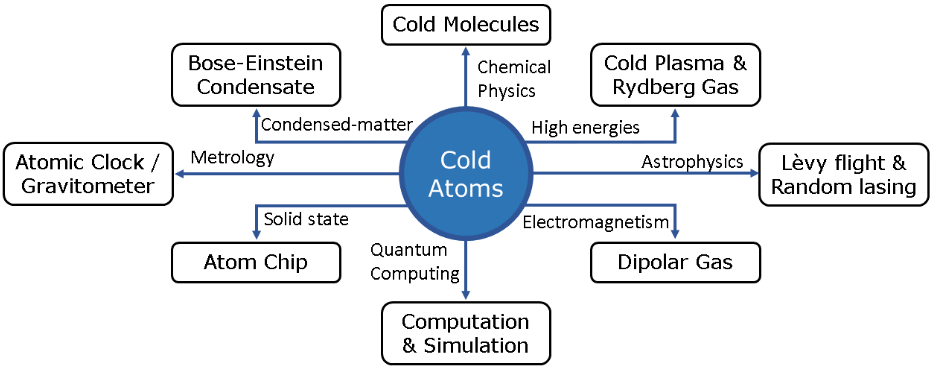

Figure 1.2: Concept map detailing several physics fields where cold atoms are being engaged, among others, like determining fundamental constants or quantum networking. Scheme based on the mind map depicted by the Department of Physics of the Ohio State University [13].

The alkali metals (generally rubidium "Rb" or caesium "Cs") has been the preferred atomic group when it comes to cooling atoms, although currently, an increasing number of physics groups are working with alkaline earth metals (mostly strontium "Sr"). All alkali metals have a stable excitation/decay electronic transitions (between 2S and 2P), that operate in close-loop cycles, and whose wavelength are easily achievable with the current existing laser technology. For instance, the exploited element throughout this thesis is ^{85}Rb, which (main) transition is located in the near infrared.

It has already been exposed how atoms can modify the energy and propagation of photons through scattering, but at the same time, photons can alter the motion of atoms by applying or inducing forces on them. Based on that principle, the field of laser cooling and trapping of atoms, together with the concept of cold atoms, were born in the mid-1970s. At that time, a technique to decelerate atoms from low temperatures to ∼$100\mu K$ (or several hundreds of µK), based on the forces associated to light absorption and scattering by a moving atom [14, 15], was proposed. The cooling procedure was experimentally proven shortly after, in the early 1980s [16]. The technique takes advantage of the momentum transfer between a two-level atom and a laser beam, whose frequency is close to resonance with the atom's electronic transition. It is achieved by employing the effects of a paramount well-known force, which is regarded with many names: dissipative force, scattering force, light pressure force or, frequently, radiation pressure (force).

Radiation pressure is considered to be dissipative because the action of such force can not be reversed. It was introduced by Keppler [17] more than three century ago, formalized by Maxwell [18], back in 1862, and experimentally proven at the beginning of the 20th century by Lebedew [19], Nichols and Hull [20]. The cooling method is briefly outlined, and the fundamental physics allowing its operation are explained using an oversimplified system composed of a two-level atom and a coherent light field.

Doppler cooling in two-level atoms

A laser beam is employed to irradiate a two-level atom and its wavelength is set to be close, but not equal, to the difference between the two energy states of the atom. The field's frequency is accordingly tuned below the atomic resonance in order to take advantage of the Doppler effect [21], which allows the momentum exchange between the photons of the field and the atom. In particular, the Doppler shift makes the radiation pressure force to depend on the atom's velocity ($F = -\beta v$), damping the atomic motion thus. In other words, the Doppler effect describes how the atom sees the frequency of the incoming photons, which are perceived to be compressed towards higher frequency values when the atom is moving in opposite direction to the light propagation. Consequently, the light beam needs to be detuned with a lower frequency than the one given by the atom's electronic transition, hence favouring the absorption of a photon: from the atom's point of view, the energy of a photon will match the energy difference between its ground and excited state. Due to the strong dependency of this cooling mechanism on the Doppler effect, the procedure is referred as Doppler cooling [14, 15], and is characterised as a laser cooling technique.

When an absorption of a counter-propagating photon takes place, the atom is forced to slow down, losing some kinetic energy or temperature in the process. Although associating a dissipative mechanism with a temperature is not completely appropriate, since in thermodynamics this parameter is used to define the state of a closed system in thermal equilibrium with the environment, in the field of atomic physics it is customary to allude to such quantity to characterize a set of atoms, instead of referring to its average kinetic energy. Due to the the equipartition theorem, the average kinetic energy of an atomic vapour can be calculated from the system's temperature $< E_k >= k_B T/2$.

It can be said that the discovery of laser cooling unveiled a new world, in which Doppler cooling is without a doubt the most elementary type of laser cooling mechanism. Cooling matter enabled disciplines like condensate or quantum gas physics and quantum state engineering. In fact, as mention earlier, cold atom have many application in an increasing number of scientific fields and topics, quoted in Fig.1.2, yet there is a relevant property that is interesting to highlight. When atoms are cooled under certain temperature, the large de Broglie wavelength acquired by all atoms in a system, allows to expose quantum phenomena on a macroscopic scale. This peculiar characteristic grant the scientist in atomic physics the opportunity to probe the properties of theoretical quantum system at a macroscopic level. The resulting new state of matter will be introduced in the coming Sec.1.3.2.

Doppler limit

It seems easy to be inclined to believe that this representation is not necessary at all, thinking that the dissipative process could be repeated as many times as necessary until the atom comes to a complete stop, yielding a zero temperature. After all, an arrangement of three pairs of laser beams could be set to achieve the momentum transfer between photons and the moving atom in every axial direction (the subject is covered in segment *Cooling an atomic cloud: Optical molasses* of the coming Sec.1.3). However, such outcome is not physically possible, because there exist a heating process due to the momentum fluctuations caused by the atom's recoil when it spontaneously emit photons. In these fluctuations, occurring at an average rate of Γ, the atom receive a momentum kick and recoils, changing its momentum by an average value of $\hbar k$. Moreover, its total kinetic energy is modified by at least an average value equal to the recoil energy $E_r = \hbar^2 k^2/2m = \hbar\omega_r$; being k the wavevector of the photon, $\hbar$ the reduced Planck constant and m the atomic mass. The mean momentum resulting from all kicks averages to zero, but the mean of the squared momentum, which links to the kinetic energy via $E_k =< p^2 > /2m$, is not zero. The general picture of the momentum fluctuation is represented by a Brownian motion[2] of the particle in the momentum space, i.e., a random walk of the velocity. Therefore, the sum of recoil kicks induced by many spontaneously emitted photons prevents the system from attaining a zero value for the atom's kinetic energy; what is more, it adds a heating mechanism to the cooling process.

The diffusion (heating) mechanisms and the dissipative force of the Doppler cooling compete between each other and their dispute leads to a steady state value of the kinetic energy. By considering the system to be away from saturation (linear regime that avoids stimulated emission) and equating the powers of both cooling and heating mechanisms, the steady-state kinetic energy of the atom can be calculated. The energy heating rate is given by $\Gamma\hbar\omega_r$, and the cooling power is obtained from the rate of momentum's loss ($\hbar k \cdot kv$, with kv as the detuning or rate) multiplied by the velocity $\hbar k^2 v^2$. When the two expressions are equated, the squared velocity $v^2 = \hbar\Gamma/2m$ of the steady-state can be obtained. Then, this velocity can be substituted using the expression of the kinetic energy derived from the equipartition theorem, $E_k = mv^2/2 = k_B T/2$, exposing the minimum temperature

---

[2] A Brownian motion describes the dynamics of a particles that constantly undergoes small and random fluctuations in a medium

achievable through a Doppler cooling process known as the Doppler temperature (T_D). Since this temperature represents a lower bound, it is also refereed as Doppler limit, being usually expressed as:

$$k_B T_D = \frac{\hbar\Gamma}{2}; \tag{1.1}$$

where k_B and $\hbar$ are the Boltzmann and Planck constants, respectively, and Γ is the linewidth or decay rate from the excited to the ground state. The full derivation of this limit and a better understanding of the concept can extracted from several renowned published literature, like [22, 23].

It is shown in Eq. (1.1) that the limiting temperature for the Doppler cooling technique is directly dependent on the linewidth of the atomic transition or decay rate Γ. However, the limit indirectly depends on the atom's squared mean velocity of the atoms, that in turn depends on the detuning or Doppler shift,[3] hence exposing the limit's dependency on the difference between the light frequency and the atomic resonance Δ. The typical value of Doppler temperature is usually around 100µK, so this technique is just the first step in the cooling process of matter. For future references, and considering that the present dissertation is based on Rubidium atoms, the Doppler temperature of the D_2 transition of ^{85}Rb [24] is calculated to be ~145µK.

Breach of Doppler limit: multilevel atoms

The first cooling experiments, attempting to measure the temperature from a cooled three-dimensional set of neutral atoms, seemed to agree with the Doppler limit [25, 26]. However, this threshold was experimentally overcome in 1988 [27], which somewhat made the Doppler temperature to appear as an artificial limitation. The physicist involve in this latter experiment, employed up to four different methods to measure the temperature of a sodium (Na) gas, among which the nowadays widely extended time-of-flight (TOF) method[4] was included. In each of the experimental outcomes a temperature below the one predicted by the Doppler limit ($\sim 10\mu K$ alkali atoms) was measured, being some measurements approximatly equal to a tenth of the predicted Doppler temperature. The breach of the Doppler limit was ratified for a sodium gas in [28, 29] and for a caesium (Cs) gas in [30–32]. In addition, another two contemporary experiments recorded astonishing low-temperatures for ^{4}He [30] and Cs [33], where the recoded temperatures were around 3µK, hence 120 and 50 times lower than the predicted Doppler limit, respectively.

---

[3] A moving atom, with velocity v, can match with the Doppler shifted laser frequency ω if the angle θ between such atomic velocity v and the light wave vector k satisfies $-\omega_D = \omega - \omega_a = kv\, cos\theta = \Delta$; being ω_a the resonance frequency. For a frontal collision $cos\theta = -1$, hence $\Delta = kv$.

[4] In the TOF method, the light beams involved are switched off and the atomic ensemble starts to expand as a consequence of the temperature of the atoms. Due to gravity the atoms start falling and go through a a probe laser light, recording the resulting fluorescence. The measurement has a temporal spread, caused by the ensemble's expansion, which allows to determine the temperature of the atoms when it is calculated.

The reason for the inconsistency of the two-level model comes from the fact that the Doppler cooling temperature is limited by the natural atomic linewidth, and only certain atomic species, with addition controlling measures, are subjected to this limit. The model works on elements with the presence of a closed cycling transition, granted by a specific internal energy level structure, which is given when alkali metals, alkaline earth metals and rare gasses are considered to have no degeneracy of their energy levels (or suppressed in some way). Therefore, the two-level atom model can only be applied to atoms where the light field couples a single ground and excited state, which can be achieved with a low intensities optical field and, in 1D, with a pair of counter-propagating laser beams with no polarization gradient (see segment Sisyphus cooling in Sec. 1.3.2).

Conversely, real atoms are composed of several energy levels, which makes the interceding light field to couple with more than two levels at the same time. The strength of the atoms multiple transitions capacity is defined by the orientation of its atomic dipole moment with respect to the polarization of the light, which has also been neglected so far. The multilevel nature of the atoms, allows the ground state to degenerate into two states Zeeman sub-levels and opening the possibility for the atom to be transferred from one ground sub-level to another by a fluorescence cycle. Consequently, it appears an additional neat decay rate from one sub-level to the other one that can be defined as Γ', representing the width of the degenerate ground state, that is much smaller than the excited state decay rate Γ. The probability of pumping the atom into the new ground state is higher than the probability to do it into the excited state, which explains why slow moving atoms are able to be cools down even further.

In summary, the experimental measurements of cooled gasses' temperature forced an update on the models describing laser cooling, because they made clear that, in a 3D cooling system, the oversimplified two-level atomic structure is sub-optimal. A good contrast study comparing the two-level theory of Doopler cooling in a 3D system and the the theories of multilevel cooling can be found in [34]. Consequently, new models and novel techniques for cooling and trapping atoms to explain and to control the achievement of these surprising temperatures, below the Doppler limit, were soon proposed. For the sake of naming a case example, the laser cooling technique known as resolved sideband cooling can be referred, which is a technique that is applied in cycles using a harmonic trapping frequency that exceeds the atomic transition rate from ground to excite level. The idea is originally attributed to Wineland and Dehmelt [15], and the experimentation was initially performed in [35], but its contemporary meaning was proven some years latter in [36]. Nevertheless, before applying these so-called sub-Doppler techniques, atoms are usually pre-cooled to the Doppler limit employing the Doppler cooling mechanisms. The most common sub-Doppler techniques, together with a more specific explanation on the Doppler limit breach, are briefly presented in Sec. 1.3.2.

1.3 Atomic ensembles with low temperatures

Along the current subsection, it will be presented the procedure that is often followed when cooling atoms. The first subsection contains an initial segment reporting how to cool a large assemble of atoms to reach the Doppler limit, and the subsequent step encompass the tools employed to stabilize this cold vapour. The second subsection, and the final part, focusses on overcoming the temperature that can be obtained in Doppler cooling —see Eq. (1.1)—. However, before describing the usual procedure employed for cooling and trapping matter, a short digression on the active range or capture temperature of a cooling technique is introduced.

Capture temperature

Any cooling technique has a velocity threshold above which the cooling damping force, proportional to the velocity, is not effective. This limit is measured by the capture velocity and, in laser cooling, it is defined as the ratio between the atomic decay rate Γ, and the radiation wavevector k. As the Doppler limit, this velocity can also be associated to a characteristic capture temperature. The average kinetic energy dependency either on the temperature or the average mean square velocity, is given by the equipartition theorem by the expression $E_k = mv_c^2/2 = k_B T_c/2$. For the Doppler cooling mechanism, since the capture velocity $v_c \equiv \Gamma/k$ [22], the corresponding capture temperature is defined as:

$$k_B T_c = \frac{m\Gamma^2}{k^2}, \tag{1.2}$$

where the already defined m represents the mass of the atom, Γ the decay rate, k the wavevector and k_B the Boltzmann constant. Although this temperature sets a limiting range within which the Doppler damping force can be applied, there are several techniques that grant the means to enhance that range beyond such velocity: high light intensity [37], inhomogeneous magnetic field [38], curved wavefronts [39], among others also cited in [22].

1.3.1 Cold atomic clouds

The assembly of atoms into a stable cold atomic vapour is frequently called "cold atomic cloud". It is customary to have some number of atoms between 10^6 and 10^{10} in these clouds. The continuous chain of events generated by the constant absorption and re-emission of photons by the atoms in a system, will determine the diameter of the atomic cloud. This can be explained by following the random walk experienced by a photon as it jumps from one atom to another. Initially, a so-called "first" atom that emits a photon will recoil from its position, towards the backwards direction of the axis outlined by the emitted photon. Next, a "second" atom absorbing the previously emitted photon will be pushed away, along the forward direction of the photon, due to the momentum exchanged with the photon. The push perceived by this second particle will be proportional to the intensity of the light coming from the first one, ergo the photon. The intensity can obviously be derived dividing the power of the scattering light by the squared of the distance separating the two atoms. All this process leads to a repulsive force that scales as a Coulomb force, which arbitrates in the final size of the cloud [40]. Usually, cold atom ensembles have a maximum diameter of a few millimetres, typically 1 or 2 millimetres. The usual techniques to cool and assemble atoms into a cold atomic cloud are now briefly presented.

Cooling an atomic cloud: Optical molasses

Forming a system of N $\gg$ 1 cold neutral atoms is initially accomplished with a technique named *optical molasses* [25], which was probed in the mid-1980s; up until that time, only ion cooling had been explored[35, 41]. This technique aids to slow down a cloud of neutral atoms to the Doppler limit fixed by the element employed, due to the exposed balance between recoil heating and Doppler cooling. It consists in a configuration of three pairs of mutually orthogonal laser beams, where every couple of lasers is orthogonal to the other two pairs, i.e, drafting a three-dimensional axis of coordinates. As a result of such configuration, atoms endure a friction force in any of the three spatial dimensions, due to the Doppler cooling mechanism resulting from the interaction of any laser beam and the atom's velocity component that points towards this beam. Therefore, due to the tuned-below-resonance laser beams, it is like the atoms were experiencing a confinement in a viscous medium; hence the given named for this technique. Nonetheless, the big issue that this approach presents, is that it does not trap the particles permanently, because sooner or later the atoms diffuse, escaping from the centre of action of the three pairs of lasers. The required next step would be to obtain a stable atomic gas, a mechanism which keeps the particles from diffusing out of the system.

Trapping a cold atomic cloud: Magneto-optical trap

The method that is most widely adopted for cooling and trapping atoms is the magneto-optical trap or MOT and it was validated during the last half of the 1980s [42]. The MOT is a hybrid system, because besides the three counter-propagating mutually perpendicular laser pairs that cool the cloud, it includes a magnetic trap that keeps the atoms from sliding away from the radiation centre. The reason why these hybrid systems are broadly employed for cooling matter, is because they are rather simple experiments to build and they have been proven to be robust against the undesirable systematic errors. In addition, they have a high capture velocity/temperature, comparing with the ones achieved by the optical molasses, being able to trap atom at room temperature. The capture velocity of a magneto-optical traps is defined as the maximum velocity an atom can have when entering the trap at one edge, that will become null by the time such atom reaches the other edge of the trap. The complete arrangement of a MOT can be inspected in Fig. 1.3. The *modus operandi* of such apparatus, together with the setting of its parts, is following briefly described.

The two counter-propagating beams in every cardinal direction are set with opposed circular polarization, fixing one with a clockwise rotation σ^+ and the other

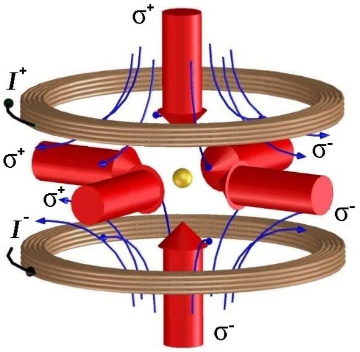

Figure 1.3: Magneto-optical scheme. The magnetic field (blue arrows) is generated by an anti-align Helmholtz magnetic system, with the current flowing clockwise (I^+) in one coil and counter-clockwise (I^-) in the other one. The optical molasses has three pairs of counter propagating laser beams (in red) with σ^+-σ^- polarization: one with a right hand circular polarization σ^+ and the other one with its counterpart σ^-. This figure, showing how to generate a cold atomic cloud (in yellow), is an adaptation from the one compiled in [43].

one with a counter-clockwise rotation σ^-. The polarization of every laser pair could also be fixed to be linear with opposing perpendicular orientation using a lin⊥lin scheme, but the σ^+-σ^- polarization is more commonly employed. The molasses system is intertwined with a couple of identical air-cooled circular coils, that generate a weak quadrupole magnetic field. The currents within the Helmholtz coils are anti-aligned, causing them to flow in the opposite direction from each other. This configuration creates a net field that is zero at the centre of the system ($\vec{B} = 0$), whenever the coils are separated 5/4 times their radii. The task of the coils is to generate a coaxial inhomogeneous magnet field $\vec{B}$, that will generate an extra level of degeneracy in the quantized energy distribution of the atoms (Zeeman effect), pushing them towards the centre of the optical molasses. The demonstration of such magnetic action dates from the early 20s of the 20th century [44]. There are several published text books that can be addressed for a much broader explanation [22, 23], along with many papers. For instance, a straightforward overview of a MOT with a Rubidium atomic cloud can be found in [45].

1.3.2 Ultracold atomic clouds

Although the temperatures achieved with the laser cooling techniques introduced so far are extremely low, considering that the temperature in outer space is close to 3K, there exist several methods that allow to reach even lower temperatures, e.g., grey-molasses [46]. However, there are two popular approaches, both developed in the mid-1980s, that successfully acquire lower temperature than the Doppler limit: Sysiphus cooling [47] and evaporative cooling [48]. Both experimental techniques, or their consequent results, were awarded the physics Nobel prize in 1997 and in

2001, in that order. The full explanation on how these two cooling methods operate falls beyond the scope of this thesis work. However, both technique will be briefly introduced. The detailed description of each one of them can be acquired from many different references, including the Nobel lectures of 1997 [49] (together with optical molasses [50] and MOT [51]) and 2001 [52, 53], respectively. Nevertheless, before proceeding any further, it is important to introduce another characteristic temperature it is refereed as the recoil temperature and it can be defined as the lowest attainable temperature with any laser cooling technique.

Recoil temperature

As it has been introduced earlier that the stimulated emission of a photon can be controlled using a lower intensity pump. Once an atom has been excited to an excited state, it will eventually and unavoidably decay to a ground state. This random emission produce a small variation in the atom's kinetic energy, triggering a heating mechanism that defines a cooling limit. The resulting kinetic energy can be linked to the recoil velocity, which can be determined by dividing the momentum of the involved photon $\hbar k$ by the mass of the atom, rendering $v_r = \hbar k/m$. As in the Doppler limit, it can also be related to a temperature, which is straightforwardly labelled as the recoil temperature. This characteristic temperature is usually regarded as the lowest temperature for any optical cooling processes and, once again, it is easily determined making use of the kinetic energy derived from the equipartition theorem, $E_k = mv_r^2/2 = k_B T_r/2$, which gives:

$$k_B T_r = \frac{\hbar^2 k^2}{m}. \tag{1.3}$$

A more thorough derivation for such temperature is covered in several publications, like the broadly used when teaching/learning atomic physics written by Christopher J. Foot [23], or others like [22]. In order to have a fair comparison of the enhancement that this limit means to the already known Doppler temperature of the D_2 transition of ^{85}Rb (145µK), the recoil temperature for this elements is announced. The temperature is roughly a four hundred times —more than two orders of magnitude— lower than the Doppler limit, being close to 357nK [24].

Sisyphus cooling

It has been referred how the Doppler cooling was crushed by the experimental result obtained when cooling an atomic cloud in a three-dimensional system, together with the incomparability of the two-level system to explain these results. Therefore, a novel model able to explain these low temperatures was presented by the groups of Claude Cohen-Tannoudji [31, 54] and Steven Chu [29, 55], who defined and exploit a new cooling mechanisms to reach sub-Doppler temperatures. The mechanism was labelled as polarization-gradient cooling, nowadays more often regarded as Sisyphus cooling [56], because it is based on the evidence that the optical field's polarisation varies with position in the optical molasses.

In any direction of an optical molasses a dipole potential is defined, due to the standing wave generated by the pair of counter-propagating laser beams. The potential gradient caused by the specific opposing polarizations (lin⊥lin or σ^+-σ^-) defined in the standing wave of each axis, which changes its orientation along a wavelength distance, affects the atoms while it moves along such axis every. The atoms climb up the hills of that potential, loosing some of its kinetic energy, and that loss is enhanced further in the process of excitation an decay of the atom between the degenerate ground state and the excited stated. The atom has higher chances of being optically pumped to the excited state once it reaches the top of the higher degenerate ground sub-level, and it has higher probability to decay from the excited state into the valley of the degenerate ground sub-level. Therefore, like in the Sisyphus myth,[5] the atoms will always travel uphill, gradually reducing its kinetic energy. By exploiting the polarization-gradient mechanism, atomic cooling can be achieved in standing waves with frequencies below the atomic resonance (red-detuned) [27, 33] and above an atomic resonance (blue-detuned), using a grey molasses [57] or a dark optical lattice [58].

Evaporative cooling

Evaporative cooling consist in a selective removal of high-energetic atoms from an atomic cloud, together with the collision balance of those that remain in the system. The first process reduced the number of atoms in the system, decreasing the phase-space density of the cloud,[6] and the second one needs a low phase-space density in the ensemble to be optimal. Nevertheless, to achieve an effective cooling the phase-density needs to be sufficiently high. Both techniques can be applied simultaneousness to increase this density by shrinking the ensemble overcompensating for the loss of atoms [59] ; thus decrease the temperature of the cloud. Simplifying the scheme, evaporating cooling works much like cooling a cup of hot liquid (e.g. tea or coffee), by blowing on the surface one can cool down such liquid. Although, in this case, instead of blowing over cold cloud, it is done by increasing the phase space density. The evaporative cooling mechanism was originally proposed by Hess in 1986 with the goal of achieving the Bose-Einstein condensate or BEC. He targeting to trapping and cooling of hydrogen atoms, which was successfully experimented a couple of years later [48]. The technique was complemented with laser cooling to achieve the same goal for alkali neutral atoms, and a simple formalism was introduced in 1994 [60].

Even though, the main flaw of the evaporating cooling technique is that the atomic density of the cloud is sorely diminish, it was the first technique to keep it high enough to achieve a 70-years-old theorized rare state of matter, the Bose-Einstein condensate [61] (physics Nobel prize 2001). Under a certain critical temperature, atoms start to condense in a single quantum state, overlapping into a unique synchronized wave. The average temperature in the BEC are below 1µK and under such threshold, matter is no longer labelled as *cold*, but as *ultracold*

---

[5] Sisyphus was a Greek mythology character whom the gods punished to roll up a boulder to the top of a hill, which would roll off every time it hit the top.

[6] Quantum mechanics shows that each state must occupy a certain volume in phase space all by itself, hence the number of states per element of volume in phase space is the phase-density of states

atoms. The amount of atoms present in this ultracold clouds can decrease a couple of orders of magnitude from the smallest cold atomic ensemble, down to 10^4 or a few tens of thousands. An important advantage of evaporative cooling is that it has no fundamental lower limit, granting the possibility of achieving temperatures below the sub-recoil limit. Other techniques that allow to attain sub-recoil temperatures are velocity-selective coherent population trapping [30], and Raman cooling [62].

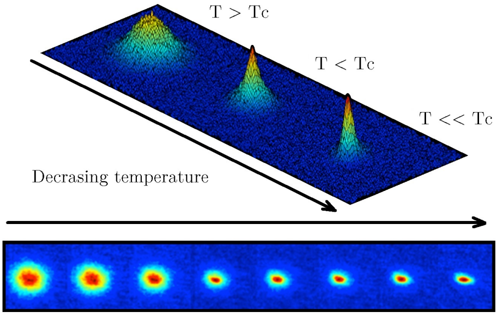

Figure 1.4: Rearranged and embellished sequence of images (adaptation from NASA's Cold atom Laboratory (CAL) website [63]), showing a BEC formation as the temperature is decreased under a critical temperature (T_c), below which atoms have practically zero kinetic energy. The diameter of the atomic cloud is reduced and the red areas (or peaks), in each figure, indicates higher density.

An important observation, although not relevant for the present work, is that the introduction of an optical resonator[7] assists to achieve a stable cold system and to reach very low temperatures. The possibility of cavity-assisted cooling for a single atom was first investigated at the end of the 20th century [64], based on previous experiments of quantum electrodynamics assisted with an optical cavity (CQED) [65, 66]. The system losses can be controlled trough the cavity losses, or cavity linewidth κ, instead of occurring in random fluctuations due to the photon spontaneous emission by the atoms [67]. Adding such cavity reduces the recoil heating and grant the opportunity to manage other problems, like the photon reabsorption or the pumping into different states. In addition, the temperature is limited by the cavity linewidth and can be set to $k_B T \approx \hbar\kappa$, far below from the Doppler limit —see Eq. (1.1)—. A good summary on the matter can be found in a theoretical review from the begging of the 2000s [68].

---

[7] An optical cavity or optical resonator is an arrangement of optical components (mirrors) that forces a beam of light to propagate in a closed loop path, e.g., a laser device contains an optical cavity as one of its components, causing a gain amplification due to constructive interference.

1.4 Collective light scattering in cold atomic clouds

The explanation of what constitute the light scattering effect, together with a few renowned examples, has been given in previous subsection 1.1, but so far, the phenomenon has only been discussed for an scenario where a lone scatterer is present. When a cold atomic cloud —regarded as a two-level system— is irradiated by an optical field within a certain parameters, the response of the system is reshaped greatly as a result of the collective behaviour originated from optical forces produced by several scattering events. Both the atomic cloud and the external field hold the key to this feedback: the laser via its intensity, its angle of incidence and its detuning with respect to the electronic transition of the atom; the clouds by means of its dimension, density, and shape. Every atom in the cloud is affected by the scattering produced by the others, that is the reason why many studies of collectivity with cold and ultracold atoms exploit optical cavities [69, 70]. An optical resonator allows to increase the interaction time between matter and light. A review on the cavity-generated dynamical optical potentials using cold atoms can be found in [71]. Moreover, a very short review on the cooperative dynamics of collective light scattering phenomena using optical fibres, lasers and amplifiers can be found in [72].

As it has been shown, the average momentum of an atomic cloud can be comparable to the recoil momentum resulting from light scattering, which means that light-matter interactions contribute significantly to the internal and external dynamics of each atom. When similar multiple-scattering events happen in the same system, they act together and generate a varied range of collective phenomena, which outcome does not result from a direct sum of the individual scattering events (or classical result for many-body system). Generally, it is of extreme importance to control these cooperative effects in cold atomic ensembles, by developing an interpretation both at a quantum and at a classical level. If such interpretation is obtained, making possible the extraction of conclusions from the system, new physical properties can be unveiled. In addition, atomic clouds seem to be outstanding study cases to investigate deviation from the classical many-body features.

The collective phenomena in quantum optics, more precisely the coherent spontaneous radiation caused by gases when these interact with an electromagnetic field, were originally introduced in 1954 by Dicke [73]. At the time, Dicke had to come up with a new solution to describe the measured fluorescence light from an excited atomic vapour, after establishing the incapability of the accepted model. Back then, particles were considered to behave as independent radiators, where they did not see each other. Hence, within a cloud of neutral atoms, one would expect to have similar behaviours to those of occurring in an ideal gases, seeing only short-range interactions (collisions) among the particles. However, when a system composed of some millions of atoms is forced to react with even the least complex source of light (a very weak incident field, e.g., a photon) and if the density of the cloud is sufficiently large, collective/cooperative responses are generated. In reality, every scatterer of an atomic cloud can be devised as a new wave front, since any re-emitted photon from a single atom can be reabsorbed by another one. Thus, every time an atom re-emits a new photon, the whole cloud will see it as a new spherical wave. The sum of N events translates into a collective behaviour of the cloud [40], transforming N one-body problems into a unique many-body problem. As a peculiar example, the radiation pressure that determines the size of the cloud can successively lead into photon bubbles [74].

Nowadays, there is still some controversy on how to label the many-body problems produced by an atomic cloud when it interacts with light. They are mainly cited as collective or cooperative effects and can stem from local or long-range interactions, being the latter ones sometimes wrongly regarded themselves as collective effects. There have been attempts to elucidate which are the distinct characteristics that allow to distinguish between collective and cooperative phenomena [75]. An easy-to-grasp definition is given on the website of the *Deutsches Elektronen-Synchrotron (DESY)*, where cooperativity is seen as a consequence of collectivity, and it quotes [76]: "*Cooperative emission describes a number of optical phenomena that result from the collective interaction of an ensemble of identical two-level atoms with a common, resonant radiation field*". Nonetheless, Dicke's statement that cooperative/collective effects are those occurrences not explained by the traditional single-particle theory approach, is rather accepted. Atomic clouds are not seen and as ensembles of point-like dipolar emitters, because atomic homogeneous distributions have a tendency to scatter cooperatively [77]. Consequently, it is not the ambition of the present dissertation to determine how these many-body effects are labelled. The exclusive plain fact to bear in mind is that whenever an atomic gas is lighted with a radiation field close to its resonance (or even with a significant detuning), it triggers a collective/cooperative response from the whole cloud, which is not equivalent to the one calculated by adding the individual responds of each atom independently.

1.4.1 Superradiance

Among all collective effects the one that stands out, deserving a distinct explanation, is the collective spontaneous emission, widely known as superradiance [73]. The phenomenon is broadly regarded as the most noticeable and studied collective phenomenon and it has been proven to exist both in experiments employing optical cavities [78] and free space [79]. It involves an acceleration of the decay process of the atomic cloud, with the first experimental observations in the far and near infrared spectrum respectivelly reported in the 1973 [80] and in 1976 [81]. Dicke originally stated that a small dense collection of N cold atoms radiates as $N\Gamma$, instead of Γ, when the collection is forced to interact with a resonant field. Basically meaning that N atoms, strongly coupled, re-emit light much faster than a single atom.[8] Dicke defined a '*small dense cloud*' as the vapour that has a diameter smaller than the incident wavelength. The system response can also be explained if a macroscopic mode (or a unique macroscopic dipole) is defined, subsequently

---

[8] Remember that Γ is regarded as the decay rate of the electron transition in a two-level atom, therefore a rate that should be constant if there was no collective process and the N scatterers were to re-emit independently.

allowing to treat the system with mean-field theory. [9] Moreover, besides the accelerated decay of excited atoms, superradiance is also responsible for transforming a possible initial isotropic incoherent spontaneous emission of the ensemble of dipoles into a coherent directional radiation.

Superradiance is considered as a long-range effect and, recently, it has been shown that the effect also emerge in cold atomic clouds with much smaller density and larger volumes [82]. In such dilute systems, atomic clouds have an inter-atomic distance much larger than the wavelength of the incident light and their radiation rate is not proportional to the density anymore, but to the optical thickness as $b_0\Gamma$. The optical thickness parameter is defined as $b_0 = aN/(kR)^2$ at resonance [83]; being k the wavenumber of the incident light, R the radius of the atomic cloud, N the number of atoms, and with a constant factor that varies its value depending on the nature of the optical external field: set to $a = 2$ for a scalar field, with no polarization, and $a = 3$ for a vectorial one.

An extensive review unifying several points of view and formalisms from different investigations, and introducing the basic physical concepts to the superradiance phenomenon can be followed in [84]; it was written in the 1980s by Gross and Haroche. A comparison between the responses of a cold atomic cloud with or without cooperative effects, can be inspected in Fig. 1.5.

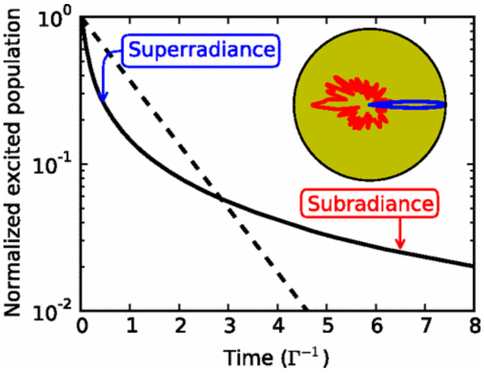

Figure 1.5: This illustration, borrowed from [83], displays the time evolution of the normalized excited stated computed in a linear process. A cold atomic cloud is exposed during a certain time to a coherent light source, letting the system to achieve a steady state from the starting ground state. Once the beam has been disconnected, the decay rate of the cloud (continuous line) is compared with the single atom decay (dashed line), labelling the two evolution regimes regarded as the collective phenomena of superradiance and subradiance. In addition, inside the upper right circle, the emission diagram of these two effects is depicted, being the superradiance a unique directional forward lobe (in blue) and the subradiance a quasi isotropic, but mostly backscattered, multi-lobe radiation.

---

[9] The mean-field theory approach states that the effect on one atom of the cloud caused by the rest of atoms can be approximated to a single averaged phenomenon.

1.4.2 Additional cooperative effects

Even though collective effects were discovered more than 70 years ago by Dicke, it has not been until recently that some attention and recognition has been given to them. Collective effects seem to be a rising new sub-field of atomic physics, perhaps becoming a new branch of the field, due to an increasing computational power that allows to test old and new theoretical models. Moreover, the number of experimental set-ups assembled by different groups around the globe, where many are specially focusing their attention on quantum computation and quantum information, might hold the key for real upraise of the subject. Two recent awards could be considered as significant forefathers of what is to come related to the collective effects study. They are the physics' Nobel prizes awarded in 1995 and 2018, associated with a new state of matter (BEC) and the manipulation of matter at an atomic level, respectively. The first one has already been introduced and will be latter regarded in the first section of chapter 2, whilst the second one will be briefly introduced in the first section of chapter 3. Yet, the awards do not prize the collective effects emerging from the awarded findings.

The collective behaviours emerging in cold atomic systems are the origin of other phenomena like: self-organization [85–87], reviewed in chapters 2 and 3; collective cooling [88–90], with new cases exposed in chapter 3; symmetry breaking [86, 91, 92]; and pattern formation [74, 93–96], exposed in chapter 2 as well; among others. For the sake of attaining a better grip on how collective effects alter the responses of an interacting atomic cloud, several renowned collective/cooperatives phenomena will be shortly described in a qualitatively manner. The coming list is not essential to understand the collective effects exposed along the main core of the current dissertation, and the more experimented readers can resume their reading after this itemization with Sec. 1.5.

Subradiance

Intrinsically linked to superradiance, there is another cooperative effect long forgotten, but that has attracted some attention in recent years; for instance in [97], among many others. The phenomenon was coined as *subradiance* and it was also proposed in 1954 by Dicke himself [73], yet it was not experimentally proven until 30 years later [98]. Essentially, it is described as a partial trapping of light by the system due to a destructive interference effect, which means that there is a cooperative inhibition of spontaneous emission. The atomic decay is utterly suppressed when an antisymmetric state is decoupled from the environment. However, in real systems, there exits always some coupling with the environment, thus leading to longer decay times in comparison with ensembles of completely independent atoms when this collective effect occurs (check Fig. 1.5).

Recently, it has been experimentally proven, that a dilute cloud —theory conceived in [83]— is indeed an ideal system to reproduce this effect and that the trapping time is strongly related to a parameter already introduced, the optical thickness; being the decay time delayed when such parameter has large values [99]. Contrary to superradiance, in subradiance, the states are metastable and fragile but they do not get suppressed close to resonance [100]. It can be observed, in Figure 1.5, how subradiance is somehow related with superradiance; where superradiance is the first response of an irradiated atomic cloud, followed by a subradiance emission response afterwards.

Superfluorecence

The phenomenon of *superfluorescence* or cooperative spontaneous emission [101, 102] is the collective emission of fluorescent radiation. It is produced by a system of excited atoms, or ions, due to the spontaneous correlation of excited atomic states. The main difference between this effect and superradiance is due to the absence of the initial macroscopic coherent dipole phase.

An initial step is required to observed this collective phenomenon, so it is necessary to generate a cloud of uncorrelated excited atoms; for instance, using an specific pump. In such a cloud, the population difference between the excited and the fundamental state is uniform and, initially, no macroscopic dipole moment can be considered. Finally, the initially absent macroscopic dipole builds up spontaneously and the synchronized atoms release the stored energy in a pulse of light, which has a decay rate proportional to N and a maximum emission peak of light intensity that scales as N^2. Therefore, the pulse maximum experience some delay, and the total pulse duration is actually shorter than the atomic decay rate.

Anderson localization

During the 1950s, Anderson [103] derived the initial theory to model the absence of diffusion in certain random potential lattices. The model was initially introduced for localizing electrons in a lattice potential, explaining the phase transition from a conductor to an insulator. In solid state physics, it is difficult to find non-interactive waves and there are few suitable scattering materials, like semi-conductor powder [104] or white paint [105] (suggested by Anderson hemself [106]). Instead, in atomic physics, cold atoms are used as effective scatterers and a non-interacting wave is easily achieved by using light, i.e., during a scattering process in linear optics (or linear process), photons do not interact with each other. Due to this preliminary research, the collective interference effect studying how the localized light in a region of a cloud is prevented to diffuse to other regions of the same cloud, has been coined as *Anderson localization*. It is also known as strong localization of light.

The trapping time elapsed when a photon is thrown into a system, can be explained by radiation trapping or random walking, but these latter processes do not involve interference effects. Dicke's subradiance can also help to keep a photon in the system by making the atoms oscillate together in and out of phase, sharing the excitation state, but that is not the case either. In this phenomenon there are some modes of the system, which are shared with several atoms at a sector of the system, but the mode sharing is not notice by atoms located in other regions of the cloud.

Despite that Anderson localization have been already observed and more or less well understood for system of one and two dimension, the three dimensional transition of light from diffusion to localization remains unsolved; only 3D metal-to-insulator transition has been observed. Therefore, neither macroscopic exact theory of Anderson localization exists, just some numerical simulation models, nor has the effect been observed so far. Some rare observation has been announced [107], but the results were disputed by the very same authors [108]. The question hovering on the scientific community is whether this 3D case does exist. Indeed, there are some theories that claim that it does not exist [109, 110] and other ones that are on the way of trying to unveil the conundrum. Regarding this latter ones, there is an approach working with cold atoms called weak localization or Coherent Backscattering of Light (CBS) [111–113], which was demonstrated in the 1980s and that it is believed to be the precursor of Anderson localization.

Single-photon superradiance

By using the tinniest laser intensity to radiate a cold vapour, the one generated by a single photon, it is possible to generate a cooperative feedback from the system. The effect is dubbed as *single-photon superradiance*, and it was proposed just a few years ago in 2006 [114, 115]. A decade later in 2014, an experiment capable of tuning the decay rate by controlling the number of atoms in the ensemble was reported [116]. This collective effect starts the path for a methodical bottom-up study of superradiance.

The effects proves that a unique photon can be absorbed and stored by an atomic cloud and due to the presence of this relativistic particle any atom can be excited. Although this pumped atom will be unknown, it will still constitute a superposition Dicke state.[10]The photon is shared among the atoms inside the cloud, triggering a collective spontaneous decay, which can become superradiance when the atoms are set in the proper phase. With only one atom excited, one would expect that the decay rate was equal to the one corresponding with the decay of a single atom, Γ, but if the atoms within the cloud are symmetrically organized, the observed decay rate is actually $N\Gamma$.

Cooperative radiation force

The radiation pressure force has already been announced for a lone scattered in section 1.1. However, when many atoms get together under the influence of such force, due to a coherent light source, a new collective effect can be generated. When radiation force acts on a large cloud of atoms, combining itself with the cooperative emission of the ensemble, results in a drastic reduction of the measured radiation emission. The effect occurs because there is an increase of directionality

---

[10] A Dicke state is a coherent superposition state of multiple particles, where N atoms behave collectively as a unique particle. For instance, if all atoms in a cloud are excited an only one decays, the Dicke state is the superposition of all possible states where just a single atom is in the ground state

on the scattering picture (forward scattering emerging) and a reduction in the total scattering cross section,[11] which implies a modification of the absorption process.

The described collective effect is known as *cooperative radiation force* [77, 117]. A good analytical derivation can be found in [118] and some experimental proofs in [117–119]. It provides a mean of measuring the amount of disorder in a system, which can be controlled by the optical thickness of the cloud [77, 119]. The phenomenon is a sort of primal consequence of light-matter interaction, granting a mechanism to study other cooperative effects like superradiance, subradiance and localization of light. Radiation pressure force can lead to pattern formation, compressing atomic clouds due to intensity attenuation in the scattering direction.

Collective Lamb shift

It was predicted that superradiance escorts a radiative shift of the atomic transition energy, which is based on the Lamb shift[12] [120] that founded quantum electrodynamics (QED) in 1947 and for which Lamb received the Nobel prize in 1955 [121]. Such collective effect is designated as *collective Lamb shift* or cooperative frequency shift. The effect was theoretically calculated in the mid-1970s [122], recently extended in [123]. However, its experimental confirmation was proven more than 35 years later, in 2010 [124], and in excellent agreement with theoretical predictions. The connection between collective Lamb shift with single-photon superrandiance has recently been studied in [125].

In this effect, besides the transition energy correction due to vacuum fluctuations characteristic from the Lamb shift, there is an additional collective contribution emerging when a virtual photon generated by one atom is not re-absorbed by the same atom, but by another identical atom within the ensemble. A cloud of identical atoms can be devised as a huge atom, where the constant emission and re-absorption of photons within itself leads to self-energy correction of the transition energy. This correction represents both the collective Lamb shift, with its real part, and the superradiant decay width, with its imaginary part. Consequently, a distinct red shift appears in the radiation emitted by the atomic cloud, comparing to the frequency that would be detected if the scatterer were to be an isolated atom.

---

[11] The scattering cross section is the probability that scattering takes place in a collision of two particles, e.g. interaction between a photon and an atom. It is generally larger than the geometric size of the particles because of dipole-dipole interaction

[12] The Lamb shift is defined as the slightly energy shift beyond the fine structure energy sublevels of an atom, not explained by the Dirac equation [126], as result of the interaction between the fluctuations of the vacuum electromagnetic field and the atom itself. This frequency shift happens when an excited atom emits and re-absorbs light several times, before its final decay to the ground state

1.5 Concepts to recall throughout this thesis

This PhD thesis is developed employing rubidium cold atoms (^{85}Rb) as the matter that interacts with a light field, which is assumed to be scalar (with no polarization effects) unless otherwise stated.

On the one hand, and regarding matter, the two-level atom model is characterized by using the D_2 transition[13] of ^{85}Rb, which is established to have a wavelength approximately of $780nm$ or what is the same, an energy difference between ground and excited state close to $1.5eV$ [24].

On the one hand, and regarding the electromagnetic radiation, the incident photons are set with a red detuning frequency, which gives them an energy that is below the atomic transition energy, hence allowing the atom to absorb the ones moving in its opposite direction (explained Doppler effect). Since the atoms are known to have dimensions within the order of magnitude of the Angstrom unit ($1\AA = 10^{-10}m$), and the two-level model adopted only allows for two energy levels, it can be asserted that Rayleigh scattering is the scattering effect taking place throughout the whole work.

In addition, the interaction between light and matter is described adopting semiclassical models, where quantum mechanics is exploited to describe the atoms' discrete energy levels, and light is treated as a classical electric field, i.e. a plain wave.

---

[13] Electronic transition energy from $5^2S_{1/2}$ to $5^2P_{3/2}$; where S/P is defined as the ground/excited state.

Chapter two

Collective light-matter interactions using the atomic recoil of cold atoms

The chapter present a known collective scattering effect generated when a 1D atomic ensemble in free space is irradiated by a single coherent optical filed (pump field). The coupled dipoles model is extended to provide a 2D and 3D description of the phenomenon. The so-called pump field is far-detuned from the atomic decay or electronic transition of a two-level system, and the effects of the polarization vector on this interaction are also regarded. As a consequence of the cooperative scattering, a spatial structure emerges in the cold atomic vapour, which makes the initial homogeneous density distribution to become periodic, with a separation between bunches of atoms related to the laser beam's wavelength. Moreover, this atomic cloud endure a transition from an isotropic spontaneous emission to a stimulated anisotropic scattering following a preferred direction.

2.1 Historical introduction

The novel tunable laser concept denoted as collective atomic recoil laser (CARL) or collective atomic recoil lasing effect (CARL effect), was originally proposed in 1994 by Bonifacio and De Salvo [1]. Both of them also contributed to further explain the effect by co-authoring and authoring another two letters [127] and [128], respectively. The mechanism has its roots in the free electron laser (FEL), which was developed a little over a decade earlier by Madey [129]. Bonifacio, who co-authored some articles on FEL some years before [130–132], and De Salvo make constant reference to the similarities between FEL and CARL in their three articles, where the CARL is described as the atomic equivalent of the FEL, which works through electrons.

Essentially, the CARL effect needs two elements to be generated: an atomic cloud, considered as a system composed of several two-level particles —uniformly arranged, or following a Gaussian distribution, in one, two, or three dimensions—, and a coherent external monochromatic optical field, labelled as "pump". CARL is nowadays mainly reproduced, theoretically and experimentally, using a third element, an optical cavity. By placing the cold atomic cloud within an optical resonator, a longer transient CARL operation is achieved, which was originally indicated by Bonifacio *et al.*, and the effective coherence time of the system is increased. The latter fact means that the chances of the photons to interact with an atom are higher, because they keep travelling among the particles for extended longer times before leaving the cavity. The optical cavity is also essential to have a single radiation mode and a small cavity damping rate. The usual type of cavity employed is called ring cavity[1].

The effect is based in a combination of Rayleigh light scattering and collective behaviours, both concepts presented in the introductory Chapter 1. The cold atomic cloud produces a scattered field intensity that varies with the number of atoms $I \sim N$ and that stems from the independent scattering of the N atoms randomly distributed inside the cloud. The phenomenon is driven by a coherent optical source, with certain intensity and a accurately defined detuning with the cloud's electronic transition (devised as a two-level system). Here is a more detailed, step-by-step explanation of how the CARL process works, graphically supported with a simple scheme represented in Fig. 2.1 (mentioned several times):

– Initially the two-level system composed of many particles, with neglecting initial velocity, is illuminated by a far detuned laser beam with weak intensity, or within linear optical regime (check upper left schematic (a) in the figure).

– Using this pump field, with such detuning, allows to neglect the population of the excited state, hence granting the possibility to consider the system at the fundamental level.

---

[1] There are two typical types of optical cavities: the standing-wave cavity, the light bounces back and forth (the one used in a laser), and the ring cavity, the light can do round trips in two opposing directions

- Shortly after this first event is initiated, a counter-propagating field arises from the intrinsic atomic noise fluctuations, or spontaneous photon emission, backscattering the pump field (see opposing overlapped arrows in panel (b) of the same figure).
- The new backscattered field is coined as "probe" and, as stated, it can be originated from the weak and incoherent scattered light in the same axial direction as the probe mode.
- Once there are two fields facing each other in the same axial direction, they start to interfere, producing a weak standing wave that creates a periodic optical potential (still in the given figure, see (d) representation).
- The potential starts to generate a bunching effect (modulation) in the cloud density by displacing the center-of-mass of the atoms, arranging them into bunches with a periodicity that coincides with $\lambda/2$; half of the external field's wavelength (inspect both right panels, (b) and (d), of the figure).
- The bunching process is perceived by the pump as a polarization grating in the active medium, hence resulting into a stimulated emission that favours the backscattering direction, i.e., the probe field.
- Finally, the gain on the strength of the probe triggers an increase of the standing wave, which translates into more bunching that contributes to the backscattering.

The whole process works in a loop, allowing to amplify both the bunching or grating contrast and the gain or intensity of the probe field, which grows exponentially from a tiny fluctuation into a rather strong signal. This feedback mechanism is the hidden engine that generates the CARL effect, although the phenomenon survives only for an interval that is in the order of the cooperative time, which can be some tens of microseconds.

There are two predominant displacement possibilities for the center-of-mass motion of each atom, due to the dipolar force that stems from photon scattering. This force, together with the atomic cloud's geometry, usually assumed with a cigar shape, favouring the scattering along the longer axis if no cavity is present [133], generate a stimulated emission onto the two directions of the pump axis. On the one hand, with a roughly 50% chances, the atoms are likely to experience a double momentum kick in the forward direction: one resulting from the scattering of a pump photon, and another one due to the backscattering of a photon into the probe. On the other hand, with the other 50% chances, the atom may remain nearly motionless in the same position, due to the counteracting effect of scattering a photon, which pushes the atom forward, and the forward scattering a photon, which provides the atom with a recoil kick in the backward direction. The latter outcome is because the wave vector of the external field and the atomic transition can be considered to be close to each other ($k \approx k_0$), even when the detuning assumed is large. The main advantage of working with a large-detuned pump is to neglect the radiation pressure force pushing the atoms away; in practice, scattering

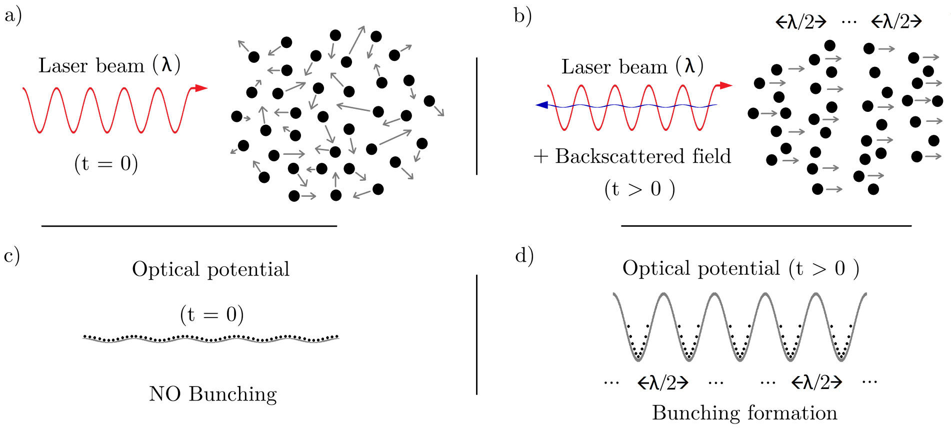

Figure 2.1: Carl Schematics displaying the cloud rearrangement from the initial random distribution (a) to the grating formation at time $t > 0$ (b). The bunching formation is portrayed in a simplified 1D example, where atoms are uniformly distributed at $t = 0$ (c) and are periodically gathered at time $t > 0$ (d) due to the appearance of an optical potential, consequence of the interference between the laser beam and the backscattered light (arrows in b).

dominates over absorption. Under this circumstances, and using the photon picture of a scattering event, the two more likely atomic final momenta can be described by: $\hbar\,(k - [-k_0]) \approx 2\hbar k$ and $\hbar\,(k - [+k_0]) \approx 0$, respectively. This scenario is depicted in Fig. 2.1(b), where the atomic cloud shows some bunching formation at a certain time t > 0; there are some atoms moving forward with a momenta $\sim 2\hbar k$ and others staying at rest with negligible momenta.

As it has been summarized, the CARL effect emerges when a cold atomic cloud is irradiated by a coherent optical field. Such a system has implicitly been shown to be characterised by two main responses: a gain in the strength of the so-called probe, which results from the organized backscatter radiation of the cloud (opposing the incident field), and the self-organization of the system into a grating. These two phenomena, a consequence of the feedback of the system to an external stimulus, are closely coupled and this was proved by Hemmer *et al.* in [134] using a hot steam cell[2], shortly after the idea of CARL was presented. Hemmer's study represents the first time that the effect was experimentally probed using a strongly driven hot atomic vapour. That experimental investigation matches its outcomes with the effect described by Bonifacio *et al.* and the complementary picture elegantly probed by Courtois *et al.* in [135], which is based on theory developed by Guo *et al.* [136, 137] and later [138]. The theoretical idea presented by Guo, where the gain —hence the resonance structures— is considered to be a result of

---

[2] Shielded nuclear radiation containment chambers, commonly referred as hot cells, are usually employed as a containment chambers for radioactive materials (meaning of the word "hot"). In this case, it provides a good containment box for an atomic sample.

the atomic recoil occurring due to absorption or emission of radiation, is nowadays known as the recoil-induced resonances (RIR). The RIR were experimentally investigated by Zimmermann's group in [139] and the theoretical comparison between this transitions and CARL can be found in a single-authored article, signed by Berman, in [140]. Anyway, the important fact is that Courtois *et al.* measured the gain of the recoil-induced probe using cold caesium atoms, which are proven to be more effective to see self-organization (greater bunching factor), whilst Lippi *et al.* worked with hot sodium atoms [141].

Although both Courtois and Lippi succeed in explaining the formation of the self-organizing grating that allows to maintain the CARL instability for a long time, they missed to show how the probe feedback mechanism works. Therefore, despite having cited some CARL experiments, with other extant verifications not cited, the feedback mechanism needed to see the CARL long time scale instability and characterizing the entire effect had not yet been tested. It was not until a decade later that Kruse*et al.* formally presented the first CARL experimental results [139], by applying a high-Q optical ring cavity[3] [142] in a collision-free environment. In order to represent this lower collisions environment, they employed ^{85}Rb atoms at a temperature of several 100μK, achieving atomic clouds of 10^6 particles and densities higher than $2{\cdot}10^{11}$ atom/cm^3. There is one main point where this experiments diverge from what was envisioned in the original CARL theory: the usage of an optical molasses to achieve the desired environment, allowing the system to reach a constant emitting-light steady-state.

At the beginning of the 2000s', the aforementioned Zimmermann's group, set an experiment placing the CARL system into a cavity to test the properties of the effect (see schematic in Fig 2.2) and they were very prolific in achieving results from that experimental set-up. Soon after having observed the recoil lasing effect, studying its relationship with the RIR [139], they probed the linked between the effect and the Kuramoto model [143] (theoretically studied in [144]), studying the threshold behaviour of CARL as a phase transition of the Kuramoto type [145]. By extending their original setting, they targeted the steady-state of CARL, which they labelled as "viscous CARL" [146]. Such stable and adjustable CARL emission frequency was achieved by adding an optical molasses to the set-up. They also compared the collective effect of superradiant Rayleigh scattering (SRyS) produced by a BEC [133] with the recoil lasing effect a couple of years later in [147]. In that latter comparison, they concluded that there is an intrinsic link between SRyS and CARL, which comes from tuning the cavity decay width κ —whenever the temperature is sufficiently cold, there is no need of a cavity for SRyS to occurs—. The CARL effect is obtained when this decay is smaller than the collective gain, obtaining superradiant emission otherwise. The explanation is simple, when the cavity losses are above a threshold value, the coherence time is too short for the initial fluctuations to work as a seed for the probe, so they exit the cavity in form of superradiance. The whole experiment has a relevance for this thesis, because it showed that CARL (also SRyS) is not based on quantum statistics, but on

---

[3] A high-Q cavity simple characterize how well an optical cavity stores light: the higher the Q, the longer the cavity confines the light.

cooperativity. This fact was extended and further extended in the next study of the group a few months later [148].

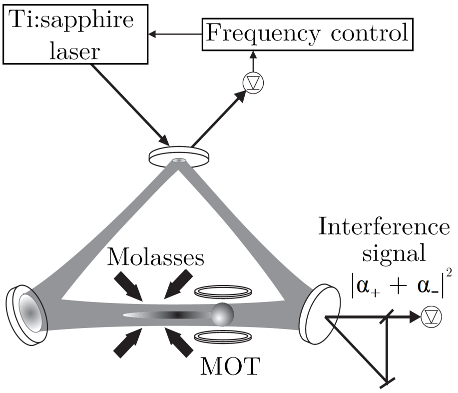

Figure 2.2: The optical layout of the CARL experiment employed in the review [146] is here depicted. Captured cold atoms from a magneto-optical trap are loaded in a dipole potential generated by a ring cavity and, afterwards, they are exposed to an optical molasses. The phase shifts of the standing wave are monitored using the frequency beat of the cavity modes, which propagate in opposite direction.

A few years later of the initial CARL proposal, where the CARL equations were presented semi-classically considering a quantized optical field and ballistic-like particles with continuous motion, the regime was extended to a fully quantum approach [149], by also describing the atomic center-of-mass motion with quantum mechanics. The extension was needed because the original model fails to explain such effect when the temperature of the cloud is lower than the recoil temperature (Eq. 1.3). Employing such enhanced model in the late 1990s', allowed to theoretically prove that the SRyS generated by a BEC can be described by a CARL mechanism [150].

The theory was later simplified by Bonifacio's group, who explained that the semi-classical approach [151] could be employed, instead of the full quantum equations, for large atomic densities. The group also improved and simplified the full quantum model [152] (later extended in [153]), allowing to described the system's response at recoil temperatures easily, which enabled an interpretation of the experimental results obtained in [133]. They defined an ingenious parameter, denoted as "collective parameter" (ρ), which represents the average number of scattered photons or, equivalently, the average number of momentum kicks the atoms receives. The system is in the quantum regime when the collective parameter is less than one and it describes the situation where all atoms backscatter coherently a single photon. They studied the light scattering from a BEC using these equations in different CARL schemes/configurations: variation of the angle of incidence of optical field; extending the common 1D system to a bidimensional description [154];

studying the quantum fluctuations and the atom-photon entanglement [155]; the propagations effect of short pulses using the quantum model [156]; and the acceleration of superradiance and the recoil lasing effect using two-frequency pumps in an optical cavity [97]. In addition, together with Zimmermann's group, they also analysed the CARL effect including friction and diffusion effects [157].

During the last decade, and after the experimental proof of the existence of the BEC, the attention over CARL has faded away, with just a couple of studies released by Zimmermann's groups: one placing a BEC in the optical ring resonator CARL scenario (setup presented in [147]) to investigate its stability diagram [158], and the other one comparing these findings with the CARL's diagram [159], where the theoretical description is performed using the classical CARL equations introduced in [143]. The present chapter picks up from this point, although away from the low temperatures that characterized the BEC. It presents the multimode model that allows to describe the CARL effect in two and three-dimensions without the assistance of an optical resonator, i.e., in free space. The time evolution results for either a 2D and a 3D system, considering both scalar and polarized light, are accompanied with numerical simulations showing the two characteristic responses of the CARL effect: atomic self-organization and coherent backscattering.

2.2 Models for the dynamics of an atomic cloud

So far, the features of the CARL effect have been described by exploiting different single-mode/mean field models. Good approximate results are obtained employing such models, which are suited for specific cases where the atomic ensemble has a certain favoured scattering axis. In this approach, the propagation of the scattering radiation is forced along one axis and within a single mode; for instance, when the atomic cloud is placed in an optical cavity. Although, in general, the shape of real atomic clouds has more than a single spatial mode, especially in free space, and the phenomenon of collective scattering is generated accordingly due to the collaboration of many modes. That is why in the current model, contrary to previous works, the incident photons are scattered into all possible three-dimensional vacuum modes. This particularity is taken into consideration when deriving the equations of motion. Furthermore, the superradiant scattering of the system that takes place along a certain direction is not determined by a cavity, but by the spatial distribution of the cloud; for example, when its shape is elongated along a particular axis.

Throughout this section, two main models will be studied, one considers the external laser beam as a scalar field, without polarization effects, and the other treats the vector components of this external field. The atomic cloud is obliviously compose of cold atoms, which are assumed to be ^{85}Rb for this thesis, and is regarded as a two-level system. As mentioned above, both models have been derived from a multimode theory, expanding on previous mean field theories. In addition, the vacuum radiation modes are adiabatically eliminated. There is an analogy between the models presented here and the characteristics observed with a BEC in [133], where a density grating appearance gives way to an enhancement in the light scattering intensity due to collective effects. However, there is also a main difference between the current study and the one performed with the BEC. While in [133], the bunching of the system is observed in the momentum space for ultracold atoms, with spacing $\hbar\boldsymbol{q} = \hbar(\boldsymbol{k}_0 - \boldsymbol{k})$ —where $\hbar\boldsymbol{k}_0$ and $\hbar\boldsymbol{k}$ are the momentum of the incident and scattered photon, respectively—, cold atoms are employed in the current case, the grating is observed in real space, and the atoms rearrange themselves into groups with a period of $2\pi/q$.

Alongside the scalar and vectorial approaches, a relevant observable parameter is reported in a third subsection. It is not a third model *per se*, but it has been given a dedicated subsection due to its importance when describing an atomic system under CARL. It is the optical magnetization and is often regarded as "bunching factor"; describes the grating strength in a specific axis direction.

2.2.1 Scalar external field

Following the line applied in the published investigation [160] —attached in Sec. 5.3—, where the model is described, a N two-level atoms driven by a laser field is considered. The optical field has a frequency $\omega_0 = ck_0$, with wave number $\boldsymbol{k}_0 = k_0\hat{\boldsymbol{z}}$, and propagates along the z axis. The Rabi frequency is defined by $\Omega_0 = dE_0/\hbar$, where E_0 is the electric field, d the atomic dipole and, $\hbar$ the well-known educed Planck constant. The external field frequency is far detuned from the atomic frequency ω_a by $\Delta_0 = \omega_0 - \omega_a \gg \Gamma$, with $\Gamma = d^2k_0^3/2\pi\epsilon_0\hbar$ is the atomic linewidth or spontaneous decay rate. Furthermore, in the far-detuned limit and when a dilute gas is deemed, the re-absorption from scattered photons can be neglected, thus reducing the process in the cloud to single-scattering. Therefore, each vacuum mode $\boldsymbol{k}$ results from the atomic scattering of the incident light with the mode $\boldsymbol{k}_0$. The atoms experience the recoil motion every time they scatter a photon from the incident light, and the energy of this shift is proportional to the recoil frequency $\omega_{rec} = \hbar k^2/2M$

The complete derivation of the atoms' motion equation can be followed in the appendix of Sec. 5.3. In such derivation, the excited state population has been neglected, due to the large or weak detuning field (linear optical regime). As previously stated, considering $\Gamma \gg \omega_{rec}$, the internal degree of freedom of the atoms is adiabatically eliminated assuming it is synchronized with their external motion. The radiated field has been incorporated into the moment equation by disregarding the vacuum fluctuations, only reckoning the radiation field due to Rayleigh scattering. Adding all these radiated modes, a set of N coupled equations is obtained, thus describing how each atom j endures the radiation force exerted by the other m-atoms ($N-1$) contained in the system. Adding all these considerations, results in the following differential equations describing the position $\boldsymbol{r}_j$ and the momentum $\boldsymbol{p}_j$ of each j-atom.

$$\dot{\boldsymbol{r}}_j = \frac{\boldsymbol{p}_j}{M}, \tag{2.1}$$

$$\dot{\boldsymbol{p}}_j = A\sum_{m\neq j}\left\{(\hat{\boldsymbol{z}} - \hat{\boldsymbol{r}}_{jm})\frac{\sin[k_0(r_{jm} - z_{jm})]}{k_0 r_{jm}} - \hat{\boldsymbol{r}}_{jm}\frac{\cos[k_0(r_{jm} - z_{jm})]}{(k_0 r_{jm})^2}\right\}, \tag{2.2}$$

with the constant A, reported separately in a third expression for future reference, being described as

$$A = \Gamma\hbar k_0 \left(\frac{\Omega_0}{2\Delta_0}\right)^2 . \tag{2.3}$$

The atomic mass is symbolized by M and a change of variable, representing the distance between two atoms, is applied $\boldsymbol{r}_{jm} = \boldsymbol{r}_j - \boldsymbol{r}_m$, with $\hat{\boldsymbol{r}}_{jm} = \boldsymbol{r}_{jm}/r_{jm}$ (where $m \neq j$).

The oscillating force represented by Eq. (2.2) couples each atom j with all the other ones along two direction components: the one related to the external field, $\hat{\boldsymbol{z}}$, and the one connecting the atom j toward the other atoms, $\hat{\boldsymbol{r}}_{jm}$. In addition, the force has a finite range, having two terms that decrease with the atoms separation as $1/r_{jm}$ or $1/r_{jm}^2$.

2.2.2 Optical field including polarization effects

The derivation above is extended to include the vectorial components of the light, which is no longer considered scalar. This polarization is linear, perpendicular to the propagation direction, and it will be shown that it produces a suppression or alteration of the grating that appears in the cloud. Adding such polarization will allow to study new aspects of the system, but it will make the expression describing the system's motion somewhat denser. The derivation of the new equations of motion is performed along the first two sections of the appendix B and the final expressions that give a description of the momentum and the position of every atom "j" inside the cloud is:

$$\begin{aligned}
\dot{\boldsymbol{r}}_j &= \frac{\boldsymbol{p}_j}{M}, \qquad (2.4)\\
\dot{\boldsymbol{p}}_j &= A \sum_{\alpha,\beta} (\hat{\epsilon}^*_{0\alpha}\hat{\epsilon}_{0\beta}) \sum_{m\neq j} \Bigg\{ (\hat{\boldsymbol{z}} - \hat{\boldsymbol{r}}_{jm})\,(\delta_{\alpha\beta} - \hat{r}_\alpha \hat{r}_\beta)\, \frac{\sin[k_0(r_{jm} - z_{jm})]}{k_0 r_{jm}} \\
&\quad + [\hat{\boldsymbol{z}}\,(\delta_{\alpha\beta} - 3\hat{r}_\alpha\hat{r}_\beta) - 2\hat{\boldsymbol{r}}_{jm}\,(\delta_{\alpha\beta} - 2\hat{r}_\alpha\hat{r}_\beta)]\, \frac{\cos[k_0(r_{jm} - z_{jm})]}{(k_0 r_{jm})^2} \\
&\quad - (\hat{\boldsymbol{z}} - 3\hat{\boldsymbol{r}}_{jm})\,(\delta_{\alpha\beta} - 3\hat{r}_\alpha\hat{r}_\beta)\, \frac{\sin[k_0(r_{jm} - z_{jm})]}{(k_0 r_{jm})^3} \\
&\quad + 3\hat{\boldsymbol{r}}_{jm}\,(\delta_{\alpha\beta} - 3\hat{r}_\alpha\hat{r}_\beta)\, \frac{\cos[k_0(r_{jm} - z_{jm})]}{(k_0 r_{jm})^4} \Bigg\}, \qquad (2.5)
\end{aligned}$$

being the constant A the same one utilized for the scalar model and introduced in Eq. (2.3).

These new vectorial equations of motion, (2.4) and (2.5), have some similarities to those of the scalar model, (2.1) and (2.2). In the vectorial equations the components of the pump polarization unit vector ϵ_0 are included. The force on the jth atom is proportional to the same constant A proportional to the pump intensity. There are three differences in the force equation of each atom "j" that stand out:

- The 'long-range' term $1/r_{jm}$ has not changed from the scalar model, but additional 'short-range' terms ($1/r_{jm}^n$ with $n \geq 2$) have made an appearance. There are two new terms that affect the particles at a shorter range (the last two terms containing the $1/(k_0 r_{jm})^3$ and $1/(k_0 r_{jm})^4$) and the term with $n = 2$ has an additional factor 2.

- A new polarization factor $\delta_{\alpha\beta} - n\hat{r}_\alpha \hat{r}_\beta$, with $n = 1, 2$ or 3, has made its presence. It comes as a consequence of an additional sum that arise due to the interaction between the vacuum modes and the two possible perpendicular polarization vectors (refer to appendix B, specifically Eq. (B.11)). The unit vectors in these factor, $\hat{r}_\alpha$ and $\hat{r}_\beta$, represent the components of r_{ij} along the components α and β of the pump polarization units vector; they are the short representation of $(\hat{r}_{jm})_\alpha$ and $(\hat{r}_{jm})_\beta$, respectively

- There is a new sum $\Sigma_{\alpha,\beta}$, which represents the projections of the polarization onto the two axes perpendicular to the direction of propagation of the optical field, when the system is in a real 3D free space. However, when the system is confined into a plane, there is only one projection, leaving the other one as null.

It can be noticed from the momentum's expression (2.5), that if the atomic motion is constrained to a 2D plane —the (x, z) plane— and the pump is linearly polarized along $\hat{y}$, then $\hat{\epsilon}_{0\alpha} = \delta_{\alpha y}$, which makes the terms $\hat{r}_\alpha \hat{r}_\beta$ equal to zero (see Fig. 2.12 of future Sec. 2.6 for graphic interpretation). The differences between this model and the one with scalar light is that now the short-range terms of the radiation force have more representation, i.e., $1/r_{jm}^n$ with $n \geq 2$. Therefore, the scalar model can be considered a good approximation for a 2D case, as long as the long-range interaction is dominant.

2.2.3 Bunching parameter

The "bunching" is a parameter that will be measured for both scalar and vectorial model. The concept is a reminiscence of the free-electron laser [129] and, since CARL is labelled as its atomic version, it is an important parameter to study the phenomenon. While in the case of FEL the bunching described the ensemble of electrons, in CARL the bunching give a knowledge of how periodically distributed the atoms are. Therefore, by calculating such parameter, it is possible to know how strong the density grating formation is in the cloud along a certain axis. It can take values between zero, when the atoms are uniformly distributed with no detectable organised set, and one, when the atoms are periodically distributed with a $\sim \lambda/2$, or $\pi/\boldsymbol{k}_0$, spacing between bunches of atoms (given $\boldsymbol{k} \approx -\boldsymbol{k}_0$).

The bunching produced by all the atoms contained in a cold cloud is described by the following expression:

$$M(\boldsymbol{k}, t) = \frac{1}{N} \sum_{j=1}^{N} e^{i(\boldsymbol{k}_0 - \boldsymbol{k}) \cdot \boldsymbol{r}_j(t)}, \tag{2.6}$$

where $r_j(t)$ is the position of a particle at a certain time, $\boldsymbol{k}_0$ and $\boldsymbol{k}$ are the wavevectors of the incident field and the scattered modes, respectively. The bunching derivation for both models is provided in: the appendix of one of the aggregated paper [160] in Sec. 5.3 for the scalar system, and Sec. B.III of the chapter Appendices for the vectorial case.

The bunching parameter appears in the expression of the light intensity scattered in the direction $\boldsymbol{k}$, through the following expression.

$$I_s(\boldsymbol{k}) = I_1 N^2 P |M(\boldsymbol{k}, t)|^2, \tag{2.7}$$

where $I_1 = (\hbar\omega_0\Gamma/8\pi r^2)(\Omega_0/2\Delta_0)^2$ is the single-atom Rayleigh scattering intensity, the parameter P is manually introduced to distinguish between the scalar ($P = 1$) and the vectorial ($P = \sin^2\psi$) models, and ψ is the angle between the pump vector and a scattering direction.

On the one hand, the only step required to achieve an analytical expression for a bidimensional system is to considerer the radiation mode with two components $\boldsymbol{k} = k\sin\theta\hat{x} + k\cos\theta\hat{z}$, and the optical field propagation along $\boldsymbol{k}_0 = k_0\hat{z}$. Then, these two considerations are both included in Eq. (2.6) to obtain the polar expression of the bunching

$$M(k,t) = \frac{1}{N}\sum_{j=1}^{N} e^{-i[\,(\sin\theta)kx_j(t)\,-\,(k_0 - k\cos\theta)z_j(t)\,]} \tag{2.8}$$

The two orthogonal components of the plane are represented by x_j and z_j, where the second component belongs to the axis along which the pump field propagates. It would be possible to attain a polar plane intensity profile inserting Eq.(2.8) into Eq. (2.7), but such intensity will no be displayed throughout this dissertation. On the other hand, the bunching profile is also investigated in three-dimensional radiation pattern for a 3D cloud. To attain such an expression, it is enough to transform the bunching equation (2.6) into spherical coordinates, which renders

$$M(k,t) = \frac{1}{N}\sum_{j=1}^{N} e^{-i[\,(\sin\theta\cos\varphi)\,kx_j(t)\,+\,(\sin\theta\sin\varphi)\,ky_j(t)\,-\,(k_0 - k\cos\theta)\,z_j(t)\,]} \tag{2.9}$$

Again, the propagation of the optical field occurs along the z axis and an intensity profile could be calculated if the expression (2.9) were to be applied into Eq. (2.7).

There are three direction cosines that are contained in three possible planes of the this last three-dimensional case. In sub-section 2.5, 2.6 and 2.7, the 3D lobes representing the bunching formation are accompanied by each of the 2D Bunching factor calculations for each one of these cardinal planes. Such bidimensional bunching pictures are obtained scanning the radial angle $0 < \varphi < 2\pi$ and the azimuthal angle $0 < \theta < \pi$ (using an extended range until 2π) in the conversion of the scattered wave vector into spherical coordinates $\boldsymbol{k} = k(\sin\theta\cos\varphi, \sin\theta\sin\varphi, \cos\theta)$. The values to see the emission in each plane are:

- For (x,z) plane: setting $\varphi = 0$, gives $\hat{k} = (\sin\theta, 0, \cos\theta)$.

- For (y, z) plane: fixing $\varphi = \pi/2$, yields $\hat{k} = (0, \sin\theta, \cos\theta)$.
- For (x, y) plane: assuming $\theta = \pi/2$, renders $\hat{k} = (\cos\varphi, \sin\varphi, 0)$.

2.3 Particle interaction inside an atomic cloud

The concept of particles interacting in vapour was first introduced by Johannes Diderick van der Waals in his PhD thesis in 1873 [161] and was described and published by Maxwell in [162]. The scientist proposed a model that modified the ideal gas law, a system of non-interacting particles, which explains the effective interactions between particles. For this reason, the known particles interacting forces or intermolecular forces are sometimes regarded as "van der Waals forces". Due to the significance of the discovery, van der Waals was awarded the Physics' Nobel prize in 1910 [163].

The way in which atoms interact with each other plays a fundamental role in the numerical resolution of the equations of motion of a system. If only two atoms in a system made up of a few thousand of them get too close, the whole system runs the risk of exploding like a bomb; all particles start escaping radially from the cloud in a very short time. For instance, considering the motion equations for the scalar model (2.1) and (2.2), and imagining that atoms j and m reduce the distance between them to a value in the order of $k_0 r_{jm} \sim 10^{-5}$, the short term $1/(k_0 r_{jm})^2$, gathered in the force expression (2.2), soars to the ridiculous value of 10^{10}; leading to a system melt down. The situation gets even worse in the vectorial model, where there are two additional terms that described the interaction between atoms at even shorter distances ($1/(k_0 r_{jm})^n$ with $n = 3, 4$). Therefore, it is imperative to add a save mechanism that prevents the system from leaking atoms.

In this section, two strategies are proposed: the Lennard-Jones potential and the Plummer's idea. The first one is a formal solution, according to a well-known intermolecular potential energy between a pair of neutral atoms or molecules. The second is a more recent method applied to atomic physics, although it is a concept that is commonly used in gravitational simulations. This latter method achieve a less realistic but reliable result, with a lower cost in computational time, compared to the previous orthodox solution.

2.3.1 Repulsive short-range potential

To avoid the complex situation that arises when atoms get too close to each other, it is necessary to implement a short-range repulsive pair potential[4] in the system dynamics. In a situation where no other forces are present, the atoms in a cloud have two types of interactions, either they repeal or attract each other. The repulsion between a pair of atoms is a consequence of the repulsion between two atoms that occurs when the two clouds of electrons that surround each of the nuclei

---

[4] Besides the pair potentials, there are other kind of potentials, labelled as "many-body potentials", where the system dynamics is calculated for more than a pair of particles. However, since the approach here used is semi-classical, there is no need to go deeper than the pair interaction.

of the two particles repel each other. However, atoms can simply be seen as two hard spheres that undergo an elastic collision with each other. The attraction is due to the momentary dipoles emerging from electronic fluctuations in the cloud, whenever the atoms undergo electronic excitation or decay.

There are two classical options when it comes to short-range potentials in order to calculate van der Waals forces, these are: the Morse potential [164] and the Lennard-Jones potential [165]. There exist a third commonly known option, regarded as Kratzer potential [166], which was introduced to described the inter-atomic vibration and rotation of diatomic molecules; represents an important model interaction in quantum physics, because it allows an exact solution of the Schrödinger equation. However, given that the model developed throughout this thesis is semi-classical, this third option can be ruled out. Long-range attraction and short-range repulsion between a pair of atoms is accounted for in the other two possible candidates, both having a couple of adjustable parameters. The Morse potential was initially conceived to describe the interaction between two particles (or between a particle and a surface), generally representing the dynamics of a covalent bond[5] binding two atoms into a molecule, which does not make this potential the best choice either. The Lennard-Jones potential is left as the most appropriate candidate for the given system. This option is the simplest and most used of the trio presented when it comes to representing such interactions. The form of the Lennard-Jones potential is delineated in Fig. 2.3. If the readers needs to deepen their knowledge on the matter, a couple of single-authored studies from the same scientist, comparing Morse and Lennard-Jones potentials, can be found in Refs. [167, 168].

This simple pair potential can accurately characterize the repulsive-attractive interactions caused by van der Waals forces betwen neutral atoms, and when it is applied in the CARL equations, it allows to counteract the singularities that eventually arise from the proximity of pairs of atoms caused by the bunching effect. The potential form depicted in Fig 2.3 is analytically defined as

$$V_{LJ} = 4\eta \left[\left(\frac{\sigma}{r} \right)^{12} - \left(\frac{\sigma}{r} \right)^{6} \right] = \eta \left[\left(\frac{r_m}{r} \right)^{12} - 2 \left(\frac{r_m}{r} \right)^{6} \right], \tag{2.10}$$

where the aforementioned adjustable parameters are η, representing the bonding energy or potential depth, and σ, characterizing the bond length or the finite distance at which the repulsive potential is zero. The distance between the particles is symbolized by the variable r and the distance at which the potential reaches its minimum,[6]where the repulsive and attractive terms compensate each other, is symbolized by r_m. The first term, related to the repulsive force and dominant at short-range, decays faster than the second one, linked to the weak van der Waals attractive force and which governs the interaction over longer ranges.

The positive aspects coming from the application the Lennard-Jones potential are that it allows to control what is the value of the potential depth η and where it begins to work as a repulsive mechanism σ. For the boundary value σ, where

---

[5] A covalent bond is a chemical bond that involves sharing electron pairs between atoms

[6] The minimum value of the potential r_{jm} is related to the bond length σ as $r_m = 2^{1/6}\sigma$.

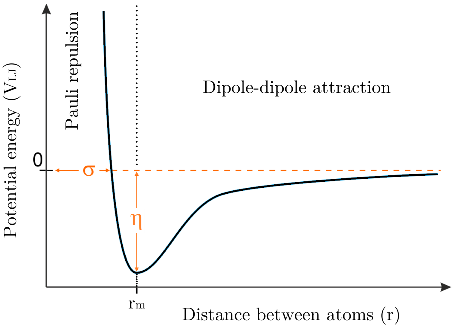

Figure 2.3: Schematics of the Lennard-Jones potential characterized using the separation between a couple of particles as the independent variable. There are two regions of action, dipole-dipole attraction and repulsion, separated by a black dotted line that coincides with the distance r_m at which the two action are equivalent to each. The two tunable parameters are: the minimum potential η, located at distance r_m and separating the two regions, and the effective distance σ, which represent the potential repulsion V_{LJ} is zero and where the effective repulsion begins.

the effective repulsion begins, the usual parameter to use is the scattering length a, which is set to be around $100nm$ for the D2-line transition of ^{85}Rb. The value can be derived from the formula connecting the cross section σ_{cs} and the scattering length a for bosons $\sigma_{cs} = 8\pi a^2$ [22], where the cross section for the exploited element is approximately $10^{-9}cm^2$ [24]. Nonetheless, the Lennard-Jones does not account for all long-range interactions, disappearing for an infinite distance and becoming almost zero for distances not too great, but it is sufficient for the case under study, since the main scope is to introduce a repulsion mechanism between particles.

2.3.2 Minimum inter-particle distance definition

Instead of taking into accounting the entire calculation of a short-range potential, another less orthodox option is proposed in terms of how to describe repulsion between atomic pairs. The idea is to add a constant minimum distance between atoms, which is computationally easier to calculate than the repulsive effect for every couple of atoms at each time-step. The concept comes from astrophysics, where is used in the numerical resolution of the gravitational force in stellar systems (e.g., galaxies or star clusters), which are not very different from an atomic cloud computationally speaking. The method slightly decreases the realism of the model, but substantially improves its calculation times. There are several self-consistent models: starting with the first ones considering galaxies (clouds) as spherical, based on the pioneer Plummer model [169] of the first decade of the 20th century, up to the contemporaries considering more complex elliptical sets and additional aspects.

A couple of rich reviews on the matter can be found in Ref. [170, 171]. The idea of this model is to avoid singularity points in the system, which lately, continuing with galaxies, have been located in central black holes and/or dark halos.

Nowadays, due to increased computational power and better knowledge of the physics of many bodies, this model is being exploited more and more frequently. In this work, Plummer's idea is simplified using a similar concept to avoid the singularity-like reaction generated for short-range terms ($1/r_{jm}^n$ with $n \geq 2$) in Eqs. (2.2) and (2.5). A limit or cut-off ξ is defined and added to the distance between particles

$$r_{jm} \rightarrow \sqrt{r_{jm}^2 + \xi^2} \tag{2.11}$$

to force the existence of a minimum value, thus avoiding the smaller values that can fragment the system. The term $r_{jm} = |\boldsymbol{r}_j - \boldsymbol{r}_m|$, simply represents the distance between two atoms of the cloud; more information on that variable will be given in the coming subsection 2.4.1.

The parameter ξ does not affect the behaviour of the particles in the system when they are separated at great distances and works as if there were a repulsive effect, generated by van der Waals forces, whenever two particles meet. In the real picture, the particles undergo an overlapping crossover, which can be explained as a virtual elastic collision. This term prevents the force value from rising above a certain threshold, keeping it constant inside the imaginary sphere with radius ξ until it begins to decrease when the colliding particles move away from each other. It can be stated that the defined cut-off acts as the numerical scattering length.

2.4 Settings for the numerical solutions

Until a few years ago, computing power was not available to everyone, when it existed. Modelling large particle systems in geometries larger than one dimension could be considerably expensive in terms of time or computational power, even solving a one-dimensional system with many particles was far-fetched. Today, on the contrary, the subject is quite accessible to the public, being more economical to acquire a greater computational power to solve numerically systems of many particles. However, the more powerful the available computers become, the more is needed to compute N-body systems with greater complexity and/or larger size. That is why it is important to choose wisely the software or, more precisely, the algorithm with the best resolution capabilities to achieve a numerical solution.

Numerical algorithms for N-body simulations began as a tool for calculating the dynamics of particle systems in astrophysics, for example, involving long-range interactions between particles [172]. However, they have become crucial tools for understanding the various areas of physics and other sciences, such as plasma physics, nuclear physics and meteorology, any type of engineering or the entire discipline of biology. When it comes to studying the evolution of atomic/molecular systems, they are beginning to be recognized as an important tool, being then referred to as “molecular dynamics” (MD) codes, due to extended use in biology. These type of codes or algorithms can solve complex systems of micro-organisms describing their complex dynamics and behaviours. Today, in the 2020s, these codes are widely used and many of them are conceived as "open access" codes (no royalties or fees are required to use them). Nonetheless, as noted in [160]—attached paper in Sec. 5.2—, *"MD codes have not been used in the study of light interacting with cold atomic gases"*. Sometimes this MD codes are part of an open access algorithm, and sometimes they can be composed of specific functions of particular (or many) coding languages, i.e., ODE functions (see segment Optimized differential equation solving functions in subsection 2.4.2 on page 46).

The first part of this section is reserved for an even more important task, which is a prerequisite to implementing the algorithm. It is a reordering of the analytical equations to be solved, which allows a better implementation of the MD algorithm. The equations of the dynamics of motion suggested in Sec. 2.2 need to be scaled and redefined in other to simplify their calculation; speeding up each iteration the time needed to achieve the final solution. At the end of this first subsection, a short segment is devoted to establishing and defining the parameters involved in the new scaled equations. In the second part of the section, three possible numerical tools that have been used in this thesis are announced and explained; along with a brief definition of what is considered a symplectic algorithm. In addition, this part also presents a small segment dedicated to exposing the chosen algorithm and the configuration of the selected simulations.

2.4.1 Scaling equations of motion for both models

The equations of motion for both scalar and vectorial models must be scaled to avoid increasing the numerical error. This can be achieved by working with dimensionless variables with smaller absolute values, when it comes to position, momentum, and time. Following the change of variables proposed in Ref. [160] (or Sec. 5.2):

- The position vector of each atom is now scaled with the wavevector of the incident light, like $\boldsymbol{r}' = k_0\boldsymbol{r}$. Therefore, when $\boldsymbol{r}' = 1$ is mentioned, it will represent $\lambda/2\pi$.

- The momentum variable is redefined as $\boldsymbol{p}' = \boldsymbol{p}p_0^{-1}$, hence normalizing the atomic momentum to the momentum of an incident single photon $p_0 = \hbar k_0$.

- The new time variable is $t' = \omega_r t$, where $\omega_r = \hbar k_0^2/2M$ is the atomic recoil frequency.

All variables with a "prime" notation will be from now on referred as variables without prime, i.e, r' will become r, but still in representation of $k_0 r$.

Scalar Model

The new variables are introduced in the scalar model described in Eqs. (2.1) and (2.2), obtaining a new set of computational equations:

$$\dot{\boldsymbol{r}}_j = 2\boldsymbol{p}_j \ , \tag{2.12}$$

$$\dot{\boldsymbol{p}}_j = A \sum_{m\neq j} \left\{ (\hat{\boldsymbol{z}} - \hat{\boldsymbol{r}}_{jm}) \frac{\sin[r_{jm} - z_{jm}]}{r_{jm}} - \hat{\boldsymbol{r}}_{jm} \frac{\cos[r_{jm} - z_{jm}]}{r_{jm}^2} \right\} , \tag{2.13}$$

with the constant parameter A being the same parameter defined in Eq. (2.3), but now slightly modified as

$$A = \frac{\Gamma}{\omega_r} \left(\frac{\Omega_0}{2\Delta_0} \right)^2 , \tag{2.14}$$

due to the changes of variable; thus becoming a dimensionless constant. Moreover, the distance between two atoms r_{jm} has actually been rescaled employing the singularity-avoiding parameter to $r_{jm} \to (r_{jm}^2 + \xi'^2)^{1/2}$; the cut-off parameter being also rescaled as $\xi' = k_0 \xi$ and later on simply regarded as ξ.

Vectorial Model

The same transformations are applied to the vectorial model, ending with the following equations of motion:

$$\dot{\boldsymbol{r}}_j = 2\boldsymbol{p}_j \ , \tag{2.15}$$

$$\begin{aligned} \dot{\boldsymbol{p}}_j = A \sum_{\alpha,\beta} (\hat{\epsilon}_{0\alpha}^* \hat{\epsilon}_{0\beta}) \sum_{m\neq j} \Bigg\{ & (\hat{\boldsymbol{z}} - \hat{\boldsymbol{r}}_{jm}) (\delta_{\alpha\beta} - \hat{r}_\alpha \hat{r}_\beta) \frac{\sin[r_{jm} - z_{jm}]}{r_{jm}} \\ & + [\hat{\boldsymbol{z}} (\delta_{\alpha\beta} - 3\hat{r}_\alpha \hat{r}_\beta) - 2\hat{\boldsymbol{r}}_{jm} (\delta_{\alpha\beta} - 2\hat{r}_\alpha \hat{r}_\beta)] \frac{\cos[r_{jm} - z_{jm}]}{r_{jm}^2} \\ & - (\hat{\boldsymbol{z}} - 3\hat{\boldsymbol{r}}_{jm}) (\delta_{\alpha\beta} - 3\hat{r}_\alpha \hat{r}_\beta) \frac{\sin[r_{jm} - z_{jm}]}{r_{jm}^3} \\ & + 3\hat{\boldsymbol{r}}_{jm} (\delta_{\alpha\beta} - 3\hat{r}_\alpha \hat{r}_\beta) \frac{\cos[r_{jm} - z_{jm}]}{r_{jm}^4} \Bigg\} , \end{aligned} \tag{2.16}$$

where the constant parameter A is same as in the scalar case, presented in Eq. (2.14); the same goes for the cut-off parameter ξ.

Scaling the Bunching equations

Even with a not so large detuning, it is possible to make an additional approximation for the wavevectors of the field and the electronic transition, $|\boldsymbol{k}| \approx |\boldsymbol{k}_0|$. By adding such approximation to the one applied to the positions of the atoms, it is possible to scale the bunching in Eq. (2.8) for a 2D system as

$$M(t) = \frac{1}{N} \sum_{j=1}^{N} e^{-i[\,(\sin\theta) x_j(t) \,+\, (1-\cos\theta) z_j(t)\,]} , \tag{2.17}$$

and the one expressed in Eq. (2.9) for a tridimensional cold gas as

$$M(k,t) = \frac{1}{N}\sum_{j=1}^{N} e^{-i[\,(\sin\theta\cos\varphi)\,x_j(t) + (\sin\theta\sin\varphi)\,y_j(t) - (1-\cos\theta)\,z_j(t)\,]}. \tag{2.18}$$

The last two equations are the same expressions represented in Sec.2.2.3 —Eqs.(2.8) and (2.9), respectively—, but they are basically represented for future references.

Parameter definition for the scaled equations

One of the scopes of this doctoral thesis is to model and physically represent systems in interaction, in this case cold atoms, in order to obtain detailed information on their dynamics. The procedure requires integrating Newtonian equations of motion over a long period of time, using some specific initial conditions and predefined parameters. The atomic clouds studied in free space can be thought of as two- or three-dimensional systems, containing $N = 5 \cdot 10^3$ or $N = 10^4$, respectively. Real systems have a much larger number of atoms (typically $N = 10^{10}$). The numerical results can be scaled to larger system, for instance increasing N and the cloud's size, keeping constant the density or the optical thickness. There are common variables for both atomic ensembles and for the sake of simplicity, trying to avoid describing the same parameters present in expressions 2.12, 2.13, 2.14, 2.15, 2.16, 2.17, and 2.18 —,over and over again, they are listed here:

- From the decay time of the D2-line transition of ^{85}Rb, $\tau = 26ns$, it is possible to set the atomic decay rate to $\Gamma = 1/\tau \approx 3.8 \cdot 10^7 s^{-1}$.
- The recoil frequency that changes the time in a dimensionless variable is $\omega_r = \hbar k_0^2/2M \approx 2.3 \cdot 10^4 s^{-1}$.
- The constant characterized in Eq. 2.3 is simplified to $A = 1$, and adding the parameters defined above, the same equation shows the relationship between detuning and the pump field as $|\Delta_0| \approx 20\Omega_0$. Consequently the normalized detuning value is defined as $|\delta| = 20\Omega_0/\Gamma$.

A main distinction has been made when setting the value of the cut-off parameter ξ in each of the models. The value has been set to $\xi = 1$ due to the presence of higher order short-range terms in the vector model, while the scalar model can employ a smaller limit of $\xi = 10^{-2}$. This implies that the effective scattering length of the atoms is different depending on the model employed, approaching the wavelength for the vectorial model $\sim \lambda_0$ and $\sim 10^{-2}\lambda_0$ for the scalar one.[7] If the additional short-range are manually suppressed (forcing them to be zero) the value used for the vectorial case approximates the one employed for the scalar one; exposing the source of divergence between models. If a lower value is defined for the singularity-avoiding parameter, the cloud will experience a slow but constant expansion, caused by a large value of the force equation, due to the small distance between the atoms.

---

[7] The distance $r = \lambda_0$ is equal to 2π due to the change of variables applied to the position $k_0 r = (2\pi/\lambda_0)r$.

2.4.2 Simulation algorithms and ODE functions

Now that the form of the system of equations for the scalar and vector model has been adapted to facilitate its implementation in MD codes, there is still a need to define the tools that will be used to solve them, i.e., showing the time evolution for each system. Personal computers, in the current year 2020, are very powerful machines with a huge capacity to perform billions of operations per second, but they are still very simple machines in terms of algebraic capabilities. Since they work with a simple binary system of “0” and “1”, which basically allows them to do addition and subtraction operations, they excel at calculating any analytic equation by doing exactly that, adding and subtracting terms. As a result, the most robust algorithms are those that are based on these two algebraic operations, making a differential equation one of the most suitable and prolific mathematical expressions to be solved using a computer. These types of equations represent the counterpart of an integration, relating one or more functions or variables to their derivatives or changing ratios. Conversely, integrations are nothing more than sums of infinitesimally small differential increments from point a to point b of a specific mathematical function. Therefore, two integration methods —Verlet velocity and Leapforg algorithm— are introduced in the current subsection, along with some predefined functions, which are generally used to solve ordinary differential equations in modern programming languages.

Verlet velocity

Probably the most famous MD’s model for computer simulation, the Verlet integration (or Verlet algorithm), was introduced in 1960s by one of the MD computation pioneers Loup Verlet in [173]. Verlet used the Lennard-Jones potential as the repellent mechanism to study the inter-particle interactions of many-body systems. It was not actually the first time the algorithm was used, which originally dates back to 18^{th} and had already been employed in the early 1900s, but it was the first time the algorithm was applied to computers.

The idea is based on the calculation of the Taylor expansion for the third-order derivative position, both in the forward and backward direction of time, thus obtaining the following expression:

$$\boldsymbol{r}(t+\Delta t) = \boldsymbol{r}(t) + \boldsymbol{v}(t)\Delta t + \frac{1}{2}\boldsymbol{a}(t)\Delta t^2 + \frac{1}{6}\boldsymbol{b}(t)\Delta t^3 + \mathcal{O}(\Delta t^4), \tag{2.19}$$

$$\boldsymbol{r}(t-\Delta t) = \boldsymbol{r}(t) - \boldsymbol{v}(t)\Delta t + \frac{1}{2}\boldsymbol{a}(t)\Delta t^2 - \frac{1}{6}\boldsymbol{b}(t)\Delta t^3 + \mathcal{O}(\Delta t^4). \tag{2.20}$$

The position, velocity, and acceleration of each particle at a certain time are represented, by $\boldsymbol{r}(t)$, $\boldsymbol{v}(t)$ and $\boldsymbol{a}(t)$, respectively. The time-step increment, or expansion point is normally set with the range $0 < \Delta t < 1$. The $\boldsymbol{b}(t)$ represent the jerk or jolt, the rate at which the acceleration of an object changes with respect to time or $\boldsymbol{b}(t) = \dot{\boldsymbol{a}}(t)$. The last term $\mathcal{O}(\Delta t^4)$, simply represent the next higher other of the expansion proportional to Δt^4 (and the derivative of the jolt).

Afterwards, these two expressions are added, leading into the general form of the Verlet algorithm:

$$\boldsymbol{r}(t+\Delta t) = 2\boldsymbol{r}(t) - \boldsymbol{r}(t-\Delta t) + \boldsymbol{a}(t)\Delta t^2 + \mathcal{O}(\Delta t^4). \tag{2.21}$$

This analytical expression can be transformed into a discrete iterative equation that allows the position to be obtained from a set of initial conditions, for example, random initial position and zero initial acceleration for each particle. From there, and considering a sequence with a total of "n" sampling points, $t_n = n\,\Delta t$, the position of an atom at time-step n can be extracted from the expression:

$$\boldsymbol{r}_{n+1} = 2\boldsymbol{r}_n - \boldsymbol{r}_{n-1} + \boldsymbol{a}_n\Delta t^2; \tag{2.22}$$

being the past step represented by $n-1$, the present step with n, and the future resulting step as $n+1$.

In this work, the collective light scattering of a cold 2D or 3D atomic cloud is studied, but to describe the scattering picture of the entire system, it is necessary to calculate the positions and velocities of the atoms. The problem with the Verlet algorithm is that the velocity is not calculated explicitly because it is not needed to obtain the temporal evolution of the system, which makes this system suboptimal for the investigated case. Nevertheless, the velocity of each atom in the gas can be calculated at any time from its past and future position. Taking the last expression (2.22), this velocity is calculated considering the previous and next iteration position

$$\boldsymbol{v}_n = \frac{\boldsymbol{r}_{n+1} - \boldsymbol{r}_{n-1}}{2\Delta t}. \tag{2.23}$$

The downside of using this method to calculated the velocity is that the algorithm's truncation error (or local error) increases from $\mathcal{O}(\Delta t^4)$, for positions, to $\mathcal{O}(\Delta t^2)$, for velocities. The solution to this problem comes with a slight modification of the algorithm, which is labelled as Verlet velocity and in which the velocity calculation does not compromise the truncate error of the position Δt^3. Thus, using the same discrete total time $t_n = n\,\Delta t$, the system position and velocity for any atom can be perfectly represented by:

$$\boldsymbol{r}_{n+1} = \boldsymbol{r}_n + \boldsymbol{v}_n\Delta t + \frac{1}{2}\boldsymbol{a}_n\Delta t^2, \tag{2.24}$$

$$\boldsymbol{v}_{n+1} = \boldsymbol{v}_n + \frac{\boldsymbol{a}_n + \boldsymbol{a}_{n+1}}{2}\Delta t. \tag{2.25}$$

This improvement is generally chosen over the original form of the integration method.

There are two main drawbacks that arise from the whole Verlet integration method: the first one is that the acceleration $\boldsymbol{a}_n$ only depends on the position $\boldsymbol{r}_n$, being completely independent from $\boldsymbol{v}_n$; and the second one is that if the calculated velocity is stored, which is not always necessary, the algorithm becomes slower. Another important flaw of this algorithm is that despite having a better truncation error with its second version, the global error in both Verlet integration and Verlet velocity is exactly the same $\mathcal{O}(\Delta t^2)$ (see [174] for a good clarification on this otherwise confusing, matter). However, this recursive method improves on the most basic algorithm available, the Euler method[8], providing stable numerical solutions, reversibility and "conservation" of its symplectic (concept reviewed later on page 45) form in the phase space.

Leapfrog algorithm

The previous algorithm has been used in one of the publications related to this thesis [160] (attached in Sec. 5.2), where this method is implemented in a molecular dynamics code coined as PEPC (Pretty Efficient Parallel Coulomb Solver) [175] to trace the trajectories of atoms in a cold gas. The PEPC solver is a parallel sorting algorithm that is used to to obtain the best performance from of the Verlet velocity algorithm, but several settings must be adjusted. Since many of these parameters do not need to be used in the current system, the simulations presented in this dissertation have been done with another algorithm, called the Leapfrog algorithm. It is an algorithm rather easy to implement in any programming language and, as the Verlet velocity, is a symplectic method faster than the Euler method; being second-order accurate ($\mathcal{O}(\Delta t^2)$).

It is not clear who introduced the leapfrog algorithm, but some early references to this method can be found in the first volume of *The Feynman Lectures on Physics* [176] from the 1960s. It was popularized in the 1980s by the hands of Hockney and Eastwood [177]. In the Leapfrog technique, velocity and position are not calculated in the same time step, there is a half-step lag between them. The study of the evolution of a system with particles begins by establishing the initial positions, then the velocity (*leaps*) over the positions, then making the velocity *leap* over the position, and so on until the desired time steps are acquired. See Fig. 2.4 for a graphical overview.

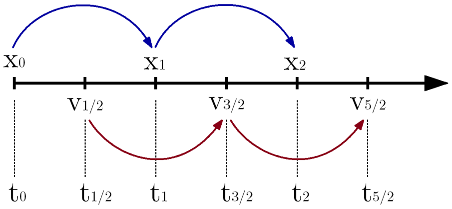

Figure 2.4: Schematics that describes how the leapfrog algorithm works. Position and velocity jump one over the other, repeatedly until the predefined simulation steps are reached. Position, velocity, and time are symbolized by x, v and t, respectively, where the subscripts represent the time step.

A brief example is now represented using an oversimplification of the expression used to solve CARL with an scalar optical field, Eqs. (2.12) and (2.13). A single

---

[8] The Euler method is a first-order numerical method for solving non-stochastic differential equations. It has a local error of $\mathcal{O}(\Delta t^2)$ and a global error of $\mathcal{O}(\Delta t)$

direction of motion is allowed, in a reduced system composed of only two atoms, generating the following equations of motion:

$$\dot{z}_j = 2v_j \ , \tag{2.26}$$

$$\dot{v}_j = -\frac{1}{(z_j - z_m)^2}. \tag{2.27}$$

The changes of variable $\boldsymbol{r}' = k_0\boldsymbol{r}$ and $|\boldsymbol{r}_{jm}| = |\boldsymbol{r}_j - \boldsymbol{r}_m|$ have been undone. As a consequence, assuming $k_0 = 1$, $A = 1$ and choosing the direction along the z axis, the variables in the equation become: $\boldsymbol{r}'_j = \boldsymbol{z}'_j$, $\hat{\boldsymbol{r}}_{jm} = \hat{\boldsymbol{z}} = 1$ and $r'_{jm} = z'_{jm}$, which in turn defines $\cos(r'_{jm} - z'_{jm}) = 1$. In a further simplification of this example the m-particle is placed in a fixed position d. In this way, the calculation of the dynamics is directed to obtain the position z_j and the velocity v_j of the particle j, which respectively become z and v, giving the following system of equations:

$$\frac{dz(t)}{dt} = 2v(t) \ , \tag{2.28}$$

$$\frac{dv(t)}{dt} = -\frac{1}{[\, z(t) - d\,]^2}, \tag{2.29}$$

where the derivative expressions have been transformed from Newton's to Leibniz's notation and the implicit time dependence of the variables has been brought to light.

The system of equations is now transformed from its analytical form to a fully explicit numerical integration system, which is more suitable for the application of the Leapfrog algorithm:

$$\frac{z_{n+1} - z_n}{\Delta t} = 2\left(\frac{v_{n+1/2} + v_{n-1/2}}{2}\right) \ , \tag{2.30}$$

$$\frac{v_{n+1/2} - v_{n-1/2}}{\Delta t} = -\frac{1}{[\,\frac{z_{n+1}+z_n}{2} - d\,]^2}, \tag{2.31}$$

where the current time step of position z is represented by z_n and the subsequent velocity time step is referred as $v_{n+1/2}$. Finally, the recurring leapfrog expressions to obtain the position and velocity of the only particle that is capable of moving are:

$$z_{n+1} = \left(v_{n+1/2} + v_{n-1/2}\right)\Delta t + z_n, \tag{2.32}$$

$$v_{n+1/2} = \frac{z_{n+1} - z_n}{2\Delta t} - \frac{2\Delta t}{\left(z_{n+1} + z_n + d\right)^2}. \tag{2.33}$$

To avoid inconsistencies, the initial values of the unknown time steps are set to be zero, e.g., the values of $v_{n+1/2}$, $v_{n-1/2}$ and z_{n+1}, are set to zero for the first iteration $n = 0$.

The leapfrog algorithm is less expensive, computationally speaking, than other numerical methods. Allowing particle drift to be calculated with a high level of precision (although not exact) and with very little compromise on the overall picture of energy conservation. This last fact represents a great advantage when calculating large systems with many particles, such as the cold gas that is studied in this thesis. In terms of memory usage, this method requires less storage than the well-known RK4 method of the Runge-Kutta family, whose introduction predates the computational times (between the 1890s and the early 1900s).

Symplectic algorithms

Both leapfrog and Verlet velocity are similar algorithms, because they are analytically identical, with few computational differences. The two of them are regarded as symplectic and time-reversible numerical methods. A numerical method that conserves the total energy, or more accurately its Hamiltonian, is generally considered a symplectic algorithm; and a time-reversible numerical integration method means that when the algorithm takes k steps forward in time followed by k steps backwards in time, it reaches the same starting point. These two features are desirable when choosing an algorithm, because they help to reflect the physical reality of a particular simulation. In this sort of algorithm, the time-step is fixed and constant throughout the entire simulation. The application of these characteristics to the simulated dynamics of a cloud of atoms, allows to control the position and velocity of every atom in each iteration step of the way. In this way, the long-time numerical solution achieved for the whole cloud can be expected to be like the exact solution.

When talking about energy conservation, contrary to the popular believe, symplectic integrators do not exactly conserve energy. However, they are perfect candidates to properly handle a physical trajectory problem. Quoting from [178]: *"What symplectic integrators actually do is solve for a trajectory which rests on a symplectic manifold that is perturbed from the true solution's manifold by the truncation error"*. It basically means that when a system of particles is solved numerically using a symplectic algorithm, the trajectory of each element does not deviate "too much" from the exact analytical solution of that trajectory. The larger the drift, the more difficult it is to achieve conservation of energy, and symplectic integrators have a small drift, which grows linearly and is related to the floating-point error. Therefore, they can represent a closer trajectory than those obtained using other algorithms with higher drift (for example, Runge-Kutta of the 4th order or RK4). In summary, the resulting trajectories represented by this type of integrator do not exactly represent the true solution of the system in phase space, exposing a periodic energy difference —especially for long-term simulations—, but they are considered to be those who described a physical system in a more realistic way.

The two properties described above come at a price: lower precision and lower stability. Therefore, although symplectic methods are recommended when solving long-time integrations in relatively short simulation times, another algorithm must be implemented when it is necessary to obtain speeds and positions with very high precision. For example, solving with greater precision using more sophisticated and updated RK4 methods to reduce error, but paying the price with significantly longer simulation time.

In conclusion, a symplectic algorithm is perfect for solving the current cold gas radiated by a laser beam, because the objective pursued here is to see the organization of all the atoms present in this cold system. Although a small error will be made in the path that each of them will follow, it is not significant in the overall result, which is obtained with one of the best algorithms for energy conservation that can be achieved. Also, there is the advantage of obtaining a numerical solution, even for large systems, much faster than with other methods.

Optimized differential equation solving functions

Two well-known programming languages have been used throughout the current chapter, which deals with collective optomechanical effects in atomic clouds. The preliminary language used was MATLAB®,[9]a commonly used high-level programming language with many predefined functions, a simple structure, and intuitive coding. When the time has come to deal with a system that demands more computational power and efficiency, the language has changed to Julia[9], which is also a high-level coding language, but incorporating new processing techniques and tweaks from older computer languages. The latter language has recently been developed by the Massachusetts Institute of Technology (MIT) and is experiencing rapid growth.

On the one hand, MATLAB, developed in 1984, provides a quick tool to obtain a visual representation (graphics and videos) of the temporal evolution of a certain physical model in moderate computational time. Since it is a world-wide language, it is quite easy to find sample code that can help anyone avoid any programming hurdles they might encounter. Nevertheless, it has its limitations in terms of calculation speed, even though the issue has improved over the years. The problem is most evident when it comes to exploiting iterative algorithms (like the two introduced in the current subsection) to solve differential equations of complex systems. In that case, this programming language can get quite cumbersome or thick, making the numerical solving process slow for algorithms like leapfrog or Verlet velocity, although it does wonders with its built-in functions. For example, the CARL three-dimensional vector model for a few thousand particles requires a considerable amount of time to solve; the number of time steps achieved for the night simulation is too small to see meaningful results.

On the other hand, Julia, thanks to its novelty (it exists since 2012), has been able to combine an intuitive high-level coding structure with a very strong computing power when dealing with highly iterative codes. Therefore, unlike the first language, Julia provides a magnificent tool to run MD codes using iterative algorithms [179], such as leapfrog integration. In addition, it is an open access software; there is no need to pay to use it and the root code is available for modification by the public. These are some of the reasons why this more contemporary programming language has been used to simulate the CARL effect on large two-dimensional and three-dimensional particle systems. Julia's main disadvantage for its novelty is that there is not as much support available on the internet as in MATLAB,

---

[9] In digital version: click language's name to check the developer's website

although the manuals and examples are increasing exponentially, especially in the last couple of years. A nice benefit of using Julia is that it provides the ability to work with multiple threads[10]; the feature has been recently incorporated by MATLAB but it is not as easy to implement as in Julia. This is not the same as multithreaded programming, which involves parallel programming and a more advanced understanding of the coding language, which can be quite cumbersome. Another interesting advantage in Julia is that both the Verlet velocity and the leapfrog algorithm can be found in pre-defined functions, which speeds up the coding part, since it is not necessary to obtain a specific discrete iterative expression of the equations of motion.

What both coding languages have in common is that they both have several functions that are specially designed to solve ordinary differential equations (ODE) and stochastic differential equations (SDE). The way the functions work is transparent in Julia and not so much in MATLAB, but in addition to that, they were developed to efficiently solve a specific type of differential equation in both languages —it is the author's personal opinion that Julia has outdone MATLAB with the number of functions available to solve these types of equations; A link can be found in Ref. [180]—. In summary, the functions tested are $ode45$ for MATLAB[181], together with $Tsit5$ (both are adaptive 5^{th} order Runge-Kutta methods) and $KuttaPRK2p5$ for the Julia programs [182]. In particular, $KuttaPRK2p5$ is a function that works very fast because it is, quoting from description manual [182]: *"a 5 parallel, 2 processor explicit Runge-Kutta method of 5th order"*.

In conclusion, Julia provides access to predefined symplectic algorithm function packages, including a hybrid algorithm composed of the two methods mentioned above and additional ones with greater precision [180]. These higher-order methods are obviously slower than leapfrog and Verlet velocity, but with less error in the computation of the trajectories. These packages are a great advantage when using Julia because the coding process can be very fast, since it is not necessary to adapt the differential equation with a recurring expression (as perform with the leapfrog example earlier). Additionally, they have proven to be the fastest option when computing time is considered.

Settings and algorithms employed in the simulations

In a similar way to what has been done when defining the physical variables that intervene in the equations of the models to be solved numerically (see page 40), in segment "*Parameter definition for the scaled equations*", it is also important to define the parameters and conditions of the simulation. The dimensionless time-step has been fixed to $\delta t = 10^{-3}$ and the total simulation time has been set at $t = 0.3$, which produces a total of 300 steps and represent a total real time of $t = 0.3\omega_r^{-1} =\approx 70\mu s$. The time steps used in [160] is roughly 6 times smaller, but using such time interval simply increases the simulation time with no visual impact

---

[10] Programs can decide themselves into two or more task which can execute simultaneously and they are referred as thread of execution ore threads. It is common for computer to have at least two threads for core.

in the results. Although several pre-defined functions and different symplectic algorithms have been announced, all simulation are finally solved using Julia's hybrid predefined function "VerletLeapfrog" [180]. However, other predefined functions and an additional symplectic algorithms have been used to check the consistency of the results presented.

2.4.3 Outline of the presentation of results

All the necessary tools to produces some numerical results have already been presented and it is now possible to visualize the numerical solutions obtained from the two (scalar and vectorial) models. There are several variables that can be adjusted to obtain various results by holding the system parameters (such as, pump frequency, detuning, etc) fixed, for instance: the number of spatial dimensions of the gas (2D or 3D); the orientation of the cloud with respect to the incident laser beam, for the vectorial model, the polarization of the pump field; the shape of the cloud, being elliptical, which includes different degrees of elongation, or circular; and the density distribution of the atoms in the cloud (e.g., gaussian or uniform). There are other tunable settings that have already defined like: the number of atoms present in the cloud, which do not actually alter the results, but increase the clarity with which the particle rearrangement is presented and modulates the necessary simulation time; the number of atoms is set to $N = 5000$ and $N = 10000$ for the 2D and 3D systems, respectively; the type of interaction exploited when it comes to accounting for the internal interaction inside the cloud between pairs of particles, which is set to be the cut-off parameter ξ that has a different value when applied either to the scalar or the vectorial model, $\xi = 10^{-2}$ and $\xi = 1$, respectively.

To give a certain hierarchy to all the listed variables, the central concept that will allow characterizing such a complex system is the scalar or vectorial nature of the radiation field, thus respecting the two models introduced. That is why the numerical results will be presented in two main sub-sections: one that provides various simulations of the scalar model and another that exposes the new features introduced by the vector model. Inside in each of those sub-sections, two main segments will further subdivide the results between a 2D and a 3D system. Additionally, there is a third small subsection showing the time evolution of a typical cigar-shaped 3D atomic cloud parallel to the polarized external optical field.

Moreover, now that the simulation system have been defined, some information can be added to the data provided in previous segments *"Parameter definition for the scaled equations"* and *"Settings and algorithms employed in the simulations"*:

- A random seed has been introduced when defining the initial positions of the atoms inside both types of cloud: flat elliptical and volumetric ellipsoidal clouds. This seed makes the clouds with their major axis oriented along the external field direction axis (z axis), identical to their respective versions rotated 90°. The use of an initial Gaussian distribution for the positions seems to give similar results to the random case employed.

– A colormap has also been applied radially to the atomic distributions, both for the 2D and the 3D cases, to improve depth perception and to better distinguish pattern formation.

– The atoms have been given some transparency, which makes the groups of particles appear darker in both 2D and 3D cases.

– The central atoms of the system have been given a darker blackish brown hue, which gradually lightens until it reaches the orange hue of the outer ones.

– The external optical field, either with or without polarization vector, is always assumed to be along the z axis and comes from negatives values ("from the left side of the sheet of paper to the right side").

2.5 Scattering of scalar light in 2D or 3D cold atomic clouds

In this subsection, the results for the scalar model (Sec. 2.2.1) are shown, using its scaled version (Sec. 2.4.1); distinguishing between a two-dimensional space and a more realistic system with three dimensions. Within each of these two subdivisions it is possible to find different orientations of the system and variations in the shape of the cloud. The bunching parameter, which is described in Sec. 2.2.3 and with a scaled version presented in Sec. 2.4.1, is shown together with each simulation of a cloud.

2.5.1 Different pump orientations and cloud shapes in a bidimensional system

The study of such 2D systems can be followed in the published review [160] attached in Sec. 5.2. Aside from the fact that the atomic distributions are random in both studies, the simulations in that study differ from current research in the algorithm used to solve the dynamics of the system. While [160] used the PEPC algorithm [175] and the Verlet velocity symplectic method, the next subsection uses the Leapfrog algorithm and does not use any parallel solver. This could be the reason why, together with the initial random seed, the results obtained in [160] may show some differences from those shown in the current thesis. Nonetheless, the results achieved in the current thesis are qualitatively identical to those displayed in [160], hence validating both studies as numerical solutions for the investigated system. Although all the results shown are obtained with the numerical method leapfrog, which is explained in detail in Sec. 2.4.2, other alternative algorithms have been applied to perform a double check. These addition methods, considering higher orders of other symplectic algorithm, can be found in [180]) and some predefined Julia functions optimized to solve ordinary differential equations announced in Sec. 2.4.2 are available in [182].

Optical field parallel to the major axis of an elliptical cloud

The first case under scrutiny is also the most typical layout, where an elongated cloud is presented with its major axis parallel to the direction of the incoming external field (z axis). The atoms are randomly distributed in the cold vapour, which has a eccentricity of $\sqrt{3}/2$, with a semi-major axis of $k_0 z = 9$ and a semi-minor axis of $k_0 z = 4.5$. Defining this cloud allows preserving the geometric parameters used in [160] and/or Sec. 5.2.

In Fig. 2.5, two time instants are depicted: in the first one, shown in panel (a), the cold particles are placed in random locations inside the cloud at $t = 0$; and the second time instant, displayed in panel (b), shows the instant when the atoms develop the maximum bunching along the z axis, revealing the density grating announced in the detailed evolution of the CARL phenomenon on page 24. As detailed in this CARL evolution process, the 1D grating is formed because the scattered light (predominantly backward) encounters the forward radiation from the pump, already present in its direction of propagation. The two waves interference, generating a standing wave, which produce an optical potential that traps the atoms at its minima, with a spacing period $\approx \lambda/2$, or equivalently $\approx \pi/k_0$.

The radiation profile of the bunching formation for the initial distribution and the maximum manifestation of the CARL effect are shown respectively in panels (c) and (d) of the same Fig. 2.5. The main scattering lobe, in addition to that caused by laser radiation at 0°, results in the opposite direction, due to the geometry of the atomic cloud. The other smaller lobes, represented in random symmetric directions, are due to the non-negligible height of the cloud. If the cloud had an eccentricity closer to one, these small lobes would disappear.

On a sheet of paper, it is not possible to show every time step of the backscattered lobe evolution, without giving an overwhelming number of images which are totally unnecessary. However, by observing such evolution, it can be identified how this lobe grows from a small bulge, smaller than the harmonic modes represented in another angular direction different from 180° in Fig. 2.5(d), up to the main lobe pointing backwards in the same plot. Eventually, in future time frames, the atoms are pushed away in the direction of the pump [183], disintegrating the pattern into a chaotic whole and displacing the system's center of mass out of sight; towards the positive values of the z axis (or the right side of the sheet of paper). Conversely, a compression force is observed in the transverse direction with respect to the propagation of the laser, which generates a flattening effect on the thermal cloud of cold atoms. The mechanism originating this electrostrictive effect is not yet completely understood, although different descriptions of it have been proposed in refs. [184, 185].

The atomic dynamics of the cloud can be directly characterized with a single photon interaction image of a scattering event, where the incident photon $\hbar k_0 \hat{\boldsymbol{z}}$ interferes with the scattered photon $\pm\hbar k_0 \hat{\boldsymbol{z}}$ (due to $k \approx k_0$); creating a total momentum transfer in the scatterer of 0 or $2\hbar k_0$. Again, when looking at each time step, these two preferred scattering events can be easily detected, with about half of the atoms remaining immobile and the other half shifting towards the positive values of the z axis (right side of the page).

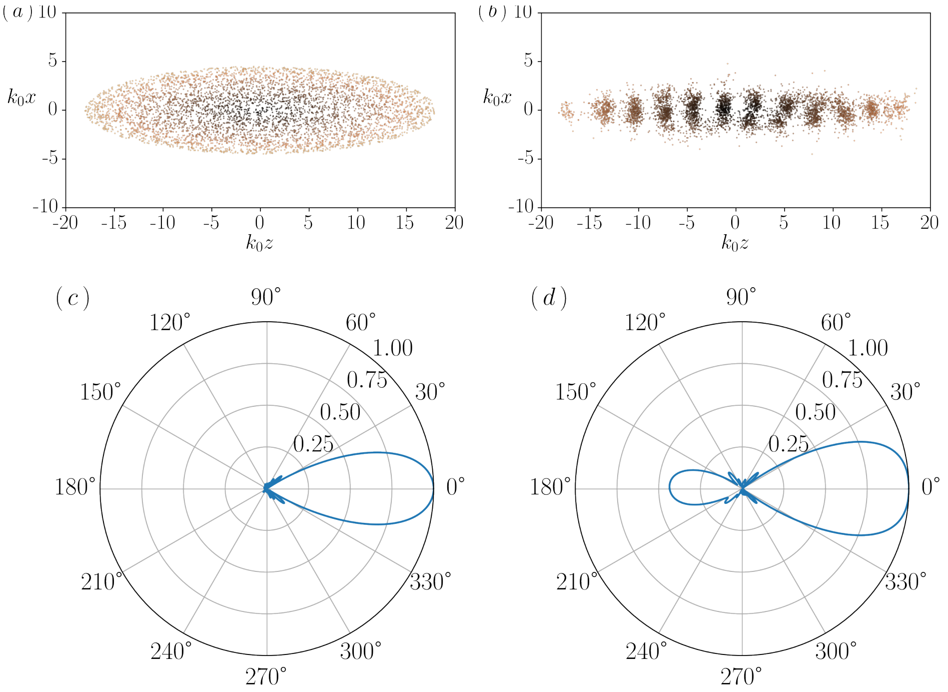

Figure 2.5: Collective scattering and pattern formation from an elliptical 2D atomic cloud irradiated with a scalar pump laser propagating parallel to its major axis: (a) Shows the initial atomic density distribution at $t = 0$ of $N = 5000$ atoms randomly distributed. (b) Depicts the density grating formation due to collective scattering at $t = 0.168 w_r^{-1}$. The corresponding bunching factors $|M(k,t)|$ for both time instants are displayed in (c) for $t = 0$ and in (d) for $t = 0.168 w_r^{-1}$.

Laser beam propagation perpendicular to the major axis of an ellipses

The system is now irradiated transversally, i.e., the laser propagation is set to hit the elliptical atomic cloud perpendicularly to its main axis. However, since the employed Julia code is better suited to a cloud rotation than a to laser translation/rotation, the entire atomic system is rotated 90°; keeping the laser beam propagating along the z axis, as in the previous case.

The same two time instants are characterized for this case in Fig. 2.6, being the initial random atomic distribution portrayed in subfigure (a) and the moment of maximum density grating illustrated in subfigure (b). Unlike the previous case, pattern formation for this case is a two-step process. In the first step, a faint grid is formed along the direction of the pump, z axis; consequence of the width of the cloud ($k_0z = 9$), which is not negligible because it constitutes a quarter of the total height of the cloud ($k_0x = 36$). The second step is the strong bunching formation across the transversal direction, x axis, which is represented in the symmetrical lobes represented at 90° and 270° in the same panel. A lingering lobe representing the faint initial vertical grating is observed in the small backwards bump depicted in panel (d) and on the same frame a couple of twin transversal lobes attain an equivalent size (one appears earlier than the other).

The formation of the grating is no longer restricted to one dimension, because the scattering light adds the vertical component (x axis) to the horizontal direction (z axis) of the incident light. As in the parallel cloud alignment, the pump field interferes with the scattered light, but this time they form a dynamically evolving 2D optical grating potential [151]. This potential is a consequence of two components optical force —(x, z) plane— generated due to unbalance between the recoil along

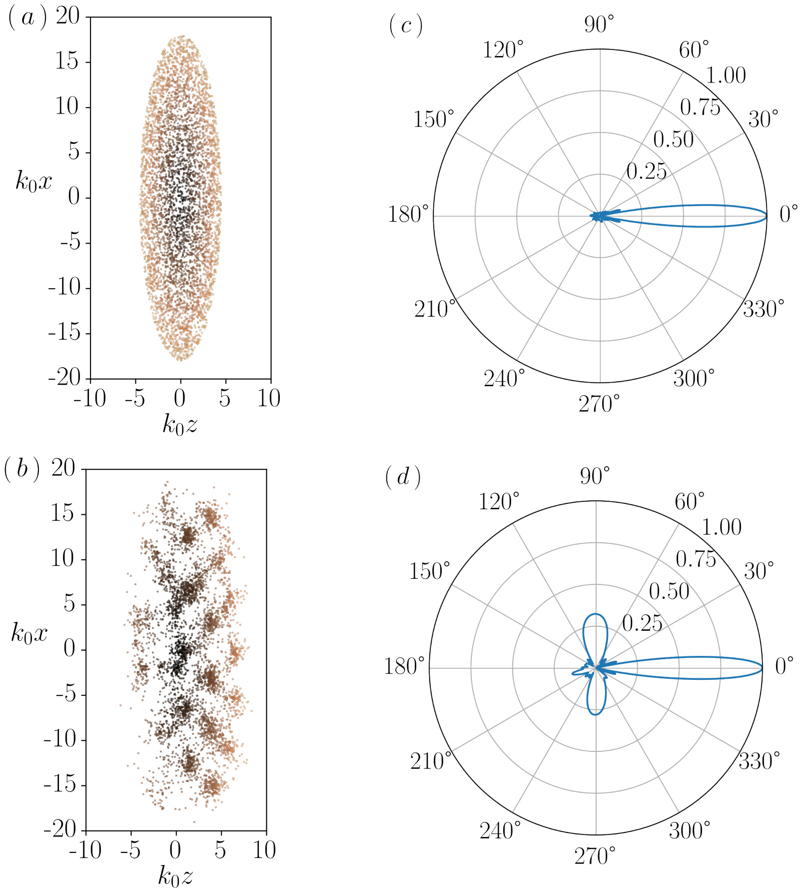

Figure 2.6: Collective scattering and pattern formation from an elliptical 2D atomic cloud irradiated with a scalar pump laser propagating perpendicular to its major axis: (a) Shows the initial atomic density distribution at $t = 0$ of $N = 5000$ atoms randomly distributed. (b) Depicts the density grating formation due to collective scattering at $t = 0.210 w_r^{-1}$. The corresponding bunching factors $|M(k, t)|$ for both time instants are displayed in (c) for $t = 0$ and in (d) for $t = 0.210 w_r^{-1}$.

two different directions. This optical force, born from the combination of these two fields, acts on the atoms of the cloud approximately along the directions ±45° from the z axis, generating the bidimensional pattern illustrated in Fig. 2.6(d).

The bidimensional atomic rearrangement can, once more, be described via the photon picture of a scattering event, involving an incident photon of momentum $\hbar k_0\hat{\boldsymbol{z}}$ and a resulting scattered photon with momentum $\pm\hbar k_0\hat{\boldsymbol{x}}$. The atom mediating this event experiences a total momentum change of $\hbar k_0(\hat{\boldsymbol{z}} \pm \hat{\boldsymbol{x}})$, i.e., depending whether the photon is emitted downward (positive sign) or upward (negative sign).

This perpendicular interaction was performed by Inouye et al. [133] for the case of an elongated elliptical BEC. They observed a similar grating but in the momentum space. Conversely, in the current system the pattern appears in real space and not in momentum space. Therefore, as for the BEC in free space, the current perpendicular cloud example clearly illustrates that the scattering is strongly driven towards the longest scattering path of the spatial distribution.

Scattering from a circular atomic cloud

The two most extreme possible orientations of the pump that give completely different results have already been reviewed; there are other angles of rotation, but they would only show intermediate grid formations with angles that differ from 45°. The current segment shows what happen when there is no preferred scattering direction, i.e., a cloud with no elongation or without longest scattering path. To verify this situation, the system that is inspected here is one composed of a circular cloud with the atoms distributed randomly. The circular cloud is irradiated with the usual scalar external optical field on the z axis, which remains unchanged.

Observing some density grating with a symmetric cloud shape seems difficult, *a priori*; scattering should probably occur randomly and equally in any direction due to lack of elongation of the cloud. Nevertheless, a two-dimensional density grating appears when the system is allowed to evolve for a short time. A visual explanation of the appearance of a grating in such spherical cold gas can be found in the repositioning of particles within the cloud observed from Fig. 2.7(a) to Fig. 2.7(b). The initial perfectly circular cloud is modulated by the external field into an elongated structure, with a kind of “egg” shape. This egg-shaped vapour, represented in panel (b), resembles the ellipse illustrated in Fig. 2.5(a-b), but with no symmetry.

When observing the evolution of the cold vapour, the electrostrictive force together with the radiation force seem to press the circular cloud forward, stretching it along the z axis. The cloud would probably support a symmetric compaction effect along the x axis (stretching itself long z axis), if it were not for the force of radiation that strongly counteracts it from the negative values of $k_0 z$, thus producing the elongation of the circular cloud in this characteristic egg-shaped cloud. Consequently, a longest scattering propagation path is defined and the grating begins to appear. Contrary to what can be observed when studying an elliptical cloud, the grating emerges simultaneously in both parallel and transverse directions, thus constituting a 2D grid from its beginning. In this example, this is supported by observing the evolution of the bunching formation from Fig. 2.7(b) to Fig. 2.7(b),

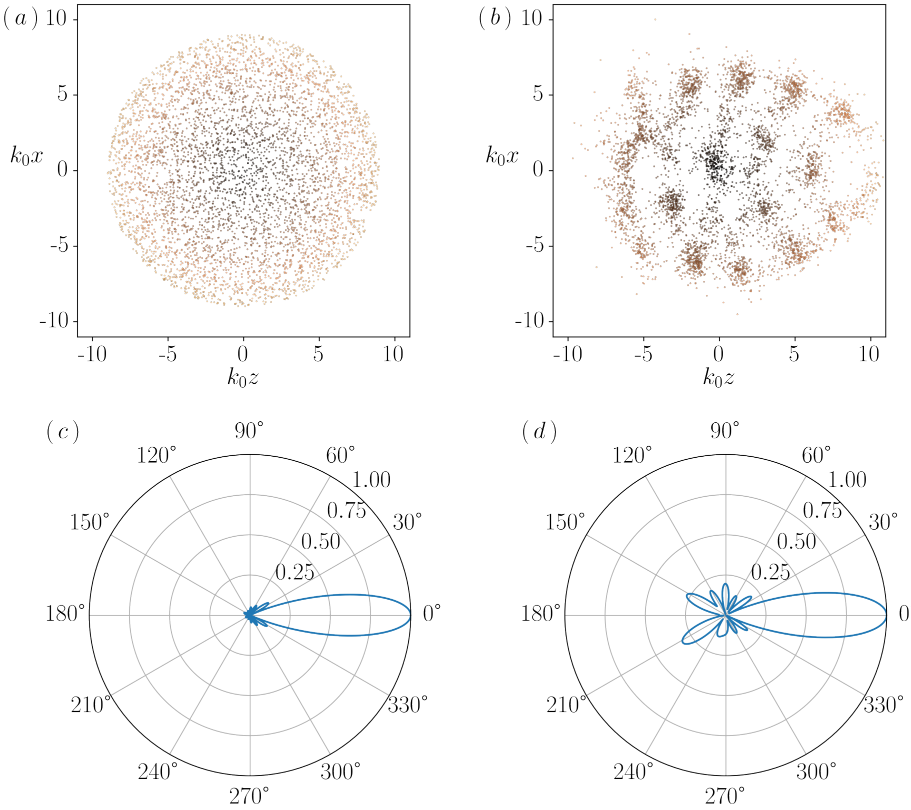

Figure 2.7: Collective scattering and pattern formation from a 2D circular atomic cloud irradiated with a scalar field: (a) Shows the initial atomic density distribution at $t = 0$ of $N = 5000$ atoms randomly distributed. (b) Depicts the density grating formation due to collective scattering at $t = 0.144 w_r^{-1}$. The corresponding bunching factors $|M(k, t)|$ for both time instants are displayed in (c) for $t = 0$ and in (d) for $t = 0.144 w_r^{-1}$.

whose backscattering lobes appear as the cloud stretches toward the positive values of the z axis. This is not always the case, but the grating always forms a 2D pattern right from the start.

Regarding the nature of the bunching formation, the polar plot in Fig. 2.7(d) shows a couple of facts: firstly, there are two preferred scattering directions, which are roughly directed at ±150° (or backscatter at ±30°), and secondly, the bunching formation is rather symmetric, probably derived from the initial symmetric geometry. An analytical explanation can be obtained by looking at the resulting shape in Fig. 2.7(d), which can be described by an imaginary triangle. The cloud deforms into a triangular shape, like an arrowhead, pointing toward the positive values of the z axis. It has two almost identical angles located in the negative semi-axis of the z direction and a third one, more acute, located in the positive semi-axis of the same direction. This latter angle is the one that defined the angle between the two preferred scattering directions, and it is close to 60° in the current example. Once more, by defining the angles between each of the scattered directions and the z axis as $\pm\vartheta$, it is possible to study the scattering event of a photon, as in two previous cases. On the one hand, there is an incoming photon with a momentum defined by $\boldsymbol{q}_{in} = \hbar k_0 \hat{\boldsymbol{z}}$. On the other hand, a scattered photon is produced along the directions $\pm\vartheta$ with a momentum $\boldsymbol{q}_{\pm} = \hbar k_0[\hat{\boldsymbol{z}} \cos\vartheta \pm \hat{\boldsymbol{x}} \sin\vartheta]$. Then the final atomic recoil momentum is

$$\Delta \boldsymbol{p} = \boldsymbol{q}_{in} - \mathbf{q}_{\pm} = \hbar k_0[\hat{\boldsymbol{z}}(1-\cos\vartheta) \mp \hat{\boldsymbol{x}} \sin\vartheta], \tag{2.34}$$

with an angle ϕ with respect to the $\boldsymbol{z}$ axis[11] given by

$$\tan\phi = \mp\frac{\sin\vartheta}{1+\cos\vartheta}, \tag{2.35}$$

where the negative sign represent a photon emitted upwards and the positive sign otherwise.

Observing Fig.2.7(d), the scattering angles can be approximated to $\pm\vartheta \approx 150°$, such value can be entered in Eq.(2.35), giving the orientation of the two existing cross lattices oriented respectively at $\phi = \mp 75°$ with respect to the z axis. The result is in agreement with the graphic results illustrated in Fig. 2.7(b). The formula reduces to the two previous cases displayed in Fig.2.5 and 2.6 —depicting a horizontal and a vertical ellipses—, when ϑ is π and $\pi/2$, respectively.

The results obtained for this system are marginally different when compared to those presented in [160] (Sec. 5.2). Here, the two symmetric backscatter directions are oriented along ±30°, while in the cited review the preferred angles are ±45°. Such orientations generate gratings with different inclination with respect from the pump axis, the horizontal z axis; being ±67.5°[12] for the cited paper and ±75° for the present case. The reason for such difference is reduced to the initial randomness of the particles' positions, small variations in the particle distribution cause the system to drift towards different possible outcomes. Nonetheless, the result are qualitatively similar, an egg-like shape is formed in the cloud due to its stretching (with similar but not equal eccentricity) towards the positive values of the z axis, which allows to define a two preferred backscatter directions. Another important cause of this difference is that the algorithm being used in this investigation is different from the one employed in [160] When the random seed is preserved, modifying the order of the symplectic algorithm instead, the results generated are quantitatively diverse, but remain qualitatively identical (a 2D grating is formed).

In the present job, a random seed has been established for all stimulation, but when this restriction is removed, the resulting scatter image (Fig. 2.7(d)) are slightly different. For this reason, a peculiarity of this system, comparing with the two previous examples, is that the usual random seed has been modified, to show more clearly the formation of the two symmetrical backscatter lobes.

---

[11] A typo in the formula has been corrected from the original expression in [160]

[12] The value has been recalculated using the corrected expression, Eq.(2.35)

2.5.2 Diverse three-dimensional system shapes mixed with different laser beam orientations

The same external scalar field, which propagates along the z axis from negative to positive values, is still applied towards cold atomic vapour. However, the former study of the scattering of this field, varying the orientation and the shape of a cold cloud, is now inspected for a three-dimensional cloud. Since the current atomic vapour has a volume, the bunching formation for each tested cloud shape and orientation is also represented in a volumetric intensity pattern.

This bunching radiation profile follows the expression introduced in Eq. 2.9, and is also calculated onto each of the cardinal planes that contain the three possible direction cosines. These two-dimensional calculations facilitate the evaluation of the grating in each cardinal direction, e.g., the bunching in the external field axis z axis can be examined by studying the shapes on planes (x, z) and (y, z). It is worth mentioning that each of these so-called "projections" represents the bunching calculated according to the configuration defined at the end of Sec. 2.2.3 on page 34. They only show the bunching contour of the two cardinal components defining the plane, neglecting the third one, this action makes the plotting a little bit different than an actual projection of the 3D bunching shape. This trick allows to better understand the lobes of the bunching formation represented by a three-dimensional intensity pattern, which is represented using a scatter plot. The scatter plots would be closer to a uniform shell shape of the 3D bunching with a larger number of particles, but there exist some computational power limitations to either adding more particles or constructing a 3D mesh with the given particles.

The fastest algorithm method, the predefined function Verletleapfrog [180] from the Julia language, is exploited to represent the upcoming simulations. The reason is simple, the computational resources needed to show the evolution of a 3D system, which also contains more particles, are much greater than for a two-dimensional case. Even with a 3D cloud that is less densely populated than its analogous 2D case, with a density three times higher, the simulation time is increased a tenfold.

External field parallel to the major axis of an ellipsoidal cloud

The first system examined is the solid of revolution of the ellipse introduced in the previous segment of this subsection on page 50. The seed for the random generation of the initial positions remains the same, but now the particles are contained in an ellipsoidal shape. Therefore, the same scalar laser beam propagated along the major axis of the ellipsoidal shape (z axis), results in a one-dimensional grating formation composed of three-dimensional clusters of atoms.

The grating formation of this system can be followed in Fig. 2.8, where the initial atomic arrangement, in panel (a), is modulated to an ordered grid in one direction, in (b). The pattern, instead of being made up of what looks like the lines drawn in the cloud for the 2D analogous case, is made up of a collection of small spheres distributed along the z axis. It is evident from panel (b), that the grating has a distance between clusters of particles of $\lambda/2$ or $\pi/2$.

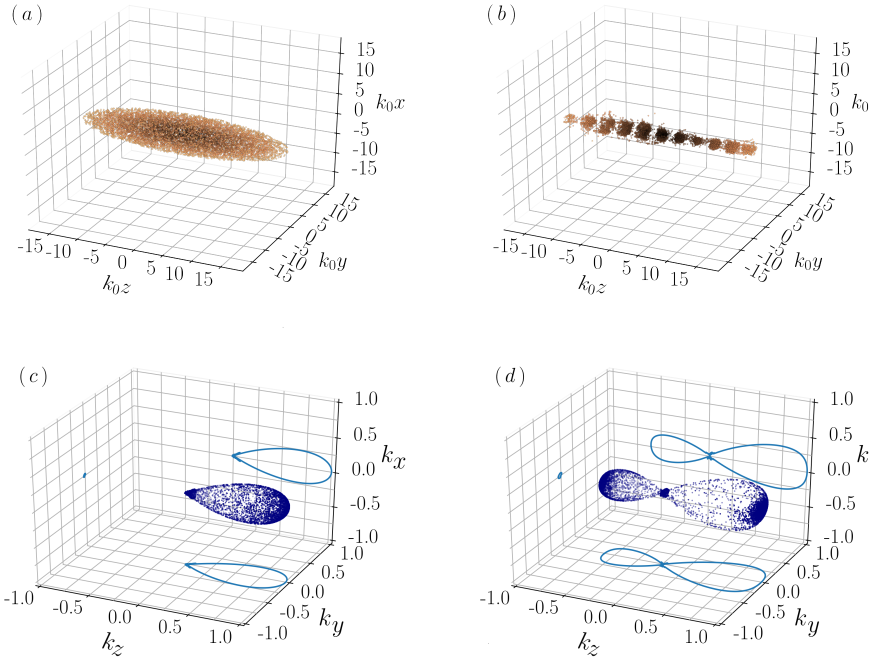

Figure 2.8: Collective scattering and pattern formation from an ellipsoidal 3D atomic cloud irradiated with a scalar pump laser propagating parallel to its major axis: (a) Shows the initial atomic density distribution at $t = 0$ of $N = 10000$ atoms randomly distributed. (b) Depicts the density grating formation due to collective scattering at $t = 0.158w_r^{-1}$. The corresponding bunching factors $|M(k,t)|$ for both time instants are displayed in (c) for $t = 0$ and in (d) for $t = 0.158w_r^{-1}$.

When it comes to studying the radiation profile of the bunching formation, the two lower panels (c) and (d) in Fig. 2.8, show how the system goes from a single emitting lobe in the z axis, due to the laser beam, to a bunching profile that contains an additional radiation lobe, which represents the consequent backscatter emission of the CARL effect. As in the two panels above of the same figure, (a) and (b), the intensity profile of the atomic bunching also represents a solid revolution of the one obtained in the analogous 2D case. This latter fact is even more obvious if the projections onto the (x, z) and (y, x) planes are examined. It is particularly interesting to highlight the intensity of the backscattered lobe, which appears to be notably greater than in the flat case, showing the collective nature of the CARL effect.

Laser beam propagation perpendicular to a cloud shaped as an ellipsoid

In this segment a simple 90° rotation along the y axis to the former 3D cloud has been performed, keeping the incoming scalar optical field incident along the z-axis.

The system is allowed to evolve for a certain time and the results are shown in Fig. 2.9. The initial atomic distribution and bunching profile are illustrated in plots (a) and (c), respectively. When the cloud is observed after a certain time a grating appears, although this time the grating is a 3D structure composed by small spherical atomic clusters —see Fig. 2.9(b)—. Corresponding to the same time frame, Fig. 2.9(d) gathers the intensity profile of the bunching of the main directions of the scattered modes that allow to a three-dimensional grating.

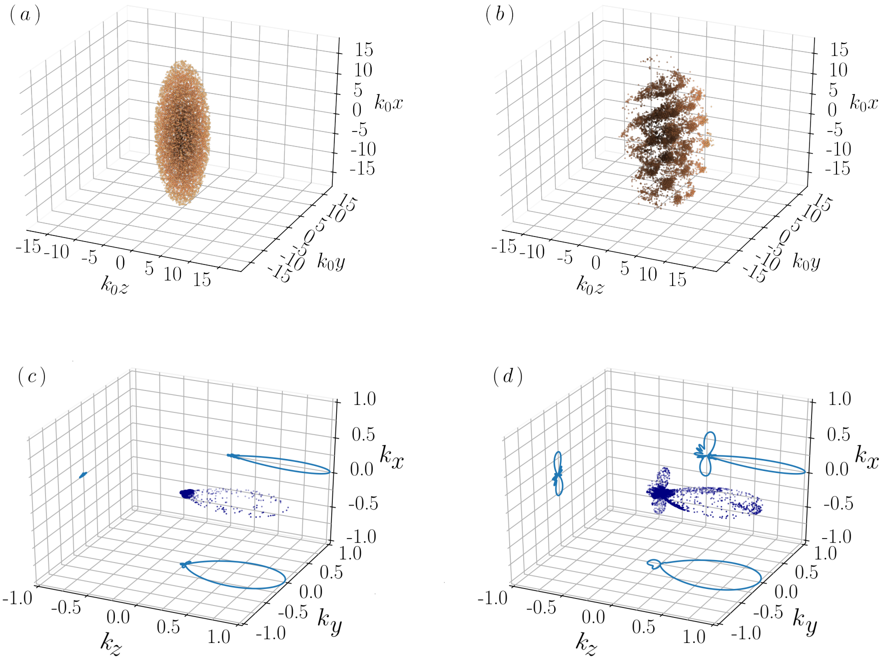

Figure 2.9: Collective scattering and pattern formation from an ellipsoidal 3D atomic cloud irradiated with a scalar pump laser propagating perpendicular to its major axis: (a) Shows the initial atomic density distribution at $t = 0$ of $N = 10000$ atoms randomly distributed. (b) Depicts the density grating formation due to collective scattering at $t = 0.211 w_r^{-1}$. The corresponding bunching factors $|M(k,t)|$ for both time instants are displayed in (c) for $t = 0$ and in (d) for $t = 0.211 w_r^{-1}$.

As in the equivalent flat case of the elliptical cloud in the second segment of the previous subsection 2.5.1 (page 51), the grating is formed through the atomic recoil that occurs from a combined action between the incoming photons from the pumping field and the scattering of photons along the longest scattering path of the cloud. Again, the major axis of the cloud is the one that defines the main scattering directions, which are found along the x axis. For that reason, a 3D grating generation can be seen in the cloud following perpendicular directions: one tilted with a positive slope (45°) and another with a negative slope (−45°), with respect to the horizontal plane (y, z). The right angle formed between these two directions is a consequence of the scattering event described in Fig. 2.6 (the aforementioned matching 2D cloud).

There is a faint trail of tilted planes in Fig. 2.9(c), which become more clearly visible as the system evolves towards the presented time frame. Since the figure has a thickness that cannot be neglected, the temporal pattern formed by these planes is finally replaced by the final three-dimensional arrangement; due to small out-of-plane scattering along the y axis. The planes with a positive slope $(x > 0)$ are more visible than those with a negative slope $(x < 0)$, because the first lobe that appears in the evolution is the positive one, which is a purely random event. It can be anticipated that such tilted planes will be exposed in later figures, when a vectorial pump field is used to irradiate the same cloud (see Fig. 2.14 on page 67).

A peculiarity of this system is that the lobe due to the laser beam, illustrated along the positive values of the z axis in plots 2.9(c) and 2.9(d), it is no longer symmetric when compared to the previous case (Fig. 2.8). This lobe flattens on the x axis, due to the lower probability that a photon will scatter along the $\pm y$ directions. If the ellipsoid underwent a rotation along the z axis by an angle $\pm\alpha$, the flattening of the lobe would also undergo a rotation of the same magnitude $\pm\alpha$. Such an effect is already observed in Fig. 2.5, in the analogous 2D case, but in the current 3D case, the compression of the lobe can be better captured thanks to the projections on the (x, z) and (y, z) planes represented in Fig. 2.9(d).

Scattering from a spherical atomic cloud

As a final case for the current subsection, the circular cloud system in the example presented in 2.5.1 on page 53 is transformed into its solid revolution to generate a spherical cloud. As in the other two cases in the subsection, the external optical field is still considered independently of its polarization effects and continues to propagate along the z axis, from negative to positive values. The evolution of this system is illustrated in Fig. 2.10, where the system cloud and bunching pattern at time $t = 0$ are represented in plots (a) and (c), respectively. Furthermore, the figure depicts the time frame in which the scattering is maximum in plots (b) and (d). The flat, egg-shaped outline appears to be reproduced in a three-dimensional shape, with a resemblance to a real egg that is displayed in panel (b).

As in the previous case, the emergent grating is three-dimensional with a spherical group of atoms, but now there are no visible inclined planes. This is due to the symmetry of the initial spherical cloud, there is no preferred initial scattering direction and the atoms start to scatter randomly. Two dynamics occur simultaneously in this type of set: the first moves the internal atoms towards the outer shell and the external atoms towards the interior of the cloud; the second distributes the particles in clusters.

On the one hand, the first action is due to the electrostrictive force (outer atoms moving inwards) and the scattering effect (inner atoms moving outwards, thanks to a higher optical thickness along the z axis), which combined elongate the edges of the cloud into an egg-like shape. In addition, their combination forces the atoms to be forward displaced faster the closer they are to the outer shell, due to the definition of a preffered scattering path.

On the other hand, the second dynamic arises due to photon scattering, which begins to occur through this newly defined longer path over the outer layer of the cloud. The photon scattering helps to draw concentric circles of atoms on the outer surface, which is represented in Fig. 2.10(b). In fact, looking closely at the core of the cloud, it is possible to observe that these concentric circles, apparently contained in different (x, y) planes, have a different k_0z value when approaching to the z axis. This is because these supposed circles are actually representing the edges of shallow circular cones, which have their center located to the left of the z axis with a smaller value than the k_0z values of the edges of their circular bases located on the right.

Analysing the bunching formation, in Fig. 2.10(d), it is possible to see, with a little imagination and with the help of projection on the plane (x, y) plane, four small scattering lobes, which are weakly represented in the other two projections (two in each one). These lobes are the symmetrical way of representing the two

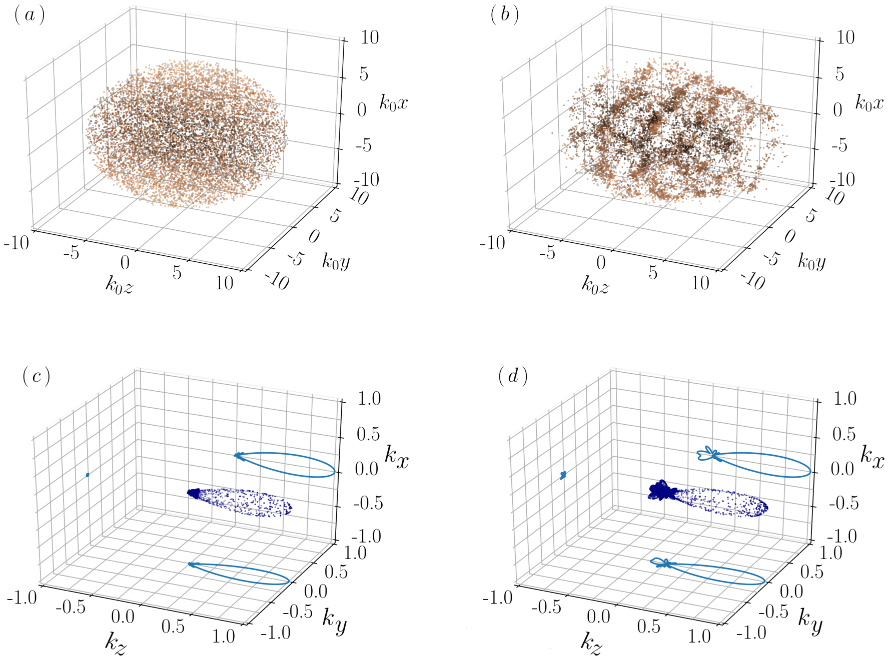

Figure 2.10: Collective scattering and pattern formation from a 3D spherical atomic cloud irradiated with a scalar field: (a) Shows the initial atomic density distribution at $t = 0$ of $N = 10000$ atoms randomly distributed. (b) Depicts the density grating formation due to collective scattering at $t = 0.185\omega_r^{-1}$. The corresponding bunching factors $|M(k, t)|$ for both time instants are displayed in (c) for $t = 0$ and in (d) for $t = 0.185\omega_r^{-1}$.

flat lobes depicted in Fig 2.7(d) with a certain volume. This type of flower or four-petal clover, drawn in panel (b) of the current figure's 3D intensity pattern, are the main scattering modes that interact with the pumping field to form the 3D pattern design within the egg-shaped cloud.

Summarizing, in order to simplify the explanation, the situation is similar to the one presented in the flat egg-like shape, represented in Fig. 2.7, but in this case the dynamics occurs radially from the z axis, thus confirming this case as another solid revolution of its analogous flat representative.

2.6 Polarized light scattering in 2D and 3D cold atomic clouds

In this subsection, the simplified external field is left behind and updated with a more complex and realistic field, which accounts for polarization effects. The field's polarization is linear, perpendicular to its propagation axis (z axis) and parallel to one of the other two transverse cardinal axes (x and y axes). To restrict the number of available system configurations, only off-axis scattering is investigated here; elongated 2D/3D clouds with their major axis perpendicular to the direction of propagation of the external field. The analysis of this orientation makes it possible to better present the effects derived from having the polarization field parallel or perpendicular to the major cloud's axis, both in two-dimensional and three-dimensional space. Furthermore, the same random seed, used in the previous simulations of the scalar model, is used in all the following elongated clouds and the initial shape of these 2D and 3D perpendicular clouds is not represented. If it is necessary to check the initial random distribution and the clustering profile of any two-dimensional or three-dimensional cloud, it is sufficient to check panels (a) and (b) of Figs. 2.6 or 2.9, respectively.

2.6.1 Optical field with different linear polarizations in an elliptical cold vapour

In the first part of the subsection, as for the scalar case, a flat cloud is investigated. In-plane polarization is examined when applied along the x axis, while out-of-plane polarization is examined when the y axis is chosen.

Pump field perpendicular to the major axis of an elliptical cloud with in-plane polarization

For the figure representing a cloud parallel to the propagation of an external scalar optical field in Sec. 2.5.1 on page 51, it has been calculated that an atoms experiences a total momentum change of $\hbar k_0(\hat{\boldsymbol{z}} \pm \hat{\boldsymbol{x}})$, i.e., depending on whether the photon is emitted downwards (positive sign) or upward (negative sign). When the fact that light cannot be scattered along the direction of its polarization is added to this calculated scattering event, the only possible scattering direction for the current case is the z axis; thus suppressing the $\hat{x}$ component of the total recoil moment. This situation has obvious implications both in the grating generated in the cloud, due to the action of the external field, and in the bunching profile, which shows towards which direction the photons are scattering.

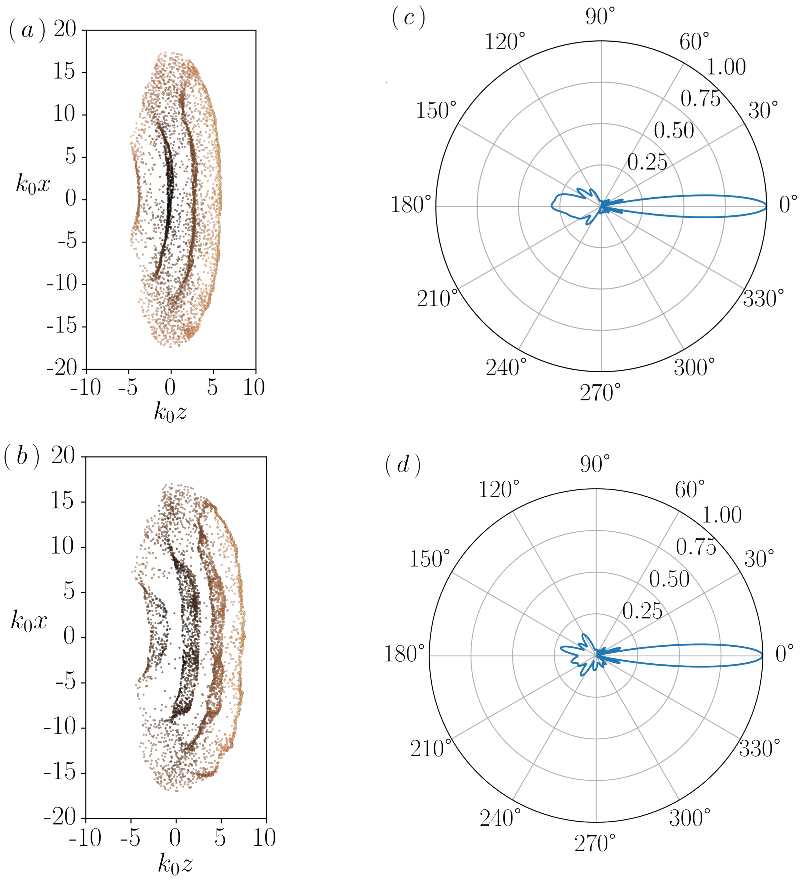

Figure 2.11: Collective scattering and pattern formation from an elliptical 2D atomic cloud irradiated with a pump laser propagating perpendicular to its major axis and linearly polarized along the x axis: (a) Shows the atomic density distribution of $N = 5000$, with a random initial distribution, at the time instant $t = 0.167\omega_r^{-1}$. (b) Depicts the atomic density distribution at time $t = 0.230\omega_r^{-1}$. The corresponding bunching factors $|M(k,t)|$ for both time instants are displayed in (c) for $t = 0.167\omega_r^{-1}$ and in (d) for $t = 0.230\omega_r^{-1}$.

The results of this case are shown in Fig. 2.11, where notable changes are exhibited in the grating pattern, compared to the scalar case, due to the scattering restriction imposed by the vector polarization. The very definition of a planar system already suppresses a possible direction of scattering (y axis), and the polarization blocks the other transversal direction (x axis); leaving the light with the only option but to scatter along the propagation axis of the external field (z axis).

The situation is represented in two instants of time, in graphs (a) and (b) of the same figure, where the evolution of the atomic distribution generates a pure 1D grating pattern as a consequence of the forward and backward scattering of light, and the pump field. In the frame of panel (b), the initially formed strips, shown in panel (a), have a higher thickness, which represent the effects of having a continuous incoming radiation field combined with the only two possible scattering directions: some atoms remain almost motionless, with a net momentum change of 0, while others endure a double momentum kick, with momentum $2\hbar k_0$. Contrary to the analogous scalar case, this example actually exploits the non-negligible thickness of the cloud, scattering the atoms along this direction, because the polarization cancels all possible scattering along the cloud's major axis.

The analysis of the bunching radiation profiles of both time instants, displayed in plots (c) and (d) of Fig. 2.11, confirms the situation predicted by the theory and represented by the grating patterns in plots (a) and (b) of the same figure. The intensity pattern shows more similarities with that represented by the scalar case with an elliptical cloud parallel to the propagation axis (shown on page 51), than with the scalar case that presents the same cloud orientation (see page 52): only the lobes representing the forward and backward direction are generated. The backscattering lobe is somewhat distorted and not as clear as depicted in Fig. 2.5(d), although it retains some symmetry with respect to the axis of field propagation. The main cause of such deformation can come from the dipole-dipole force, which starts to push the atoms towards the right of the plot. The force pushes with greater intensity the atoms located near the origin at $k_0x = 0$, where their numbers is greater and the optical thickness is higher, moving them towards positive values of z faster than the ones located at the tips of the cloud (with higher $|k_0x|$ value).

In summary, the radiation force transforms the straight stripes of bunches of atoms into arcs, which are equally spaced with a periodic space between them of $\approx \lambda/2$, or $\approx \pi/k_0$. The distances between these clusters are a consequence of the optical potential generated by the standing wave that arises from the interaction of the external field and the scattering light, which is modulated by the polarization of the pump.

Systems' longest axis perpendicular to an external field with out-of-plane polarization

A copy of the previous system is simulated in this segment, but this time the pump field polarization axis is rotated around the non-existing third dimension —y axis—, also referred as out-of-plane axis. The new system does not experience any propagation restriction, because the polarization is not contained in the plane of the cold gas. Therefore, a bidimensional grating similar to the one shown in Fig. 2.6(b) is observed for this system in Fig. 2.12(b). Nevertheless, the grating portrayed in panel (b) of the current segment's picture is not identical to the one represented in the same panel of the figure from the scalar model. This variation arises from the differences existing between the equations of motion describing the scalar case —Eqs. (2.12) and 2.13— nd those that govern over the current vectorial case (Eqs. 2.15 and 2.16). The force equation of the current case has additional short-range terms ($1/r_{jm}^n$ with $n > 2$), and the terms that are typified in both models ($1/r_{jm}^n$ with $n \leq 2$), are not identical. In addition, the cut-off parameter has been adapted to each situation, being $\xi = 1$ when the incoming field is polarized and $\xi = 10^{-2}$ when is scalar. Adjusting this parameter does not affect the validity of the results, but these alterations certainly introduce a slight modification in the way the particles interact with each other. Analysing the bunching intensity pattern in plot (d) of the same figure allows to see that the system eventually

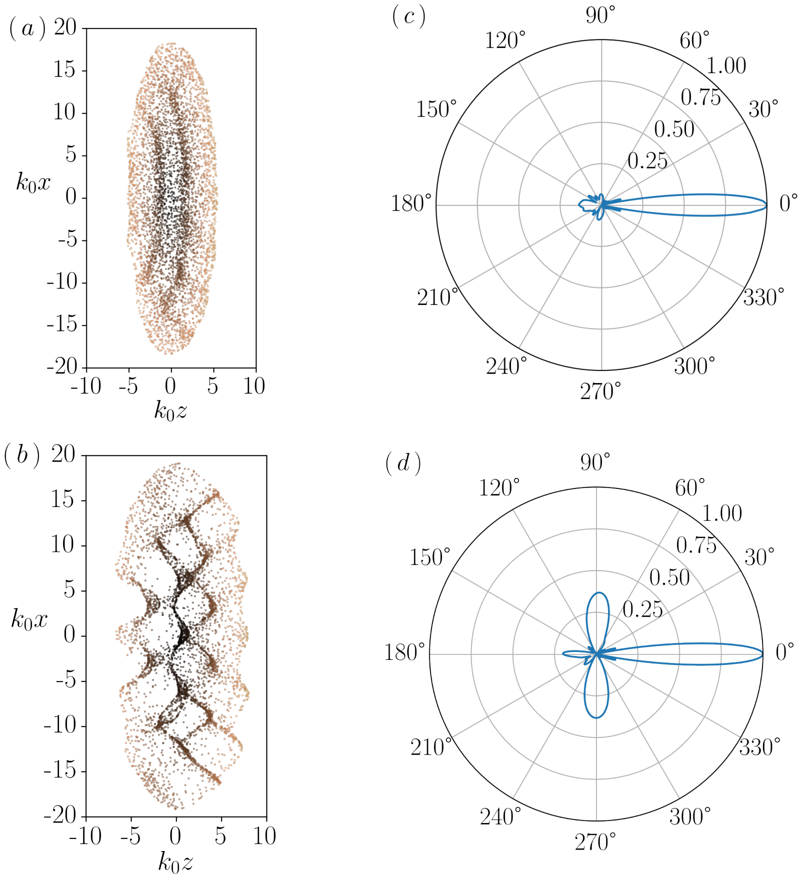

Figure 2.12: Collective scattering and pattern formation from an elliptical 2D atomic cloud irradiated with a pump laser propagating perpendicular to its major axis and linearly polarized along the out-of-plane direction (non existing y axis): (a) Shows the atomic density distribution of $N = 5000$, with a random initial distribution, at the time instant $t = 0.120\omega_r^{-1}$. (b) Depicts the atomic density distribution at time $t = 0.239\omega_r^{-1}$. The corresponding bunching factors $|M(k,t)|$ for both time instants are displayed in (c) for $t = 0.120\omega_r^{-1}$ and in (d) for $t = 0.239\omega_r^{-1}$.

responds as in the scalar case, providing a 2D pattern similar to that illustrated in panel (d) of the scalar case on page 52.

Figs. 2.12 (a) and (c) present an earlier stage in the temporal evolution, where the effects of a non-negligible surface thickness allow to generate a 1D grid. The final expected two-dimensional grating of the atomic distribution of the cloud does not appear immediately, but in a second phase shown in panels (b) and (d). Therefore, once the interference between the backscattering and the pump field has formed the 1D grating (along the z axis, seen in the previous transverse polarization example), the main scattering direction is defined through the longest scattering path (x axis), reshaping the temporal 1D grating into the final 2D grating.

There is something else to comment on regarding the two flat systems presented so far. In both polarizations examples depicted so far, a sort of "burst" can be perceived when they are compared with panel (a) of Fig. 2.6, i.e., the atoms of these clouds seem to be drifting outward from the center of the ellipse. This is a consequence of the value of the cut-off parameter, because if the value used in the scalar case ($\xi = 10^{-2}$) was applied to the vector model, the cloud would suffer a strong and fast repulsion, making impossible for 2D grating to appear. The collision avoidance parameter is already set to unity, hence in the order of magnitude of the external field wavevector, and since bunching is already present, it did not seem necessary to decrease it further.

2.6.2 Interaction of laser beam with different linear polarizations with an ellipsoidal cloud

A similar vectorial study is performed, when the cold atomic ensemble is exchanged for a three-dimensional shape, everything else stays the same. Adding a dimension to the system in hand allows to further expose the effects of the light scattering when a polarized optical field is applied. Furthermore, in three dimensions, the polarization vector is always contained in one axis of the cloud, leaving the atoms free to scatter in either of the other two directions in a more realistic three-dimensional space.

Pump field with in-plane polarization perpendicular to the major axis of ellipsoidal system

The first case, as in the 2D system, is simulated with a transversely polarized optical field along the x axis. As mentioned earlier, polarization along a certain axis does not allow atoms to scatter in that direction. Consequently, since the other two axes are non-forbidden directions, the light is expected to form a series of atomic bars (made up of several hundred atoms each) along the axis of the polarization vector. The atomic bars are the result of the combination of the incoming photons from the pump field and those scattered along the y and z axes.

The theorized scheme can be discerned in Fig. 2.13(a), where the so-called atomic rods are not completely straight, showing a bended shape due to the effect of the constant dipole-dipole force. Again, the constant force and a greater optical thickness in the central (y, z) plane, located at $k_0x = 0$, the central segment is pushed more firmly than the tips of the cloud; giving the atomic rods their characteristic shape. The complete suppression of the bunching along the polarization axis can be inspected in Fig. 2.13(c), where the lobes along the polarization directions (x axis) are completely missing.

In the plots (b) and (d) of Fig. 2.13 a second later instant of time is shown. The same rods are still present in the atomic distribution of the cloud — panel (b) —, although now they show weak cuts along their tubular structure, which can be explained by the subtle lobe (pointing upwards) that appears in the bunching formation intensity profile —panel (d)—. The reason for the appearance of such forbidden lobe are unknown and they need a further study. Perhaps, such situation takes place due to some sort of screening effect imposed by the particles placed closer to the incoming optical field.

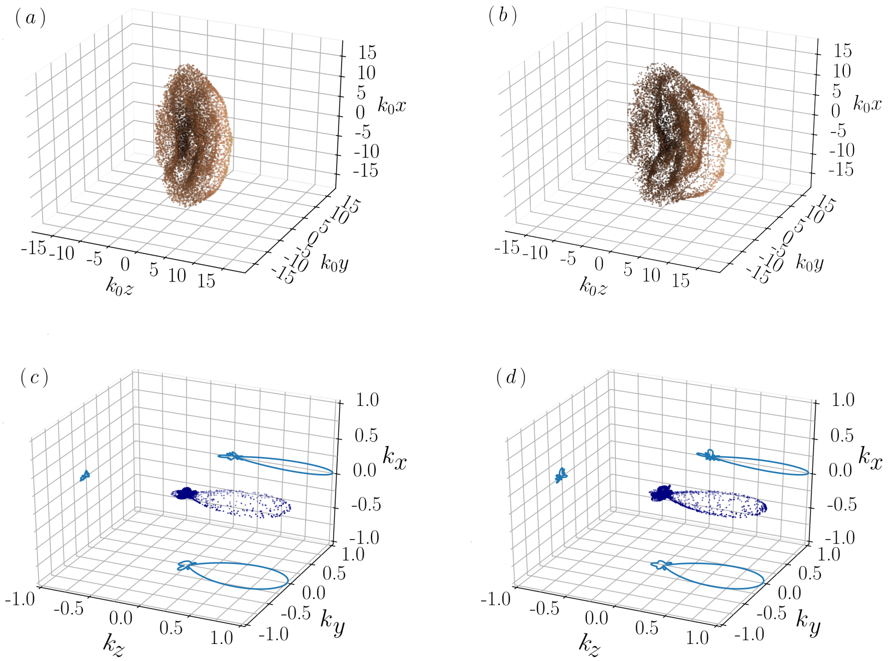

Figure 2.13: Collective scattering and pattern formation from an ellipsoidal 3D atomic cloud irradiated with a pump laser propagating perpendicular to its major axis and linearly polarized along the x axis: (a) Shows the atomic density distribution of $N = 10000$, with a random initial distribution, at the time instant $t = 0.173\omega_r^{-1}$. (b) Depicts the atomic density distribution at time $t = 0.260\omega_r^{-1}$. The corresponding bunching factors $|M(k, t)|$ for both time instants are displayed in (c) for $t = 0.173\omega_r^{-1}$ and in (d) for $t = 0.260\omega_r^{-1}$.

Systems' longest axis perpendicular to an external field having polarization vector out of plane

The external optical field is considered here with the polarization vector rotated 90° with respect to the previous case, and this polarization is still perpendicular to the propagation axis of the field, but here along the y axis instead of the x axis. Being the scattering forbidden along the "out-of-plane" direction or y axis (the direction that would be perpendicular to the sheet of paper if this were to be considered within the (x,z) plane), the inclined planes mentioned in the second segment of the third part of the previous subsection 2.6 (figure on page 58) appear completely defined in panel (b) of Fig. 2.14.

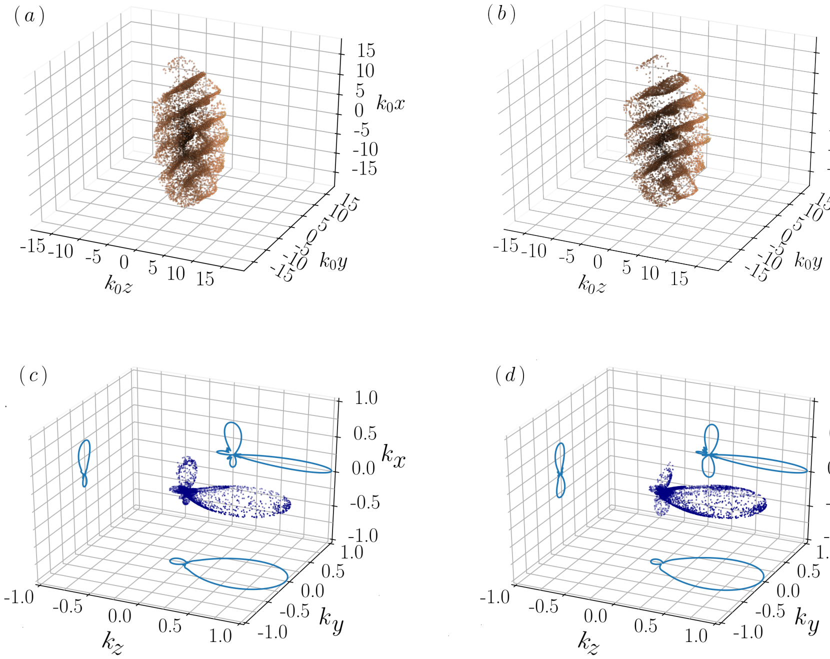

Figure 2.14: Collective scattering and pattern formation from an ellipsoidal 3D atomic cloud irradiated with a pump laser propagating perpendicular to its major axis and linearly polarized along the y axis: (a) Shows the atomic density distribution of $N = 10000$, with a random initial distribution, at the time instant $t = 0.188\omega_r^{-1}$. (b) Depicts the atomic density distribution at time $t = 0.222\omega_r^{-1}$. The corresponding bunching factors $|M(k,t)|$ for both time instants are displayed in (c) for $t = 0.188\omega_r^{-1}$ and in (d) for $t = 0.222\omega_r^{-1}$.

A first chosen time instant of the evolution of the system, plot (a) in Fig. 2.14, shows a grating composed of the same tilted planes in formation. Those with a positive slope are more visible because the atomic recoil is directed downward first (towards the negative value of the x axis), which is confirmed by the lobe of the bunching formation in panel (c) pointing up. A second time instant is depicted in panel (b), where the tilted planes with a negatives slope are activated but are drawn weakly due to the latter appearance of the downward scattering. This second scattering direction along the x axis is represented by the lobe in panel (d) growing downwards.

In addition, the absolute absence of the tiny lobes arising in Fig. 2.9 can be detected along the cross section of the ellipsoid; consequence of the presence of the polarization vector ($\pm y$ directions). Notice that in this case there is no emerging bunching along the y axis, due to the same fact; only a faint gathering of the atoms is observed due to the radial symmetry of the cloud.

2.7 Typical elongated 3D cloud considering a polarized pump field

This short section is introduced because the main objective of the chapter is to show the appearance of the CARL effect with different cloud orientations, shapes and various polarization vectors of an optical pump filed. Therefore, it is of interest to illustrate the typical shape and orientation of clouds with polarization effects, thus assisting in an easy comparison with other systems, for example, the characteristic "cigar-shaped" BEC experiment with ultracold atoms. The same cloud represented in Fig. 2.8 with a scalar field is developed here using the vector model with a polarized pumping field: along the x axis in plots (a) and (c) of Fig. 2.15, and along the y axis in plots (b) and (d) of the same figure. All plots represented in this figure correspond to the same time frame ($t = 0.170\omega_r^{-1}$) of the evolution of the same cloud with the same initial condition.

There is nothing new to say about the plots representing the bunching formation, Fig. 2.15(c) and (d), both feature a large and noticeable backscatter lobe, adding to Initial lobe generated by the pump field. However, a couple of peculiarities can be highlighted when talking about the other two panels —(a) and (b)—, which show the redistribution of the atomic density of the cloud in a 1D grid along of the z axis. On the one hand, the effects of the polarization vector are visible in either systems: the left panel shows a flat grating, due to the suppressed scattering in the vertical direction, whereas the right panel presents a squeezed vertical grating, consequence of the forbidden scattering along the horizontal direction. On the other hand, both clouds undergo a compressing effect on the radial traverse direction with respect to the z axis, marked at the right end of both ensembles. This electrostriction effect is usually displayed by dielectrics, which are able to change their shape, whenever they are subject to an electrical field.

The announced electrostriction effect can be equally seen both in the scalar and the vectorial model, and with a 2D and a 3D cloud, but it seems to be more obvious with the present configuration and the current model. The force is not yet well understood and further investigation is needed for a satisfactory explanation, but it looks that the effects ride along the cloud like a wave. It starts at the right tip, as displayed in panels (a) and (c) of Fig. 2.15, and it goes backwards along the z axis. After this sort of backwards-propagating wave has passed a section, this section is not susceptible to the polarization vector of the field any more, but it is still reactive to the gradient of the radiation force. There are some studies that have already observe this effect experimentally, like the one presented in [185].

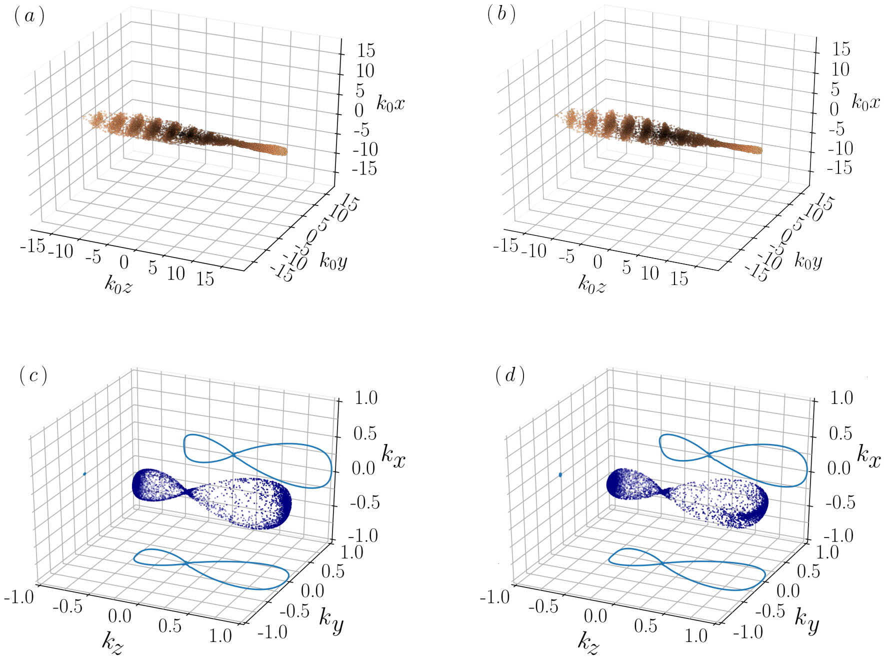

Figure 2.15: Collective scattering and pattern formation from an ellipsoidal 3D atomic cloud of $N = 10000$, whose initial positions are random, irradiated with a pump laser propagating perpendicular to its major axis and linearly polarized. The polarization along the x axis is portrayed in (a), whereas the polarization along the y axis is illustrated in (b). In both systems the density grating formation due to collective scattering is pictured at $t = 0.170\omega_r^{-1}$. The corresponding bunching factors $|M(k,t)|$ for both polarizations, are displayed in (c) and (d), respectively

Chapter three

Trapping and Cooling Atoms with Optical Binding

A novel collective scattering effect is presented in this chapter. This new phenomenon is based in the optical binding of particles with light, which has been applied to dielectric particles along the last decades. Only recently has the optical binding effect been proposed in cold atomic systems. The chapter begins introducing the optical binding concepts, to later develop the models that allow to study the phenomenon with cold atoms. It also exposes how the unique feature of atoms, resonance, has the ability of harnessing the optical binding effect to achieve a cooling mechanism. The cooling process is enhanced when several atoms are included in the system, overcoming the heating mechanism produced by quantum fluctuations. Nevertheless, this topic is at its dawn and the ideas contained in the current chapter are mere theoretical proposals.

3.1 Introduction to Optical Binding

The unofficial origin of optical binding could be established in 1989 with a physics letter whose title has given name to the effect [2]. Although there were theoretical approaches already that involved the subject [186], it was the review written by Burns, Fournier and Golovchenko, the one that defined the OB phenomenon. In the review, they discussed the forces induced by intense optical fields between dielectric objects. They explicitly studied the emergent bound states between two plastic spheres (diameter $\sim 1 \mu m$) placed in a conductive or dissipative fluid (plain water), when a strong perpendicular electromagnetic field is applied to them. Solving the Lorentz generalization of Maxwell's equations, they determined that these bounded states are only formed when particles, treated as oscillators, are located at distances close to integer multiples of the adopted wavelength of light. The greater the distance between particles, the lower the potential well caused by the long-range internal forces induced between the two oscillators. They also presented experimental evidence, where the particles are pushed, using radiation pressure generated by light, against an installed blocking surface, forcing the system to move exclusively in a perpendicular direction.

Since its discovery, optical binding has been behind cutting-edge fields of atomic physics, like laser cooling. This remarkable technique eclipsed the community working on the light-matter interaction for nearly two decades, and it still does. It was not after the discovery of the so-called "holy grail" in physics, the BEC, that optically bonded atoms began to regain some attention. During the first two decades of the 21th, the trend has been reversed and the topic is becoming increasingly popular within the scientific community. Indirectly, some recognition came with the award of the 2018 Nobel Prize in Physics to Ashkin. The award, not strictly related to OB but rather to manipulation of matter with light, recognized fundamental work in the development of the bases of the optical tweezers[1], which made it possible to capture live bacteria using light [187]. What is more, Askin [188, 189] is also credited with some initial contribution to the binding of neutral particles with light and investigation that dates from before the dawn of laser cooling.

Unlike optical tweezers, optical binding has generally been linked more to a spontaneous reorganization of the spatial configuration of the particles [190] —thanks to the radiation of light—, than to their manipulation through light. Each element of these structures, by diffracting or re-emitting light, can alter the others, whose alterations, in turn, will affect each element. Since all particles have the same probability of scattering photons from the field, their collective emission generates a superposition of re-emitted fields.

There are two fundamental optical forces that act in optical binding: the radiation pressure force and the dipole-dipole force, which is the interaction that arises between two or more dipole moments, being these dipoles induced by an external

---

[1] The so-called "Optical tweezers" is a technique that allows to manipulate particles, as small as a single atom, with light. The induced dipole force by the field of a single high-intensity tightly focused laser beam helps to hold micro-particles in a stable three-dimensional potential.

field.[2] The radiation pressure (or scattering) force (introduced on page 5), propels particles in the direction of an incident photon, and in the opposite random direction when the photon is emitted. The dipole-dipole force, is a force between particles that does not arise exclusively from the external field, but mainly from the multiple scattering of coherent light by the elements of the system. This second force can give rise to attraction or repulsion reactions between particles, determined mainly by the position of all the particles in the system. Once a system reaches a position of equilibrium, the dipole-dipole force plays an important role in maintaining a steady state; this fact is fully described in the subsection 3.4.3.

Although the basic mechanism of optical binding is simply the one describe above, the way in which this phenomenon is observed has led the experimental settings to two different scenarios: transverse (or lateral) binding and longitudinal binding. In the first experiment, in 1989, the OB effect was examined using the transverse configuration. In that set-up, used throughout this thesis, the field is applied orthogonally to the plane where the optically bonded particles extend. In a different way, the longitudinal configuration sets the pump along the particle axis [191–193]. Unlike the transverse layout, the longitudinal configuration is studied mainly in one-dimensional systems. However, it is plausible to investigate two-dimensional arrangements by directing a laser beam in one of the directions in the plane of a 2D structure. Regardless of its configuration, any OB system becomes more difficult to examine and control when the number of scatterers is increased.

In addition to the two configurations used to scrutinize the optical binding, different materials and configurations have been applied to test the physical responses of the effect. Some representative studies are listed to show the expansion of OB over the past two decades.

- The OB effect has been analysed employing several particle sizes from diverse material compositions and with different polarizations [194]. Although the effect is not really affected by the size of the particles, the potential energy landscape is actively modified by the actual number of particles in the system. Together with the action of the wavevector and polarization of the external field, the number of particles also dictates the ideal self-organization/arrangement of the system [195].

- There has been some research on adopting nanoparticles because, after all, Burns *et al.* did not experiment with spheres smaller than the wavelength. An up-to-date review of what has been done for the past 10-15 years regarding OB with nanoparticles can be found in [196].

- Evanescent fields escaping from optical nanofibers have also been exploited to trap atoms. The theoretical derivations combined with some numerical and experimental evidence are discussed in [197].

---

[2] The electric dipole moment is the magnitude to measure the polarity of a system. When atoms experience an excitation/decay of an electron, a dipole moment is created due to the uneven distribution of charges within the atom.

- Different input fields have been used to observe the phenomenon: plane waves, for building even more complex clusters in two dimensions [198]; Bessel beams (non-diffractive beams), to obtain stable configurations when binding larger number of particles [199]; or Gaussian beams to better explore the ulterior motives and mechanisms that give shape to the OB effect [200, 201].

- Two counter-propagating optical fibers have been manipulated to trap particles in the standing wave generated by the guided fields [202]. The particles are trapped in space, simply held back by a generated standing wave, which grants the possibility of forming one- or two-dimensional structures of particles. This last technique can make an important contribution to grant the viability of the experimental set-up for the current theoretical doctoral thesis.

It has been established since the 1860s [203] that, due to heat transfer, the resonance properties of a material play an important role in determining the absorbed and emitted envelope wavelength. However, it was not until a couple of years ago, in 2018, that neutral cold atoms were proposed for optical binding [204]. Atoms, unlike dielectric particles, can be in resonance with incoming light. This characteristic allows optically bound atoms to have a decoupling between internal and external degree of freedom: the atom can vibrate with a different frequency in external motion than in its internal oscillation between and excited ground states.[3] Taking advantage of this atomic resonance and lack of synchronicity, it will be shown throughout this chapter that OB, in addition to being a capture tool, can become a cooling (or heating) mechanism for atomic systems through cooperative scattering effects.

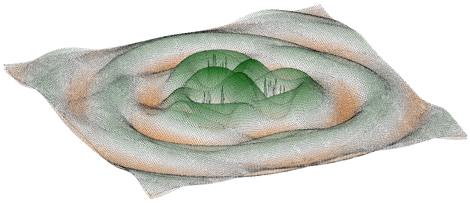

Figure 3.1: Schemes of the landscape of two-dimensional dynamic potential generated by three atoms under OB, when they are established in a stable configuration; equilateral triangle with the side close to the wavelength of the external standing wave.

To conclude the introduction to the evolution of bounding matter with electromagnetic waves, the author would like to draw the reader's attention to a less scientific clarification. The optomechanical effect of optical binding should not be confused with its almost homonymous term ”optical bonding”. This second

---

[3] The oscillation between excited and ground state in a two-level atom, driven by an electromagnetic oscillating optical field, is referred as Rabi frequency. Each oscillation cycle is a Rabi cycle or Rabi flop.

moniker refers to the improvement of the readability of a display, when this is affected by the environment (i.e., fog and reflection of sunlight), by gluing a protective glass in front of it.

3.2 External and internal dynamics of cold atoms bound by light

So far it has been announced what the optical binding effect means and how it has been applied. From now on, the focus will be on promoting the phenomenon a little more. To do this, this section presents the equations of motion used to describe the dynamics of the two models that will be presented in the next subsection 3.3. Using the introduced two-level atom model and an external coherent light source disregarding polarization effects, it is possible to derive the two main equations ruling the OB effect: one linked to the atoms' internal degree of freedom (DOF), dipole equation, and another one connected to their external DOF, force equation.

First, to avoid repeating the symbolic definitions of various parameters and variables, used throughout the description of these two equations, they are identified and briefly described. Some may seem trivial, but full labelling is important to avoid misunderstandings. The bold characters are not intended to refer to vector variables, which are indicated here with an upper arrow, but to facilitate the reader's possible future need to relocate a variable definition.

- The **atomic mass of ^{85}Rb** is represented by $\boldsymbol{m}$ and it has a value of approximately $1.4 \cdot 10^{-25}$ Kg.

- The **atomic decay rate** from excited to ground state, **or linewidth** for the D2 line (transition $5^2S_{1/2} \rightarrow 5^2P_{3/2}$) of this element, is characterized with $\boldsymbol{\Gamma}$.

- There are two identical counter-propagating laser beams that functions as the system's external pumping field, which have a **Rabi frequency $\boldsymbol{\Omega}$**, with an **amplitude maximum** of $\boldsymbol{\Omega_0}$. Furthermore, there is a capture mechanism, constituted by a standing wave, generated by two or four scalar counterpropagated monochromatic plane waves, which create a trapping system in the (x, y) plane or along the z direction, depending on the number of DOF(s) of the system, one ore two, respectively.

- As in Chapter 2, for the usual detuning adopted, we can safely set $lambda \approx \lambda_0$, with $\boldsymbol{\lambda}$ as the **laser wavelength** and $\boldsymbol{\lambda_0}$ as the **atomic wavelength**.

- Knowing the wavelengths allows to establish the **field wave vector $\vec{\boldsymbol{k}}$** and the **^{85}Rb transition wave vector $\vec{\boldsymbol{k}}_\mathbf{0}$**, both having moduli determined by $k = 2\pi/\lambda$.

- The **atomic frequency** of the same D2 line is expressed with $\boldsymbol{\omega_0}$, which is calculated as $\omega_0 = k_0 c$ or $\omega_0 = 2\pi c/\lambda_0$, being c the speed of light in the vacuum. The **laser beam frequency** is represented by $\boldsymbol{\omega}$.

- The resonance offset is measured with the **detuning** between the frequencies of the external pump field and the electronic transition and is described by $\boldsymbol{\Delta} = \omega - \omega_0$.

- It is also convenient, due to simplification of equations and the representation of the results, to define the **normalized detuning $\boldsymbol{\delta}$**, obtained from the ratio Δ/Γ.

- The **recoil frequency** is symbolized with $\boldsymbol{\omega_r} = \hbar k^2/2m$, where $\hbar$ is the reduced Planck constant and m the atomic mass.

Once the symbolism for each variable and parameter has been introduced, it will retain its meaning along this chapter, unless explicitly stated otherwise. Given that a low intensity pump field is considered in this chapter, a classical approach is employed to derive the system's dynamics; considering the atoms as semi-classical oscillators [205] and the light as a continuous plane wave. Although more accurate results can be achieved with a quantum representation [206], they are not necessary in this work.

3.2.1 Cooperative force: external atomic dynamics

The average of the fundamental force arising from a coherent light source acting on the center of mass of N two-level atoms is the origin of the equation that describes the external motion of the elements of the system. Its derivation can be attained by applying the gradient of the positions to a two-component interaction Hamiltonian ($\boldsymbol{\nabla}_{\boldsymbol{r}_j} H$): one component accounts for the laser-atom interaction and the other one considers the interaction of the vacuum modes. In this subsection a concise representation is announced, but the full calculation of such a force can be followed in the work of Bienaimé *et al.* [207], or its extension by means of a master equation performed in [208]. In these two cited letters, it is also possible to find the complete definition of the two components of the interaction Hamiltonian.

Besides the position gradient of the system's Hamiltonian, one assumption and two main approximations are needed to achieve the force that describes the dynamics of the center of mass of the optically bound atoms. The two exploited approximations are widely known in the atomic physics community: the rotating-wave approximation (RWA) and the Markov approximation. The assumption adopted is necessary to easily extract observable values from the system's equations and to reduce the complexity of the problem: weak atomic excitation or linear regime assumption. These three points are briefly introduced before revealing the first main equation of the chapter.

The RWA approximation allude to the cancellation of the rapidly oscillating terms of the Hamiltonian. This is done by ignoring the terms that arise from the sum of frequencies ($\omega + \omega_0$), because they have zero average contribution. Thus, only the slowest oscillating terms, produced by the subtraction of frequencies ($\omega - \omega_0$), have a significant contribution. The approximation is valid when the external field applied is near resonance with the current atomic transition (or slightly detuned) and has a low intensity. This mathematical simplification facilitates the observation of the evolution of ground and excited states.

The Markov approximation guarantees that the system has no memory and that its current conditions only depend on the current event. This approximation is a tool to ignore multiple atom excitation and saturation. This means that the atomic ensemble only re-scatter photons from the external field and not from the other atoms. Again, to apply this approximation, it is necessary to work with weak excitation, i.e., in linear optical regime.

The linear regime assumption can be considered when the system is far from saturation, which occurs when the value of the saturation parameter is much smaller than $s << 1$ [22]. Therefore, a system with a certain detuning Δ between the frequencies of the optical field and the atomic resonance, a decay rate Γ, and a Rabi frequency Ω, is said to be in the linear regime when $s = 2\Omega_0^2/(\Gamma^2 + 4\Delta^2) << 1$ or $s = 2(\Omega_0/\Gamma)^2/(1 + 4\delta^2) << 1$. For a small detuning, the system can be considered within the linear regime when the pump frequency is not beyond 25-30 % of the decay rate $s \approx 2(\Omega_0/\Gamma)^2 << 1$ Although, a difference of one order of magnitude is assumed to be safe limit, hence ($\Omega \leq 0.1\Gamma$) with a small detuning. Being under this regime allows to simplify the scheme efficiently, adopting both the Markov approach and the RWA.

Finally, the first main equation of the chapter comes from taking the position gradient of the two-component interaction Hamiltonian, applying the three simplifications just described, obtaining the following expression for the force:

$$m\frac{d^2\boldsymbol{r}_j}{dt^2} = -\hbar\Re\left[\boldsymbol{\nabla}_{\boldsymbol{r}_j}\Omega\left(\boldsymbol{r}_j\right)\beta_j^*\right] - \hbar\Gamma\sum_{m\neq j}\Im\left[\boldsymbol{\nabla}_{\boldsymbol{r}_j}G_{jm}\beta_j^*\beta_m\right], \tag{3.1}$$

where almost all variables have been described, except for the dipole moment of each atom β_j, which will be analysed in the following Sec. 3.2.2. The Green function G_{jm} operating as a kernel of the light-mediated dipole-dipole interaction is defined as

$$G_{jm} = \frac{\exp ik\left|\boldsymbol{r}_j - \boldsymbol{r}_m\right|}{ik|\boldsymbol{r}_j - \boldsymbol{r}_m|} = \frac{\sin\left(k_0 r_{jm}\right)}{k_0 r_{jm}} - i\frac{\cos\left(k_0 r_{jm}\right)}{k_0 r_{jm}}, \tag{3.2}$$

with the position of the center of mass for atoms j and m being represented respectively by $\boldsymbol{r}_j$ and $\boldsymbol{r}_m$, and the modulus distance between these two particle by $r_{jm} = |\boldsymbol{r}_j - \boldsymbol{r}_m|$. The definition of Eq. 3.2 comes naturally when deriving the coupled dipole equations, related to β_j, which can be found in appendix A; being defined precisely on page 155.

Two familiar collective effects are described with the final real sine and imaginary cosine terms in Eq.(3.2): the cooperative decay [114] and the cooperative phase shift [122]. Besides, the kernel G_{jm} can be thought of as the representation of scalar dipoles (scalar light approximation), or a vectorial system of dipoles oriented at a magic angle that cancels out the near-field terms. In linear optical regime, the dynamics of this interactions can be obtained either from a quantum [206] or a classical description of the oscillators [205, 209]. When numerically solving a system with N atoms, this interaction term is embodied by a NxN symmetric matrix for each of the dimensions of the existing external DOF. Each atomic interacting pair is represented by an element of this matrix, forcing the self-interaction to be null by fixing the diagonal terms to zero. For each spatial coordinate, the sum of each row gives the interaction force contribution of all atoms acting on the element in the diagonal.

The first term on the right hand side (RHS) in Eq.(3.1) gives a description for the scattering and dipole forces acting on a single atom. The second RHS term yields the cooperative forces acting on the atomic arrangement, in particular the cooperative force between a pair of atoms (j,m) due to scattered fields. Nevertheless, due to the geometry of the here exploited OB transverse configuration, the final force or equation of motion that describes the system is reduced to

$$m\ddot{\boldsymbol{r}}_j = -\hbar\Gamma \sum_{m\neq j} \Im\left[\nabla_{\mathbf{r}_j} G_{jm}\beta_j^*\beta_m\right], \tag{3.3}$$

consequence of the first term being zero. The term cancels out because Ω is uniform in the transverse direction —(x, y) plane—, hence making the gradient $\boldsymbol{\nabla}_{\boldsymbol{r}_j}\Omega\left(\boldsymbol{r}_j\right)$ to be null because Ω is a constant. The differential term, on the left-hand side (LHS) of the equation, has simply been transformed from Leibniz's notation to Newton's notation for a more compact representation.

It is convenient to re-express Eq. (3.3) using two changes of variables: the first rescales the position with the wavevector of the atoms into a dimensionless variable $r_j = kr_j$, and the second represents the time as a dimensionless variable as well, by using the transition decay rate $t = \Gamma t$. Therefore, rearranging the equation's terms, the acceleration of the center of mass of each atom is finally symbolized as

$$\ddot{\boldsymbol{r}}_j = -\frac{2\omega_r}{\Gamma} \sum_{m\neq j} \Im\left[\nabla_{\mathbf{r}_j} G_{jm}\beta_j^*\beta_m\right], \tag{3.4}$$

where now the time derivative represents a dipole time scale Γt and the position kr_j; the recoil frequency ω_r follows the above definition.

3.2.2 Coupled dipole equations: internal atomic dynamics

Whenever there is a force, which depends on some gradient of the systems' internal dynamics Hamiltonian, acting on an atom, it will induce a dipole in the atom. This force will cause an electron in the atom to oscillate between the ground and the exited state, due to absorption and spontaneous emission, and this oscillation will be shared collectively throughout an ensemble of atoms. Eventually, the internal oscillation of the atoms couples to the external motion of the atoms.

The internal dynamics, or dipole moment, of each of the atoms located within a set that is irradiated by a plane wave, can be classically described by the coupled dipole equations, or CDE (see derivation in appendix A):

$$\frac{d\beta_j}{dt} = \left(i\Delta - \frac{\Gamma}{2}\right)\beta_j - i\frac{\Omega_0}{2}e^{i\vec{k}_0\vec{r}_j} - \frac{\Gamma}{2}\sum_{m\neq j}\frac{exp\left(ik\left|\vec{r}_j - \vec{r}_m\right|\right)}{ik\left|\vec{r}_j - \vec{r}_m\right|}\beta_m. \tag{3.5}$$

The first term on the RHS of the above expression is related to the light's detuning and atom's linewidth; the second one is associated with the incident plane wave and its Rabi frequency; and the last term on the right corresponds to cooperative re-emitted radiation from other scatterers into vacuum modes. The last term is responsible for the cooperative frequency shift and has been obtained by adding the hitherto neglected RWA contribution linked to the exchange of virtual photons among atoms [205, 207]. Moreover, the positions of every particle of the system is represented using $\boldsymbol{r}_j$, with $j = 1..N$. Due to the transversal OB configuration used, $k_0 \cdot r_j = 0$ in Eq. (3.5).

When inspecting Eq.(3.5), it is fairly obvious that the dipole moment of an atoms is not described with a single equation, but rather with a set of them; there are as many equations as there are atoms in the system. These equations are designated as coupled dipole equations because each atomic dipole depends on the other dipole atoms. The CDEs describe the dynamics of the main peculiarity of using cold atoms, instead of dielectric particles: the resonance between the external field and the electronic transition frequencies. The full derivation of these equations from the interaction Hamiltonian using similar approaches, exploiting the same approximations and assumption adopted in subsection 3.2.1, can be retrieved from several reports [118, 119, 205, 207, 208]. Nevertheless, an extract of the 4th chapter [210] of the 2nd volume from the *annual review of cold atoms and molecules* from 2014 [211] has been added in appendix A.

Since along each possible direction of translation the system being under scrutiny interacts with a standing wave generated by two identical laser, the second term of the RHS in Eq.(3.5) must be adapted. Conversely, the rightmost term, which explicitly shows the dependence of any atomic dipole on the position of all other particles, can be reduced to a more compact representation. Therefore, Eq.(3.5) can be re-expressed as

$$\dot{\beta}_j = \left(i\Delta - \frac{\Gamma}{2}\right)\beta_j - i\Omega(\mathbf{r}_j) - \frac{\Gamma}{2}\sum_{m\neq j} G_{jm}\beta_m, \tag{3.6}$$

where the comparative emission term described by G_{jm}. The latter expression can also be rewritten applying the two changes of variables adopted in Eq. (3.3), which are $r_j = kr_j$ and $t = \Gamma t$, given the following expression

$$\dot{\beta}_j = \left(i\delta - \frac{1}{2}\right)\beta_j - i\frac{\Omega}{\Gamma} - \frac{1}{2}\sum_{m\neq j} G_{jm}\beta_m. \tag{3.7}$$

The position transformation keeps values close to unity, reducing the chances of floating-point numerical errors; the time transformation allows to simulate longer times with fewer steps, tracking the oscillations of the dipoles at the same time.

When working in the optical linear regime ($\Omega \ll \Gamma$), the atomic dipole is linearly proportional to the external optical field $\beta \propto E$, which allows to compute experimental observables. For instance, the dipole moment of an atom β can be used to estimate the probability of the atom to be in the excited state $|\beta^2|$. In addition, a broad knowledge of the system can be retrieved calculating the eigenvalues of the scattering matrix G_{jm} if motionless atoms are considered.

3.3 Models for optically bound cold atoms

The two sets of coupled equations, (3.3) and (3.5) -or their normalized re-scaled versions (3.4) and (3.7)-, that describe the external and internal dynamics of an atomic ensemble in a transverse optical binding system have already been exposed. Now is the time to define the structure of the cold atomic systems that will provide a means of testing these equations. Consequently, in this section the two schemes used to reveal the OB effects are announced.

Regarded in the first part 3.3.1, a simple pair of atoms helps to present how, in addition to trapping atoms in crystalline structures, OB's multiple scattering can be used to cool down the system. Multiple scattering is linked to optical thickness $b(\Delta) = b0/\left[1 + (4\Delta/\Gamma)^2\right]$, where b_0 is the optical thickness at resonance, defined in Sec. 1.4.1 (page 17). In addition, multiple scattering and absorption could be neglected for a dilute gas with weak field and in the far-detuned limit, as seen in previous Chapter 2; hence the system considered throughout the current chapter differs from the previous one. Developed in the second segment of the section, a one-dimensional chain of atoms of varying size assists on understanding a new cooperative cooling mechanism. Both system have some stability issues because of the atomic resonance, which are handled latter in Sec. 3.4.3.

3.3.1 Two atoms optically bound

The first system is composed of a pair of cold atoms and a scalar external field continuously radiating both particles. There are two laser fields in counter-propagation along the z axis and the atoms are suspended within a (x, y) plane; thanks to the external standing wave generated by the opposing laser beams. In Fig. 3.2, the schematics of such a model is represented and shows the allowed displacement directions of both particles, which is free within the plane. The only restriction of movement comes from the confinement provided by the standing wave, which is not shown in the figure (only the laser beams from the pump are shown).

Since the system is only composed of two atoms, the sum present in Eq. (3.7), containing the Green function reported in Eq.(3.2), can be simplified to a simple variable depending on the position $G = \exp(iq)/iq = \sin(q)/q - i\cos(q)/q$. This position has been redefined as a dimensionless variable, substituting the distance from the center of mass of each particle $\boldsymbol{r}_{1,2}$ by $\boldsymbol{q} = k_0(\boldsymbol{r}_1 - \boldsymbol{r}_2) = q(\cos\theta, \sin\theta)$, with $q = kr$. The dumb indices become $j = 1$ and $m = 2$, although there is not much need for them, because the sum of the Green function becomes unique and identical for the two possible sums $G_{12} = G_{21} = G$.

Considering the definition of G, the new position variable q, and two new changes of variables $B = (\beta_1 + \beta_2)/2$ and $b = (\beta_1 - \beta_2)/2$ (proposed in [204]), each of the two equations that describes the external and internal DOF is subdivided into two expressions. Therefore, the equation of motion for both atoms

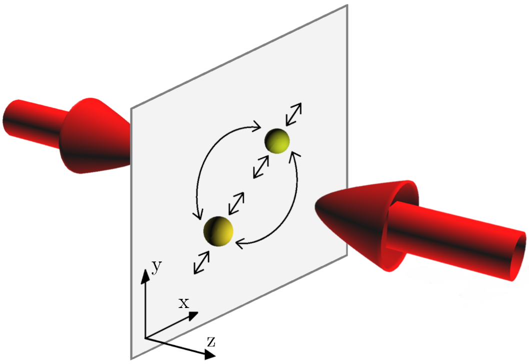

Figure 3.2: Scheme of the system that allows the effects derived from the OB applied to a pair of atoms. The atoms are confined in an optical plane and trapped due to reciprocal scattering forces. The pair of plane wave are represented by red arrows, the atoms, with their external DOF characterized with back arrows, are drawn in yellow-green, and the invisible capture plane is depicted in soft blue-grey.

Eq. (3.4) is expanded accounting for the angular momentum.

$$\ddot{q} = \frac{4\omega_r}{\Gamma}\left[\frac{4\Omega^2}{\Gamma^2}\frac{\ell^2}{q^3} - \left(\frac{\sin q}{q} + \frac{\cos q}{q^2}\right)\left(|B|^2 - |b|^2\right)\right], \tag{3.8a}$$

$$\dot{\ell} = 0. \tag{3.8b}$$

The dipole moment (3.7) is re-expressed as the average dipole moment (β) and the differential dipole moment (b),

$$\dot{B} = -\left[1 + \frac{\sin q}{q} - i\left(2\delta + \frac{\cos q}{q}\right)\right]\frac{B}{2} - i\frac{\Omega}{\Gamma}, \tag{3.9a}$$

$$\dot{b} = -\left[1 - \frac{\sin q}{q} - i\left(2\delta - \frac{\cos q}{q}\right)\right]\frac{b}{2}. \tag{3.9b}$$

The four new equations describing the dynamics of the entire system, are now set in a different relative coordinate frame. However, the system still evolves with the renormalized atomic dipole lifetime $1/\Gamma$ and the new equations contain all the known parameters, already introduced in Sec.3.2. The new short expression, Eq.(3.8b), includes the conservation of the angular momentum of the system $L = (m/2)r^2\dot{\theta}$, by means of a new variable

$$\ell = \sqrt{\omega_r\Gamma}(L/\hbar\Omega). \tag{3.10}$$

In the above expression the radial velocity of the angular momentum is symbolized as $\dot{\theta}$, instead of ω, to avoid any confusion with the already characterized atomic frequency.

A particularity given in the atomic pair scheme is that the dipoles of both atoms are inevitably synchronized after a short transient time Γ time, which will be reviewed in section 3.4.1. Therefore, the two dipole variables can be reduced to $\beta_1 = \beta_2 = \beta$, which transforms the employed changes of variables to: $B = \beta$ and $b = 0$. Consequently, once again it is possible to reduce the two sets of equations (3.8) and (3.9), into two coupled expressions that describe the internal and the external dynamics of both atoms:

$$\dot{\beta} = \left[1 + \frac{\sin q}{q} - i\left(2\delta + \frac{\cos q}{q}\right)\right]\frac{\beta}{2} - i\frac{\Omega}{\Gamma}, \tag{3.11}$$

$$\ddot{q} = \varepsilon^2\left[\frac{\ell^2}{q^3} - \left(\frac{\sin q}{q} + \frac{\cos q}{q^2}\right)|\beta|^2\right]. \tag{3.12}$$

It is useful to define a new parameter $\varepsilon = 4\Omega/\Gamma\sqrt{\omega_r/\Gamma}$ in the second expression 3.12. It comes from the analytical study of the dynamics of the atomic pair under OB, it will be later referred in Eq. (3.20) on page 85. This parameter allows to accelerate the evolution of the system, allowing to see the dynamics of the molecule in $\Gamma t > 1$ without having to use a long simulation time; i.e., allowing to control the time scales of the cooling and heating mechanism. The trick is to increase the recoil frequency, which in turn induces the same dynamics that the system would have for the real value, but in a shorter time. The two equations that describe the dynamics of the system represent a single synchronized dipole moment β for both atoms together with the variation of the distance between them q. Unless explicitly declared, the angular momentum of the system will be considered null, so the first RHS term containing ℓ in Eq. (3.12) is dropped. In this way, the motion of the atomic pair can be better compared with the second system, characterized in the next section.

3.3.2 Optical binding in a unidimensional chain of atoms

The second system employed to study the OB effects in cold atoms is an ensemble of particles distributed along a one-dimensional system. In this case, the atoms are trapped with two pairs of counter-propagating lasers with the same characteristics than the pair applied in the first two-atom system. Due to this set-up, an extra DOF is completely suppressed, leaving the atoms with the only option to oscillate back and forth in 1D motion, with no possible angular momentum. The internal dynamics of the atoms are intact, which will provide a unexpected seed for discovering a new collective phenomenon.

In a real experiment, the 1D chain can be effectively trapped in a two-dimensional optical lattice and, with a little extra adjustment, can be reduced into a one-dimensional assembly of could atoms (chain). The possibility of a 1D structure of ultracold atoms has been explored since the beginning of the 21th in several experiments [212–214], but recent advances have also been made in cold atom systems [215]. The schematics of this second model is depicted in Fig. 3.3, where the coordinates have been rearrange, causing the chain to stretch along the z direction and setting the external fields on the perpendicular axes x and y.

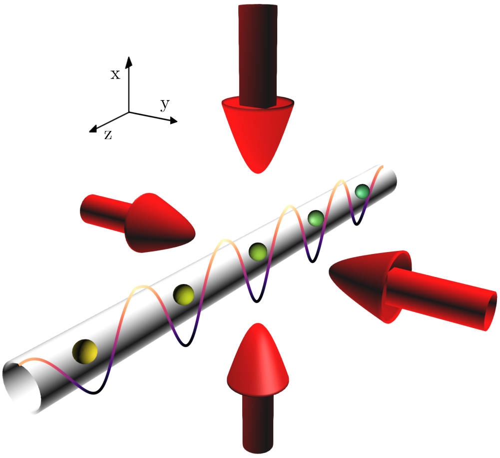

Figure 3.3: Scheme of a cold atomic constrained to one-dimensional displacement using four identical laser beams. The minima of the self-generated potential landscape (illustrated by an oscillating curve) are determined by the distance between atoms; its lowest energy points are found when this spacing is close to the optical wavelength λ. The cold atoms are embodied by yellowish-green spheres, the laser sources with red arrows and the transparent tube is a mere representation of the invisible optical confinement in one dimension.

In the award-winning optical tweezers technique, a dielectric particle is trapped in a single potential well generated from a single beam gradient force, but when it comes to cold atoms in a one-dimensional optical binding structure, the particles are trapped by dynamic potential wells emerging from the atomic mutual forces. The potential minima are generated individually for each atom due to the multiple scattering of all particle involved in the system, which self-organize the system into a central symmetric chain, with a distance between each link close to the external field wavelength.

As in the previous case, the force induced in any atom along the allowed external DOF is only caused by the scattering photons from the other atoms, because the external fields do not produce any contribution onto the chain's axis. The equations representing this system are the general ones, revealed in Eqs. (3.3) and (3.6), respectively describing the interal atomic force and the dipole dynamics for each atom. For practical reasons, that will be exploited in the second segment the next subsection, the external motion can be represented slightly different for this case:

$$\begin{aligned} m\frac{d^2\boldsymbol{r}_j}{dt^2} &= -\hbar\Gamma\sum_{l\neq j}\Im\left(\beta_j^*\beta_l\nabla_{\boldsymbol{r}_j}G_{jm}\right) \\ &= -\hbar\left(\beta_j^*\nabla_{\boldsymbol{r}_j}\Omega_j(\boldsymbol{r}_j)+c.c.\right), \end{aligned} \tag{3.13}$$

where the position of atom j is symbolized by $\boldsymbol{r}_j$ and the field is now represented by the effective Rabi frequency labelled $\Omega_j(\boldsymbol{r}_j) = \Omega_0 - i(\Gamma/2)\sum_{l\neq j} G_{jm}\beta_m,$. The effective Rabi flop includes the external field amplitude Ω_0, and the collective field due to dipole scattering, contained in the second term including G_{jm}.

This 1D chain system does not allow any extra change of variables due to lack of synchronization of the dipoles, unless the case taken in consideration is again an atomic pair. Consequently, the equations to solve this system are the altered expression that describe the atoms displacement, Eq. (3.4), and the dipoles' moments, Eq. (3.7), presented in Sec. 3.2. Recalling the expressions where a couple of changes of variables were applied to the two equations representing the internal and external motion of every atom in a system under the OB effect, the dynamics of a chain of atoms is described by

$$\dot{\beta}_j = \left(i\delta - \frac{1}{2}\right)\beta_j - i\frac{\Omega}{\Gamma} - \frac{1}{2}\sum_{m\neq j} G_{jm}\beta_m, \tag{3.14}$$

$$\ddot{\boldsymbol{r}}_j = -\varepsilon_c^2 \sum_{m\neq j} \Im\left[\nabla_{\mathbf{r}_j} G_{jm}\beta_j^*\beta_m\right]. \tag{3.15}$$

Due to the change of variables applied to make time and position dimensionless variables, both expressions (3.14) and (3.15) use the time scale Γt and the redefined position for each atom $r_j = kr_j$. In addition, the small parameter announced in the previous model is defined here using the initial scaling parameters of Eq (3.15) instead, $\varepsilon_c = \sqrt{2\omega_r/\Gamma}$. As in the atomic molecule with ε, the parameter ε_c allows to shorten the simulation times for the atomic string. In addition, it provides a more compact expression, which is like the one employed in the case of the atomic pair. When dealing with the exact equation describing the atomic chain the value of this parameter will be $\varepsilon_c = 0.3$.

After having described the two systems that are utilized to probe the OB effect, an important remark needs to be made. In the force applied to both systems compiled in Eq.(3.3), the stochastic effects linked to spontaneous emission have been ruled out. However, the role these effects play when added to introduced systems is discussed in Sec. 3.6.

3.3.3 Adiabatic approximation approach

Although in this thesis there are only two real systems exploited to observe the OB effects in cold atoms, the author has decided to separate into an individual subsection what is here called the adiabatic approximation. This new approach is a mere assumption about Secs. 3.3.1 and 3.3.2, where the synchronicity between the atomic dipole and the external field is speculated by eliminating the internal dynamics of the atoms. This assumption allows investigating what are the consequences of the distinctive feature that atoms have and that dielectric particles lack, resonance.

When carrying out the adiabatic approximation, it is considered that the time it takes an atom to execute an internal oscillation is negligible, compared to the time it takes to carry out an external oscillation, caused by the binding potential, i.e., the relaxation time of a dipole is assumed to be negligible ($\tau = 1/\Gamma \approx 0$). This makes the internal decay to be instantaneous, the only thing that needs to be done to derived such dynamics, hence β_j is synchronized in time with the position $r_j(t)$. Therefore, $\dot{\beta}_j$ can be meglected in (3.14) and $\beta_j(t)$ can be obtained solving the system of the now algebric equations (3.14) for given positions $r_j(t)$ The calculation is fulfilled for the two systems introduced, making the internal and external coupled equations of both systems to become a unique equation describing the motion of the atoms.

Two-atom system

Equating the LHS term of Eqs. (3.11) to zero and rearranging terms, allows to derive the square dipole modulus for a pair of atoms as

$$|\beta|^2 = -\frac{4\Omega^2/\Gamma^2}{\left[2\delta + \cos(q)/q\right]^2 + \left[1 + \sin(q)/q\right]^2}. \tag{3.16}$$

The only thing left to do, to obtain the adiabatic equation of motion for two atoms, is the equation (3.16) into expression (3.12), which gives

$$\ddot{q} = \frac{4\omega_r}{\Gamma}\frac{4\Omega^2}{\Gamma^2}\left\{\frac{\ell^2}{q^3} + \frac{\sin(q)/q + \cos(q)/q^2}{\left[2\delta + \cos(q)/q\right]^2 + \left[1 + \sin(q)/q\right]^2}\right\}. \tag{3.17}$$

The expression describes the evolution of the system on a time scale Γ and can be further simplified in a more compact form

$$\ddot{q} = \varepsilon^2\left\{\frac{\ell^2}{q^3} - w(q)\right\}, \tag{3.18}$$

where the two new elements denote the function

$$w(q) = \frac{\sin(q)/q + \cos(q)/q^2}{\left[2\delta + \cos(q)/q\right]^2 + \left[1 + \sin(q)/q\right]^2}, \tag{3.19}$$

depending on the variable distance between particles and the fixed normalized detuning; and the already introduced constant coined as "small" parameter

$$\varepsilon = \frac{4\Omega}{\Gamma}\sqrt{\frac{\omega_r}{\Gamma}}, \tag{3.20}$$

which is determined using three known frequencies: the rabi flop, the decay rate, and the recoil frequency.

As introduced in section 3.3.1, the ε parameter helps to speed up the dynamics of the systems, allowing to see long-term effects, such as the new cooling mechanism (Sec. 3.4.3), with shorter simulation times. Its derivation comes from a multiscale analysis detailed in part III of Sec. 5.1, which is possible due to two times scales present in the system. Throughout the chapter, and when dealing with the analytically derived expression, it will be assumed to have a constant value of $\varepsilon \sim 0.085$, unless it is explicitly stated otherwise. Knowing that the system operates in the linear regime, here adopted with $\Omega = 0.1\Gamma$, using such a ε value is like rescaling the recoil frequency to approximately 70 times higher.

One-dimensional chain system

Similarly, the procedure is applied to the unidimensional arrangement of cold atoms, but in this case the adiabatic elimination of the internal dynamics ($\dot{\beta} = 0$) is applied to Eq.(3.14). By using the already characterized effective Rabi frequency $\Omega_j(\boldsymbol{r}_j) = \Omega_0 - i(\Gamma/2)\sum_{l\neq j} G_{jm}\beta_m$, it can be defined the dipole moment of each atom as

$$\beta_j = \alpha\Omega_j(\boldsymbol{r}_j), \tag{3.21}$$

which is proportional to this effective frequency through a constant defined as the normalized atom polarization, $\alpha = 1/(\Delta + i\Gamma/2)$. This is possible because, unlike with the pair of atoms, no additional change of variables is applied when calculating the dipole moments.

Adding the value of the dipole moment β_j into the external dynamics, Eq. (3.13) can be rewrite into a two component force

$$\begin{aligned} m\ddot{\boldsymbol{r}}_j &= -\hbar\left(\beta_j^*\nabla_{\boldsymbol{r}_j}\Omega_j(\boldsymbol{r}_j) + c.c.\right) \\ &= \frac{\hbar}{\Delta^2 + \Gamma^2/4}\left(\Gamma|\Omega_j|^2\nabla_{\boldsymbol{r}_j}\varphi_j - \Delta\nabla_{\boldsymbol{r}_j}|\Omega_j|^2\right), \end{aligned} \tag{3.22}$$

with a generic external field represented by $\Omega_j = |\Omega_j|e^{i\varphi_j}$. The radiation pressure force is represented by the first RHS term of the equation, whereas the second terms describes the dipolar force.

3.4 Inspecting the genuine atomic feature of resonance

All the necessary tools to study an atomic system under the optical binding effect have already been provided, so everything is prepared to show some results. The current section presents the results acquired taking advantage of the attribute that makes the atoms unique compared to dielectric particles, the atoms' internal dynamics. This feature may be regarded as the most fundamental aspect of the chapter because it is due to the delay between the dipole and external field oscillations, that a novel cooling mechanism emerges. Besides this phenomenon, the lack of synchronization among the dipoles, together with the field-dipole delay, can also trigger the opposite outcome: instabilities in the system long-term evolution or heating mechanism.

In the first part of the subsection, the focus falls on the synchronization among the atomic dipoles of the system, then the attention is directed to extract the consequences of having resonance with the external field. Using the specific case of adiabatic systems presented in Sec. 3.3.3, the behaviour of the system when atoms behave as dielectric particles is exposed. The approximation allows to calculate certain parameters of the system such as the potential of the potential landscape generated by the OB effect. In addition, the key role that the internal dynamics has on the instability of the system is investigated, hence allowing to study how the lack of synchronism between the internal motion and the external motion triggers an instability in the system, that cannot be explained with the adiabatic model and generates a new cooling mechanism. Most of the resolution is done numerically, due to the complexity required to determine the analytical expression of the systems, although some analytical derivations are made for the case of two atoms. The writer advises to check on the published paper fruit of this investigated added in Sec. 5.1, where the whole analytical derivation for a couple of atoms. The last part gives a short characterization of the key factors aiding to the systems instability.

3.4.1 Dipoles synchronization

It has been mentioned above how the dipole moments of an atomic pair inevitably oscillate in synchrony, regardless of their initial amplitudes, as long as the atoms are separated from each other by a distance that corresponds approximately to a multiple of the optical wavelength λ. Unlike the atomic pair, the opposite holds true for a system with more atoms ($N \geq 3$), no synchronization is achieved even if the outer DOF of the system is reduced to one dimension, as in an atomic string model (Sec.3.3.2).

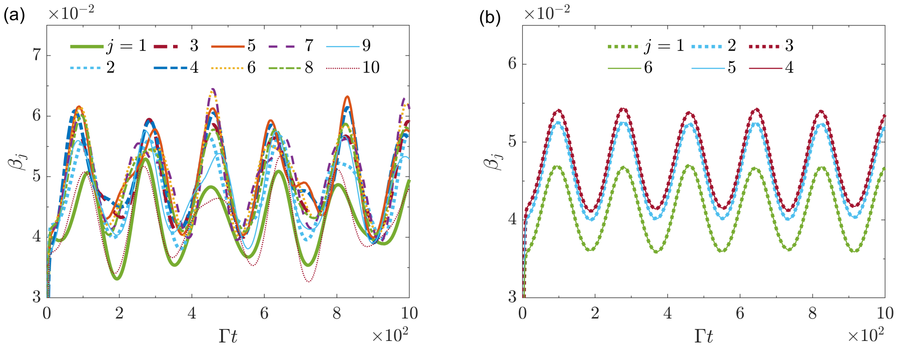

Figure 3.4: The dipole dynamics of atoms in a string system, stretching towards positive values of the z axis —starting from the j-atom "1"—, is examined for a some oscillations (initially $\beta_j = 0$). In (a), the atoms with odd labels (first row of the legend) are displaced 0.03λ from their initial positions, performing a sort of unsymmetrical shift of the chain, which has a distance between particles of $kr = 2\pi$ or λ. In (b), the atoms are set at the distance close to equilibrium λ and the system is allowed to relax. The symmetry in this second case gives way to three different oscillation graphs resulting from mirrored-pairs of atoms: 1-6, 2-4 and 3-4. All particles in both plots have zero initial velocity, the pump is set at $\Omega = 0.1\Gamma$, and the normalized detuning at $\delta = -0.3$.

In Fig. 3.4, for the purpose of demonstrating such asynchronous situation, the contrast between two distinct spaced distributions of atoms in a chain are presented. Different initial positions of the particles in each case lead into different dipole oscillating pictures of the same system, none of which reaches synchronization. However, it is interesting to note that a certain synchronization arises between atoms equidistant from the center of the chain, here defined as “mirrored pairs”. One may thing that, in Fig. 3.4(b), these mirrored pairs are executing a perfectly harmonized vibration with some displacement between them, but when the data is studied closely, the phase difference becomes evident. It can be seen that when the central value of all represented oscillations is set on the same horizontal line, the delay between pairs is evident. The oscillating curves have a lag between them, with the lower 1-6 green pair being the one that comes first, followed by the 2-5 blue couple and ending with the 3-4 red duo. The pairing oscillations between mirrored-pairs represented in panel (b)can only occur when a symmetric agitation is imposed on the system. This pairwise synchronism takes a little longer as the initial amplitudes of the atomic dipoles are forced to be randomly different, but it eventually appears; first joining the pairs into an intertwined oscillation and later harmonizing all mirrored pairs vibrations.

There is not much need to show what the dipole oscillation plot would look like for a two atom system, it is enough to observe the perfect synchronization experienced by any of the three atomic mirrored-pairs on Fig. 3.4(b). As shown in Eq. (3.11), the dipole moment is unique for both atoms after the system has evolved for a very short transient time, almost instantaneously —see the same panel(b)—. The same goes for dual dipole arrays that have random initial amplitudes $\beta_j \neq 0$, after a short transient type, the dipoles will synchronize perfectly; much faster than the 1D chain of many atoms would. In addition, a hypothetical situation is presented in appendix D, where the atoms of the chain are force to behave as if they were as synchronized like in an atomic pair. Allowing, to show what are the direct consequences in the later described cooling effect.

3.4.2 Adiabatic approximation: atoms operating as dielectrics

When atoms are considered as dielectric particles, losing their internal oscillation, they can be trapped in equilibrium points, oscillating with an everlasting constant maximum amplitude. Thus, in such an adiabatic case, the effects of optical binding are reduced to the trapping phenomenon into stable crystalline-like structures, allowing the system to be rearranged at will. Although this is not the natural behaviour of resonant atoms, this approach allows certain properties of the system to be derived. For example, the resulting conservative central force allows the dynamics of the system to be obtained from the trapping potential,[4]

$$V(q) = \varepsilon^2 \int_q^{+\infty} \left(\frac{\ell^2}{q^3} - w(q) \right) dq. \tag{3.23}$$

It depends on the distance between the two atoms q and other variables ℓ, w and ε, which have already been defined, in the same order, in Eqs. (3.10), (3.19) and (3.20).

It is possible to obtain the equilibrium points of the potential by setting the force acting on the atoms to be zero, i.e., equating Eq. (3.18) to zero or by setting the

---

[4] Conservative central forces can be described by means of the negative gradient of a potential as $F(\boldsymbol{x}) = -\nabla V(\boldsymbol{x})$.

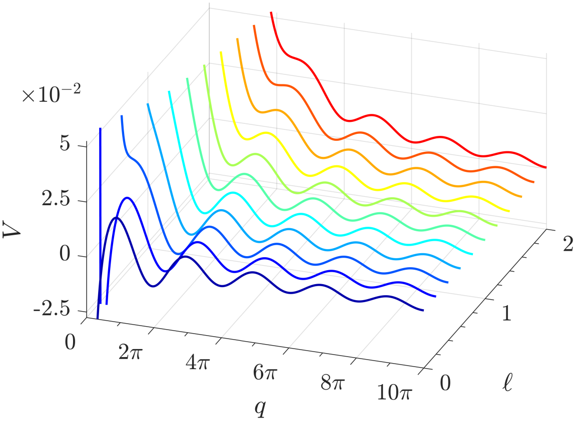

Figure 3.5: Potential landscape $V(q)$, following Eq. 3.25, for different angular momenta, $0 \leq \ell \leq 2$ (with step of 0.2), and a fixed detuning, $\delta = -2$.

expression inside the parenthesis in Eq (3.23) to zero, which yields the equilibrium points $q_n^3 w(q_n) = \ell^2$. The subscript n represents the order of the minimum being considered, for example, $n = 1$ refers to the first minimum located at $\sim \lambda$ or $\sim 2\pi$ (see the the curve with darker blue or $\ell = 0$ in Fig. 3.5). The maxima and minima of the potential alternate between each other periodically, so the unstable values are found at $q_s \approx \pi(2n+1)$ and the stable values at $q_s \approx 2\pi n$, respectively; considering the angular momentum ℓ is small.

Under this conditions of angular momentum and considering the periodicity of the solutions —odd multiples of π for maxima [π, 3π, ...) and close to even multiples of π for maxima [$\sim 2\pi$, $\sim 4\pi$, ...)—, an approximation of the potential energy $V(q)$ can be derived around these points. First, Eq. (3.19) can be reduced to:

$$w(q) \approx \frac{1}{1+4\delta^2}\left[\sin(q)/q + \cos(q)/q^2\right], \tag{3.24}$$

where the denominator becomes the first initial factor $1/(1+4\delta^2)$, as a result of the π-periodicity of the solution points: $\sin(q)/q$ is almost null and $\cos(q)/q$ tends rapidly to zero due to the power of two; the denominator stays the same, due to the lack of this power of two in the sine and cosine terms. Second, Eq. (3.24) is inserted into Eq. (3.23) and the integral is calculated, giving the final approximate expression of the potential energy

$$V(q) \approx \varepsilon^2 \left[\frac{\ell^2}{2q^2} - \frac{1}{1+4\delta^2}\frac{\cos q}{q}\right]. \tag{3.25}$$

From the last formula, it can be deducted that the greater the angular momentum, the greater the value of the centrifugal forces. Consequently, increasing the angular momentum produces a molecule that is less stable, making it easy to overcome the effect of optical binding. The situation can be analysed effortlessly in

Fig. 3.5, where it can also be detected that the potential wells become shallower for higher multiple of λ, following the curve $-(\cos q)/q$ (Eq. 3.25), announced in [2].

Comparing the adiabatic and the exact solution

The time evolutions of the two mapped atomic systems, described in Secs. 3.3.1 and 3.3.2, are compared to their analogous adiabatic adaptations, proposed in Sec. 3.3.3. The comparison between this two solutions for both systems are illustrated in Fig. 3.6. It can be easily observed how whenever the atoms are considered adiabatically, both systems evolve with a conservative motion of constant amplitude, which is represented through the normalized osculations of the kinetic energy of the entire ensemble; represented using the lighter grey plots in both panels (a) and (b). On the contrary, when the exact dynamics is analysed for the atomic pair —Eqs. (3.11) and (3.12), with $\ell = 0$— and for the 1D chain —Eqs. (3.14) and (3.15)—, the amplitude of the normalized kinetic energy decreases in time; displayed with the darker curves in the same panels. The reduction in energy represents a progressive contraction of the amplitude in the oscillating movement of the atoms, which can be translated into a cooling mechanism. This new cooling mechanism is described in detail in the following Sec. 3.4.3.

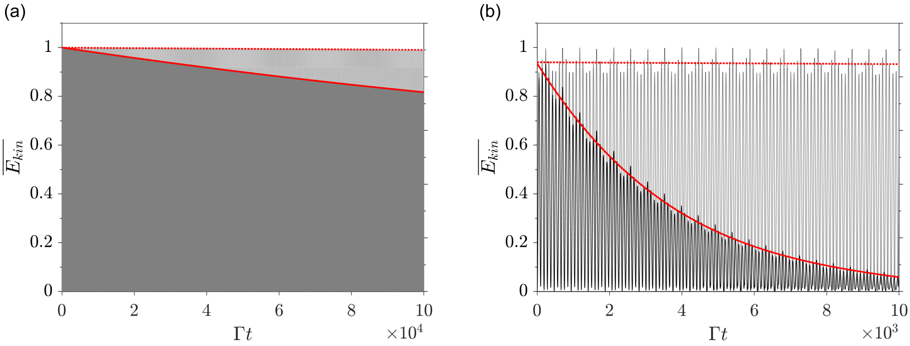

Figure 3.6: Time evolution of the normalized kinetic energy of the two current OB systems, comparing the exact and the adiabatic solution for both. In (a), the $N = 2$ system is depicted using a detuning $\Delta = -0.4\Gamma$, while this is set to be $\Delta \approx -0.15\Gamma$ for a chain constituted of $N = 10$ atoms, represented in (b). Both systems have the same pump $\Omega = 0.1\Gamma$ and the same initial conditions for position, with an inter-particle distance of λ, and velocity, which is zero for each particle.

Note that in Fig. 3.6, the evolution in the total time of panel (b) represents only 10% of the total time of panel (a). The reduction of the normalized kinetic energy in the first $\sim 0.3ms$ ($10^3\Gamma t$) in the 1D string of atoms is more than 90%, but in the atomic pair it is approximately $2-3\%$. Although there are just 5 times more atoms involved, from $N = 2$ to $N = 10$, the reduction of the energy is 30 times higher with an atomic chain. This is the result of the action of the collective effects, which suggests a new cooperative cooling because of the effect of optical binding. It will be explained in detail in Sec. 3.5, along with the reason why the two systems are evolved using two different detuning.

There are some other facts and comments, related to plots represented in Fig. 3.6, that are worth noting and mentioning:

- The normalized energy is defined for both OB systems (1D-chain and atomic pair) as the maximum kinetic energy achieved by the system, either in its adiabatic form or using the exact equations.
- The envelope of each curve represented in red for all curves, drawn with solid lines for the exact solutions and dashed lines for the adiabatic approximations, is calculated by averaging the peaks of the kinetic energy oscillations.
- The two cooling processes are exponential, but the one in (a) has a much lower cooling rate, so it appears as if it were linear cooling.
- The evolution of each curve is obtained by numerically solving the equations introduced by means of an ordinary differential equation solver (ODE). The same results can be obtained with other symplectic integrating methods, such as the leapfrog algorithm or velocity Verlet (the subject has been explained in detail in Chapter 2).

3.4.3 Dynamics of an optically bound atomic molecule: new cooling mechanism

The external motion of the atoms in an optically bound system is coupled to their internal vibration. Therefore, the internal oscillations are going to affect, sooner or later, the external trajectories described by the particles. The amplitude of the external motion oscillations of an optically formed molecule determines its stability, the formation of which is highly dependent on the detuning of the atomic decay and the optical field. That is why the coupled internal dynamics of the system is a distinct stability feature, which can either glue an atomic pair together or break it down. It has been shown how by solving the exact equations of the two-atom system without considering the decay rate Γ as instantaneous, it experiences the reduction of its kinetic energy or the amplitude of oscillation; the system may also yield to dissociation. Such instability, was observed in [204] solving Eqs. (3.11) and (3.12) numerically, when cold neutral atoms were used in an OB system for the first time. Subsequently, this instability was derived analytically and numerically simulated to discover the conditions necessary to exploit it as a new cooling mechanism [216] (or Sec.5.1).

The whole stability research is possible thanks to the trapping dynamic potential, determined in the previous section, which is generated by the interaction between the local filed and the scattered photons by both atoms. This mutually induced potential landscape is depicted in Fig. 3.7 for a zero angular momentum ($\ell = 0$), where the maxima an minima are displayed in the depicted plane. To distinguish a maximum from a minimum, simply look at the one-dimensional graph, located on the left side, which represents $V(q)$ as a function of $q/2\pi$ from Eq. (3.23).

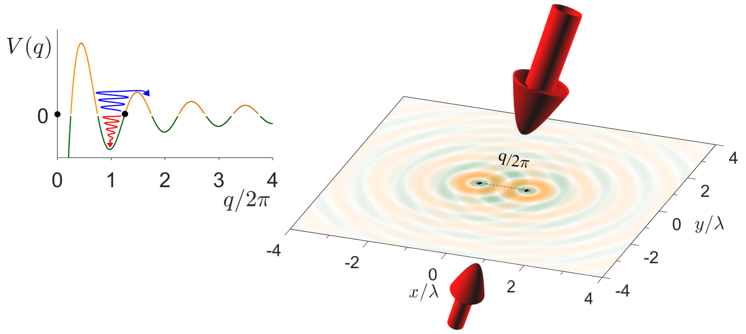

Figure 3.7: Optical potential landscape generated by the interference between confining laser beams (red arrows) and radiation from atoms. The pair of atoms (black dots) is trapped at the first potential minimum, with $|\mathbf{r}_1 - \mathbf{r}_2| \approx \lambda$. The upper box describes the profile of the self-generated potential $V(q)$ where $q = k|\mathbf{r}_1 - \mathbf{r}_2|$, in the absence of angular momentum.

This graphic legend also describes what happens if an atom follows a cooling trend (red spiral), associated to a red detuning, or a heating trend (blue spiral), linked to blue detuning. However, the spontaneous emission of a photon is not considered, neglecting the possible stochastic heating (see Sec. 3.4.3).

In short, the desired result is to activate and take advantage of the cooling mechanism caused by the optical binding effect. A concise analytical derivation is now presented with the main results, but a more extensive analytical derivation can be reviewed in the attached letter in Sec. 5.1.

Dipole moment beyond the adiabatic case

The cooling phenomenon is triggered due to the effects of a dissipative force generated from the time delay that emerges from the reaction time of the dipole when it tries to couple to the oscillation of the external field. To represent this delay, it is necessary to abandon the adiabatic approximation, so the response time of the dipole is not considered to be zero, with a finite decay rate. In fact, instead of completely forgetting the adiabatic case, the finite time can be perceived as a correction of the adiabatic approximation, resulting from an existing dual time scale present in the system. For reasons that will be clarified later, the only system that is characterized after this correction of the adiabatic case, are the equations for a pair of atoms.

The dipole moment that was derived from setting the LHS term of Eq. (3.11) equal to zero, with its modulus square expressed in Eqs. (3.16), can be extended with a correction term, ending up reading as follows (refer to appendix C for its derivation):

$$\beta(t) \approx -\frac{2i\Omega/\Gamma}{[1 - 2i\delta + g(t)]} - \frac{4i\Omega}{\Gamma} \frac{\dot{g}(t)}{[1 - 2i\delta + g(t)]^2}. \tag{3.26}$$

All variables are known except for $g(t)$, which refers exactly to the complex term in the kernel of Eq. (3.2) expressed in its exponential form $g(t) = exp(iq(t))/iq(t)$, with the dimensionless change of variable already used for the position $q = k\,|r_j - r_m|$. Although now there is a crucial difference in this kernel, because it is assumed to be time dependent; thus allowing to adopt a first order deviation term, represented by $\dot{g}(t)$, when deriving the dipole moment from Eq. (3.11). Also note that the LHS of Eq. (3.11) is no longer equated to zero to obtain β, but rather that the integral of said equation is calculated to obtain β beyond the adiabatic approximation. The complete derivation of this new dipole moment can be followed from the appendix of an attached article in Sec. 5.1.

Consequently, the dipole moment in Eq. (3.26) now includes two components: the first, proportional to $q(t)$, corresponds exactly to the instantaneous response of the dipole to the atomic motion or adiabatic approximation; and the second, proportional to $\dot{q}(t)$, which describes the first-order delay of this response.

Equation of Motion beyond the adiabatic approximation

The internal dynamics of the molecule are now described by the time-dependent dipole moment shown in Eq. (3.26). Matching the actions taken when calculating the motion equation of the adiabatic "model" in Sec.3.3.3, the squared modulus of expression (3.26) needs to be introduced into the motion equation, Eq. (3.18), to obtain these new equations of motion. Therefore, by keeping only the linear term of $\dot{q}(t)$, these calculations culminate in a non-conservative equation of motion that reads

$$\ddot{q} = -\frac{dV}{dq} - \epsilon^2 \lambda(q)\dot{q}. \tag{3.27}$$

This new dissipative term that changes between positive and negative value as q oscillates, determines if the system reduces its kinetic energy or increases it, if it is cooled or heated, respectively. The term is defined on this line:

$$\lambda(q) = \frac{4w(q)}{A(q)^2 + B(q)^2}\left\{\frac{\cos(q)}{q} - \frac{\sin(q)}{q^2} - 2w(q)A(q)B(q)\right\}, \tag{3.28}$$

defining the coefficients A and B, depending on the distance between atoms q, as

$$A(q) = 1 + \frac{\sin(q)}{q}, \tag{3.29a}$$

$$B(q) = 2\delta + \frac{\cos(q)}{q}. \tag{3.29b}$$

Comparing the exact dynamics of the two system with this new approach

For the sake of comparison, the equivalent equation of motion for atoms arranged in a line, the derivation of which can be found in the appendix C, is calculated:

$$\ddot{q}_j = -\varepsilon^2 \left(1 + \lambda_N\right) \sum_{m \neq j} w(q_{jm})\hat{u}_{jm}, \tag{3.30}$$

where $w(q_{jm})$, ε and λ_N are in that order the mirror images of Eqs. (3.20), (3.19) and (3.28), for the one-dimensional system; and the unit vector $\hat{u}_{jm} = u_{jm}/\boldsymbol{u_{jm}}$ is the projection of the motion, being in this case along the z axis.

A parallel comparison like the one performed in Fig. 3.6 is now carried out in Fig. 3.8, but this time, instead of showing the adiabatic case, it is represented the exact solution together with the dynamics obtained with the label as "beyond the adiabatic solution". In the left panel (a) of the figure and using Eq. (3.27), the time evolution of the system for two atoms is illustrated, while the characterization of the chain of atoms is represented in the right panel (b) using Eq. (3.30).

On the one hand, when observing the system with a pair of atoms in panel (a), it is possible to see that the approximate solution beyond the adiabatic case, can represent the instability depicted by the exact equations. This new solution introduces the necessary disturbance that leads to the end of the perpetual oscillations of the adiabatic case. It is true that it is not a precise coincidence, but it allows a detect of the origin of the instability, which is intrinsically linked to the delay experienced by the dipole when synchronizing with the external movement of the molecule. Therefore, the resulting graphs in (a) certify that the lack of synchronism between the internal and external DOF triggers the instability of the system in a new cooling mechanism. Unfortunately, it can also be the spark that unbalances the system towards a not so desired heating phenomenon.

On the other hand, when the right panel (b) of such figure is analysed, it can be quickly detected that not only the same approximate solution flatly fails to describe the cooling effect, but also how inadequate it is to declare that there is a cooling. The reason for the observed evolution of the system is exactly linked to the same origin as in the left panel, but in this case the heating mechanisms are a consequence of the lack of synchronization among the atomic dipoles. In fact, as explained in Sec. 3.4.1, it is not possible to have dipole synchronization in systems with more than two atoms. The how and why of this unexpected result are carefully examined in the next Sec. 3.5.

In addition, it can be seen that in Fig. 3.8 the normalized kinetic energy has been redefined as the maximum initial energy acquired by solving the exact equations of motion. Again, as in the comparison with the adiabatic case (Fig. 3.8), the darker grey curves represent the exact solutions for both systems, but now the lighter ones correspond to the labelled "beyond the adiabatic solution" and the small parameter is considered to be $\varepsilon \sim 0.085$ instead.

Particle self-organization is more likely to occur with a distance between particles close to λ. For instance, an optically bound molecule is more likely to form when the distance between particles matches the distance required to find the deepest potential well, the first minimum (check small plot on the left in Fig. 3.7). Like any cooling mechanism, a capture rate can be estimated by equating the kinetic energy required to overcome the shallower maxima of the potential well, located at higher separation distance. Focusing on the simplest studied system, the kinetic energy linked to the radial velocity difference δv between two atoms is related to the dimensionless potential barrier U. The potential barrier is calculated by taking the difference in potential energies between the first minimum and the second maximum —the derivation of this barrier can be traced at the end of the third

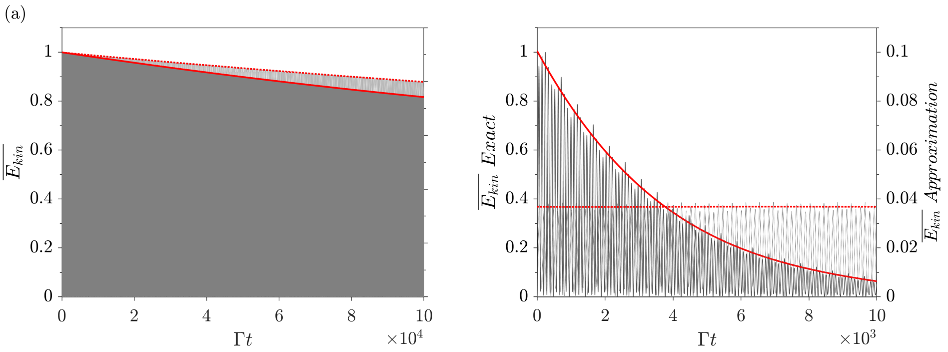

Figure 3.8: The time evolution obtained solving the exact equations is compared with the new approximate solution (beyond the adiabatic case) for the two current OB systems, using the normalized kinetic energy. In (a), the system with $N = 2$ is represented using a detuning $\Delta = -0.4\Gamma$, while it is set to be $\Delta \approx -0.15\Gamma$ for a string constituted of $N = 10$ atoms in (b). Both systems have the same pump $\Omega = 0.1\Gamma$ and the same initial conditions for position, with a distance between particles of λ, and velocity, set to zero for each particle.

subsection of the attached document in Sec. 5.1—. Thus, two atoms can form an optical bound when

$$\frac{1}{2}m(\delta v)^2 < \left(\frac{\hbar\Gamma^2}{2\omega_r}\right)U, \tag{3.31}$$

where the parameters inside the parenthesis in the RHS of the equation only represents the change of variables applied when calculating the equation of motion $m\Gamma^2/k^2 = \hbar\Gamma^2/4\omega_r$. This factor allows to transform the general form of the kinetic energy, expressed in the LHS of the equation, into the actual coordinate framework employed in the current system of equations.

Although no consideration is giving to the heating mechanism caused by the spontaneous emission of photons, the possibility of the system to evolve towards its annihilation in a heating process is very much alive. No time evolution representation of this heating process is given to represent any of the revised solutions: exact, adiabatic and beyond adiabatic. It is trivial to understand how the envelope curves illustrated so far, in each plot of both Figs. 3.6 and 3.8 (in red), would look like; however, some representation can be found in Fig 3.18 of Sec. 3.5.3.

3.4.4 Parameters affecting the cooling mechanism

There are three parameters that affect whether the two announced systems follow a desired cooling trend or fall into a heating spiral that breaks them apart.

Detuning

The first parameter that defines whether there is cooling or heating in an OB system is the detuning. The detuning value has been a fundamental concept since laser cooling was born in the mid-1970s [14, 15]. As introduced in Chapter 1, Doppler shift is the phenomenon responsible for allowing or preventing an atom from interacting with an incoming photon, when its wavelength detuned with respect to the electronic transition of the atom. Therefore, the cooling mechanism described by optical binding is also strongly subject to this parameter. However, in the current case, the detuning value that establishes the barrier between cooling and heating of a pair of atoms is close to resonance than in the well-known Doppler cooling. For the case of a string of atoms, as it will be represented in the next section in Fig. 3.15 on page 104, the current cooling mechanism can also be detected for small positive detuning, thanks to a cooperative effect.

Angular momentum

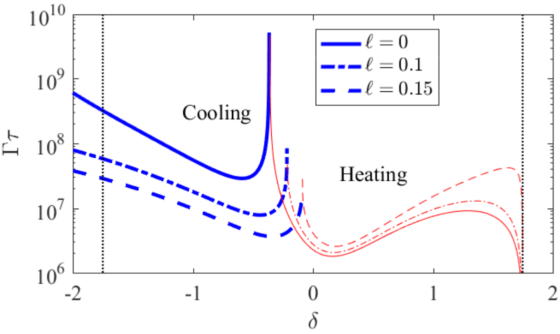

Figure 3.9: Plot representing the dependence of the heating mechanism (thin red lines) and cooling process (thick blue lines) on the angular momentum. Using the detuning δ as the scaling canvas, the heating escaping time and the cooling half-energy time are plotted for three different values of the angular momentum ℓ. All curves are obtained for a fixed value of the small parameter $\varepsilon = 0.1$ and a constant initial energy value.[7] Beyond the vertical line of black dots near $\delta = \pm 2$ there is no stability, due to shallower potential depth.[7] All three curves have a divergence at a critical detuning, close to resonance, that marks a regime change.

The second parameter, the angular momentum (Eq. 3.10), has already been indirectly analysed with Fig. 3.7 of Sec. 3.4.2. This parameter/variable affects the potential picture, making an atomic molecule less stable for higher values of rotation velocity. Obviously, this falls into common sense, but what is really surprising is that higher cooling rates and higher system stability can be achieved with a small non-zero angular momentum. It has to do with the fact that the friction coefficient, describe in Eq. 3.28, is forced to spend more time in the potential region where it takes on a negative value than the one where is positive, hence producing the downward sloping kinetic energy cooling curve. It has been stated that the detuning value setting the barrier between cooling and heating for a pair of atoms is close to

---

[7] See [216] or Sec. 5.1 for more details.

resonance, but angular momentum has the ability to slightly modify said threshold, if an atomic pairs is considered.

Taking the detuning as an independent variable, the cooling time, considered as the moment when the initial energy is halved $\tau^{(1/2)}$, and heating time, referring to the moment when the molecule is dissociated $\tau^{(esc)}$, are plotted for three different angular momenta in Fig.3.9. For each of the three curves, the heating time reach a maximum rate for very close to resonance at blue detuning ($\delta \approx 0.15\Gamma$), because the dipolar force (responsible for the OB) is overcome by the radiation pressure force. In contrast, the cooling mechanism reaches its peak efficiency for light with slightly negative (red) detuning. Both heating and cooling regimes have in common that their rates decrease as the detuning moves away from resonance, because of a greater inefficiency in coupling between light and atoms. The cooling phenomenon is more sensitive to changes in the angular momentum of the molecule than the heating process. For instance, looking at Fig.3.9, here is an order of magnitude gain in the cooling rate from $\ell = 0$ to $\ell = 0.15$; with a slight increase of the detuning.

Parameter ε

In the system where a pair of atoms are optically bound, there are two separate time scales: one associated with the vibration of the bound state and the other one connected to the dipole oscillation. For instance, in the case under study with two-level atoms and within the linear optics regime ($\Omega \ll \Gamma$, since $\delta \approx 0$), a single oscillation of the molecule extends over hundreds of dipole oscillations [204]. Generally, if $\varepsilon \ll 1$ and $\ell \ll 1$, the dipole relaxation time Γ will be much shorter

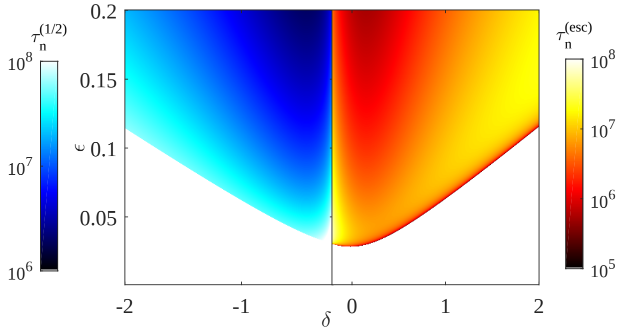

Figure 3.10: The heating escaping time and the cooling half-energy time are illustrated in a plot showing the detuning δ versus the parameter ε and with fixed angular momentum $\ell = 0.1$. The black vertical line marks the separation between the two regimes, cooling for $\delta \lesssim -0.21$ and heating for $\delta \gtrsim -0.21$; and the white/blank area represents the unbound states where the trapping potential is smaller than the initial kinetic energy. The simulation has been carried out for a constant initial kinetic energy, considering the first and deepest well of the decreasing series of the potential minima $\sim -\cos q/q$ (being q the separation between the two atoms).

than the vibrational mode period. This small parameter plays an important role on how fast a bound molecule will heat or cool down. Although in the current segment the only parameter studied is the one related to the case with a pair of atoms (ε), the same qualitative behaviour applies for the unidimensional chain of atoms, when the exact equations are employed to follow the system dynamics; defining the parameter ε_c.

The aforementioned heating and cooling times are represented using colour bars in a stability diagram in Fig.3.10, where the ε parameter is plotted against the detuning; keeping the angular momentum with a constant value $\ell = 0.1$. The cooling mechanism is more efficient at red detuning close to resonance, coinciding with the results obtained with the angular momentum variation, and when the values of ε are higher ($0.15 < \varepsilon < 0.2$ in the figure). The same situation occurs for the heating phenomenon, but with blue detuning close to resonance. Both processes have a smaller rate close to the barrier between the bound (coloured) and the unbound (white or blank) regions for increasing values of ε and moving away from resonance.

3.5 Cooperative cooling in optical binding

Through the inspection of how the internal oscillation differences of various dipoles trying to synchronize with the external field affects the stability of the system an unforeseen cooperative cooling effect was revealed. The cooling phenomenon is caused by the synchronization delay between the movement of atoms and their dipoles, but its enhancement, the collective effect, occurs as a result of the multiple scattering interaction between several atomic dipoles. The system with a pair of atoms is set aside and the 1D atomic chain, made up of a variable number of atoms ($N \geq 3$), is evaluated throughout this section; thus presenting a new collective cooling mechanism derived from optical binding. This new cooperative phenomenon is also analysed in [217], which is attached in Chapter 5, Sec. 5.3.

This self-cooling effect observed in a chain of atoms shows some similarities with the collective cooling in optical cavities [71]. Furthermore, cavity-mediated self-organization effects have already been studied theoretically by a couple of groups in the 2000s [88, 218] and experimentally by another two, Black et al. [219] and by Brennecke et al. [220]. The main difference here, where no cavity is used, is that there is no single preselected mode, but rather multimode scattering into countless vacuum modes.

It has already been represented in Figs. 3.6 and 3.8, how the cooling rate for a string of a chain of ten atoms is faster than that observed for an atomic molecule. However, this could be a characteristic resulting from the lack of dipole synchronism, illustrated in Fig. 3.4, which is not better for increasing number of atoms. For that reason, Fig. 3.11 represents the time evolution of three atomic chains with different number of atoms and identical initial conditions. These simulations result from the numerical resolution of the coupled general expressions that describe the external and internal evolution of each atom, Eqs.(3.4) and (3.7), respectively. It is obvious that the kinetic energy vibration of a chain is reduced more rapidly for larger assemblies. Every one of the three chains ($N = 5$, 10 and 15) has unsynchronized dipoles, as in the example depicted in Fig. 3.4(b). It is important to mention that the small parameter ε is constant for all curves; otherwise, the result would be a bias due to the acceleration of the system time evolution introduced by ε.

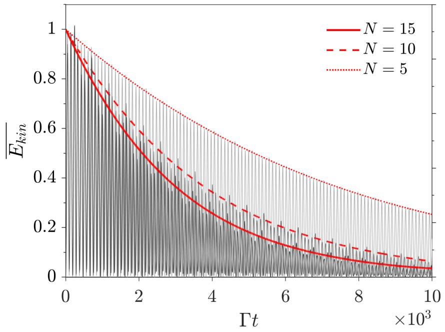

Figure 3.11: The cooling evolution for three chains of atoms is shown. All three cases have zero initial velocity and a particle distance λ. The kinetic energy oscillations are represented by the grey areas, where the shortest chain is represented in darker hue and the longer one in light grey. The envelopes are represented in red following the same pattern, the solid line being attached to the smallest chain and the lighter dotted line to the largest. The normalized $\overline{E_{kin}}$ represents the maximum kinetic energy achieve for each calculated envelope, making it easy to establish a common starting point for comparison.

Throughout the first part of the section, it will be shown how the potential landscape of the steady state solution achieves deeper wells with an increasing number of elements in the chain. This segment is followed by an investigation of the trend some key parameters of the system follow, when studied for chains with growing number of particles. As a first parameter, it is stated that the deepening of the potential wells obeys a logarithmic progression. Subsequently, how the detuning, which is one of the control parameters of the cooling/heating mechanism, has a different optimal cooling value for each chain and also changes logarithmically with the number of atoms in the string. Then, the same cooling mechanism is analysed by measuring the variation of the cooling rate with different chain sizes, which again follows a logarithmic growth. Finally, in the last part of the section, another stable state achieved by solving the exact equations of motion numerically is shown; it is defined as ”vibratory mode” of the system. The least desirable result, the heating mechanism, is also presented alongside this final part.

3.5.1 Local potential for each particle in a 1D chain

Following the same trail than in the case of two atoms, an attempt has been made to obtain a central force that makes it possible to determine a potential from which the dynamics of this system can be better understood. However, as shown in Fig. 3.8, the dynamics described with the analytical approach beyond the adiabatic case does not match the exact solution in the 1D chain system. Therefore, the dipole cooling contribution cannot be identified as the expansion of the adiabatic case with a disturbance term that depends on the position derivative $\dot{q}$; therefore, unlike with the atomic pair, no potential can be derived.

A useful method to have some prediction about the evolution of the system is to study the local potential of each atom in its stable or minimum position, points that are the solution of a self-consistent problem. These points represent the most stable position in the system, where the kinetic energy is at its lowest level, and define the local potential of each atom organized in a one-dimensional ensemble. It is possible to obtain such an instantaneous potential from the same definition of central force $\boldsymbol{F_j} = -\nabla U_j$, which applied into Eq. (3.3) translates into:

$$U_j = \hbar\Gamma \sum_{m\neq j} \Im\left[G_{jm}\beta_j^* \beta_m\right]. \tag{3.32}$$

This expression shows that the local potential of each atom depends on all the other particles present in the structure. Therefore, the slightest modification in the position of a particle affects the magnitude of the rest, as well as its own (indirectly). Due to the oscillating nature of the potential, illustrated in Fig. 3.12, the depth of minima are more or less opposite to the barrier heights of maxima and the potential is defined as zero over long distances. An atom that wants to escape the trap has to overcome a barrier twice as large as the minimum potential, $\Delta U = 2|U_{\min}|$; being $U_{\min}$ defined in the first part of the next segment —see expression (3.34)—.

The local potential depths for each of the atoms belonging to three chains of different sizes are shown in Fig. 3.12. It is clear that all wells deepen, from shallow to deeper, when the number of scatterers increases and from the edge of the chain to the center. If the kinetic energy of the outer atoms exceeds the boundaries of the edges, the shallowest potentials of each chain, the system breaks into pieces or clusters of particles.

The systems must be induced to the lowest energy state to achieve such a potential, and this is achieved by forcing the atoms to their resting positions with a stronger cooling mechanism. The extra dissipation is accomplished adding an additional term ξ proportional to the velocity $\dot{q}$, which introduces an artificial friction force in the total force expression introduced in Eq.(3.3). The atomic dipole remains as in Eq. (3.14), but the force describing the atomic external motion reads:

$$m\ddot{\boldsymbol{r}}_j = -\hbar\Gamma \sum_{m\neq j} \Im\left[\nabla_{\mathbf{r}_j} G_{jm}\beta_j^* \beta_m\right] - \xi\dot{q}_j. \tag{3.33}$$

Several rounds of simulation have been done with the code to find the optimal value for the artificial friction coefficient ξ and to determine the time it takes for the system to evolve. Then, the system has been allowed to cool for a long time using the exact equations and no additional dissipation mechanism, storing the values of the position of the atoms and their dipoles obtained. Always considering an efficient simulation time, the most accurate result that matches this exact result,

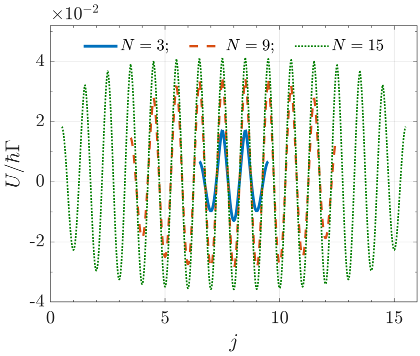

Figure 3.12: (a) Potential energy landscape for chains of $N = 3$, 9 and 15 atoms in equilibrium, with a normalized detuning $\Delta/\Gamma = 0.0,\ -0.13$ and -0.2, respectively. The potential is computed using Eq.(3.32), considering all the atoms except for the one for which the potential is being calculated, since it generates a local singularity.

when simulated without the additional friction term, have been with $t = 10^5\Gamma$ and $\xi = 0.02m\Gamma$; its units are $m\Gamma$ to keep consistency with the systems equation.

3.5.2 System parameters scaling as $ln\ N$

The two images depicted so far in this section, Figs. 3.11 and 3.12, show how there is an enhancement of the cooling rate and the trapping potential, which means that there is an increase in the response of the system when it is extended. How this cooperative effect scales becomes evident when three system variables are studied for a few chains with a different number of elements. These variables are: the instantaneous local potential, the optimal detuning and the same cooling rate. Reviewing these parameters allows to understand how the cooling mechanism is enhanced into a collective effect, adding increasing interactions between particles to give an additional cooling boost.

Trapping local potential

The trapping potential is calculated for each atom at the edge of several 1D chains —using Eq. (3.32)—, giving a trend of the local potential that increases with increasing N. This tendency is represented in Fig.3.13, where the local potential for the shallower atoms (first or last one of each chain) have been depicted.

The logarithmic growth of the optical potential seen in Fig. 3.13, for chains ranging from $N = 3$ to $N = 30$ atoms, can be numerically fit to a logarithmic curve. The extracted progression curve, for the atoms at the ends of the chain, follows the following approximate expression:

$$U_{min} \approx -0.8\hbar\Gamma \left(\frac{\Omega_0}{\Gamma}\right)^2 \ln N. \tag{3.34}$$

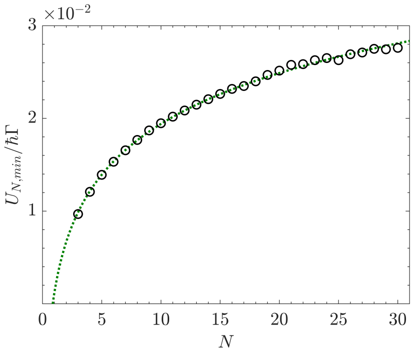

Figure 3.13: The system is cooled down by following Eq. (3.33) during a time $10^{-5}\Gamma$ and setting the artificial cooling parameter at $\xi = 0.02m\Gamma$, allowing to calculate the steady local potential for the atoms at the edge of each chain. The absolute value of this optical potential for these atoms is plotted against the number of particles N contained in the chain; using the detuning value that optimizes the cooling mechanism (see page 106). The logarithmic fit of the tendency described by the potential values (small black circles) is traced with a dotted green line.

If the middle atom, or the deepest potential, of each chain were represented, the first numerical value of the RHS of the equation would be -1.6. This potential variation within the chain comes from the contribution that each atom adds to a local potential U_j. Atoms that are further apart from each other have a smaller mutual contribution due to the distance between them (check potential shapes of Figs. 3.5 or Figs. 3.7, where the potential decreasing depth for greater multiples of λ). The same screening effect, due to the greater finite optical thickness, is the reason for the slight decrease in perceived potential depth for larger systems.

The deepening effect of the optical potential for increasing N can be explained from the $1/r$ decay of the electric field. To understand how this potential scales, it is assumed that each atomic dipole is only driven by the laser field, $\beta_j = \Omega_0/(\Delta + i\Gamma/2)$, considering the coupling contribution of the other dipoles to be insignificant. When this last definition of β_j is introduced in Eq. (3.32), the potential expression becomes

$$U_j = \hbar\Gamma \frac{\Omega_0^2}{\Delta^2 + \Gamma^2/4} \sum_{m\neq j} \Im(G_{jm}). \tag{3.35}$$

Moreover, it can be assumed that consecutive atoms are spaced λ from each other, letting the position variable become $\mathbf{r}_j = j\lambda\hat{z}$. The separation between particles is not exactly identical to the wavelength of the field, but it is quite close. This constant spacing gives the possibility of further simplifying the potential as

$$U_j = U_0 \sum_{m\neq j} \frac{1}{|m-j|} = C_j U_0, \tag{3.36}$$

with $U_0 = -\hbar(\Gamma/2\pi)\Omega_0^2/(\Delta^2 + \Gamma^2/4)$ as the minimum potential for a pair of atoms, and with $C_j = \sum_{m \neq j} 1/|m - j|$ as the cooperative parameter for the j atom. The trend of the minimum local potential when the atoms increase in an optically bonded chain seems to be closely related to this cooperativity parameter, whose discrete sum has a logarithmic growth when studied as a continuous variable. Additional information, like the approximate potential value for the atoms located in the center or in the edges of a chain, are derived in part II.C of Sec. 5.3 (attached paper).

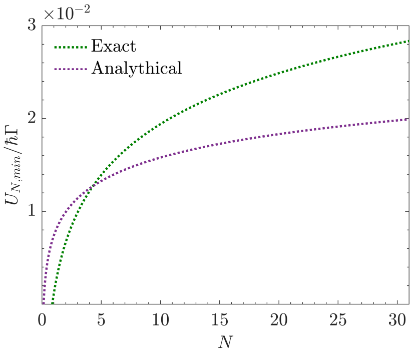

Figure 3.14: Shows the optical potential (in absolute value) for the edge atoms of a 1D OB system as a function of the length N of such a system, and for the detuning that optimizes this value (page 3.5.2). The purple line corresponds to potential logarithmic fit announced in Eq. (3.36), whereas the green line represents the exact value calculated employing Eq. (3.32)

The result of the analytical approach, from Eq. (3.36), is compared with the exact numerical solution, from Eq. (3.32), in Fig. 3.14. The main reason of the larger and larger difference between the two curves at large N is because the contribution of the other dipoles to the local potential of atom j has been ignored. The exchange of photons between two distant atoms is filtered by the atoms located between them, modifying the phase and amplitude of the wave, so resulting in the invalidation of the coherent sum in Eq. (3.36). The stronger screening effects endured by longer chains constitute a limit to the achievable length of optically bound chains.

It has been shown that the potential grows linearly with the logarithm of the number of atoms N and, at first glance, the other two quantities (cooling rate and detuning) should not have to evolve with the same trend, but they do. In addition, an important aspect to note again is that for each string the detuning has been modified, adopting the detuning for which the chain achieves the best cooling performance; it is explained on page 106.

Maximizing the cooling mechanism

The long-range nature of the interaction among resonant scatterers under OB reveals its presence not only in the depth of the potential wells generated from the energy distribution, but also in the magnification of the cooling phenomenon. This feature is analysed in Fig. 3.15, where the cooling rate has been calculated for various systems, with different lengths, within a range of detuning values. The cooling mechanism has been studied by monitoring the total kinetic energy of the system, considering that the center of mass of the system is at rest. The system is allowed to evolve, relaxing to its lowest energy configuration from an initial distance between closest neighbors that matches the wavelength of the local field. The LHS plot of the figure represents the cooling rate due to optical binding for short one-dimensional atomic ensembles and the RHS plot depicts the same parameter for chains containing a few dozens of atoms.

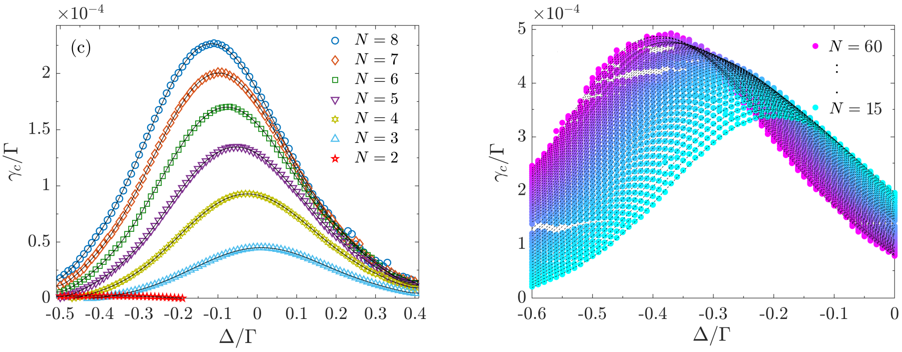

Figure 3.15: Cooling rate γ_c/Γ as a function of the normalized detuning $\delta = \Delta/\Gamma$ for several one-dimensional sets of cold atoms with different lengths. The optical binding cooling rate for short 1D chains ranging from $N = 2$ to $N = 8$ is represented in (a), whereas the same parameter for strings varying from $N = 15$ to $N = 60$ is depicted in (b). The cooling rate γ_c is obtained by calculating the inverse of the time that takes the system to reach the 90% of its initial energy. The particle are initially at rest with an inter-particle separation of λ.

Since there are several peculiarities that attract attention in Fig. 3.15, they are briefly announced and explained in the description below:

- The first curiosity is the way in which the case of an atomic molecule ($N = 2$) is dissociated from the main trend. This system has its cooling mechanism starting slightly away from resonance than the rest, due to the intrinsic difference that exists with respect to dipole synchronization (shown in Sec. 3.4.1). Moreover, the cooling efficiency is visibly lower than the larger systems, this variation is the question that is being tested in this segment.

- The second aspect that can be noticed in Fig. 3.15 is that the cooling rate varies considerably over the tested detuning range, which is about ten times higher for any chain from the tails of the curve to its peak, but for the case of two atoms. This behaviour was somewhat expected, since it also occurs in another cooling mechanism for neutral atoms, e.g., Doppler cooling, where cooling is attained for negative detuning, reaching its maximum at $\Delta \approx -\Gamma/2$.

- The third striking attribute is that there is a shifting pinnacle detuning value for which the cooling rate of each string is maximized. The detuning value for this cooling rate zenith is denoted as "optimal detuning" and can be verified to be unique for each string. The optimal detuning value is far from resonance for larger systems; always keeping in mind that the case of the two atoms is a small exception due to the inevitable dipole synchronism. This parameter is further developed on page 106, in the last segment of the current subsection, although the concept is already exploited in the current segment.
- The last observation, which is more of an interrogation derived from the third point, is to ask how the optimal detuning varies with the number of links that make up the chain.

Extending the concept from the last point, if the cooling rate at its maximum γ_c is considered for each chain (nothing more than calculating the cooling rate for each chain, considering its optimal detuning), the cooling rate can be adjusted into a logarithmic fit,

$$\gamma_c \approx \omega_{\mathrm{r}} \left(\frac{\Omega_0}{\Gamma} \right)^2 [0.4 \ln N - 0.3] \,. \tag{3.37}$$

The expression is obtained following the procedure described in the caption of Fig. 3.15, for strings ranging from $N = 3$ to $N = 30$, where the cooling rate is calculated letting the system evolves until it reaches 90% of the initial kinetic energy.

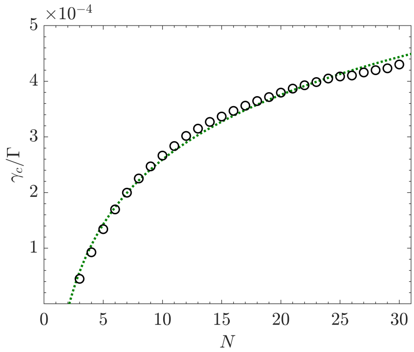

Figure 3.16: Characterisation of the maximum cooling rate γ_c as a function of the particles number N existing in several atomic strings. The small black circles are the result of solving the equations Eqs. (3.14) and (3.15) numerically, with a detuning that corresponds with the peaks depicted in Fig. 3.17. TThe green line is the continuous representation extracted from the trend described by the small black circles (reported in Eq.(3.37)). All particles are initially at rest and with the usual λ spacing.

The data that make it possible to derive expression (3.37) is represented in Fig. 3.16. In such representation, the maximum cooling rate for each chain γ_c

is acquired using its optimal detuning. This way a fair comparison between the different systems is achieved, because the image of the shifting cooling rate shown in Fig. 3.15 makes it difficult to show an unbiased γ_c when a fixed detuning is taken into account.

The envelope, which helps to calculate the cooling rate, is an illustrative trend and becomes less accurate for larger systems due to emerging harmonic frequencies (see Fig. 3.11). However, identical cooling rates can be obtained for each chain using various percentages of final kinetic energy, which makes the algorithm used quite robust.

In addition, checking appendix D, the reader can find out how the 1D chain system behaves if the dipoles of a string are forced to oscillate with synchronization. The situation is not the same as the adiabatic approximation, where the dipoles are set to vary instantaneously with the local field, it is more like an artificial synchronization, where the dipoles are averaged at each simulation step.

Optimal detuning trend

Unlike any other cooling mechanism, the cooling for a 1D chain finds its highest efficiency close to the atomic resonance, specially if the string is not too long and apart from the one composed of two particles. Nonetheless, it has already been shown that the cooling process is not constant over a range of detuning values. For that reason, in addition to seeking a fair comparison between the cooling possibilities of each system, it is useful, as well as necessary, to extract a trend that can be linked to the here called optimal detuning value.

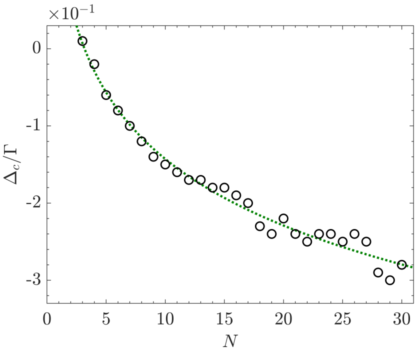

Figure 3.17: The plot shows the detuning Δ_c at maximum cooling rate, as a function of the number of atoms present in different 1D chain N. As usual, all particles are initially at rest and with a λ distance between them. The obtained results (small black circles) can be fit into a logarithmic trend traced in green and calculated in Eq. (3.38).

In Fig. 3.17, the optimal detuning is plotted against the length of the string it represents and the trend can be easily detected, even without the logarithmic fit drawn through a green dotted line. The optimal detuning for any string can be extracted using the trend represented in the figure. Therefore, given an expression similar to those obtained for the local potential (3.34) and the cooling rate (3.37), given by

$$\frac{\Delta_c}{\Gamma} \approx 0.14 - 0.12 \ln N. \tag{3.38}$$

The optimal detuning Δ_c could be redefined as the normalized optimal detuning $\delta_c = \Delta_c/\Gamma$, but this form is not employed to facilitate comparison with other cooling methods.

In summary, with the trend of this last parameter, it can be clearly stated that in the system described here varies logarithmically with the number of atoms contained in a 1D chain. Therefore, making the system's outcome intrinsically dependent on the number of elements that their contain, which undoubtedly lead to describe the cooling mechanism enhancement as a collective effect, in contrast with the other single-atom cooling mechanism. However, the weak dependence as $\ln N$ makes OB induced collective cooling mechanism not very efficient for a possible experimental implementation.

3.5.3 Other system evolutions besides cooling

There are two other feasible outcomes for the unidimensional array of atoms when allowed to evolve in time. Both results, together with the third possibility, the cooling phenomenon, depend on the initial conditions of the particles and the configuration of the local field. For example, the initial particle velocity around the equilibrium points or relative position among them and the detuning parameter of the external scalar field. Obviously, throughout this work no polarization components have been considered for optical field, but if they were to be considered it would probably affect the resulting system dynamics.

Heating

The system can lean towards the result directly opposite to the cooling mechanism, experiencing a heating phenomenon that increases its kinetic energy until the chain reaches a breaking point. The situation is the one with higher probability of revealing itself if the parameters are not accurately adjusted and, especially, if the spontaneous emission is also considered (see next Sec. 3.6). However, some stabilization can be achieved effortlessly for systems with increasing number of atoms (view also next Sec. 3.6). In Fig. 3.18 two cases are reproduced, in both cases the total normalized kinetic energy increases, showing signs of system heating. The LHS panel (a) represents the heating of two short arrays of atoms, which depict an enhancement of the heating mechanism. However, in graph (b), the two short chain envelopes are compared to a third larger chain, showing how the larger systems are actually less sensitive to heat under the same initial conditions.

Vibrational mode

The fluctuation of the system can lead to an eternal oscillation resulting in a third stable state here coined "vibrational mode". The result of this system has nothing

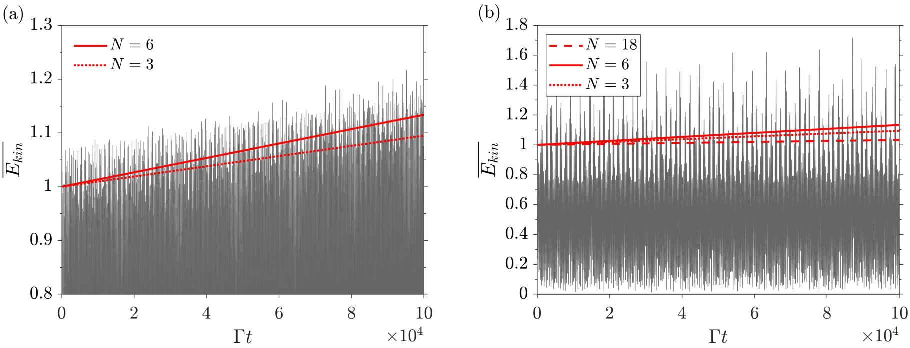

Figure 3.18: Time evolution of three strings of atoms with $N = 3$, $N = 6$ and $N = 18$ atoms. The particles are distributed with an initial inter-particle distance of λ and are perfectly still. However, a small disturbance is introduced, shifting 0.01λ the second atom from the right ($j = 2$, $j = 5$ and $j = 17$, respectively). (a) portrayed the kinetic energy oscillations for two small chains (grey coloured areas: dark for $N = 6$ and lighter for $N = 3$) and their envelopes (red lines: continuous and dotted, respectively). (b) Keeps the envelops of the short ensembles, adding the oscillation and the envelope (lightest grey and red discontinuous line, respectively) of a sequence of $N = 18$ atoms. The normalized kinetic energy is here normalized to the first value of the osculation for each system, for a better exposure of the heating mechanism.

to do with the perpetual oscillation that is obtained with the adiabatic solution of the case for a pair of atoms, because the exact equations are the ones involved here. Furthermore, the adiabatic case gives a completely incorrect evolution for the one-dimensional organization of atoms, which has already been shown in Fig. 3.8(b).

A representative case is provided in Fig. 3.19, where the usual initial conditions (zero velocity and space between particles coinciding with the wavelength of the local field) are minimally altered, culminating in a result completely different from cooling and heating. mechanism. he particles undergo a cooling process from their initial energy (check the first $0.5 \cdot 10^5 \Gamma t$ for all curves in both panels), then there is a metastable state, which is eventually broken, reaching a perpetual vibrating mode (approximately after $6 \cdot 10^5 \Gamma t$ in the figure).

Some work has been developed with this third new state, although the results had not been as rewarding as expected. In addition, the time required to deepen into the matter do not harmonize with the main scope of the thesis. Nevertheless, some interesting fact have been extracted by solving the exact equations for several short chain ($N = 3$ to $N = 6$):

- The oscillation frequencies of the vibration mode can be extracted easily, performing a Fourier transformation of the vibrational mode. In the presented case, it can be computed by considering the final 20% of the simulation time (from $8 \cdot 10^5 \Gamma t$ until the end).

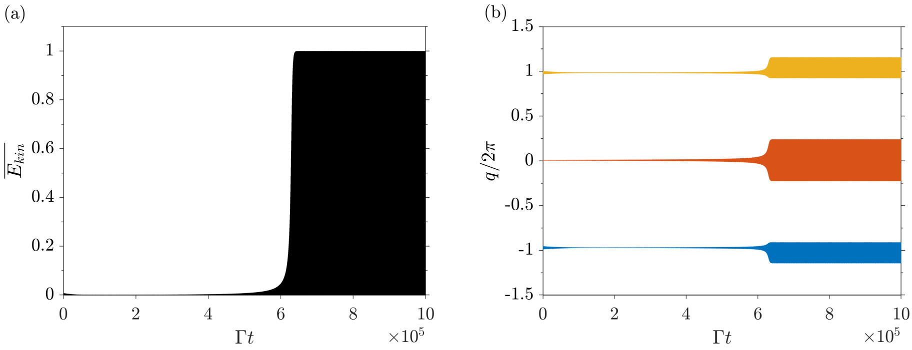

Figure 3.19: Time evolution of a 1D-chain with 3 atoms, where (a) represents the total normalized kinetic energy and (b) the three atomic positions in $q = kr$ units. The vibrational mode can be detected in both plots, observing that the system is in equilibrium, reaching a constant oscillation amplitude —in energy and positions—, but without remaining perfectly still. The detuning is fixed at $\Delta = -0.1\Gamma$ and the atoms rightmost atom is slightly shifted to the right with an increment 0.01λ. The other parameters are as usual $v = 0$, $\Omega = 0.1\Gamma$. The kinetic energy is normalized to the constant maximum amplitude value that it reaches during the "vibrational mode".

- The perturbation shift 0.01λ could be applied to any other atom in the chain. When that is studied for the $N = 3$ example, it translates into a binary combination for each particle, resulting in 8 possibilities (2^N). In a binary transformation of the shift, "0" is assigned when the inter-particle distance matches a wavelength's multiple and "1" when it is shifted from that position, e.g., it would be '001' for the example in Fig.3.19. Some combinations leading to a cooling mechanism and others to this peculiar mode. The percentage of combinations leading to a cooling mechanism increases with N: 25% for $N = 3$, 50% for $N = 4$, 75% for $N = 5$ and 87.5% for $N = 6$.
- The derived oscillation frequencies can have a second and even a third harmonic, which results in a small ripple at the maximum amplitude of the constant vibratory mode; not evident in the example given.
- The vibration mode seems to have no continuity beyond the strings composed of a certain number of particles. For the present perturbation, it is impossible to find a final steady state that oscillates with chains $N \geq 7$; from that size, there are two possible outcomes: heating and cooling.
- A meticulous study of the origin of the vibrational mode reveals that the tiny amplitude difference between the dipoles' vibrations (check Fig. 3.4), eventually become comparable to the oscillation amplitudes of the dipoles; hence triggering the change in the system's evolution. In the present case, there is one mirrored pair composed by atoms $j = 1, 3$, with the central atom $j = 2$ oscillating with its own frequency. The dipole of the middle atom,

which is somehow “independent”, at some point close to $2 \cdot 10^5 \Gamma t$, stops to oscillate. The dipole curve β_j starts to be more resemblance to a noise input, hence becoming the source of instability that breaks the cooling process.

This state is a very specific case, derived from the applied initial condition. By applying stronger disturbances and more chaotic noise to the system, such a mode could be prevented. This leads to the next section 3.6, cited several times throughout the chapter, where the effects of the spontaneous emission generated by the random emission of photons by the atoms, are included in the dynamics of the system.

3.6 Effects of stochastic emission in the stability of the 1D system

The model and systems introduced so far do not consider the fluctuations in the moment of the atoms caused by spontaneous stochastic emissions of photons. Each atom every now and then receive a random momentum kick $\delta\mathbf{p} = \hbar\mathbf{k}$, whenever a photon is spontaneously emitted. The photon can be emitted in any direction within a three-dimensional sphere which affects the particle's momentum radially along angular directions as $\delta\boldsymbol{p} = -\hbar k(\sin\theta\cos\varphi, \sin\theta\sin\varphi, \cos\varphi)$, for a typical spherical coordinates diagram. The kinetic energy associated with the particles is also altered, because each scattering event contributes to heating the system, increasing it by an average

$$\delta E_{\mathrm{r}} = \frac{\hbar\omega_r}{3} \tag{3.39}$$

for each allowed translation direction, where the 1/3 comes because of projecting the total recoil energy on each axis. It is better to present the energy of each cardinal axis, because the systems being investigated in this thesis are set into one and two dimensions.

The spontaneous scattering process is mainly by the laser field, so it is necessary to calculate the total scattering rate of light from this source. This rate can be extracted from [22] or [23], which has already been derived as

$$R_{sp} = \frac{\Gamma}{2}\frac{s_0}{1 + s_0 + 4\Delta^2/\Gamma^2}, \tag{3.40}$$

where all parameter are already known, except for the defined on-resonance saturation parameter $s_0 = 2|\Omega_0|^2/\Gamma^2 = I/I_s$, as described in [22]. Since all the study in this chapter is carried out working in the linear regime, the intensity of the laser is far from being able to saturate the system; therefore the saturation parameter can be eliminated in the denominator. Considering that $s_0 \ll 1$, the scattering rate can be repressed as

$$R_{sp} \approx \frac{\Gamma\Omega_0^2}{\Gamma^2 + 4\Delta^2}. \tag{3.41}$$

This expression can be multiplied to the defined energy kick endured for every atom to obtain the rate of kinetic energy induced by spontaneous emission

$$\left(\frac{\delta E}{\delta t}\right)_{\mathrm{SE}} = \frac{\hbar\omega_r}{3}\frac{\Gamma\Omega_0^2}{\Gamma^2+4\Delta^2}. \tag{3.42}$$

This energy rate that can be defined as the heating perturbation introduced by the stochastic process of the spontaneous emission of a photon.

To get a complete picture of the total energy of the system, the heating contribution of the thermal fluctuations must be added to the variation of energy generated by the optical binding cooling mechanism. Since the OB cooling phenomenon has been shown to evolve exponentially (check appendix E), it can be expressed as a linear coefficient of the energy in a differential equation. Consequently, the evolution of the total kinetic energy of each atom in the system can be defined as a process leading to the following Langevin equation,

$$\frac{dE}{dt} = -\gamma_c E + \left(\frac{\delta E}{\delta t}\right)_{\mathrm{SE}}, \tag{3.43}$$

where the coefficient γ_c is given by the expression extracted from the logarithmic fit introduced in Eq. (3.37) of the second segment of Sec. 3.5. It is now trivial to calculate the steady-state energy from expression (3.43) by equating its LHS to zero, thus obtaining the approximate value of

$$E_{\mathrm{s}} = \frac{1}{\gamma_c}\left(\frac{\delta E}{\delta t}\right)_{\mathrm{SE}} \approx \frac{0.83}{\ln N - 0.8}\frac{\hbar\Gamma}{1+4\delta_c^2}, \tag{3.44}$$

where the normalized optimal detuning definition $\delta_c = \Delta_c/\Gamma \approx 0.14 - 0.12\ln N,$, introduced in Eq. (3.38), has been employed to further simplify the expression.

After calculating the steady state kinetic energy, the only thing left to examine is the total energy of the system. For this purpose, it is convenient to retrieve the minimum potential wall ΔU established in the expression (3.34). However, to make the text easier to read, the extracted expression (3.34) is combined here with the potential barrier definition $\Delta U = 2|U_{\min}|$, announced on page 100, which generates the potential energy of the system.

$$\Delta U \approx 1.6\hbar\Gamma\left(\frac{\Omega_0}{\Gamma}\right)^2 \ln N. \tag{3.45}$$

Once both components of the total energy have been obtained, it is now possible to define when the optical binding cooling mechanism is capable of overcoming the stochastic heating phenomenon, thus becoming a stable mechanism for cooling the atoms. Such situation is achieved when the kinetic energy is smaller than the minimum potential barrier $E_{\mathrm{s}} < \Delta U$. By equating expression (3.44) and (3.45), both normalized to the $\hbar\Gamma$, it can calculated how long the chains must be for the cooperative cooling to overcome the spontaneous heating.

The situation is illustrated in Fig. 3.20, where the steady-state energy Es (using a straight line in dark blue from the upper left corner to the right bottom corner) is graphically compared to various potential barriers (other curves), built by applying different pumping fields. For instance, for $\Omega_0/\Gamma = 0.2$ stability should be reached for $N \gtrsim 40$. Since the case with the shortest chain, containing two atoms, is a special case due to the perfect dipole synchronization, the chains are only plot from $N = 3$. A thorough investigation regarding the stability for the specific case of an atomic pair can be followed in Sec. 5.2 or [216].

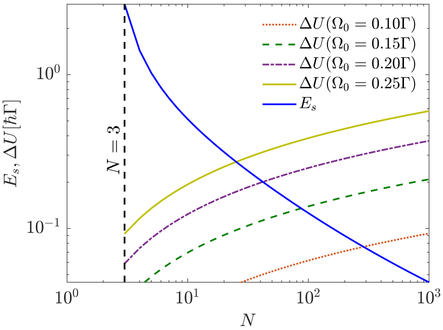

Figure 3.20: Several potential barriers are calculated by plotting Eq. (3.45), using different pump fields within the range $0.1\Gamma \leq \Omega_0 \leq 0.25\Gamma$ with a step of 0.05Γ. They are represented with nearly parallel curves in different colours and styles, and compared with a plot of the steady-state energy E_s, which is obtained with Eq. (3.44) and represented by a dark blue straight line. Both energies are displayed using the number of particles as a independent variable. The cases are only displayed for $N \geq 3$, marking that limit with a black dashed line.

Once the potential barrier of the system has been calculated, a capture rate can also be defined as it is always done in another cooling mechanism. The only operation to carry out is to consider the kinetic energy of the atom smaller than the potential barrier delimited by the Eq. (3.45) ($(m/2)(\Delta v)^2 < 2|U_{\min}|$), in order to described an atom as trapped. Thus being able to obtain the velocity from the following expression

$$k\Delta v \lesssim 2.5\Omega_0\sqrt{(\omega_r/\Gamma)\ln N}. \tag{3.46}$$

Taking into account that the atoms used in this essay are ^{85}Rb in the D2 line transition($5^2S_{1/2} \rightarrow 5^2P_{3/2}$), it is possible to defined that $\omega_r/\Gamma \sim 6\times10^{-4}$ [24], which returns $k\Delta v/\Gamma \sim 0.06\sqrt{\ln N}(\Omega_0/\Gamma)$. This expression can be compared with the Doppler cooling values in optical molasses, $k\Delta v/\Gamma \sim 1$, and the value obtained for Sisyphus cooling, $k\Delta v/\Gamma \sim \sqrt{\omega_r/\Delta_0}(\Omega_0/\Gamma)$ [54]. herefore, the cooperative cooling mechanisms announced here share a scale closer to Sisyphus cooling, with the difference that it is more efficient closer to atomic resonance. However, the calculated potential is self-generated by the positions of the atoms, which makes the calculated value a mere estimate of the order of magnitude of the capture rate.

Chapter four

Conclusions

In this chapter, the conclusions and summary of the investigations carried out on the optical binding (OB) effect, due to multiple scattering in cold atoms, and the collective atomic recoil lasing (CARL) effect, thanks to single scattering in free space, are here presented. Since they share different features of are different cooperative effects, they are discussed in different subsections throughout the first section. The same separation occurs in a second section where different perspectives are presented both for CARL and OB.

4.1 Summary

This section resumes all the conclusions derived from the investigations carried out throughout this doctoral thesis for a better understanding of two optomechanical effects: the collective atomic recoil lasing and the optical binding effects. Both the probed mechanisms are a consequence of the collective scattering of light by cold atoms of an optical field, whose vectorial nature is taken into account for the atomic recoil laser, where polarization effects are relevant. On the contrary, a scalar description of the optical field is adopted in optical binding, where polarization effects seem to be less important.

4.1.1 Collective atomic recoil lasing

Systems of cold atomic clouds radiated by an optical field are generally confined in an optical cavity, which forces the scattering of light to occur in the mode set by the resonator. On the contrary, the novelty of CARL throughout this thesis is the fact that the system is considered in free space, which leads to a multimode scattering in vacuum. Therefore, it is exposed how the optical cavity model is not necessary to achieve a coherent collective emission by an atomic ensemble; a preferred scattered path occurs along the main axis of the cloud. The derivation of the equations used to represent the results obtained in the CARL effect, using two models referred to as the scalar and the vector, are also presented in the dissertation. Additionally, molecular dynamics algorithms, generally employed in other scientific fields, are used to numerically solve the derived multiple-particle equations to describe the motion of each atom in a cloud in two or three dimensions.

The simulations show that both the atomic density distribution and the collective scattering pattern of that atomic distribution are sensitive to the orientation and shape of the cloud. Numerical solutions are presented by studying the evolution in time of three main systems, either in two or three dimensions. The three systems studied consist of clouds: elongated along the axis parallel to the direction of propagation of the external field, stretched along this direction and with a round symmetrical shape.

All simulations related to the cases in which the cloud is oriented parallel to the direction of the pump field reveal a one-dimensional grating formation in the atomic distribution along that direction. While in the planar structure the pattern is purely one-dimensional (equidistant lines), in the volumetric arrangement the clusters of atoms present a an array of periodically spaced small spheres. The study of the intensity radiation profile in the atomic bunching formation shows how the backscattered light is amplified, producing the so-called collective atomic recoil laser effect. The CARL phenomenon is similar to the effect observed by its electronic counterpart, the free electron laser (FEL), but it occurs with neutral atoms rather than electrons.

Whenever the cloud on the major axis is rotated at right angles, such that it is perpendicular to the pump field, the grating emerging in the cloud gains one dimension, both for 2D and 3D analysis. The change in momentum induced in the atoms by the backscattered photons, combined with that generated by the photons scattered in other directions, defines the trajectories that the atoms follow from said 2D and 3D grating. By analysing the lobes of the bunching formation, it is possible to see how the main direction of the atomic scattering is also rotated with a right angle. These observations confirm that radiation resulting from collective scattering occurs predominantly along the longest axis of the cloud. The pattern that appears is similar to that shown in the superradiant Rayleigh scattering experiment of Inouye *et al.* [133], but instead of tracing a pattern in momentum space, it emerges in real space.

When the cold atomic cloud is configured in a circular or spherical distribution, the simulations clearly show the electrostrictive nature of the force generated by the collective scattering process. At first, there are several scattering paths, due to the symmetry of the system, but soon two main directions are determined with an angle smaller than a right angle. Both two-dimensional and three-dimensional clouds undergo elongation along the axis of propagation of the pump field, thus establishing the longest scattering path. This path is drawn along the edge and outer layer of the 2D and 3D systems, respectively. The scattering produced in this direction gives way to patterns like those observed with the rotated elongated cloud, but with a more acute angle between the scattering directions. The situation is easily detected by studying the lobes that emerge in the bunching formation intensity profile that accompanies these circular examples. The precise mechanism of this collective electrostrictive force, emerged only recently from the simulations, is not yet completely understood and needs further study, beyond the aim of this thesis.

The variation in the orientation and shape of the cloud is complemented by a study of the effect when considering a polarized external optical field. The scattering picture of the cloud grating formation and the bunching intensity profile using this field have only been tested on the perpendicular elongated cloud. The results obtained are like those observed in scalar cases, but now, the scattering direction that coincides with the polarization vector of the pumping field is completely suppressed. This image is exposed when the grating formation is shown, where one of the dimensions of the atomic distribution grating disappears. This suppression is not detected if the polarization does not fall in one of the dimensions of the cloud, for example, a two-dimensional cloud within a plane is not affected by a polarization along the axis coinciding with the plane's normal vector. Minor differences are seen between the scalar and the vectorial model, due to the presence of different short-range terms in the equations of the models and the different cut-off parameter chosen.

Furthermore, both scalar and vectorial models depend only on the position of the particles; facilitating its implementation in molecular dynamics (MD) algorithms, typically used in other scientific fields, like biology. Two well-known symplectic algorithm are explained in detail, these are the Verlet algorithm and the leapfrog method. The new open access programming language Julia has proven to be a great tool for implementing these MD codes, due to its large number of packages, including several useful symplectic algorithms; they allow to follow the trajectory of each particle with sufficient precision and respecting the energy conservation of the system. The Julia algorithms included in some of these packages, in addition to offering decent performance when simulation time is considered, also prove to be ideal tools for representing the dynamics of systems with many particles.

4.1.2 Optical binding

To date, optical binding has been studied with dielectric particles of different sizes, down to the nano scale, both theoretically and experimentally. Dielectric particles do not have any internal dynamics that are affected by the external optical field when they scatter light. In contrast, the cold atoms used here reduce the size of the system to Angstrom units and possess a resonance characteristic. This unique feature allows a completely different range of responses to be displayed from the same optical binding systems.

When optical binding is applied to dielectric scatterers, they reorganize into crystalline structures with periodic arrangements; the distance between each particle in the array is approximately the wavelength of the external optical field. Whereas, when the same implementation is performed with cold atoms, the effect not only triggers similar reorganization patterns, but the entire system is affected by a non-conservative force. The force comes from the non-adiabatic reaction of the internal degree of freedom of the atoms (atomic dipoles), when they try to follow the external movement of the atoms. Hence, the synchronization delay between these two oscillations, when averaged over a period of oscillation of a system, made up of an optically bound molecule, results in a friction-like mechanism capable of slowly cooling or heating the system.

Throughout the current thesis, the cooling effects of this dissipative force have been investigated using two different systems, one with a pair of atoms, which can move within a 2D plane, and another that is composed of a different number of atoms ($N \geq 3$), which are forced to move along a 1D chain. The first system is used to study such cooling phenomenon and to explore the parameters that allow these mechanisms to be controlled. There are three key parameters: the main one is the detuning between the optical field and the atomic transition; the other two, which have been studied in combination with detuning, are the angular momentum of the molecule and a small parameter defined as ε proportional to the pump field.

The study of the atomic molecule has made it possible to define the key values of these parameters to achieve the desired cooling effect. To detect a cooling trend, the detuning must be negative with values very close to resonance, because at positive values the atoms experience a heating effect. Surprisingly, from the study of angular momentum (complemented in [216]), it is extracted that a low value of angular momentum helps to achieve higher rates in the cooling phenomenon. Meanwhile, the defined ε parameter helps to identify the time scale difference between the oscillations of the bound and the cooling mechanism, which is analytically identified here as a deviation from adiabatic dynamics.

The main problem with this cooling phenomenon is that when the stochastic heating process characterized by the recoil experienced by an atom when it spontaneously emits a photon is considered, the cooling potential mechanism of the effect is overthrown. For that purpose, the OB molecule is then enlarged by adding more atoms to generate the second system under investigation: a one-dimensional chain of atoms that is no longer allowed to rotate. It seems that from the two main difference between these two systems, more than two atoms and dipole synchronization (or the lack of it in this case), this second system is capable of experiencing an enhanced collective cooling effect. In this context, the dipole-dipole interaction of the chain seems to be able to counteract the spontaneous heating phenomenon. This one-dimensional 1D system could be eventually be employed to cooled a few dozen atoms, without any additional stabilizing mechanism such as the optical molasses.

In addition, the collective cooling dissipative force of the optical binding effect is demonstrated to scale with the logarithm of the number of atoms N present in the 1D system. A parallel study of the steady-state local potential of each atom contained in the chain shows how these potential wells deepen with the same logarithmic scale; making it more and more difficult to dissociate the chain as the number of atoms in it increases. What is more, he cooling mechanism exhibits its maximum efficiency at a certain detuning value, which depends on the size of the atomic string. This so-called optimal detuning follows the same logarithmic trend. The more atoms present in the chain, the closer the optimal detuning is to that defined by the Doppler limit ($\Delta \approx -\Gamma/2$), and the more intense the cooling effect becomes. In contrast, for smaller chains, the optimal cooling efficiency is close to resonance, being at a slightly positive detuning for three atoms.

4.2 Future outlook

The field of cold atoms is rapidly expanding and diversifying and will undoubtedly contribute to broadening humanity's knowledge of collective or cooperative effects, as it has done so far. There is a revolution under construction and, this time, it is not related to a device, such as a chip, but to the matter itself. Regarding the future prospect related to the line of work presented in this dissertation it can be anticipated that there is another study, linked to the CARL vectorial model, in publishing process and two additional reviews, related to OB in 2D structures and/or including simulations with the spontaneous emission heating mechanism, are also under consideration.

4.2.1 Collective recoil laser

Nowadays the attention of the AMO physics community is focus on other application, different from CARL, for the cold and ultracold matter like: Rydberg atoms (quantum memories), atom chip, atomic clocks, optical lattices, accelerometers, quantum dots, etc. The CARL experiments are no longer active, but it would be interesting if the subject were taken up again in the future for the study of new feasible applications; also making it possible to test the numerical solution obtained throughout the current thesis. For example, the easiest thing to do would be to test a 3D system in the absence of a resonator and see if it develops a grating pattern, which depends on the polarization vector of the incident beam. The latest CARL experiments were conducted in the early 2000s in Zimmermann's group in

Tübingen (Germany), where they actually used ultracold atoms in a BEC and a cavity; and in the early 2010s in Robin Kaiser's group in Nice (France), where the cavity was eventually omitted and a cooperative scattering was observed [119], although it was not CARL.

Other possible theoretical investigations would be to check the effects of a circular polarized light or to probe what happens when light is applied to the cloud using pulses. Studying the effect with more complex models, for example including three-level atoms in the model, would be the alternative route to make the system a bit more complex and realistic. However, the main goal would be to find an application for CARL as has been done for the FEL, which is being used by physicists, chemists, biologists and materials scientists and is also making its way into medical and military applications.

4.2.2 Crystalline structures of cold atoms bound with light

The optical binding effect using cold atoms has been theoretically introduced in [204, 216, 217], but there have been no experimental results so far. Among the systems that have been presented, the one that could really be implemented in an experimental configuration would be the atomic arrangement in a line, which could be tested using techniques inspired by Bragg scattering [221]. To demonstrate some preliminary theoretical numerical simulations, including spontaneous emission stochastic noise, where the stability of the system has been successfully tested. Nevertheless, these initial results need to be further examined to make a true statement.

Optically bound systems, as in the recoil laser, are studied in free space, which translates into completely different responses from the system, when compared to that detected by applying an optical resonator. However, recent theoretical studies have suggested that only one mode can arise naturally from the cooperative scattering of cold atoms in free space [222]. Such a system suffers from similar synchronization problems presented throughout Chapter 3, although the analogy with a single-mode approach remains to be demonstrated.

Another direction that could be considered would be to increase the dimension of the system, to a two-dimensional structure with a greater number of atoms; some preliminary work has already been done. Such crystalline shapes, formed due to the optical potential generated in each atom by the action of its neighbours, emerge when a kind of triangular unit cell (like the one shown in Fig 3.1) is repeated in a two-dimensional plane. This unit cell has been expanded to form hexagonal structures, starting from one atom, and surrounding it with six atoms at a distance $\sim \lambda$ from and between them. This type of crystallization has been studied for dielectric particles in [198], where these are reorganized falling to the minimum of the potential landscape generated. These 2D atomic crystals may be even more promising as a cooperative cooling mechanism. This is because the $1/r$ term of the dipole-dipole interaction scales as $\ln N$ for one-dimensional strings, but it scales as $\sqrt{N}$ when using two-dimensional systems; thus making it easier for heating fluctuations to be overcome by the dissipative force generated by optical binding (see Eqs (3.44) and (3.45) for a better understanding).

The main challenge of these latest 2D structures lies in controlling the dipole moments of the atoms, since it has been shown that they are not synchronized, which becomes the factor of instability that breaks this type of atomic lattices. Once again, some simulations have been done with crystalline structures, but the main problem seems to be the lack of synchronism of the dipoles. A hidden control mechanism for these dipole vibrations could lurk in the polarization of the optical field, which remains untested for OB with cold atoms.

Finally, an additional measure could be to work with a more complex internal structure of the atoms (three-atom level) and non-linearities, as in an electromagnetically induced transparency (EIT) configuration [223, 224], which would allow to improve the cooling transition and suppress the heating frequency.

Chapter five

Papers published throughout the present PhD

Throughout the three years that this PhD project has lasted, it has been possible to produce some contribution to the physical community of AMO through the publication of three scientific articles that are listed below in chronological order.

i) Physical Review A 99, 013619 (2019)
”Stochastic heating and self-induced cooling in optically bound pairs of atoms”
A. T. Gisbert, N. Piovella, and R. Bachelard.

ii) Physical Review A 100, 023630 (2019)
”Multimode collective scattering of light in free space by a cold atomic gas”
R. Ayllon, J. T. Mendonça, A. T. Gisbert, N. Piovella, and G. R. M. Robb.

iii) Physical Review A 102, 013312 (2020)
”Cooperative Cooling in a 1D Chain of Optically Bound Cold Atoms”
A. T. Gisbert, N. Piovella, and R. Bachelard.

The original studies, as they where published, are included in the same order in the pages of this chapter. A fourth article, related to the results obtained for the CARL vectorial model, will probably be published in the days around the defense of this thesis.

PHYSICAL REVIEW A **99**, 013619 (2019)

Stochastic heating and self-induced cooling in optically bound pairs of atoms

Angel T. Gisbert,[1,*] Nicola Piovella,[1,†] and Romain Bachelard[2,‡]
[1]*Dipartimento di Fisica "Aldo Pontremoli", Università degli Studi di Milano, Via Celoria 16, Milano I-20133, Italy*
[2]*Universidade Federal de São Carlos, Rod. Washington Luis, km 235, S/n–Jardim Guanabara, São Carlos–SP, 13565-905, Brazil*

(Received 1 August 2018; revised manuscript received 21 December 2018; published 22 January 2019)

The light scattered by cold atoms induces mutual optical forces between them, which can lead to bound states. In addition to the trapping potential, this light-induced interaction generates a velocity-dependent force which damps or amplifies the stretching vibrational mode of the two-atom "molecule." This velocity-dependent force acts on time scales much longer than the mode period or the dipole dynamics, determining the true stability of the bound state. We show that, for two atoms, the stochastic heating due to spontaneous emission always exceeds the bounding effect, so pairs of cold atoms cannot be truly stable without an extra cooling mechanism.

DOI: 10.1103/PhysRevA.99.013619

I. INTRODUCTION

The advent of the laser and the subsequent cooling techniques applied to atomic samples have been a fundamental tool to lower their temperature by many orders of magnitude [1]. Eventually, temperatures can be reached where the Doppler effect has a negligible role, and coherences between the atoms can be preserved over the size of the sample. The Bose-Einstein condensation was a major step in this direction [2], which gave access to several new phases of matter, both for disordered systems and ordered systems (such as the Mott insulating phase when ultracold atoms are trapped into optical lattices [3]). Apart from sympathetic cooling [4], cooling techniques do not involve interactions between the atoms, but rather between the laser photons and independent atoms. The atoms are thus cooled independently, and the atomic sample is spatially confined by a quasiharmonic potential.

Yet light-induced interactions between the atoms can be a powerful tool to create ordered systems [5]. A paradigmatic example of cooperation in cold atoms is the collective atomic recoil lasing [6,7] observed when a cold or ultracold atomic gas in an optical ring cavity is illuminated by an intense far-off-resonance laser beam, causing a self-induced density grating in the atomic sample. More generally, the optical dipole force on the atoms in a high-finesse optical cavity, together with the back action of atomic motion onto the light field, gives rise to nonliner collective dynamics and self-organization [8]. All these schemes with atoms in optical resonators rely on the creation of optical lattices generated by the atoms.

In a similar fashion, it has recently been proposed to optically bind pairs of atoms confined in two dimensions by a stationary wave, where each atom remains at a multiple of the optical wavelength from the other [9]. This effect stems from the generation of a nontrivial potential landscape due to the interference between the trapping beams and the wave radiated by each atom (see Fig. 1). As for atoms trapped in a one-dimensional optical lattice, the distance between the atoms is a multiple of the optical wavelength, as is well known from optical binding with dielectrics [10,11].

Nevertheless, different from the optical binding of dielectrics, which are immersed in a fluid to confine them [12–17], cold atoms are manipulated at ultralow pressure, so the surrounding medium can be considered to be vacuum. An important consequence pointed out in Ref. [9] is that, since each atom exerts a central force on the other, the angular momentum is preserved, instead of being damped by viscous forces as for dielectrics in fluids [18]. Yet, despite the apparent simplicity of the problem—a two-dimensional two-body dynamics where both total momentum and total angular momentum are conserved—an additional effect of cooling or heating was reported, on time scales much longer than that needed for the two atoms to oscillate. These results were obtained by numerically integrating the coupled differential equations for the internal and external degrees of freedom.

In this work, we further investigate the coupling between the dipole dynamics and the center-of-mass dynamics to elucidate the slow change in temperature of the system, and we study the impact of the stochastic heating due to spontaneous emission (SE). In particular, we show how friction (or antifriction) terms appear beyond the adiabatic approximation, which explains the cooling and heating regimes. The dipoles evolve on a time scale typically much shorter than the period of oscillation of the atoms center of mass in the optical potential, which allows for a multiple scale analysis. This purely deterministic analysis confirms that light detuned positively from the atomic transition mainly results in only metastable (heating) bound states, whereas a negative detuning rather results in stable (cooling) bound states. Yet, accounting for the stochastic heating due to spontaneous emission, one finds that the trapping potential is unable to maintain the binding forever. Just as a single particle cannot be trapped in the stationary wave created by the same beams that cool it, optical binding fails as spontaneous emission is dominated by the scattering from the light coming directly from the laser, while

---

[*] angel.tarramera@unimi.it
[†] nicola.piovella@unimi.it
[‡] bachelard.romain@gmail.com

the optical potential results from the scattering of that laser light by one atom onto the other, so it is necessarily weaker. As a consequence, while the presence of angular momentum in such an atom pair is associated to a more efficient cooling, the lesser depth of the trapping potential makes these rotating states unstable as well.

II. TWO-ATOM ADIABATIC DYNAMICS

Let us consider N two-level atoms (polarization effects are neglected) with an atomic transition of linewidth Γ and frequency ω_a, with positions $\mathbf{r}_j$, $j = 1 \dots N$. The atoms are pumped with a monochromatic plane wave of wave vector $\mathbf{k} = k\hat{\mathbf{z}}$, detuned from the atomic transition by $\Delta = \omega - \omega_a$, and with Rabi frequency $\Omega(\mathbf{r}_j) \ll \Gamma$. Using the Markov approximation, the resonant dynamics of the atomic dipoles β_j is given by a set of N coupled equations [19,20]:

$$\dot{\beta}_j = \left(i\Delta - \frac{\Gamma}{2}\right)\beta_j - i\Omega(\mathbf{r}_j) - \frac{\Gamma}{2}\sum_{m\neq j} G_{jm}\beta_m, \qquad (1)$$

where $G_{jm} = \exp(ik|\mathbf{r}_j - \mathbf{r}_m|)/(ik|\mathbf{r}_j - \mathbf{r}_m|)$ describes the light-mediated interaction between the dipoles. The set of equations (1) is linear in the dipoles β_j, so for motionless atoms most of the information on the system can be obtained from the eigenvalues and eigenvectors of the scattering matrix G_{jm} [21–25]. Neglecting the modification of the lifetime due to the atoms' cooperation, the dipoles relax to equilibrium on a time scale $1/\Gamma$. However, accounting for the optical forces resulting from the multiple light scattering leads to an intrinsically nonlinear problem, as the dynamics of the atoms center of mass couples to that of the dipoles:

$$m\ddot{\mathbf{r}}_j = -\hbar\Gamma\sum_{m\neq j}\mathrm{Im}(\nabla_{\mathbf{r}_j}G_{jm}\beta_j^*\beta_m). \qquad (2)$$

This equation describes the average optical force between the two atoms, without accounting for the fluctuations which originate in the scattering of both laser light (spontaneous emission) and multiply scattered light (fluctuations in the dipolar force; see Sec. V). From now on we focus on atoms confined in a plane by counterpropagating beams, as shown in Fig. 1. Assuming a plane-wave profile for these beams, the atoms are submitted to a uniform field Ω, plus the light scattered by the other atom. Furthermore, we restrict our analysis to pairs of atoms ($N = 2$), for which the set of Eqs. (1) and (2) can be cast in the relative coordinate frame with $b = (\beta_1 - \beta_2)/2$, $\beta = (\beta_1 + \beta_2)/2$, and $\mathbf{q} = k(\mathbf{r}_1 - \mathbf{r}_2)$. In polar coordinates $\mathbf{q} = q(\cos\theta, \sin\theta)$ (where $q = kr$), one obtains [9]

$$\dot{b} = -\left[1 - \frac{\sin q}{q} - i\left(2\delta - \frac{\cos q}{q}\right)\right]\frac{b}{2}, \qquad (3a)$$

$$\dot{\beta} = -\left[1 + \frac{\sin q}{q} - i\left(2\delta + \frac{\cos q}{q}\right)\right]\frac{\beta}{2} - i\frac{\Omega}{\Gamma}, \qquad (3b)$$

$$\ddot{q} = \frac{4\omega_r}{\Gamma}\left[\frac{4\Omega^2}{\Gamma^2}\frac{\ell^2}{q^3} - \left(\frac{\sin q}{q} + \frac{\cos q}{q^2}\right)(|\beta|^2 - |b|^2)\right], \qquad (3c)$$

$$\dot{\ell} = 0, \qquad (3d)$$

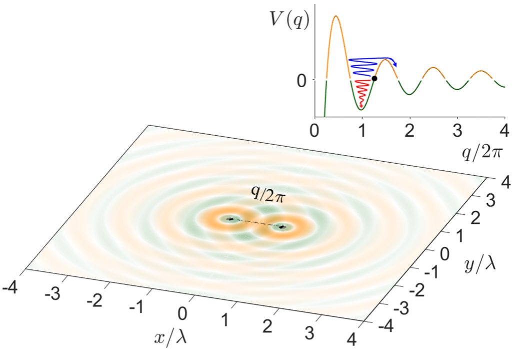

FIG. 1. Optical potential landscape generated by the interference between the confining laser beams [perpendicular to the plane (x, y), not shown in this figure] and the radiation of the atoms. The pair of atoms is trapped in the first minimum of potential, with $|\mathbf{r}_1 - \mathbf{r}_2| \approx \lambda$. The upper inset describes the profile of the self-generated potential $V(q)$, where $q = k|\mathbf{r}_1 - \mathbf{r}_2|$, in absence of angular momentum.

where time has been renormalized by the atomic dipole lifetime $1/\Gamma$. Here $\ell = \sqrt{\omega_r\Gamma}(L/\hbar\Omega)$, where $L = (m/2)r^2\dot{\theta}$ is the total angular momentum, $\omega_r = \hbar k^2/2m$ is the recoil frequency, and $\delta = \Delta/\Gamma$ the normalized detuning. Equation (3d) describes the conservation of the angular momentum: including stochastic effects such as random momentum kicks due to spontaneous emission would break this conservation law.

Equation (3a) shows that b decays to zero on the dipole time scale, so the two atomic dipoles become synchronized: $\beta_1 = \beta_2 = \beta$. After this short transient, the equations of motion reduce to

$$\dot{\beta} = -\left[1 + \frac{\sin q}{q} - i\left(2\delta + \frac{\cos q}{q}\right)\right]\frac{\beta}{2} - i\frac{\Omega}{\Gamma}, \qquad (4a)$$

$$\ddot{q} = \frac{4\omega_r}{\Gamma}\left[\frac{4\Omega^2}{\Gamma^2}\frac{\ell^2}{q^3} - \left(\frac{\sin q}{q} + \frac{\cos q}{q^2}\right)|\beta|^2\right]. \qquad (4b)$$

In order to capture the features of the short-time dynamics, we first perform the adiabatic elimination of the dipole dynamics assuming that it is synchronized with the local field. The value of β is obtained from Eq. (4a) assuming that $\dot{\beta} = 0$ at any time; then, inserting this value in Eq. (4b) leads to

$$\ddot{q} = \epsilon^2\left[\frac{\ell^2}{q^3} - w(q)\right], \qquad (5)$$

where we have introduced the "small" parameter

$$\epsilon = \frac{4\Omega}{\Gamma}\sqrt{\frac{\omega_r}{\Gamma}} \qquad (6)$$

and the function

$$w(q) = \frac{\sin q/q + \cos q/q^2}{(1 + \sin q/q)^2 + (2\delta + \cos q/q)^2}.$$

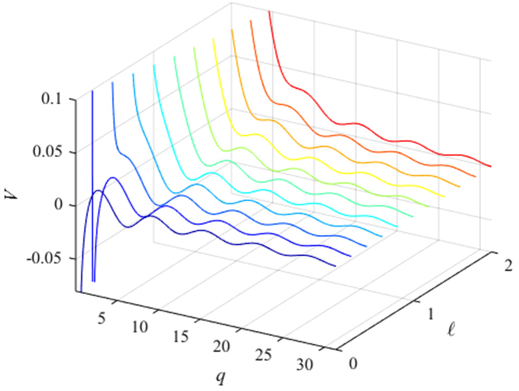

FIG. 2. Potential landscape $V(q)$ for different angular momenta ℓ, for $\delta = -2$.

Thus, in the adiabatic approximation, the dynamics of q can be derived from a potential $V(q)$ given by

$$V(q) = \epsilon^2 \int_q^{+\infty} \left(\frac{\ell^2}{q^3} - w(q)\right) dq. \tag{7}$$

The potential landscape as a function of the angular momentum is presented in Fig. 2, where a succession of minima can be observed. For large distances q between the two atoms, the potential wells become increasingly shallow as the potential decreases as $-(\cos q)/q$ [10]. Furthermore, the centrifugal force opposes to the presence of low-q potential minima, as can be observed for large values of the angular momentum ℓ. The extrema q_n of this potential are given by the equation

$$q_n^3 w(q_n) = \ell^2. \tag{8}$$

So for small angular momentum ℓ, the stable and unstable points are found at, respectively,

$$q_n^s \approx 2\pi n - \frac{1}{2\pi n} + \frac{\ell^2(1+4\delta^2)}{(2\pi n)^2}, \tag{9a}$$

$$q_n^u \approx \pi(2n+1) - \frac{1}{\pi(2n+1)} + \frac{\ell^2(1+4\delta^2)}{\pi^2(2n+1)^2}. \tag{9b}$$

The potential V around these points can be approximated by

$$V(q) \approx \epsilon^2 \left[\frac{\ell^2}{2q^2} - \frac{1}{1+4\delta^2}\frac{\cos q}{q}\right]. \tag{10}$$

In particular, the potential barrier that a pair of atoms close to the point q_n^s has to overcome is

$$\begin{aligned} U_n &= V(q_n^u) - V(q_n^s) \\ &\approx \frac{\epsilon^2}{2\pi}\frac{4n+1}{n(2n+1)}\left[\frac{1}{1+4\delta^2} - \frac{\ell^2}{4n(2n+1)}\right], \end{aligned} \tag{11}$$

which defines an admissible kinetic energy for the two particles, along the radial direction, to remain bound together. Hence, if the pair of atoms has initially a difference of radial velocities δv, it will form a bound state provided $m(\delta v/2)^2 < (\hbar\Gamma^2/4\omega_r)U_n$, or a free particle state otherwise. The system is insensitive to a velocity of the system's center of mass, and difference of normal velocities corresponds to the angular momentum ℓ. Due to the integrable nature of Eq. (5), the bound state undergoes everlasting oscillations, with an amplitude which does not vary over time.

This long-term stability is in contrast to the results reported in Ref. [9], where either a slow cooling or heating of the bound system was observed by numerical integration of Eqs. (4). To explain these results, we show in the next section that the finite time needed for the dipole to equilibrate with the local field is responsible for introducing a dissipative force in Eq. (5).

III. MULTISCALE ANALYSIS

In general, there is a clear separation of the time scales of dipole and of the bound-state vibrational mode. For example, for the rubidium atoms probed with a low pump ($\Omega \ll \Gamma$) an oscillation of the bound state spans over hundreds of dipole lifetimes [9]. More generally, one can observe from Eq. (10) that if $\epsilon \ll 1$ and $\epsilon\ell \ll 1$, the vibrational mode will have a period much longer than the dipole relaxation time $1/\Gamma$.

This difference in time scales allows us to treat the finite time for the dipole equilibration as a correction to the adiabatic equation (5). Let us introduce $g(t) = \exp[iq(t)]/[iq(t)]$, the kernel which appears in the dipole dynamics Eq. (4a), and which varies slowly as compared to the dipole lifetime. As derived in the Appendix, the first correction to the adiabatic approximation reads

$$\beta(t) \approx -\frac{2i\Omega/\Gamma}{[1-2i\delta+g(t)]} - \frac{4i\Omega}{\Gamma}\frac{\dot{g}(t)}{[1-2i\delta+g(t)]^3}, \tag{12}$$

where the first right-hand term corresponds to the adiabatic contribution, for which $\beta(t)$ follows instantaneously the evolution of $q(t)$. The second one describes, at first order, the delay in the dipole response to the atomic motion, and is proportional to $\dot{q}$. Inserting the above equation into (4b) and keeping only the linear term in $\dot{q}$ leads to a nonconservative equation for the atom's motion:

$$\ddot{q} = -\frac{dV}{dq} - \epsilon^2\lambda(q)\dot{q}, \tag{13}$$

where $\lambda(q)$ is a "friction" coefficient which takes positive and negative value as q oscillates:

$$\begin{aligned} \lambda(q) = \frac{4w(q)}{\left(1+\frac{\sin q}{q}\right)^2 + \left(2\delta+\frac{\cos q}{q}\right)^2}\Bigg[&\frac{\cos q}{q} - \frac{\sin q}{q^2} \\ &- 2w(q)\left(1+\frac{\sin q}{q}\right)\left(2\delta+\frac{\cos q}{q}\right)\Bigg]. \end{aligned} \tag{14}$$

From Eqs. (7) and (13) it becomes clear that $\dot{q}$ scales as ϵ, so the deviation from the adiabatic dynamics of Eq. (5) occurs on a time scale $1/\epsilon$ longer than the oscillations of the bound state. The long-term consequences of the nonconservative term $\lambda(q)$ will depend on its average value over an oscillation, as we now show through a multiscale analysis.

The separation of the two time scales is realized introducing the time variables $u = \epsilon t$, associated to the oscillation of the bound state, and $v = \epsilon^2 t$, over which the dynamics drifts from its adiabatic approximation. The distance $q(u, v)$ is now considered to be a function of those two, taken to be independent variables, with the chain rule

$$\frac{d}{dt} = \epsilon\frac{\partial}{\partial u} + \epsilon^2\frac{\partial}{\partial v}. \tag{15}$$

Applying the above rule to Eq. (13) leads to the multiscale equation:

$$\frac{\partial^2 q}{\partial u^2} - \frac{\ell^2}{q^3} + w(q) = -2\epsilon\frac{\partial^2 q}{\partial u\partial v} - \epsilon\lambda(q)\frac{\partial q}{\partial u} - \epsilon^2\frac{\partial^2 q}{\partial v^2} - \epsilon^2\lambda(q)\frac{\partial q}{\partial v}. \tag{16}$$

The separation of time scales is operated by considering the perturbation expansion $q = \sum_{n=0}^{\infty}\epsilon^n q_{(n)}$, which results, at the zero order in ϵ, in

$$\frac{\partial^2 q_{(0)}}{\partial u^2} = \frac{\ell^2}{q_{(0)}^3} - w(q_{(0)}). \tag{17}$$

It describes the adiabatic dynamics of $q_{(0)}$, i.e., it is formally equivalent to Eq. (5). It can be associated to the potential energy $V_1 = V(q_{(0)})/\epsilon^2$ from Eq. (7), so that it admits the following energy as an integral of motion:

$$E(v) = \frac{1}{2}\left(\frac{\partial q_{(0)}}{\partial u}\right)^2 + V_1(q_{(0)}). \tag{18}$$

This energy of the bound state varies only over the slow time scale v, and this drift is captured by the next order equation resulting from Eq. (16), which contains the nonconservative contribution:

$$\frac{\partial^2 q_{(1)}}{\partial u^2} + \left[\frac{3\ell^2}{q_{(0)}^4} + w'(q_{(0)})\right]q_{(1)} = -2\frac{\partial^2 q_{(0)}}{\partial u\partial v} - \lambda(q_{(0)})\frac{\partial q_{(0)}}{\partial u}.$$

In order to prevent the secular growth in $q_{(1)}$, its right-hand term must vanish, a condition which reads

$$\left[2\frac{\partial}{\partial v} + \lambda(q_{(0)})\right]\frac{\partial q_{(0)}}{\partial u} = 0. \tag{19}$$

For a bound state, the energy definition (18) provides the expression

$$\frac{\partial q_{(0)}}{\partial u} = \pm\sqrt{2[E(v) - V_1(q_{(0)})]}, \tag{20}$$

which in turn leads to the equation for the evolution of the energy $E(v)$:

$$\frac{dE}{dv} = -\lambda(q_{(0)})[E(v) - V_1(q_{(0)})] + \frac{dV_1}{dq_{(0)}}\frac{\partial q_{(0)}}{\partial v}. \tag{21}$$

The slow evolution of the bound-state energy is captured by integrating Eq. (21) over a period T of its oscillation:

$$T = 2\int_{q_-}^{q_+}\frac{dq}{\sqrt{2[E(v) - V_1(q)]}}, \tag{22}$$

where $q_\pm$ correspond to the extrema of the position, at which $\partial q_{(0)}/\partial u = 0$. These extrema slowly change over time, so they are actually functions of v. The averaging of Eq. (21) is realized dropping its last term as it cancels over an oscillation cycle, so one obtains

$$\left\langle\frac{dE}{dv}\right\rangle_T = -\frac{1}{T}\int_{q_-}^{q_+}\lambda(q)\sqrt{2[E(v) - V_1(q)]}dq. \tag{23}$$

This equation describes the long-term evolution of the bound-state energy, and predicts whether it is truly stable or only metastable.

The exact evolution of $\langle E(v)\rangle_T$ requires a numerical integration; nonetheless its behavior close to the equilibrium point q_n^s, given by Eq. (9), can be captured by approximating the system as a harmonic oscillator. Introducing $\tilde{q}_n = q - q_n^s$ the relative oscillation, $\omega_n = \sqrt{V''(q_n^s)}$ its angular frequency, and $\tilde{E}_n = \langle E\rangle_T - V_1(q_n^s)$ the energy relative to the equilibrium point, one can write

$$\langle E(v)\rangle_T \approx V_1(q) + \tilde{E}_n(v) - \omega_n^2\frac{\tilde{q}_n^2}{2}, \tag{24a}$$

$$\lambda(q) \approx \lambda(q_n^s) + \lambda'(q_n)\tilde{q}_n + \lambda''(q_n^s)\frac{\tilde{q}_n^2}{2}, \tag{24b}$$

$$q_\pm = q_n^s \pm \frac{\sqrt{2\tilde{E}_n(v)}}{\omega_n}, \tag{24c}$$

and $T = 2\pi/\omega_n$. Inserting these equations into Eq. (23), one finds that the linear contribution $\lambda'(q_n^s)$ of the friction term does not contribute due to the symmetry of the integral, and the remaining terms integrate as

$$\frac{d\tilde{E}_n}{dv} = -\alpha_n\tilde{E}_n - \beta_n\tilde{E}_n^2, \tag{25a}$$

$$\alpha_n = \frac{\lambda(q_n^s)}{2}, \tag{25b}$$

$$\beta_n = \frac{\lambda''(q_n^s)}{8\omega_n^2}. \tag{25c}$$

The energy $\tilde{E}_n$ is associated to the oscillations of the pair of atoms in the potential well. Due to the conservation of the angular momentum, it is naturally associated to a variation of the angular velocity as well, but it can essentially be understood as energy in the vibrational mode of the cold molecule, which can either increase (heating) or decrease (cooling) in time. Equation (25a) describes this slow drift, over a time scale $1/\epsilon$ longer than the oscillations of the bound state, and the next section is dedicated to the different relaxation regimes.

IV. STABILITY OF THE BOUND STATES

A. Stability regions

Let us first discuss the case of a bound state without angular momentum ($\ell = 0$), where the two atoms oscillate along a given direction. The equilibrium condition (8) shows that $w(q_n^s) = 0$, so the friction term (14) has no zero-order contribution [$\lambda(q_n^s) = 0$] and only the quadratic term in the relaxation equation (25a) is present. Calling $E_i = \tilde{E}_n(0) > 0$ the initial energy relative to the equilibrium point q_n^s, and assuming that $E_i < U_n$ given by Eq. (11), the bound-state energy will drift as

$$\tilde{E}_n(v) = \frac{E_i}{1 + \beta_n E_i v}. \tag{26}$$

Thus for $\beta_n > 0$ the bound state will approach the equilibrium point at an algebraic speed, and the system is in a cooling regime. The time for the energy to decrease to one-half of its

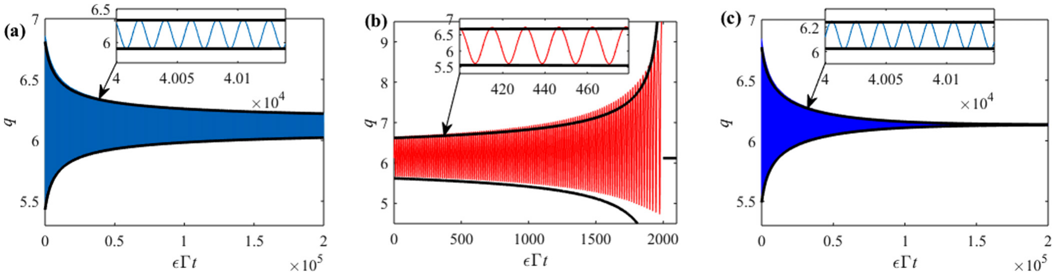

FIG. 3. Dynamics of the interparticle distance q for a pair of atoms (a) without angular momentum ($\ell = 0$) and in the cooling regime ($\delta = -0.56$), (b) without angular momentum ($\ell = 0$) and in the heating regime ($\delta = 0$), and (c) with angular momentum ($\ell = 0.5$) and in the cooling regime ($\delta = -0.5$). The other parameters are $E_i = 0.02$ and $\epsilon = 0.1$. The black curves correspond to the theoretical predictions of Eqs. (24c), (26), and (29), where ω_1, α_1, and β_1 are given by Eqs. (32a), (32b), and (32c).

initial value is

$$\tau_n^{(1/2)} = \frac{1}{\epsilon^2 \beta_n E_i} \quad (\ell = 0). \tag{27}$$

This behavior is illustrated in Fig. 3(a), where the distance between a pair of atoms in the cooling regime is shown to slowly decrease over time.

On the contrary, for $\beta_n < 0$ the atomic system is heating, and the bounded pair of atoms breaks up as its energy reaches the potential barrier U_n, provided by Eq. (11). The time for the pair of atoms to reach the escape energy is given by

$$\tau_n^{(\text{esc})} = \frac{1}{\epsilon^2 |\beta_n|}\left(\frac{1}{E_i} - \frac{1}{U_n}\right). \tag{28}$$

As depicted in Fig. 3(b), the atoms present larger and larger oscillations, until they separate and have quasiballistic trajectories. Finally, for $\beta_n = 0$, the analysis of higher-order contributions in the friction term is necessary to determine the stability of the bound state.

In the presence of angular momentum ($\ell > 0$) the friction term has in general a constant contribution around the equilibrium ($\lambda(q_n^s) \neq 0$), in which case the evolution of the bound-state energy reads

$$\tilde{E}(v) = \frac{\alpha_n E_i e^{-\alpha_n v}}{\alpha_n + \beta_n E_i (1 - e^{-\alpha_n v})}. \tag{29}$$

Thus if $\alpha_n > 0$ and $\alpha_n + \beta_n E_i > 0$, after a transient the energy $\tilde{E}(v)$ decays exponentially fast to zero, at rate α_n. The final bound state thus has angular momentum, but no motion in the vibrational mode; see Fig. 3(c). More generally, the half-life decay time of the energy is

$$\tau_n^{(1/2)} = \frac{1}{\epsilon^2 \alpha_n} \ln\left[\frac{2\alpha_n + \beta_n E_i}{\alpha_n + \beta_n E_i}\right]. \tag{30}$$

Whereas if $\alpha_n < 0$ and $\beta_n > 0$, the system decreases exponentially fast, at rate $|\alpha_n|$ toward a bound state that possesses both angular momentum and energy in the vibrational mode: $\tilde{E}(\infty) = |\alpha_n|/\beta_n$. This regime sustains everlasting oscillations.

The other case, with $\alpha_n > 0$ and $\beta_n < 0$ such that $\alpha_n < |\beta_n| E_i$, corresponds to a bound state which is only metastable, the lifetime of which is given by

$$\tau_n^{(\text{esc})} = \frac{1}{\epsilon^2 \alpha_n} \ln\left[\frac{|\beta_n| - \alpha_n/U_n}{|\beta_n| - \alpha_n/E_i}\right]. \tag{31}$$

Let us now provide an approximated expression of these stability parameters, by doing an expansion around the equilibrium points (9a):

$$\omega_n^2 \approx \frac{1}{2\pi n(1 + 4\delta^2)}, \tag{32a}$$

$$\alpha_n \approx \frac{\ell^2}{8(\pi n)^4(1 + 4\delta^2)}\left[1 - \frac{2\ell^2(\delta + 1/4\pi n)}{(\pi n)^2}\right], \tag{32b}$$

$$\beta_n \approx -\frac{2}{\pi n(1 + 4\delta^2)^2}\left[\delta + \frac{1 + \delta^2}{\pi n}\right]. \tag{32c}$$

Let us first discuss the case without angular momentum, where only the β_n coefficient is relevant [see Eq. (26)]. In this case, under the condition

$$-\sqrt{\left(\frac{n\pi}{2}\right)^2 - 1} - \frac{n\pi}{2} \leqslant \delta \leqslant \sqrt{\left(\frac{n\pi}{2}\right)^2 - 1} - \frac{n\pi}{2}, \tag{33}$$

the β_n coefficient is positive and the bound states are truly stable. Otherwise, β_n is negative and the bound states are only metastable. The behavior of β_n as a function of the detuning is

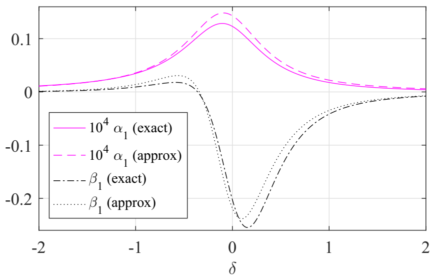

FIG. 4. Stability coefficients α_n and β_n, as calculated from Eqs. (25b) and (25c) ("exact") and from Eqs. (32b) and (32c) ("approx"). Simulations realized for $\epsilon = 0.1$ and $\ell = 0.1$.

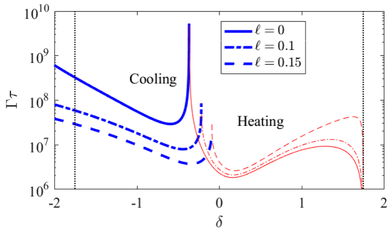

FIG. 5. Cooling (thick blue lines) and heating (thin red lines) time as a function of the detuning δ, for different values of the angular momentum ℓ, for $\epsilon = 0.1$ and $E_i = 2 \times 10^{-4}$. Both times present a divergence at the critical detuning, where the long-term stability of the bound state changes. The vertical black dotted lines correspond to the stability threshold defined by $E_i = U_n$.

illustrated in Fig. 4, where a range of negative detuning allows for stable bound states.

In the presence of a small angular momentum (that is, such that α_n is positive), the system is stable over a larger range of detuning, since $\beta_n > -\alpha_n/E_i$ is now a sufficient condition to reach a cooling regime.

Note that, while Eq. (32b) suggests that α_n becomes negative for large values of angular momentum, the approximated expressions (32) lose their validity, and the increase of ℓ actually suppresses successively the potential minima that are responsible for the bound states (see Fig. 2). A more detailed study of the high-ℓ regime will require different approximations than the ones performed here.

B. Cooling and heating time

Let us first comment that the energy in the vibrational mode $\tilde{E}$ is a function of v, i.e., it scales with $1/\epsilon^2 \sim \Gamma^3/(\Omega^2\omega_r)$. So ϵ is the fundamental parameter to control the time scales over which cooling and heating act. Then, a numerical study of the heating and cooling times reveals that it strongly depends on the detuning; see Fig. 5 for examples of this dependence for different values of the angular momentum. First, the heating time presents a minimum (which means the heating rate is maximum) very close to resonance ($\delta \approx 0.15\Gamma$); this is somehow expected from scattering of light very close to the atomic resonance, where the radiation pressure force dominates over the dipolar force. Instead, the cooling is most efficient for light slightly detuned to the red, with a maximum that depends significantly on the angular momentum. In both heating and cooling regimes, the rates decrease going farther away from resonance, where light-atom coupling is less efficient. For a given ϵ and initial energy E_i, the barrier potential U_n of the bound state decreases with the detuning [see Eq. (11)], so there is no more bound state at large detuning (see vertical dotted lines in Fig. 5).

Interestingly, the heating rate is not very sensitive to the angular momentum, but the cooling rate is. From $\ell = 0$ to $\ell = 0.15$, a factor $\sim$10 is gained on the cooling rate of the bound state. This highlights that the angular momentum of the system increases the stability of the system, possibly countering other heating effects.

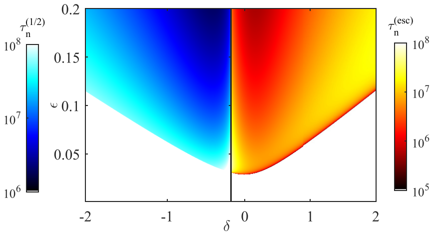

FIG. 6. Heating and cooling times as a function of the detuning δ and the parameter ϵ, for $\ell = 0.1$. The negative detuning part ($\delta \lesssim -0.21$) corresponds to the cooling regime (blue color map), whereas the positive detuning part ($\delta \gtrsim -0.21$) stands for the heating regime. The black vertical line marks the separation between the two regimes and the white area corresponds to unbound states ($E_i > U_n$). Simulations realized for $E_i = 2 \times 10^{-4}$ and $n = 1$, using Eqs. (30)–(32).

A stability diagram is presented in Fig. 6 for $\ell = 0.1$, showing the heating and cooling times as a function of the detuning and of the parameter ϵ. A larger pump strength enhances in atom-light coupling, and thus results in a higher rate of change in the energy of the bound state, just like working close to resonance.

V. IMPACT OF THE FLUCTUATIONS

The analysis up to now was purely deterministic, neglecting the effect of the fluctuations due to spontaneous emission as the atoms interact with the incident lasers, and with their mutual radiation. The atoms receive a random momentum kick $\delta\mathbf{p} = \hbar\mathbf{k}$, which introduces a stochastic contribution both in the radial and in the angular directions. Each scattering event results in an average increase of the associated energy of $\delta E_{\text{recoil}} = \hbar\omega_r/2$. Focusing at first on spontaneous emission from the driving of the confining lasers, the heating energy rate is proportional to the scattering rate:

$$\left(\frac{\delta E}{\delta t}\right)_{\text{SE}} = \frac{2\hbar\omega_r}{\Gamma}\frac{\Omega^2}{1+4\delta^2}. \tag{34}$$

Adding this term to the equation for the scaled average energy $\tilde{E}_n$ for the radial energy in Eq. (25a), using the relations $\tilde{E} = (4\omega_r/\Gamma\epsilon^2)(E/\hbar\Gamma)$ and $v = \epsilon^2\Gamma t$, one obtains

$$\frac{d\tilde{E}_n}{dt} = -\epsilon^2\Gamma\big(\alpha_n\tilde{E}_n + \beta_n\tilde{E}_n^2\big) + \frac{\omega_r^2}{2(1+4\delta^2)}. \tag{35}$$

The steady-state solution is thus given by

$$\tilde{E}_n^\infty = \frac{1}{2\beta_n}\Big(\sqrt{\alpha_n^2 + 4\beta_n C} - \alpha_n\Big), \tag{36}$$

where $C = (\omega_r/2\Gamma\epsilon^2)/(1+4\delta^2)$. Since $4\beta_n C \gg \alpha_n^2$, $\tilde{E}_n^\infty \approx \sqrt{C/\beta_n}$, which, in physical units, reads

$$E_n^\infty \approx f_n(\delta)\hbar\Omega, \tag{37}$$

with

$$f_n(\delta) = \frac{1}{\sqrt{2\beta_n(1+4\delta^2)}}. \tag{38}$$

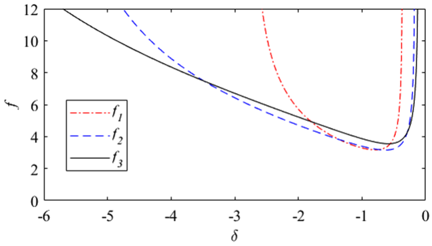

FIG. 7. Amplitude of the equilibrum energy $f(\delta)$, in units of $\hbar\Omega$, for different detuning δ, as predicted by the stochastic contribution and in the range where β_n is positive (cooling regime).

The function $f_n(\delta)$ is plotted in Fig. 7 for the values where β_n is positive (cooling regime for the deterministic dynamics), as a function of the detuning δ and for $n = 1, 2, 3$. It reaches a minimum around $\delta = -3/4$, close to the value at which the cooling term β_n is maximum, and the achieved steady-state energy is $E_n^\infty \approx 2\hbar\Omega$.

The fact that the limit temperature is proportional to $\hbar\Omega$ is rather surprising, as compared to the "standard" limit of laser cooling of $\sim\hbar\Gamma$ [26]. However, a similar temperature can be identified for a single two-level atom confined in a standing wave. Let us shortly review this situation: a standing wave along z with $\Omega(z) = \Omega_0\cos(kz)$ produces a force along the z axis

$$F_z = \hbar k\frac{\Omega_0^2}{\Gamma}\frac{2\delta}{1+4\delta^2}\left[\sin(kz)\cos(kz) + \frac{\sin^2(kz)}{1+4\delta^2}\frac{kv_z}{\Gamma}\right]. \tag{39}$$

When averaged over a spatial period $\lambda/2$ this force reduces to the usual viscous force $F_z = -\alpha v_z$, with $\alpha = 4\hbar k^2(\Omega_0/\Gamma)^2[-2\delta/(1+4\delta^2)^2]$. If instead the atom is near the potential minimum at $z = 0$, with a kinetic energy smaller than the trapping energy $\hbar\Gamma(\Omega_0/\Gamma)^2[-\delta/(1+4\delta^2)]$, the force can be locally expanded as

$$F_z \approx \hbar k^2\frac{\Omega_0^2}{\Gamma}\frac{2\delta}{1+4\delta^2}\left(z + \frac{(kz)^2}{1+4\delta^2}\frac{v_z}{\Gamma}\right). \tag{40}$$

For $\delta < 0$ the atom is trapped by the dipole force and cooled by a force which is linear in the velocity and quadratic in the position. When averaged over the oscillating motion, a multiscale analysis similar to that performed in Sec. III leads to the following equation for the energy:

$$\frac{dE_z}{dt} = -\frac{2\omega_r}{1+4\delta^2}\frac{E_z^2}{\hbar\Gamma} + \frac{4}{3}\frac{\hbar\omega_r}{\Gamma}\frac{\Omega_0^2}{1+4\delta^2}, \tag{41}$$

from which an equilibrium energy $E_z^\infty = \sqrt{3/2}\hbar\Omega_0$ can be deduced. Hence single atom cooling in a standing wave also presents a limit temperature $\propto\hbar\Omega_0$ for low-energy initial states, in addition to the usual Doppler limit $\hbar\Gamma$.

The trick is that the linear regime assumption [$s = 2\Omega_0^2/(\Gamma^2 + 4\Delta^2) \ll 1$] underlying the classical treatment of the atom dynamics is incompatible with the requirement of a trapping potential deeper that the equilibrium energy. Indeed the ratio between the trapping potential depth and the equilibrium energy is $\sqrt{s}(-\delta/\sqrt{1+4\delta^2})$, where the latter function of δ tops at $1/2$, so the confinement cannot be achieved at equilibrium.

In the case of an optically bound pair of atoms, the ratio is even worse as SE relies on the incident laser, while the trapping potential requires an additional scattering event from the atoms. More specifically, the ratio between the trapping potential depth and the equilibrium energy is $\sim\sqrt{s/(1+4\delta^2)}$. Thus radial confinement of the pair cannot be achieved without any additional cooling mechanism.

As for the rotational degree of freedom, the stochastic contribution leads to a pure diffusive behavior of the angular momentum L, as the deterministic dynamics preserves it. The diffusion makes the transverse energy grow as $\langle L^2/mr^2\rangle \sim \hbar\omega_r s\Gamma t$. Furthermore, the rotational motion of the molecule decreases its radial potential barrier [see Eq. (11)], i.e., it makes the system even less stable. Hence a cooling mechanism active on the angular motion of the molecules will be necessary to achieve optical binding with cold atoms.

Let us comment that another heating mechanism has been identified in Ref. [27], which corresponds to momentum diffusion from radiative interaction, i.e., fluctuations in the dipolar force (which is here responsible for the OB). In the case of the pair of atoms, the heating rate reads

$$\left(\frac{\delta E}{\delta t}\right)_{\text{rad}} \sim \frac{\hbar\omega_r}{\Gamma}\frac{\Omega^2}{1+4\delta^2}\overline{\nabla_q^2\left(\frac{\sin q}{q}\right)}, \tag{42}$$

where the bar refers to an average over the oscillation period. Nevertheless, close to the equilibrium position q_n^s, $\overline{\nabla_q^2(\sin q/q)} \approx 0.03$, so it only represents a correction of a few percent to the contribution of the SE from the driving laser (34).

VI. DISCUSSION AND CONCLUSIONS

To summarize, we have first shown that the optical binding of two atoms in the vacuum and confined in a plane is affected by a *deterministic* nonconservative force able to cool or heat the system. This force arises from the nonadiabatic reaction of the atomic dipole to the change of field as the distance between the atoms change. This force is strongly position dependent but, when averaged over an oscillation of the pair of atoms, it effectively results in a slow heating or cooling of the system. It may thus either lead the atoms to escape the influence of each other, typically for positive detuning, or rather drive them toward the local potential minimum, in general for negative detuning.

In particular, the specificity of the cooling associated to the angular momentum can be better understood by analyzing further Eq. (25a): the β_n coefficient, which does not involve angular momentum at first order, is associated to a quadratic dependence in $\tilde{E}$, so it is efficient only when the system is significantly afar from the stable point. On the contrary, the α_n term, which scales directly with ℓ^2, appears in a term linear with $\tilde{E}$. Hence it acts as a "friction" term and is most efficient at keeping the system very close to the equilibrium point.

Nevertheless, the effect of the stochastic heating due to spontaneous emission appears to be stronger than the confining potential that gives rise to the optical binding. Both the stretching vibrational mode and the rotational degree of freedom turn out to be ultimately dominated by diffusion effects, so the bound states are not truly bound.

The lack of stability of the OB configurations for pairs of atoms calls for alternative ways to achieve the binding. In this respect, collective effects in larger atomic systems may be a promising candidate, as the cooperative emission (such as superradiance) is an efficient mechanism for self-organization in one dimension [6,7]. As for two-dimensional systems, crystallization is expected to occur, thanks to the optical potential generated on each atom by its neighbors [18]. In this case many-atom effects may significantly alter the cooling properties of the system, as collective oscillation modes arise. In this context, the angular momentum may provide an extra degree of freedom to tune the stability properties of the system, but also to modify the spatial period of the crystal, and possibly its lattice structure.

ACKNOWLEDGMENTS

This work was performed in the framework of the European Training Network ColOpt, which is funded by the European Union (EU) Horizon 2020 programme under the Marie Sklodowska-Curie action, Grant No. 721465. R.B. holds a grant from São Paulo Research Foundation (FAPESP), No. 2014/01491-0. We acknowledge fruitful discussions with R. Kaiser and C. E. Maximo.

APPENDIX: ANALYSIS OF THE ADIABATIC APPROXIMATION

In order to discuss the adiabatic approximation, let's integrate Eq. (4a) from zero to t with $\beta(0) = 0$:

$$\beta(t) = -i\frac{\Omega}{\Gamma}\int_0^t dt' \exp\left\{-\frac{1}{2}(1-2i\delta)t' - \frac{1}{2}\int_0^{t'} g(t-t'+t'')dt''\right\}, \tag{A1}$$

where

$$g(t) = \frac{\exp[iq(t)]}{iq(t)}. \tag{A2}$$

Let assume that $g(t)$ varies slowly with respect to the term $(1-2i\delta)t'$. However, we consider the first-order deviation of $g(t)$, in order to go beyond the usual adiabatic approximation, expanding $g(t-t'+t'')$ in the integral of Eq. (A1) up to the first order in its Taylor series:

$$\int_0^{t'} g(t-t'+t'')dt'' \approx g(t)t' - \dot{g}(t)\int_0^{t'}(t'-t'')dt'' = g(t)t' - \frac{1}{2}\dot{g}(t)t'^2. \tag{A3}$$

The first term of Eq. (A3) corresponds to the usual adiabatic approximation, whereas the second term takes into account the slow variation of g due to the atomic motion in the confining potential. Since g depends on the relative atomic position $q(t)$, then $\dot{g}$ is proportional to the relative atomic velocity.

Once Eq. (A3) is inserted in Eq. (A1), it gives

$$\beta(t) \approx -i\frac{\Omega}{\Gamma}\int_0^{\infty} dt' \exp\left\{-\frac{1}{2}[1-2i\delta+g(t)]t' + \frac{1}{4}\dot{g}(t)t'^2\right\}, \tag{A4}$$

where we have extended the integration upper limit to infinity, neglecting in this way the short initial transient. By expanding the small term proportional to $\dot{g}(t)$ at the first order,

$$\begin{aligned}\beta(t) &= -i\frac{\Omega}{\Gamma}\int_0^{\infty} dt' \exp\left\{-\frac{1}{2}[1-2i\delta+g(t)]t'\right\}\left[1+\frac{1}{4}\dot{g}(t)t'^2+\cdots\right]\\ &\approx -i\frac{2\Omega}{\Gamma}\frac{1}{1-2i\delta+g(t)}\left\{1+\frac{2\dot{g}(t)}{[1-2i\delta+g(t)]^2}\right\}.\end{aligned} \tag{A5}$$

The first term of Eq. (A5) is the usual adiabatic approximation, whereas the second term corresponds to the correction due to the atomic displacement. It is similar to the Doppler effect in the optical molasses, with the difference that here the atomic displacement is not due to the thermal motion, but to the oscillation in the optical binding potential. Also we can say that in general this velocity-dependent force is due to the cooperative decay and light shift, depending on the distance between the atoms and induced by the laser. From Eq. (A5), we obtain

$$|\beta(t)|^2 = \frac{4\Omega^2}{\Gamma^2}\frac{1}{D(q)} + \frac{16\Omega^2}{\Gamma^2}\frac{1}{D^3(q)}[\mathrm{Re}\dot{g}(t)D(q) - 2\,\mathrm{Im}\dot{g}(t)(1+\sin q/q)(2\delta+\cos q/q)], \tag{A6}$$

where

$$\mathrm{Re}\dot{g}(t) = \frac{d}{dq}\left(\frac{\sin q}{q}\right)\dot{q} = \left(\frac{\cos q}{q} - \frac{\sin q}{q^2}\right)\dot{q}, \tag{A7}$$

$$\mathrm{Im}\dot{g}(t) = -\frac{d}{dq}\left(\frac{\cos q}{q}\right)\dot{q} = \left(\frac{\sin q}{q} + \frac{\cos q}{q^2}\right)\dot{q}, \tag{A8}$$

and $D(q) = (1 + \sin q/q)^2 + (2\delta + \cos q/q)^2$. Inserting Eqs. (A6)–(A8) in the force equation (4b), we obtain

$$\ddot{q} = \frac{16\omega_r \Omega^2}{\Gamma^3}\left[\frac{\ell^2}{q^3} - w(q) - \lambda(q)\dot{q}\right], \tag{A9}$$

where

$$w(q) = \frac{1}{D(q)}\left(\frac{\sin q}{q} + \frac{\cos q}{q^2}\right), \tag{A10}$$

$$\lambda(q) = -\frac{4w(q)}{D(q)}\left[\frac{\cos q}{q} - \frac{\sin q}{q^2} - 2w(q)\left(1 + \frac{\sin q}{q}\right)\left(2\delta + \frac{\cos q}{q}\right)\right]. \tag{A11}$$

[1] W. D. Phillips, Nobel lecture: Laser cooling and trapping of neutral atoms, Rev. Mod. Phys. **70**, 721 (1998).

[2] M. H. Anderson, J. R. Ensher, M. R. Matthews, C. E. Wieman, and E. A. Cornell, Observation of bose-einstein condensation in a dilute atomic vapor, Science **269**, 198 (1995).

[3] M. Greiner, O. Mandel, T. Esslinger, T. W. Hänsch, and I. Bloch, Quantum phase transition from a superfluid to a Mott insulator in a gas of ultracold atoms, Nature (London) **415**, 39 (2002).

[4] C. J. Myatt, E. A. Burt, R. W. Ghrist, E. A. Cornell, and C. E. Wieman, Production of Two Overlapping Bose-Einstein Condensates by Sympathetic Cooling, Phys. Rev. Lett. **78**, 586 (1997).

[5] G. Labeyrie, E. Tesio, P. M. Gomes, G.-L. Oppo, W. J. Firth, G. R. M. Robb, A. S. Arnold, R. Kaiser, and T. Ackemann, Optomechanical self-structuring in a cold atomic gas, Nat. Photon. **8**, 321 (2014).

[6] R. Bonifacio and L. De Salvo, Collective atomic recoil laser (CARL) optical gain without inversion by collective atomic recoil and self-bunching of two-level atoms, Nucl. Instrum. Methods, Phys. Res., A **341**, 360 (1994).

[7] S. Slama, S. Bux, G. Krenz, C. Zimmermann, and Ph. W. Courteille, Superradiant Rayleigh Scattering and Collective Atomic Recoil Lasing in a Ring Cavity, Phys. Rev. Lett. **98**, 053603 (2007).

[8] H. Ritsch, P. Domokos, F. Brennecke, and T. Esslinger, Cold atoms in cavity-generated dynamical optical potentials, Rev. Mod. Phys. **85**, 553 (2013).

[9] C. E. Máximo, R. Bachelard, and R. Kaiser, Optical binding with cold atoms, Phys. Rev. A **97**, 043845 (2018).

[10] M. M. Burns, J.-M. Fournier, and J. A. Golovchenko, Optical Binding, Phys. Rev. Lett. **63**, 1233 (1989).

[11] M. M. Burns, J.-M. Fournier, and J. A. Golovchenko, Optical matter: Crystallization and binding in intense optical fields, Science **249**, 749 (1990).

[12] T. M. Grzegorczyk, B. A. Kemp, and J. A. Kong, Stable Optical Trapping Based on Optical Binding Forces, Phys. Rev. Lett. **96**, 113903 (2006).

[13] N. K. Metzger, K. Dholakia, and E. M. Wright, Observation of Bistability and Hysteresis in Optical Binding of Two Dielectric Spheres, Phys. Rev. Lett. **96**, 068102 (2006).

[14] V. Karásek, K. Dholakia, and P. Zemánek, Analysis of optical binding in one dimension, Appl. Phys. B **84**, 149 (2006).

[15] N. K. Metzger, R. F. Marchington, M. Mazilu, R. L. Smith, K. Dholakia, and E. M. Wright, Measurement of the Restoring Forces Acting on Two Optically Bound Particles from Normal Mode Correlations, Phys. Rev. Lett. **98**, 068102 (2007).

[16] K. Dholakia and P. Zemánek, Colloquium: Gripped by light: Optical binding, Rev. Mod. Phys. **82**, 1767 (2010).

[17] T. M. Grzegorczyk, J. Rohner, and J.-M. Fournier, Optical Mirror from Laser-Trapped Mesoscopic Particles, Phys. Rev. Lett. **112**, 023902 (2014).

[18] J. Ng, Z. F. Lin, C. T. Chan, and P. Sheng, Photonic clusters formed by dielectric microspheres: Numerical simulations, Phys. Rev. B **72**, 085130 (2005).

[19] R. H. Lehmberg, Radiation from an N-atom system. I. General formalism, Phys. Rev. A **2**, 883 (1970).

[20] Ph. W. Courteille, S. Bux, E. Lucioni, K. Lauber, T. Bienaimé, R. Kaiser, and N. Piovella, Modification of radiation pressure due to cooperative scattering of light, Eur. Phys. J. D **58**, 69 (2010).

[21] A. Goetschy and S. E. Skipetrov, Non-Hermitian Euclidean random matrix theory, Phys. Rev. E **84**, 011150 (2011).

[22] S. E. Skipetrov and A. Goetschy, Eigenvalue distributions of large Euclidean random matrices for waves in random media, J. Phys. A: Math. Theor. **44**, 065102 (2011).

[23] S. E. Skipetrov and I. M. Sokolov, Absence of Anderson Localization of Light in a Random Ensemble of Point Scatterers, Phys. Rev. Lett. **112**, 023905 (2014).

[24] S. E. Skipetrov, Finite-size scaling analysis of localization transition for scalar waves in a three-dimensional ensemble of resonant point scatterers, Phys. Rev. B **94**, 064202 (2016).

[25] W. Guerin and R. Kaiser, Population of collective modes in light scattering by many atoms, Phys. Rev. A **95**, 053865 (2017).

[26] V. S. Letokhov, V. G. Minogin, and B. D. Pavlik, Cooling and capture of atoms and molecules by a resonant light field, Sov. Phys. JETP **45**, 698 (1977).

[27] B. Zhu, J. Cooper, J. Ye, and A. M. Rey, Light scattering from dense cold atomic media, Phys. Rev. A **94**, 023612 (2016).

PHYSICAL REVIEW A **100**, 023630 (2019)

Multimode collective scattering of light in free space by a cold atomic gas

R. Ayllon and J. T. Mendonça
IPFN, Instituto Superior Técnico de Lisboa, Universidade de Lisboa, Lisboa, Portugal

A. T. Gisbert and N. Piovella
Dipartimento di Fisica "Aldo Pontremoli", Università degli Studi di Milano, Via Celoria 16, I-20133 Milano, Italy

G. R. M. Robb
Department of Physics, SUPA, University of Strathclyde, Glasgow G4 0NG, Scotland, United Kingdom

(Received 31 May 2019; published 30 August 2019)

We have studied collective recoil lasing by a cold atomic gas, scattering photons from an incident laser into many radiation modes in free space. The model consists of a system of classical equations for the atomic motion of N atoms where the radiation field has been adiabatically eliminated. We performed numerical simulations using a molecular dynamics code PEPC (Pretty Efficient Parallel Coulomb Solver) to track the trajectories of the atoms. These simulations show the formation of an atomic density grating and collective enhancement of scattered light, both of which are sensitive to the shape and orientation of the atomic cloud. In the case of an initially circular cloud, the dynamical evolution of the cloud shape plays an important role in the development of the density grating and collective scattering. The ability to use efficient molecular dynamics codes will be a useful tool for the study of the multimode interaction between light and cold gases.

DOI: 10.1103/PhysRevA.100.023630

I. INTRODUCTION: SCATTERING OF LIGHT BY ATOMS

One of the most basic light-atom interactions is Rayleigh scattering. When an ensemble of N randomly distributed stationary atoms is weakly illuminated by a laser, the atoms scatter independently, and the resultant scattered field intensity varies as $\sim N$. For an ensemble of cold atoms which are free to move, the picture can change drastically due to collective behavior arising from the optical forces produced during scattering. Each atom is affected by the optical field scattered by the other atoms. Most studies of collective behaviors involving cold and ultracold atoms coupled to light have involved optical cavities [1], but similar phenomena have also been observed or predicted involving single feedback mirrors, optical fibers, and simply scattering into vacuum. These collective behaviors are at the origin of various self-organization phenomena, e.g., collective cooling [2–4], symmetry breaking, and pattern formation [5–13].

Superradiant light scattering was first demonstrated using a cigar-shaped Bose-Einstein condensate (BEC) [14] and later using a cold thermal gas [15]. In Ref. [14], superradiantly scattered light was observed to propagate along the major axis of the atomic cloud, simultaneous with the development of a matter-wave–density grating in the cloud. Some features of this phenomenon have been described by single-mode–mean-field models similar to that of the collective atomic recoil laser (CARL) [16–27]. These mean-field models are appropriate in certain specific cases where there is a well-defined propagation axis and, consequently, to a good approximation, a single spatial mode, e.g., in a single-mode cavity or in a highly elongated sample where the major axis of the sample defines an "end-fire mode" which dominates the direction of emission. In general, however, for arbitrary shapes of atomic ensembles, many spatial modes are involved simultaneously in the collective scattering process.

The computational effort required to model large systems of atoms in two-dimensional (2D) and three-dimensional (3D) geometries is significant. Large efficient publicly accessible "molecular dynamics" (MD) codes, which solve dynamical equations of motion for large collections of particles under the action of various forces (gravitational, electrostatic, and van der Waals), have become an essential tool in many areas of science, e.g., plasma physics, astrophysics, and computational chemistry. Despite the latter fact, to date, MD codes have not been used in the study of light interacting with cold atomic gases.

In this paper, we have simulated collective light scattering from a gas of cold atoms in 2D and 3D using a model which describes the positions and velocities of the atoms. The model has been derived from a multimode theory where the vacuum radiation modes are adiabatically eliminated. The result is a set of coupled N atoms where each atom is subjected to the radiation force exerted by all the other atoms present in the cloud. The form of the equations in this model makes them suitable for implementation in MD codes, which offers the possibility of efficient simulation of multimode scattering involving very large numbers of atoms by exploiting methods developed for simulating N-body systems involving long-range interactions, e.g., Barnes-Hut methods [28]. We use a public MD code, PEPC (Pretty Efficient Parallel Coulomb Solver) [29] to demonstrate that the collective scattering process described by our model has similar characteristics to those observed in Ref. [14], i.e., observation of a density grating, which is responsible for collective enhancement of scattered light intensity. Whereas, for ultracold atoms, the grating is observed in momentum space [14] with spacing $\hbar\mathbf{q} = \hbar(\mathbf{k}_0 - \mathbf{k})$—where $\hbar\mathbf{k}_0$ and $\hbar\mathbf{k}$ are the momenta of the incident and scattered photon—here, in contrast, the grating is observed in real space with atoms grouping periodically at distances which are multiples of $2\pi/q$. The model employed to depict the evolution of the cloud is presented in Sec. II along with its implementation in the MD algorithm. It is possible to see that, by using particular atomic cloud shapes and orientations, different density grating shapes and scattered light directions are achieved. These results, for a 2D cloud and for a specific 3D geometry, are presented in Secs. III A and III B, respectively.

II. MODEL OF COLLECTIVE SCATTERING

We consider a collection of N two-level atoms driven by a laser field with frequency $\omega_0 = ck_0$, propagating along the z axis with wave-number $\mathbf{k}_0 = k_0\hat{\mathbf{z}}$ and Rabi frequency $\Omega_0 = dE_0/\hbar$, where E_0 is the electric field and d is the atomic dipole. The laser field is far detuned from the atomic frequency ω_a with $\Delta_0 = \omega_0 - \omega_a \gg \Gamma$ and $\Gamma = d^2k_0^3/2\pi\epsilon_0\hbar$ as the atomic linewidth. In the far-detuned limit and for a dilute gas, absorption and multiple scattering can be neglected. In this limit, the incident light in mode $\mathbf{k}_0$ is scattered into the vacuum mode $\mathbf{k}$. The scattered optical field in mode $\mathbf{k}$ interferes with incident mode $\mathbf{k}_0$ to create a dipole force proportional to the photon momentum transfer $\hbar(\mathbf{k}_0 - \mathbf{k})$. When summed over the different vacuum modes, the resulting equations for atomic positions $\mathbf{r}_j$ and momenta $\mathbf{p}_j$ are (see the Appendix) as follows:

$$\dot{\mathbf{r}}_j = \frac{\mathbf{p}_j}{M}, \tag{1}$$

$$\dot{\mathbf{p}}_j = \Gamma\hbar k_0\left(\frac{\Omega_0}{2\Delta_0}\right)^2 \sum_{m\neq j}\left\{(\hat{\mathbf{z}} - \hat{\mathbf{r}}_{jm})\frac{\sin[k_0(r_{jm} - z_{jm})]}{k_0 r_{jm}} - \hat{\mathbf{r}}_{jm}\frac{\cos[k_0(r_{jm} - z_{jm})]}{(k_0 r_{jm})^2}\right\}, \tag{2}$$

where M is the atomic mass, $\mathbf{r}_{jm} = \mathbf{r}_j - \mathbf{r}_m$, and $\hat{\mathbf{r}}_{jm} = \mathbf{r}_{jm}/r_{jm}$. Each atom, labeled j, is coupled to all the other m atoms (where $m \neq j$) by an oscillating force with components along direction $\hat{\mathbf{z}}$ of the incident field and direction $\hat{\mathbf{r}}_{jm}$ toward the other atoms. Furthermore, the force has a finite range, consisting of terms which decrease with distance between the atoms as $1/r_{jm}$ or $1/r_{jm}^2$.

The intensity of scattered light in direction $\mathbf{k}$ is

$$I_s(\mathbf{k}) = I_1 N^2 |M(\mathbf{k}, t)|^2, \tag{3}$$

where $I_1 = (\hbar\omega_0\Gamma/8\pi r^2)(\Omega_0/2\Delta_0)^2$ is the single-atom Rayleigh scattering intensity and

$$M(\mathbf{k}, t) = \frac{1}{N}\sum_{j=1}^{N} e^{i(\mathbf{k}_0 - \mathbf{k})\cdot\mathbf{r}_j(t)} \tag{4}$$

is the "optical magnetization," or "bunching factor." It describes the strength of the density grating formed by the moving atoms, ranging from zero when the atomic positions are uniformly distributed to unity when the atoms are periodically packed into a length less than $2\pi/|\mathbf{k}_0 - \mathbf{k}|$. These equations generalize the CARL model, obtained for atoms interacting with a single mode in an optical ring cavity [17] to many modes in vacuum. Here, the incident photons are scattered in the 3D vacuum, and superradiant scattering occurs along certain directions determined by the atomic spatial distribution. In particular, for an elongated atomic distribution along the z axis of the incident field, collective scattering occurs along the backward direction $\mathbf{k} = -\mathbf{k}_0$.

The present model assumes a scalar radiation field, disregarding polarization effects. This approximation can result in an inaccurate description of the scattered light and/or the radiation force among the atoms, particularly, in the case of a 3D atomic distribution. However, a full derivation of the vectorial light model (not presented here) shows that the scalar light model describes correctly the long-range contribution—i.e., the first term of the force on the right-hand side term of Eq. (2)—for a pump linearly polarized in a direction perpendicular to the scattering plane. Differences between the vectorial and the scalar light models arise only in the short-range terms of the radiation force, which are less important in the collective recoil regime considered here. A detailed study of collective scattering using the vectorial light model will be the subject of a future publication.

Simulation algorithm

Due to the form of Eqs. (1) and (2), it is possible to simulate collective light scattering using a MD code. We used the PEPC [8], which is commonly used for simulating N-body systems where the forces involved are described by an inverse-square law, e.g., Coulomb forces in plasmas and gravitational forces. In order to model collective scattering of light by atoms, we implemented Eq. (2) as the force acting on each atom and observed the trajectories of the particles. Since the equations only depend on the positions of the particles, the force for each iteration was calculated using the position Verlet algorithm, which updates the position of each atom according to

$$\mathbf{r}_{n+1} = 2\mathbf{r}_n - \mathbf{r}_{n-1} + \mathbf{a}_n\Delta t^2, \tag{5}$$

where $\mathbf{a}_n$ is the acceleration at time-step n. The Verlet integrator provides good numerical stability as well as other properties that are important in physical systems, such as time reversibility and preservation of the symplectic form in phase space. The form of the model equations shows a singularity when the particles are close to each other. This becomes an important issue during the simulation since it results in strong forces appearing abruptly, causing the particles to be ejected from the cloud, i.e., two atoms repel one another violently when they get too close to each other. We solved this problem using the idea of Plummer [30], which is used in gravitational force simulations, and involves making the replacement,

$$r_{jm} \to \sqrt{r_{jm}^2 + \epsilon^2}, \tag{6}$$

where ϵ is a small parameter introduced in order to avoid singularities in the equations. This parameter does not change the general behavior of the system when the particles are well separated. It just allows the particles to pass each other as if they were experiencing an elastic collision characterized by the parameter (ϵ), which, in some sense, acts as a numerical scattering length. This collision could be interpreted as a repulsion generated due to van der Waals forces between a pair of atoms.

The equations have been scaled in order to work with dimensionless variables. Positions have been scaled, such as $\mathbf{r}' = k_0\mathbf{r}$; the momentum variable as $\mathbf{p}' = \mathbf{p}p_0^{-1}$, where $p_0 = \hbar k_0$ is the momentum of a single photon; and the time variable, such as $t' = \omega_r t$, where $\omega_r = \hbar k_0^2/2M$ is the recoil frequency. Introducing these variables into the equations of motion (1) and (2), we obtain equations,

$$\dot{\mathbf{r}}'_j = 2\mathbf{p}'_j, \tag{7}$$

$$\dot{\mathbf{p}}'_j = A\sum_{m\neq j}\left\{(\hat{\mathbf{z}} - \hat{\mathbf{r}}_{jm})\frac{\sin[r'_{jm} - z'_{jm}]}{r'_{jm}} - \hat{\mathbf{r}}_{jm}\frac{\cos[r'_{jm} - z'_{jm}]}{(r'_{jm})^2}\right\}, \tag{8}$$

with

$$A = \frac{\Gamma}{\omega_r}\left(\frac{\Omega_0}{2\Delta_0}\right)^2, \tag{9}$$

and $r'_{jm} \rightarrow \sqrt{r'_{jm} + \epsilon'^2}$ where the singularity-avoiding parameter becomes $\epsilon' = k_0\epsilon$.

The value of the singularity-avoiding parameter used in our simulations was $\epsilon' = 10^{-2}$. This implies that the atoms in our simulation have an effective scattering length of $\sim 10^{-2}\lambda_0$, where $\lambda_0 = 2\pi/k_0$ is the laser wavelength. Regarding other important variables, we have used $\omega_r \approx 10^4$ s^{-1} as the recoil frequency, $\Gamma \approx 10^7$ s^{-1} for the atomic decay rate, and we have selected $A = 1.0$ for simplicity. By choosing these values, we roughly achieve that $\Delta_0 \approx 15\Omega_0$, hence, fulfilling the necessary conditions of the model. For both simulations in 2D, we have adopted a time-step $\delta t' = 0.15\times10^{-3}$ with 2000 steps, which makes a total simulation time of $t = 0.3\omega_r^{-1}$. Instead, for the simulations in 3D, the selected step is $\delta t' = 0.25\times10^{-3}$ with 7000 steps, which, in turn, corresponds to a total time of $t = 1.75\omega_r^{-1}$.

III. RESULTS

A. Simulations of the scattering from a 2D atomic cloud

In this section, we restrict ourselves to a simplified configuration where the atomic distribution is two dimensional, consisting of two geometries: an ellipse (Secs. III A 1 and III A 2) and a circle (Sec. III A 3) with both distributions being contained on the (x, z) plane. It is well known from experimental studies of superradiance and superfluorescence, both in excited atomic systems of effectively stationary atoms [31] and in BECs [14,15,32], that the geometry of the atomic cloud or sample can have a significant effect on the spatial distribution of the emitted field. We will demonstrate that the spatial distribution of both the scattered radiation and the associated atomic density distribution, which is produced during collective scattering of light, are also strongly affected by the geometry of the atomic cloud.

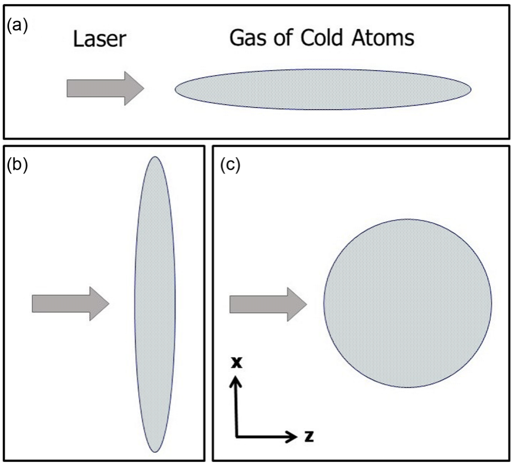

FIG. 1. Schema of the three different configurations used in our simulations. (a) Elliptical- (cigar-) shaped gas of atoms with a major axis directed parallel to the propagation direction of the laser. (b) Elliptical gas with the major axis orientated perpendicular to the propagation direction of the laser. (c) Circular-shaped atomic gas.

1. *Pump propagation parallel to the major axis of an elliptical cloud: Backscattering and one-dimensional grating formation*

The first case we examine is that of an elliptical atomic cloud illuminated by an optical pump field whose propagation direction is parallel to the major axis of the cloud as shown schematically in Fig. 1(a). Figure 2(a) shows the initial random distribution of atoms in the atomic cloud. As a consequence of the optical forces arising from Rayleigh scattering,

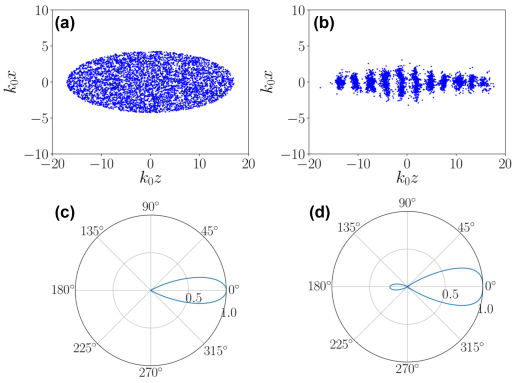

FIG. 2. Simulation of collective scattering of a pump laser propagating parallel to the major axis of an elliptical 2D atomic cloud: (a) Initial atomic density distribution showing $N \approx 5000$ particles distributed randomly. (b) Density grating formation due to collective scattering at $t = 0.135\omega_r^{-1}$. The corresponding bunching factors $|M(\mathbf{k}, t)|$ are shown in (c) at $t = 0$ and in (d) at $t = 0.135\omega_r^{-1}$.

this initially random spatial distribution of atoms develops a strong periodic modulation along the z direction with a spatial period $\approx\lambda/2$ as shown in Fig. 2(b). Consequently, the atomic cloud undergoes the spontaneous formation of a one-dimensional (1D) density grating, analogous to the ones occurring in CARL or a free-electron laser (FEL). Observing Fig. 2(d), we conclude that the 1D grating forms because light is predominantly backscattered due to the geometry of the atomic cloud, which leads to scattering along the cloud's major axis in both $\pm z$ directions. Light which is forward scattered in the $+z$ direction will not produce an optical force on an atom as there is no change in the photon momentum during scattering. We remember that we have neglected the effect of the scattering force in the limit of large detuning $\Delta_0 \gg \Gamma$ (see Appendix), which eventually pushes the atoms in the direction of the pump [33]. Conversely, light backscattered along the $-z$ direction produces an optical force on an atom as the optical field propagation direction and, consequently, momentum changes during the scattering process. This change in momentum of the optical field is taken up by an atom, moving it and modifying the atomic density. The backscattered light interferes with the pump field to form a 1D optical potential with a spatial period of $\approx\pi/k_0$, that has an amplitude and a position which evolve dynamically and consistently with the developing atomic density modulation.

The forward lobe of the scattered intensity in Fig. 2(c) is the result of the diffraction by the atoms in the initial distribution. For a uniform ellipse with semiaxes R_x and R_z, the bunching factor $|M(\theta,\phi)|$ is

$$|M(\theta,\phi)| = \frac{2J_1\left[k_0\sqrt{R_x^2\sin^2\theta\,\cos^2\phi + R_z^2(1-\cos\theta)^2}\right]}{k_0\sqrt{R_x^2\sin^2\theta\,\cos^2\phi + R_z^2(1-\cos\theta)^2}}, \tag{10}$$

where we assumed $\mathbf{k} = k_0(\sin\theta\cos\phi, \sin\theta\sin\phi, \cos\theta)$, $\mathbf{k}_0 = k_0\hat{\mathbf{z}}$, and $J_1(x)$ is the first-order Bessel function. The majority of the emission is within the diffraction angle $\Delta\theta \sim 1/(k_0R_x)$.

2. Pump propagation perpendicular to the major axis of an elliptical cloud: off-axis scattering

We now consider the case where the optical pump field propagates perpendicular to the major axis of the elliptical atomic cloud as shown schematically in Fig. 1(b). The initial random distribution of atoms in the atomic cloud is shown in Fig. 3(a). In this case, the initially random distribution of atoms again develops a strong periodic modulation and forms a density grating, but in contrast to the previous case of Sec. III A 1, this grating is now no longer restricted to the z axis but is a 2D structure on the (x,z) plane. Figures 3(c) and 3(d) show that the 2D grating forms because the geometry of the atomic cloud, which leads to significant scattering perpendicular to the pump propagation direction along the major axis of the atomic cloud in both $\pm x$ directions. Scattering of light along the $\pm x$ directions will produce an optical force on an atom directed at approximately $\mp 45^\circ$ to the z axis. This can be understood using a photon picture of a scattering event which involves an incident photon with momentum $(\hbar k_0)\hat{\mathbf{z}}$ and results in a scattered photon of momentum $\pm(\hbar k_0)\hat{\mathbf{x}}$. This results in a net momentum change of the atom of $\hbar k_0(\hat{\mathbf{z}} \mp \hat{\mathbf{x}})$, i.e., directed at approximately $\mp 45^\circ$ to the z axis, depending whether the photon is emitted upward or downward, respectively. This scattered light interferes with the pump field to form a dynamically evolving 2D optical lattice potential [19]. An atomic density distribution similar to that shown in Fig. 3(b) was observed by Inouye *et al.* [14] for the case of an elongated elliptical BEC, illuminated by a pump beam propagating perpendicular to its major axis. Whereas, in the experiment of Ref. [14], the grating is observed in momentum space after the interaction with the pump laser; here, the grating is observed in real space.

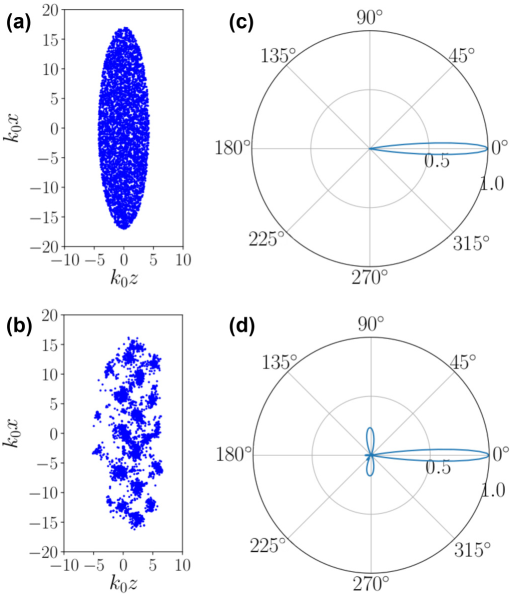

FIG. 3. Simulation of collective scattering of a pump laser propagating perpendicular to the major axis of a 2D elliptical atomic cloud: (a) Initial atomic density distribution showing $N \approx 5000$ particles distributed randomly. (b) Density grating formation due to collective scattering at $t = 0.159\omega_r^{-1}$. The corresponding bunching factors $|M(\mathbf{k},t)|$ are shown in (c) at $t = 0$ and in (d) at $t = 0.159\omega_r^{-1}$.

3. Scattering from a circular atomic distribution

We now consider the light scattering from the circular 2D distribution shown in Fig. 1(c). Since now there is not any preferred scattering direction, we would expect to observe no density grating in this case. Instead, we can still see the formation of a 2D grating due to a periodic modulation. Observing the polar plot that represents the bunching parameter for this configuration, Figs. 4(c) and 4(d), we can see that, at a certain time, the cloud scatters light in two directions at approximately $\pm 45^\circ$ from the backward direction. This can be interpreted taking into consideration the deformation of the initially round distribution. It can be observed in Fig. 4(b) that

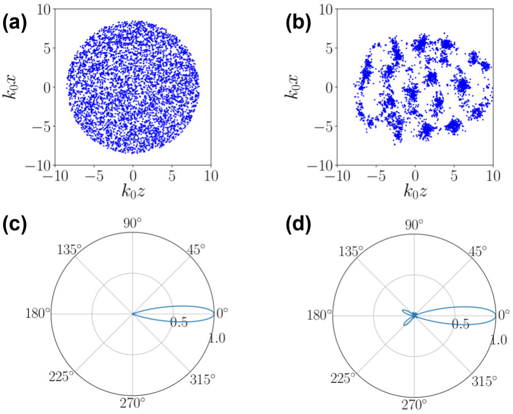

FIG. 4. Simulation of collective light scattering from a 2D circular atomic cloud: (a) Initial atomic distribution showing $N \approx 5000$ particles distributed randomly. (b) Atomic distribution at $t = 0.22\omega_r^{-1}$. The corresponding bunching factors $|M(\mathbf{k}, t)|$ are shown in (c) at $t = 0$ and in (d) at $t = 0.22\omega_r^{-1}$.

the atoms close to the z axis and on the right edge of the initial distribution are pushed forward by the pump laser, making the atomic cloud form an "egglike" shape. Since scattered light is preferentially amplified along the longest propagation path in the cloud, this path results in being along the edges of the egglike shape formed after an initial transient time. If we look at the deformed shape in Fig. 4(b) as if it was a triangle with two equal angles (located at the negative plane of the z axis) and a third one (placed on the positive z axis) that would identify the angle between the two scattered light directions. Naming θ the angle of the scattered light direction with respect to the z axis, we still interpret a scattering event using a photon picture: The incident photon with momentum $\mathbf{q}_{\rm in} = \hbar k_0\hat{\mathbf{z}}$ is scattered in the directions $\pm\theta$ as a photon of momentum $\mathbf{q}_\pm = \hbar k_0[\hat{\mathbf{z}}\cos\theta \pm \hat{\mathbf{x}}\sin\theta]$, respectively. The atomic recoil momentum is

$$\Delta\mathbf{p} = \mathbf{q}_{\rm in} - \mathbf{q}_\pm = \hbar k_0[\hat{\mathbf{z}}(1 - \cos\theta) \mp \hat{\mathbf{x}}\sin\theta], \qquad (11)$$

with an angle ϕ with respect to the $\mathbf{z}$ axis given by

$$\tan\phi = \mp\frac{\sin\theta}{1 - \cos\theta}. \qquad (12)$$

The previous cases of horizontal and vertical ellipses, shown in Figs. 2 and 3, correspond to $\theta = \pi$ and $\theta = \pi/2$, respectively. For the case of circular distribution, we estimated from Fig. 4(d), the scattering angle to be $\theta \approx 135°$. Using this value in Eq. (12), we obtained two crossed lattices, respectively. oriented at $\phi = \mp 22.5°$ with respect to the z axis, in qualitative agreement with Fig. 4(b). The shape deformation of the atomic distribution observed here is similar to the electrostrictive effect described in Ref. [34] for a BEC illuminated by laser light. We postpone the study of this rather surprising effect to a more extended 2D and 3D investigation, which will take into account also the vectorial character of the scattered light.

B. Three-dimensional simulation of scattering

In this section, we relax the assumption of a 2D distribution of atoms and consider a full 3D case. The computational effort required to model large systems of atoms in 3D is substantially greater than in 2D, so the efficiency of the computational methods used becomes more significant. Equations (7) and (8) are explicit equations whose solution does not require inversion of large matrices nor the use of a mesh, which is attractive from the viewpoint of run time of numerical simulations. In addition, use of a code such as PEPC to solve Eqs. (7) and (8) offers the potential for improved scalability to large 3D simulations involving extremely large numbers of over a "brute-force" solution of Eqs. (7) and (8). This is due to the fact that PEPC is designed to use tree algorithms (e.g., Ref. [18]) originally designed for astrophysical N-body simulations, which reduce the computational effort or run time associated with the calculations from $O(N^2)$ to $O[N\ln(N)]$. As an illustrative example, we study a 3D atomic sample, analogous to the system configuration considered in Sec. III A 1 with the

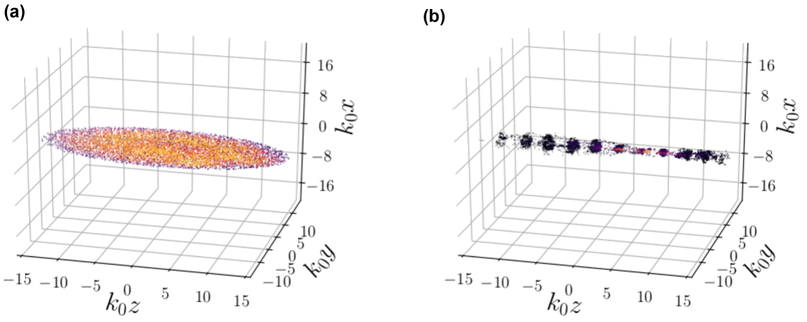

FIG. 5. Numerical simulations in 3D: (a) Initial disposition of particles in a cloud of particles. (b) One-dimensional grating formation in the case of laser propagation parallel to the major axis of the cloud of atoms at $t = 0.21\omega_r^{-1}$. In the simulation, we have used $N \approx 10\,000$ particles distributed randomly in space.

pump propagation parallel to the major axis of the cloud with a cigar-shaped distribution—see Fig. 5(a). Again, we have the atoms initially randomly distributed within the cloud. After a time $t = 0.21\omega_r^{-1}$, we observe the formation of a longitudinal density grating along the z axis, depicted in Fig. 5(b), similar to the one observed in the 2D simulation. We outline again that the scalar model of light used for the 3D simulations gives only an approximated description of the scattering so that a full vectorial model is required for an accurate description of the scattering. However, preliminary results show that, for a very elongated atomic cloud and the pump propagating along the major axis of the cloud, the scalar model describes correctly the long-range term of the exact force but not its short-range terms. Since we assume a dilute system where multiple scattering is negligible, short-range terms in the force play a minor role, and the collective recoil scattering is dominated by long-range interactions. For these reasons, the scalar model is able to reproduce the mean features of the collective atomic recoil lasing in free space.

Finally, we make some comment about the scaling laws with N and the size of the atomic cloud. In our 3D simulation, the number of atoms is $N = 10^4$, and the semiaxis of the ellipsoidal are $k_0R_x = k_0R_y \sim 5$ and $k_0R_z \sim 15$, corresponding to a volume of $V \sim 6\lambda_0^3$ which, for $\lambda_0 = 780$ nm as for the Rb atoms, conforms to a rather unrealistic density of $n \sim 10^{15}$ atoms/cm^3 and a resonant optical thickness of $b \sim N/(k_0^2R_xR_y) \sim 400$, which is large but not unreachable. Hence, it is important to know how the superradiant scattering rate scales with N and the atomic system size. It results from a single-mode theory [19] that the superradiant scattering rate is $\Gamma_{\rm SR} \sim (\Omega_0/\Delta_0)\sqrt{\Gamma\omega_r N/(k_0R_x)^2}$, i.e., it scales with the square root of the optical thickness. Hence, a realistic atomic cloud with $N \sim 10^6$ and transverse size $k_0R_x \sim 50$ would have the same optical thickness and, hence, the same superradiant rate of the simulation shown in Fig. 5. For $\Omega_0/\Delta_0 = 1/15$, $N = 10^6$, $k_0R_x = 50$, $\omega_r \sim 10^4$ rad/s, and $\Gamma = (2\pi)\ 6$ MHz, then $\Gamma_{\rm SR} \sim 10^6$ 1/s, which is much more than the two-photon recoil $4\omega_r$ and so satisfying the condition for the classical regime of superradiant scattering [35]. The initial velocity spread is negligible if $2k\sigma_v \ll \Gamma_{\rm SR}$ or, equivalently, $T_0 \ll \hbar\Gamma_{\rm SR}^2/(8k_B\omega_r)$, where $T_0 = M\sigma_v^2/k_B$ is the initial temperature and k_B is Boltzmann's constant. For Rb atoms and $\Gamma_{\rm SR} = 10^6$ 1/s, the initial temperature must be much less than 100 μK.

IV. CONCLUSIONS

We have presented a model which describes collective scattering of light in 2D and 3D due to a gas of cold atoms in vacuum that depends only on the positions of the atoms, making it suitable for implementation using a MD simulation code. Using the public MD code PEPC, we were able to follow the trajectories of the atoms and calculate the spatial and temporal evolutions of the intensity of the scattered light. The 2D simulations show that the evolution of collective scattering by an elliptical atomic cloud is sensitive to the orientation of the cloud relative to the pump field propagation direction. When the major axis of the cloud is aligned parallel to the pump propagation direction, the simulation showed the formation of a 1D grating in the density of the atoms, analogous to that occurring in CARL or a FEL, which enhances the backscattered light. In contrast, when the major axis of the cloud is oriented perpendicular to the pump propagation direction, a 2D pattern formation, similar to that observed in superradiant scattering experiments of Ref. [14], was observed; in both cases, the collectively scattered radiation propagates predominantly along the major axis of the cloud. In the intermediate case of a circular cloud, it was demonstrated that the force produced by the collective scattering process is electrostrictive in nature, leading to elongation of the cloud along the pump propagation direction, simultaneous with the development of a 2D grating. As an example of the capabilities of the code and the method we used, we have also been able to produce 3D simulations of the collective scattering process. As the importance of polarization effects can be significant for 3D scattering, an extension of the present scalar model of light scattering to a vectorial model, simulating the 3D collective scattering from different atomic distributions and orientations of the pump, is in preparation.

ACKNOWLEDGMENTS

This work was performed in the framework of the European Training Network ColOpt, which is funded by the European Union (EU) Horizon 2020 Programme under the Marie Sklodowska-Curie Action, Grant Agreement No. 721465. R.A. thanks Fundação para a Ciência e Tecnologia (FCT-Portugal) through the Ph.D. Grant No. PD/BD/105875/2014 (PD-F APPLAuSE).

APPENDIX: DERIVATION OF THE MOTION EQUATIONS

1. Multimode collective recoil equations

We consider the Hamiltonian of N two-level atoms with atomic frequency ω_a and dipole d, interacting with a laser field and the vacuum radiation modes,

$$H = \sum_{j=1}^{N}\frac{\mathbf{p}_j^2}{2M} + \hbar\sum_{j=1}^{N}\left[\frac{\Omega_0^*}{2}\sigma_j^- e^{i\,\Delta_0 t - i\mathbf{k}_0\cdot\mathbf{r}_j} + \text{Hc.}\right] + \hbar\sum_{j=1}^{N}\sum_{\mathbf{k}} g_k\big[a_{\mathbf{k}}^\dagger\sigma_j^- e^{i\,\Delta_k t - i\mathbf{k}\cdot\mathbf{r}_j} + \sigma_j^+ a_{\mathbf{k}} e^{-i\,\Delta_k t + i\mathbf{k}\cdot\mathbf{r}_j}\big]. \tag{A1}$$

Here $\Omega_0 = dE_0/\hbar$ is the Rabi frequency of the laser with electric-field E_0, wave-vector $\mathbf{k}_0$, and frequency ω_0 with detuning $\Delta_0 = \omega_0 - \omega_a$. The quantum radiation modes in vacuum with wave-vectors $\mathbf{k}$ and frequency ω_k are described by the operators $a_{\mathbf{k}}$ with $\Delta_k = \omega_k - \omega_a$ with coupling rate $g_k = d[\omega_k/(2\hbar\epsilon_0 V_{\rm ph})]^{1/2}$, and $V_{\rm ph}$ is the quantization volume of the radiation field. We disregard polarization and short-range effects using a scalar model for the radiation field. The internal dynamics of the two-level atoms are described by the operators $\sigma_j^z = |e_j\rangle\langle e_j| - |g_j\rangle\langle g_j|$, $\sigma_j^+ = |e_j\rangle\langle g_j|$, and $\sigma_j^- = |g_j\rangle\langle e_j|$. Furthermore, we also consider the dynamics of the external degrees of freedom, where $\mathbf{r}_j$ and $\mathbf{p}_j$ are operators. The Heisenberg equations are as follows:

$$\dot{\mathbf{r}}_j = \frac{\mathbf{p}_j}{M}, \tag{A2}$$

$$\dot{\mathbf{p}}_j = -\nabla_{\mathbf{r}_j} H = i\hbar\mathbf{k}_0\left[\frac{\Omega_0^*}{2}\sigma_j^- e^{i\Delta_0 t - i\mathbf{k}_0\cdot\mathbf{r}_j} - \text{H.c.}\right] + i\hbar\sum_{\mathbf{k}}\mathbf{k}g_k\big[a_{\mathbf{k}}^\dagger\sigma_j^- e^{i\Delta_k t - i\mathbf{k}\cdot\mathbf{r}_j} - \text{H.c.}\big], \tag{A3}$$

$$\dot{\sigma}_j^- = \frac{i\Omega_0}{2}e^{-i\Delta_0 t + i\mathbf{k}_0\cdot\mathbf{r}_j}\hat{\sigma}_j^z + i\sum_{\mathbf{k}} g_k\sigma_j^z a_{\mathbf{k}} e^{-i\Delta_k t + i\mathbf{k}\cdot\mathbf{r}_j}, \tag{A4}$$

$$\dot{\sigma}_j^z = i\Omega_0^* e^{i\Delta_0 t - i\mathbf{k}_0\cdot\mathbf{r}_j}\sigma_j^- + 2i\sum_{\mathbf{k}} g_k a_{\mathbf{k}}^\dagger\sigma_j^- e^{i\Delta_k t - i\mathbf{k}\cdot\mathbf{r}_j} + \text{H.c.}, \tag{A5}$$

$$\dot{a}_{\mathbf{k}} = -ig_k\sum_{j=1}^{N}\sigma_j^- e^{i\Delta_k t - i\mathbf{k}\cdot\mathbf{r}_j}. \tag{A6}$$

Introducing $\sigma_j = \sigma_j^- e^{i\Delta_0 t}$ and neglecting the population of the excited state (assuming weak field and/or large detuning Δ_0) so that $\sigma_j^z \approx -1$,

$$\dot{\mathbf{r}}_j = \frac{\mathbf{p}_j}{M}, \tag{A7}$$

$$\dot{\mathbf{p}}_j = i\hbar\mathbf{k}_0\left[\frac{\Omega_0^*}{2}\sigma_j e^{-i\mathbf{k}_0\cdot\mathbf{r}_j} - \text{H.c.}\right] + i\hbar\sum_{\mathbf{k}}\mathbf{k}g_k\big[a_{\mathbf{k}}^\dagger\sigma_j e^{i(\omega_k-\omega_0)t - i\mathbf{k}\cdot\mathbf{r}_j} - \text{H.c.}\big], \tag{A8}$$

$$\dot{\sigma}_j = (i\Delta_0 - \Gamma/2)\sigma_j - \frac{i\Omega_0}{2}e^{i\mathbf{k}_0\cdot\mathbf{r}_j} - i\sum_{\mathbf{k}} g_k a_{\mathbf{k}} e^{-i(\omega_k-\omega_0)t + i\mathbf{k}\cdot\mathbf{r}_j}, \tag{A9}$$

$$\dot{a}_{\mathbf{k}} = -ig_k e^{i(\omega_k-\omega_0)t}\sum_{j=1}^{N}\sigma_j e^{-i\mathbf{k}\cdot\mathbf{r}_j}, \tag{A10}$$

where we added the spontaneous emission decay term $-(\Gamma/2)\sigma_j$ with $\Gamma = d^2k^3/2\pi\epsilon_0\hbar$ as the spontaneous decay rate. Assuming $\Gamma \gg \omega_{\text{rec}}$, where $\omega_{\text{rec}} = \hbar k^2/2M$ is the recoil frequency, we can adiabatically eliminate the internal degree of freedom, taking $\dot{\sigma}_j \approx 0$ in Eq. (A9),

$$\sigma_j \approx \frac{\Omega_0}{2(\Delta_0 + i\Gamma/2)}e^{i\mathbf{k}_0\cdot\mathbf{r}_j} + \frac{1}{\Delta_0 + i\Gamma/2}\sum_{\mathbf{k}} g_k a_{\mathbf{k}} e^{-i(\omega_k-\omega_0)t + i\mathbf{k}\cdot\mathbf{r}_j}. \tag{A11}$$

The first term describes the dipole excitation induced by the driving field, whereas the second term is the excitation induced by the scattered field. By inserting it in Eq. (A10), the field equation, we obtain

$$\dot{a}_{\mathbf{k}} = -i\frac{g_k\Omega_0}{2(\Delta_0 + i\Gamma/2)}e^{i(\omega_k-\omega_0)t}\sum_{j=1}^{N}e^{i(\mathbf{k}_0-\mathbf{k})\cdot\mathbf{r}_j} - i\frac{g_k}{\Delta_0 + i\Gamma/2}\sum_{j=1}^{N}\sum_{\mathbf{k}'} g_{k'}a_{\mathbf{k}'}e^{i(\omega_k-\omega_{k'})t - i(\mathbf{k}-\mathbf{k}')\cdot\mathbf{r}_j}. \tag{A12}$$

The first term describes the single-scattering process where the momentum transfer to the atoms is from the incident field to the vacuum field. The second term describes multiple-scattering processes where a photon is exchanged between mode **k** and all the other modes **k**′. We limit our analysis to single-scattering processing, neglecting the second term in Eq. (A12). We also insert Eq. (A11) in the force equation (A8),

$$\dot{\mathbf{p}}_j = -\frac{i\hbar}{\Delta_0 - i\Gamma/2}\left[\mathbf{k}_0\frac{\Omega_0}{2}e^{i\mathbf{k}_0\cdot\mathbf{r}_j} + \sum_{\mathbf{k}}\mathbf{k}g_k a_{\mathbf{k}} e^{i\mathbf{k}\cdot\mathbf{r}_j - i(\omega_k-\omega_0)t}\right]\left[\frac{\Omega_0^*}{2}e^{-i\mathbf{k}_0\cdot\mathbf{r}_j} + \sum_{\mathbf{k}} g_k a_{\mathbf{k}}^\dagger e^{-i\mathbf{k}\cdot\mathbf{r}_j + i(\omega_k-\omega_0)t}\right] + \text{H.c.} \tag{A13}$$

The first and second terms in the first squared brackets describe the absorption of an incident photon with momentum $\hbar\mathbf{k}_0$ and a scattered photon with momentum $\hbar\mathbf{k}$, respectively. The second squared brackets are the response of the atom, i.e., the induced polarization of the atoms to the total radiation. Explicitly, we write

$$\begin{aligned}\dot{\mathbf{p}}_j = {}&\left[\frac{\Gamma\Omega_0^2}{4\Delta_0^2 + \Gamma^2}\right]\hbar\mathbf{k}_0 + \frac{2i\Delta_0}{4\Delta_0^2 + \Gamma^2}\sum_{\mathbf{k}}\hbar(\mathbf{k}_0 - \mathbf{k})g_k\big[\Omega_0^* a_{\mathbf{k}} e^{-i(\mathbf{k}_0-\mathbf{k})\cdot\mathbf{r}_j - i(\omega_k-\omega_0)t} - \text{H.c.}\big]\\ &+ \frac{\Gamma}{4\Delta_0^2 + \Gamma^2}\sum_{\mathbf{k}}\hbar(\mathbf{k}_0 + \mathbf{k})g_k\big[\Omega_0^* a_{\mathbf{k}} e^{-i(\mathbf{k}_0-\mathbf{k})\cdot\mathbf{r}_j - i(\omega_k-\omega_0)t} + \text{H.c.}\big]\\ &+ \frac{1}{\Delta_0^2 + \Gamma^2/4}\sum_{\mathbf{k}}\sum_{\mathbf{k}'} g_k g_{k'}\hat{a}_{\mathbf{k}}^\dagger\hat{a}_{\mathbf{k}'}e^{i(\mathbf{k}'-\mathbf{k})\cdot\mathbf{r}_j}[i\Delta_0\hbar(\mathbf{k} - \mathbf{k}') + (\Gamma/2)\hbar(\mathbf{k} + \mathbf{k}')].\end{aligned} \tag{A14}$$

Note that the first term is the radiation pressure exerted by the incident light (which is constant for a plane wave); the second and third terms describe the momentum transfer due to the exchange of photons between the incident and the scattered light. The last term is the contribution due to the exchange between two scattered vacuum photons of momentum $\hbar\mathbf{k}$ and $\hbar\mathbf{k}'$. Again, since we neglect multiple-scattering events, we drop the last term. Then, we assume $\Delta_0 \gg \Gamma$ so that the first and the third terms of Eq. (A14) are negligibly small, thus, achieving

$$\dot{\mathbf{p}}_j \approx \frac{i}{2\Delta_0}\sum_{\mathbf{k}} \hbar(\mathbf{k}_0-\mathbf{k})g_k\big[\Omega_0^* a_{\mathbf{k}} e^{-i(\mathbf{k}_0-\mathbf{k})\cdot\mathbf{r}_j - i(\omega_k-\omega_0)t} - \text{H.c.}\big]. \tag{A15}$$

The force on the atoms is the usual dipole (or gradient) force where the momentum transfer is maximum for backscattering emission (i.e., $\mathbf{k} = -\mathbf{k}_0$). In conclusion, the multimode equations describing the collective recoil are as follows:

$$\dot{\mathbf{r}}_j = \frac{\mathbf{p}_j}{M}, \tag{A16}$$

$$\dot{\mathbf{p}}_j = i\hbar g\sum_{\mathbf{k}}(\mathbf{k}_0-\mathbf{k})\big[A_{\mathbf{k}} e^{-i(\mathbf{k}_0-\mathbf{k})\cdot\mathbf{r}_j} - A_{\mathbf{k}}^\dagger e^{i(\mathbf{k}_0-\mathbf{k})\cdot\mathbf{r}_j}\big], \tag{A17}$$

$$\dot{A}_{\mathbf{k}} = -ig\sum_{j=1}^{N} e^{i(\mathbf{k}_0-\mathbf{k})\cdot\mathbf{r}_j} - i\delta_k A_{\mathbf{k}}, \tag{A18}$$

where $A_{\mathbf{k}} = a_{\mathbf{k}}e^{-i\delta_k t},\ \delta_k = \omega_k - \omega_0$, and $g = g_{k_0}(\Omega_0/2\Delta_0)$; we assumed $g_k \approx g_{k_0}$ and Ω_0 real.

2. Collective recoil equations in free space

In free space, the light is scattered in the 3D vacuum modes. Following Ref. [16], we eliminate the scattered field by integrating Eq. (A18) to obtain

$$A_{\mathbf{k}}(t) = A_{\mathbf{k}}(0)e^{-i(\omega_k-\omega_0)t} - igN\int_0^t \rho_{\mathbf{k}_0-\mathbf{k}}(t-\tau)e^{-i(\omega_k-\omega_0)\tau}d\tau, \tag{A19}$$

with

$$\rho_{\mathbf{q}}(t) = \frac{1}{N}\sum_{j=1}^{N} e^{i\mathbf{q}\cdot\mathbf{r}_j(t)}. \tag{A20}$$

The first term in Eq. (A19) gives the free electromagnetic field, i.e., vacuum fluctuations, and the second term is the radiation field due to Rayleigh scattering. If Eq. (A19) is substituted into Eq. (A17) for $\mathbf{p}_j$, we obtain

$$\dot{\mathbf{p}}_j = \hbar g^2 N\sum_{\mathbf{k}}(\mathbf{k}_0-\mathbf{k})\int_0^t d\tau\big[\rho_{\mathbf{k_0}-\mathbf{k}}(t-\tau)e^{-i(\mathbf{k}_0-\mathbf{k})\cdot\mathbf{r}_j}e^{-i(\omega_k-\omega_0)\tau} + \text{H.c.}\big], \tag{A21}$$

where the first term of Eq. (A19) has been neglected. Then, transforming the sum over $\mathbf{k}$ into an integral and using Eq. (A20), we attain the coming expression,

$$\dot{\mathbf{p}}_j = \hbar g^2\frac{V_{\text{ph}}}{8\pi^3}\sum_{m\neq j}\left[e^{-i\mathbf{k}_0\cdot(\mathbf{r}_j-\mathbf{r}_m)}\int_0^t d\tau\, e^{i\omega_0\tau}\int d\mathbf{k}(\mathbf{k}_0-\mathbf{k})e^{i\mathbf{k}\cdot(\mathbf{r}_j-\mathbf{r}_m)}e^{-ick\tau} + \text{H.c.}\right], \tag{A22}$$

in which we used the Markov approximation so that $\mathbf{r}_j(t-\tau) \approx \mathbf{r}_j(t)$. The integral over $\mathbf{k}$, in the latter equation, can be manipulated as follows:

$$\int d\mathbf{k}(\mathbf{k}_0-\mathbf{k})e^{i\mathbf{k}\cdot(\mathbf{r}_j-\mathbf{r}_m)}e^{-ick\tau} = 4\pi\mathbf{k}_0\int_0^\infty dk\,k^2\frac{\sin(kr_{jm})}{kr_{jm}}e^{-ick\tau} + 4i\pi\hat{\mathbf{r}}_{jm}\int_0^\infty dk\,k^3\left[\frac{\cos(kr_{jm})}{kr_{jm}} - \frac{\sin(kr_{jm})}{(kr_{jm})^2}\right]e^{-ick\tau} \tag{A23}$$

being $\mathbf{r}_{jm} = \mathbf{r}_j - \mathbf{r}_m,\ r_{jm} = |\mathbf{r}_{jm}|$, and $\hat{\mathbf{r}}_{jm} = \mathbf{r}_{jm}/r_{jm}$. Since $k \approx k_0$, we can replace k by k_0 in the integrals; we also extend the lower integration limit to $-\infty$, reaching the next expression,

$$\begin{aligned}\int d\mathbf{k}(\mathbf{k}_0-\mathbf{k})e^{i\mathbf{k}\cdot(\mathbf{r}_j-\mathbf{r}_m)}e^{-ick\tau} &\approx 4\pi k_0^3\frac{\hat{\mathbf{z}}}{k_0r_{jm}}\int_{-\infty}^\infty dk\,\sin(kr_{jm})e^{-ick\tau} + 4i\pi k_0^3\frac{\hat{\mathbf{r}}_{jm}}{k_0r_{jm}}\int_{-\infty}^\infty dk\left[\cos(kr_{jm}) - \frac{\sin(kr_{jm})}{k_0r_{jm}}\right]e^{-ick\tau}\\ &= \frac{4\pi^2k_0^3}{c}\left\{\frac{\hat{\mathbf{z}}}{ik_0r_{jm}}[\delta(\tau-r_{jm}/c)-\delta(\tau+r_{jm}/c)] - \frac{\hat{\mathbf{r}}_{jm}}{ik_0r_{jm}}[\delta(\tau-r_{jm}/c)+\delta(\tau+r_{jm}/c)]\right.\\ &\quad\left.-\frac{\hat{\mathbf{r}}_{jm}}{(k_0r_{jm})^2}[\delta(\tau-r_{jm}/c)-\delta(\tau+r_{jm}/c)]\right\},\end{aligned} \tag{A24}$$

where we assumed $\mathbf{k}_0 = k_0\hat{\mathbf{z}}$ and used the following two integrals:

$$\int_{-\infty}^{\infty} dk\,\sin(kR)e^{-ick\tau} = \frac{\pi}{ic}[\delta(\tau - R/c) - \delta(\tau + R/c)],$$
$$\int_{-\infty}^{\infty} dk\,\cos(kR)e^{-ick\tau} = \frac{\pi}{c}[\delta(\tau - R/c) + \delta(\tau + R/c)]. \tag{A25}$$

By inserting Eq. (A24) into Eq. (A22), together with the definitions of g and Γ, we are able to derive the final expression for the force,

$$\begin{aligned}\dot{\mathbf{p}}_j &= \frac{\Gamma}{2}\hbar k_0\left(\frac{\Omega_0}{2\Delta_0}\right)^2\sum_{m\neq j}\left[e^{ik_0(r_{jm}-z_{jm})}\left(\frac{(\hat{\mathbf{z}}-\hat{\mathbf{r}}_{jm})}{ik_0r_{jm}} - \frac{\hat{\mathbf{r}}_{jm}}{(k_0r_{jm})^2}\right) + \text{H.c.}\right]\\ &= \Gamma\hbar k_0\left(\frac{\Omega_0}{2\Delta_0}\right)^2\sum_{m\neq j}\left\{(\hat{\mathbf{z}}-\hat{\mathbf{r}}_{jm})\frac{\sin[k_0(r_{jm}-z_{jm})]}{k_0r_{jm}} - \hat{\mathbf{r}}_{jm}\frac{\cos[k_0(r_{jm}-z_{jm})]}{(k_0r_{jm})^2}\right\}.\end{aligned} \tag{A26}$$

3. Radiation field

The scattered radiation field amplitude is

$$E_s(\mathbf{r},t) = i\frac{V_{\text{ph}}}{(2\pi)^3}e^{i(\mathbf{k}_0\cdot\mathbf{r}-\omega_0t)}\int_{\Delta\mathbf{k}} d\mathbf{k}\,\mathcal{E}_kA_{\mathbf{k}}(t)e^{i(\mathbf{k}-\mathbf{k}_0)\cdot\mathbf{r}} \tag{A27}$$

being $\mathcal{E}_k = (\hbar\omega_k/2\epsilon_0V_{\text{ph}})^{1/2}$ the single-photon electric field. Using Eq. (A19), neglecting the fluctuation term and transforming the sum over $\mathbf{k}$ into an integral as performed before, we obtain

$$E_s(\mathbf{r},t) = \frac{V_{\text{ph}}}{(2\pi)^3}ge^{-i\omega_0t}\sum_{j=1}^{N}\int_0^t d\tau\,e^{i\omega_0\tau}e^{i\mathbf{k}_0\cdot\mathbf{r}_j(t-\tau)}\int_0^{\infty}dk\,k\mathcal{E}_k\frac{\sin[k|\mathbf{r}_j(t-\tau)-\mathbf{r}|]}{|\mathbf{r}_j(t-\tau)-\mathbf{r}|}e^{-ick\tau}. \tag{A28}$$

The scattered intensity will be centered about the incidence laser frequency ω_0. The quantity ck varies little around $k = \omega_0/c$ for which the time integral in τ is not negligible. We can, therefore, replace k by ω_0/c and extend the lower limit in the k integration by $-\infty$,

$$E_s(\mathbf{r},t) = \frac{V_{\text{ph}}}{2\pi^2}gk_0\mathcal{E}_{k_0}e^{-i\omega_0t}\sum_{j=1}^{N}\int_0^t d\tau\,e^{i\omega_0\tau+i\mathbf{k}_0\cdot\mathbf{r}_j(t-\tau)}\int_{-\infty}^{\infty}dk\frac{\sin(k|\mathbf{r}_j-\mathbf{r}|)}{|\mathbf{r}_j-\mathbf{r}|}e^{-ick\tau}. \tag{A29}$$

By using Eq. (A26), we obtain

$$E_s(\mathbf{r},t) = \frac{dk_0^3}{4\pi\epsilon_0}\frac{\Omega_0}{2\Delta_0}\sum_{j=1}^{N}\frac{e^{ik_0R_j}}{ik_0R_j}e^{i(\mathbf{k}_0\cdot\mathbf{r}_j-\omega_0t)}\Theta(t > R_j/c), \tag{A30}$$

where $R_j = |\mathbf{r}_j - \mathbf{r}|$ and $\mathbf{r}_j$ is evaluated at the retarded time $t - R_j/c$. Assuming $\mathbf{r} \gg \mathbf{r}_j$, we can write $R_j \approx r - i\hat{\mathbf{r}}\cdot\mathbf{r}_j$ with $\hat{\mathbf{r}} = \mathbf{r}/r$, and

$$E_s(\mathbf{k},t) \approx \frac{dk_0^2}{4\pi\epsilon_0}\frac{\Omega_0}{2\Delta_0}\frac{e^{i(k_0r-\omega_0t)}}{ir}\sum_{j=1}^{N}e^{i(\mathbf{k}_0-\mathbf{k})\cdot\mathbf{r}_j}, \tag{A31}$$

where $\mathbf{k} = k_0\hat{\mathbf{r}}$. We have obtained the expression of the Rayleigh scattering field in the far-field limit, i.e., a spherical wave proportional to the factor form, depending on the geometrical configuration of the scattering particles. For small clouds, we can neglect the retarded time R_j/c. In conclusion, the scattered intensity spatial distribution in the far-field limit is

$$I_s(\mathbf{k}) = I_1N^2|M(\mathbf{k},t)|^2, \tag{A32}$$

in which $I_1 = (\hbar\omega_0\Gamma/8\pi r^2)(\Omega_0/2\Delta_0)^2$ is the single-atom Rayleigh scattering intensity and

$$M(\mathbf{k},t) = \frac{1}{N}\sum_{j=1}^{N}e^{i(\mathbf{k}_0-\mathbf{k})\cdot\mathbf{r}_j(t)} \tag{A33}$$

is the optical magnetization or bunching factor.

---

[1] H. Ritsch, P. Domokos, F. Brennecke, and T. Esslinger, Rev. Mod. Phys. **85**, 553 (2013).

[2] P. Domokos and H. Ritsch, Phys. Rev. Lett. **89**, 253003 (2002).

[3] H. W. Chan, A. T. Black, and V. Vuletič, Phys. Rev. Lett. **90**, 063003 (2003).

[4] M. Hosseini, Y. Duan, K. M. Beck, Y.-T. Chen, and V. Vuletič, Phys. Rev. Lett. **118**, 183601 (2017).

[5] K. Baumann, R. Mottl, F. Brennecke, and T. Esslinger, Phys. Rev. Lett. **107**, 140402 (2011).

[6] E. Tesio, G. R. M. Robb, T. Ackemann, W. J. Firth, and G. L. Oppo, Phys. Rev. A **86**, 031801(R) (2012).

[7] G. Labeyrie, E. Tesio, P. M. Gomes, G. L. Oppo, W. J. Firth, G. R. M. Robb, A. S. Arnold, R. Kaiser, and T. Ackemann, Nat. Photon. **8**, 321 (2014).

[8] G. R. M. Robb, E. Tesio, G. L. Oppo, W. J. Firth, T. Ackemann, and R. Bonifacio, Phys. Rev. Lett. **114**, 173903 (2015).

[9] Y.-C. Zhang, V. Walther, and T. Pohl, Phys. Rev. Lett. **121**, 073604 (2018).

[10] J. A. Greenberg and D. J. Gauthier, Phys. Rev. A **86**, 013823 (2012).

[11] B. L. Schmittberger and D. J. Gauthier, New J. Phys. **18**, 103021 (2016).

[12] T. Grießer and H. Ritsch, Phys. Rev. Lett. **111**, 055702 (2013).

[13] J. T. Mendonça and R. Kaiser, Phys. Rev. Lett. **108**, 033001 (2012).

[14] S. Inouye, A. P. Chikkatur, D. M. Stamper-Kurn, J. Stenger, D. E. Pritchard, and W. Ketterle, Science **285**, 571 (1999).

[15] Y. Yoshikawa, Y. Torii, and T. Kuga, Phys. Rev. Lett. **94**, 083602 (2005).

[16] M. G. Moore and P. Meystre, Phys. Rev. Lett. **83**, 5202 (1999).

[17] R. Bonifacio and L. De Salvo Souza, Nucl. Instrum. Methods Phys. Res., Sect. A **341**, 360 (1994).

[18] R. Bonifacio, L. De Salvo, L. M. Narducci, and E. J. D'Angelo, Phys. Rev. A **50**, 1716 (1994).

[19] N. Piovella, R. Bonifacio, B. W. J. McNeil, and G. R. M. Robb, Opt. Commun. **187**, 165 (2001).

[20] R. Bonifacio, G. R. M. Robb, and B. W. J. McNeil, Phys. Rev. A **56**, 912 (1997).

[21] O. E. Mustecaplioglu and L. You, Phys. Rev. A **62**, 063615 (2000).

[22] O. Zobay and G. M. Nikolopoulos, Phys. Rev. A **72**, 041604(R) (2005).

[23] O. Zobay and G. M. Nikolopoulos, Phys. Rev. A **73**, 013620 (2006).

[24] J. Li, X. Zhou, F. Yang, and X. Chen, Phys. Lett. A **372**, 4750 (2008).

[25] S. Slama, S. Bux, G. Krenz, C. Zimmermann, and P. W. Courteille, Phys. Rev. Lett. **98**, 053603 (2007).

[26] S. Slama, G. Krenz, S. Bux, C. Zimmermann, and P. W. Courteille, Phys. Rev. A **75**, 063620 (2007).

[27] S. Bux, H. Tomczyk, D. Schmidt, P. W. Courteille, N. Piovella, and C. Zimmermann, Phys. Rev. A **87**, 023607 (2013).

[28] J. Barnes and P. Hut, Nature (London) **324**, 446 (1986).

[29] P. Gibbon, PEPC: Pretty Efficient Parallel Coulomb Solver Sostiger Interner Bericht ZAM-IB-2003-05 (ZAM, Julich Forschungszentrum, 2003).

[30] H. C. Plummer, Mon. Not. R. Astron. Soc. **71**, 460 (1911).

[31] M. Gross and S. Haroche, Phys. Rep. **93**, 301 (1982).

[32] D. Schneble, Y. T. M. Boyd, E. W. Streed, D. E. Pritchard, and W. Ketterle, Science **300**, 475 (2003).

[33] T. Bienaime, S. Bux, E. Lucioni, P. W. Courteille, N. Piovella, and R. Kaiser, Phys. Rev. Lett. **104**, 183602 (2010).

[34] S. Giovanazzi, D. O'Dell, and G. Kurizki, Phys. Rev. Lett. **88**, 130402 (2002).

[35] N. Piovella, M. Gatelli, and R. Bonifacio, Opt. Commun. **194**, 167 (2001).

PHYSICAL REVIEW A **102**, 013312 (2020)

Cooperative cooling in a one-dimensional chain of optically bound cold atoms

Angel T. Gisbert[*] and Nicola Piovella[†]
Dipartimento di Fisica “Aldo Pontremoli”, Università degli Studi di Milano, Via Celoria 16, Milano I-20133, Italy

Romain Bachelard[‡]
Universidade Federal de São Carlos, Rod. Washington Luis, km 235, S/n - Jardim Guanabara, São Carlos - SP, 13565-905, Brazil

(Received 10 February 2020; accepted 19 June 2020; published 14 July 2020)

We discuss theoretically the optical binding of one-dimensional chains of cold atoms shone by a transverse pump, where particles self-organize to a distance close to an optical wavelength. As the number of particles is increased, the trapping potential increases logarithmically as the contributions from all atoms add up constructively. We identify a cooperative cooling mechanism, due to the mutual exchange of photons between atoms, which can beat the spontaneous emission for chains that are long enough. Surprisingly, the cooling is optimal very close to the resonance. This peculiar cooling mechanism thus gives new insights into the cooperative physics of low-dimensional cold atom systems.

DOI: 10.1103/PhysRevA.102.013312

I. INTRODUCTION

After the pioneering work by Ashkin on optical forces for microsized particles [1,2], the manipulation of small objects using light beams has been applied successfully to a wide range of systems, from atoms [3,4] to biological systems [5]. In this context, the role of the *interparticle* optical forces was soon noted [6]. These forces can be either attractive or repulsive, depending on the specific distance between the scatterers, which suggests it can act as a mechanism for self-organization of the matter. Several years later, the self-organization of dielectric particles in suspension in a fluid was reported, with a pronounced preference for the particles to be separated by an integer number of optical wavelengths [7]. Coined optical binding (OB) at the time, it has since known various developments [8].

OB can be realized using two main configurations: In the transverse one, the scatterers are spread in a plane orthogonal to the direction of propagation of the pump, and are submitted to a rather homogeneous phase and intensity profile [9]. In the longitudinal configuration, the pump propagates in the direction of the aligned scatterers [10]. In all cases, the coupling between the scatterers becomes increasingly complex as their number increases, due to the propagation effects within the system. To circumvent these effects and generate longer bound chains, it has been proposed to resort to Bessel beams [11,12].

OB relies on the trapping optical force overcoming the stochastic effect due to spontaneous emission. The trapping component is generally analyzed in terms of potentials, considering that each particle is trapped in a potential generated by the other scatterers. Finding stable configurations is then a self-consistent problem as moving a single scatterer affects the global stability of the system [9,13,14]. More generally, while a pair of scatterers tends to self-organize at a distance equal to an integer number of optical wavelengths, larger systems suffer from diffraction effects which alter this spacing, but also the system stability [15]. Finally, despite the fact that the binding force scales poorly with decreasing scatterer size [16], OB has recently attracted a lot of attention for nanoparticles, as it appears as a potential mechanism for self-structuring at the nanoscale [17].

In this context, only recently was the possibility of binding optically cold atoms [18] discussed. Indeed, the binding force is comparatively stronger for particles of size comparable to the optical wavelengths [16], and the smallest objects such as atoms present unstable configurations as the heating due to the random recoil overcomes the binding potential [19]. Nevertheless, differently from dielectrics, cold atoms present an atomic resonance, which leads to an extra cooling mechanism for pairs of atoms in an OB configuration [18,19]. Although this extra damping is not sufficient to reach stability for pairs of cold atoms without an additional stabilization mechanism such as molasses, it represents a further step toward this goal.

In this theoretical work, we report on a cooperative cooling mechanism in a one-dimensional chain of cold atoms. The long-range nature of the light-mediated interaction manifests not only in the deepening of the OB potential, but also in the enhancement of the cooling mechanism for resonant scatterers. Differently from other cooling mechanisms, including the cooling of a pair ($N = 2$) of optically bound atoms, the cooling for larger systems ($N \geqslant 3$) is most efficient at or very close to the atomic resonance, and in the one-dimensional (1D) chain under study, it grows logarithmically with the system size. This self-generated cooling makes stable OB possible for chains of a few dozens of cold atoms. Our result shows that cooperative effects in low-dimensional cold-atom

---

[*] angel.tarramera@unimi.it
[†] nicola.piovella@unimi.it
[‡] bachelard.romain@gmail.com

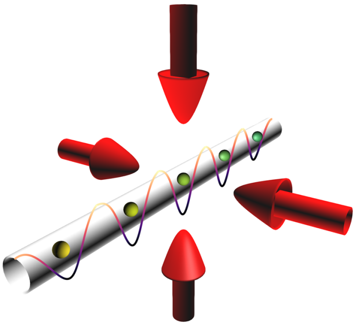

FIG. 1. Scheme of the one-dimensional cloud of atoms trapped by four laser beams, the self-organization as a chain occurring under the effect of mutual optical forces. The strongest coupling between neighbors is achieved when the mutual distance is close to the optical wavelength λ. The four laser beams drawn form a 2D optical lattice in the transverse directions and aim to emulate a one-dimensional system: They are ideally far from resonance. Differently, the near-resonant pump which generates the OB is also transverse, so it should be operated on a different transition.

systems may be particularly useful for self-organization processes.

II. OPTICAL BINDING IN A CHAIN OF COLD ATOMS

A. Modeling the atomic chain dynamics

The dynamics of the optical binding involves monitoring the coupled evolution of both the vacuum modes and the atoms internal and external degrees of freedom. In order to reach an efficient description of the system, we focus on the atom dynamics, by tracing over the degrees of freedom of the light and studying the coupled dipole dynamics [20–22]. Considering we are dealing with two-level atoms, the dynamics of their dipoles, hereafter labeled β_j and treated classically, is given by

$$\frac{d\beta_j}{dt} = \left(i\Delta - \frac{\Gamma}{2}\right)\beta_j - i\Omega(\mathbf{r}_j) - \frac{\Gamma}{2}\sum_{l\neq j} G_{jl}\beta_l, \qquad (1)$$

where Γ is the linewidth of the atomic transition, Ω the Rabi frequency of the driving field, and $\Delta = \omega - \omega_a$ the detuning of the pump field from the atomic transition frequency ω_a. We consider a setup of transverse one-dimensional OB, where the atoms are trapped in one dimension by a two-dimensional (2D) optical lattice created by four plane-wave beams in the orthogonal plane (see Fig. 1). Such a scheme allows to reduce the cold atom dynamics to one dimension and has been explored in various experiments [23–25].

It corresponds to a pump with a homogeneous phase along the chain: $\Omega(\mathbf{r}) = \Omega_0$. The light-mediated interaction between the dipole is given by the kernel $G_{jl} = \exp(ik|\mathbf{r}_j - \mathbf{r}_l|)/(ik|\mathbf{r}_j - \mathbf{r}_l|)$, where $\mathbf{r}_j$ refers to the position of the atom center of mass and $k = 2\pi/\lambda$ the light wave number. This kernel can be seen as referring to scalar dipoles (scalar light approximation), or to vectorial dipoles oriented at a magic angle such that near-field terms cancel (i.e., a pump polarization which makes an angle $\theta = \arcsin(1/\sqrt{3})$ from the chain axis). In the linear-optics regime considered throughout this work, this dynamics can be obtained either from a quantum description of the light-matter interaction [20] or from a representation of the atoms as classical oscillators [26,27].

Regarding the atom center of mass, their dynamics is driven only by the field from the other dipoles, since the trapping beams do not induce any force along the z axis:

$$\begin{aligned} m\frac{d^2\mathbf{r}_j}{dt^2} &= -\hbar(\beta_j^*\nabla_{\mathbf{r}_j}\Omega_j + \text{c.c.}) \\ &= -\hbar\Gamma\sum_{l\neq j}\text{Im}(\beta_j^*\beta_l\nabla_{\mathbf{r}_j}G_{jl}), \end{aligned} \qquad (2)$$

with $\Omega_j(\mathbf{r}_j) = \Omega_0 - i(\Gamma/2)\sum_{l\neq j} G_{jl}\beta_l$ the effective Rabi frequency at position $\mathbf{r}_j$, m the atom mass, and $\hbar$ the reduced Planck constant. In this equation, stochastic effects associated with spontaneous emission have been eliminated—see Sec. IV for a more detailed discussion.

B. Adiabatic approximation

Systems of dielectrics previously considered for OB do not possess a resonance like atoms; it is equivalent to considering that the internal degrees of freedom, here the β_js, are always at equilibrium. Performing such an adiabatic approximation, i.e., considering that the dipole relaxation time Γ^{-1} is negligible compared to the time needed for an atom center of mass to perform an oscillation in the binding potential, corresponds to taking the left-hand term in Eq. (1) equal to zero. This allows one to rewrite the dipole as $\beta_j = \alpha\Omega_j$, with $\alpha = 1/(\Delta + i\Gamma/2)$ the normalized atom polarizability. Defining $\Omega_j = |\Omega_j|e^{i\varphi_j}$, the center-of-mass dynamics in turn rewrites as

$$\begin{aligned} m\frac{d^2\mathbf{r}_j}{dt^2} &= -\hbar(\alpha^*\Omega_j^*\nabla_{\mathbf{r}_j}\Omega_j + \text{c.c.}) \\ &= \frac{\hbar\Gamma}{\Delta^2 + \Gamma^2/4}|\Omega_j|^2\nabla_{\mathbf{r}_j}\varphi_j - \frac{\hbar\Delta}{\Delta^2 + \Gamma^2/4}\nabla_{\mathbf{r}_j}|\Omega_j|^2, \end{aligned} \qquad (3)$$

where the first right-hand term corresponds to the radiation pressure force, and the second to the dipolar force.

Despite we are dealing with an open system, for a pair of atoms ($N = 2$) and after a short transient, the dipoles synchronize and the adiabatic approximation can be mapped to a conservative dynamics, derived from a potential energy [19]. This conveniently allows one to monitor the evolution of the effective energy of the system. Differently, for a many-atom chain ($N \geqslant 3$) the absence of synchronization translates into different dipole amplitudes, which in turn prevents defining a potential energy for the system: The mutual radiation pressure terms [i.e., the phase gradient term in Eq. (3)] cannot be expressed as deriving from a potential. Nevertheless, simulations of the kinetic energy with and without the adiabatic approximation show that performing this approximation leads to a conservative dynamics: On the time scales over which the system otherwise cools or heats, no significant long-term evolution of the kinetic energy is observed for the adiabatic dynamics (see Fig. 2).

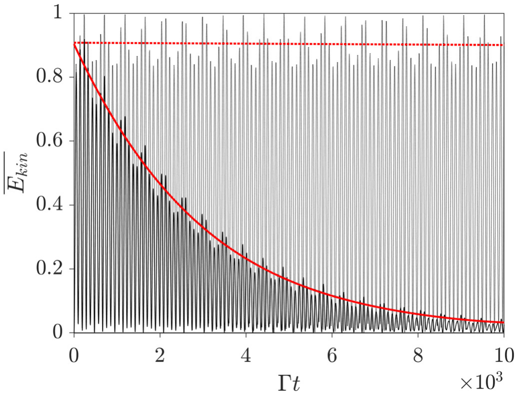

FIG. 2. Evolution of the normalized kinetic energy for a chain of $N = 15$ atoms with an initial interparticle distance λ, and pumped with a laser detuned by $\Delta \approx -0.2\Gamma$. The darker black curve refers to the evolution with the full dipole dynamics, Eqs. (1) and (2), the lighter curve was obtained from the adiabatic dynamics [canceling the left-hand term in Eq. (1)], and the red lines refer to the envelope obtained by averaging over a short time. The two kinetic energies have been normalized by the maximum of both curves.

C. Local potential at equilibrium

In this work, the system is prepared out of equilibrium as follows: A chain of atoms separated by λ is generated; the atom positions corresponding to the minima of the optical potential are then obtained by letting the system relax in the presence of an artificial friction force $-\xi(d\mathbf{r}_j/dt)$ applied to all atoms. These minima correspond to a separation of the atoms slightly different from λ, and must be found as a self-consistent problem where all scatterers mutually interact [14]: The friction allows one to reach the equilibrium in an efficient way. We have checked that the equilibrium positions are not affected by the value of ξ, which we have set to $0.02m\Gamma$ throughout this work. Then, the two atoms at the extremity of the chain are shifted away by 3% of the distance to their nearest neighbor. The dynamics is then initiated with the atoms in these positions, without any initial velocity.

In this review, we have simulated Eqs. (1) and (2) using $\Omega_0 = 0.1\Gamma$ and $\omega_{\rm rec} = 0.045\Gamma$, where $\omega_{\rm rec} = \hbar k^2/2m$ is the recoil frequency. This value of $\omega_{\rm rec}$ is low enough to neglect the shift induced by the scattering on the light frequency, yet large enough to observe the cooling over dozens of oscillations (lower ratios $\omega_{\rm rec}$ lead to larger time scales for the cooling Ref. [19]).

The OB potential for each atom strongly depends on the system size. Indeed, due to the long-range nature of the dipole-dipole interaction, all atoms contribute to the instantaneous potential U_j for atom j, which is deduced from Eq. (2) as

$$U_j = \hbar\Gamma \sum_{l\neq j} \mathrm{Im}(G_{jl}\beta_j^*\beta_l). \tag{4}$$

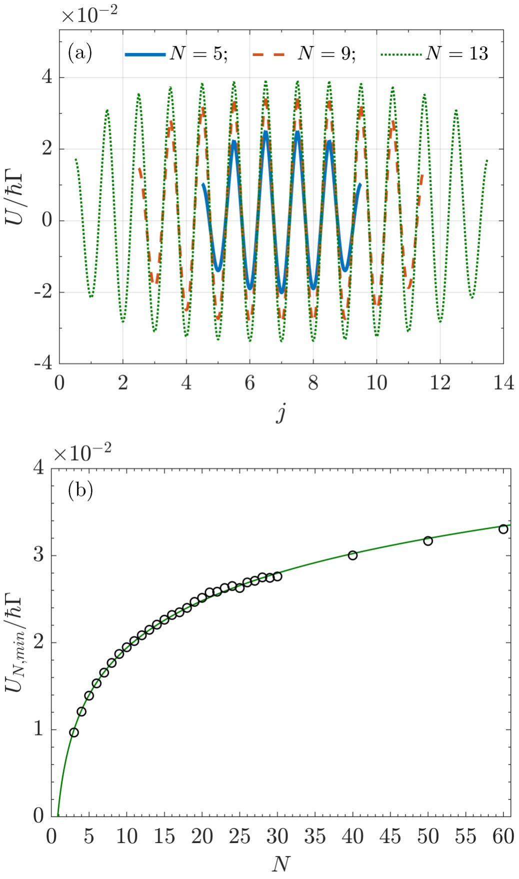

FIG. 3. (a) Potential energy landscape for chains of $N = 5,\ 9$ and 13 atoms at equilibrium, for a normalized detuning $\Delta/\Gamma = -0.06,\ -0.13$ and -0.18, respectively. The potential is computed using Eq. (4), considering all atoms apart from the closest one, as it generates a local singularity. (b) Optical potential (in absolute value) for the edge atoms of a chain of length N, as a function of N, and for a detuning that optimizes the cooling. The green line corresponds to a logarithmic fit.

Let us discuss the potential generated by atoms once they have reached the minimum of the optical potential (since, in practice, the OB potential is a dynamical quantity). As can be observed in Fig. 3(a), the optical potential for each atom becomes deeper as the chain size increases. This effect can be understood from the $1/r$ decay of the electric field. If, for simplicity, we assume that each atomic dipole is mainly driven by the laser field, $\beta_j = \Omega_0/(\Delta + i\Gamma/2)$, then the optical potential reads

$$U_j = \hbar\Gamma \frac{\Omega_0^2}{\Delta^2 + \Gamma^2/4} \sum_{l\neq j} \mathrm{Im}(G_{jl}). \tag{5}$$

Assuming that all the atoms are separated by λ (i.e., $\mathbf{r}_j = j\lambda\hat{z}$), the potential simplifies into

$$U_j = U_0 \sum_{l\neq j} \frac{1}{|l-j|} = C_j U_0, \tag{6}$$

with $U_0 = -\hbar(\Gamma/2\pi)\Omega_0^2/(\Delta^2+\Gamma^2/4)$ the potential minimum for a pair of atoms, and $C_j = \sum_{l\neq j} 1/|l-j|$ the cooperativity parameter for atom j. Thus, in a long chain, an atom in the middle of the center is submitted to a potential that is the coherent sum of the contributions of all atoms, the overall potential scaling as

$$\sim U_0 \sum_{j=-N/2, j\neq 0}^{N/2} 1/|j| \sim 2U_0 \ln(N/2).$$

An atom at the chain border is submitted to a smaller potential, $U_1 = U_N \sim U_0 \ln N$. This explains the scaling observed in Fig. 3(a), which clearly favors larger chains in terms of stability.

In Fig. 3(b), the logarithmic growth of the potential can be observed, for chains up to $N = 60$ atoms. A fit of the numerically computed potential minimum for the atoms at the extremes of the chain gives the following approximated expression:

$$U_{\min} \approx -0.8\hbar\Gamma \left(\frac{\Omega_0}{\Gamma}\right)^2 \ln N. \tag{7}$$

A slight decrease in the potential depth is observed for the largest system sizes, which can be explained from the finite optical thickness which separates remote atoms in long chains. Indeed, the exchange of photons between two remote atoms is screened by the in-between atoms, which modify both the amplitude and phase of the wave. As a result, the coherent sum (6) is no longer valid. Longer chains obviously suffer stronger screening effects, which represents a limit to the length of optically bound chains. In order to overcome such effect and bind efficiently long chains of scatterers, it has, for example, been proposed to shrink the coherence of the incident field to reduce the number of coherently interacting dipoles, or to spatially modulate the phase of the incident field [15].

III. COOPERATIVE COOLING

As mentioned earlier, an important difference of cold atoms as compared to dielectrics spheres is the presence of a resonance: It makes the atomic dipoles have a finite-time response to the local electric field. As a consequence, the system may either present a long-term cooling or heating trend [18,19], beyond the adiabatic dynamics described above. This is illustrated in Fig. 2, where the evolution of the kinetic energy of the atomic chain presents a slow decay when the dipole dynamics is accounted for. The oscillations observed occur at a frequency provided by the trapping potential, which can be estimated from Eq. (6):

$$\omega_j^2 = \frac{\omega_{\text{rec}}\Gamma}{\pi} \frac{\Omega_0^2}{\Gamma^2+4\Delta^2} \sum_{l\neq j} \frac{1}{|l-j|}. \tag{8}$$

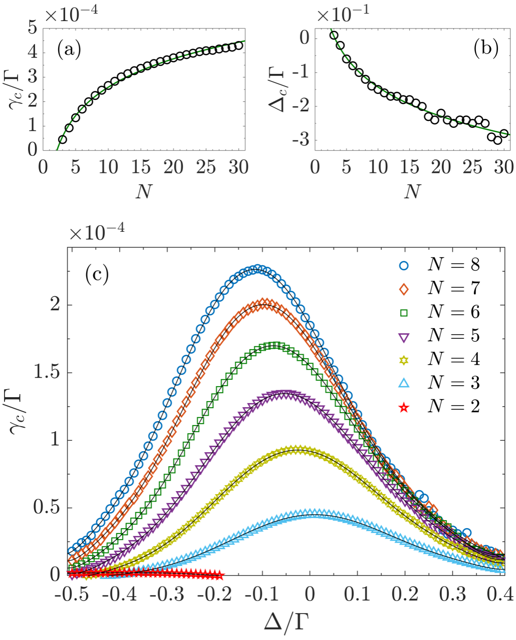

FIG. 4. (a) Maximum cooling rate γ_c as a function of the particle number N. (b) Detuning Δ_c of maximum cooling rate, as a function of N. (c) Cooling rate γ_c/Γ as a function of the normalized detuning Δ/Γ of the pump light and for different particle numbers.

where $\omega_{\text{rec}} = \hbar k^2/2m$ is the recoil frequency. This frequency contains the cooperativity parameter $C_j = \sum_{l\neq j} 1/|l-j|$, which scales as $\ln N$.

The cooling observed in Fig. 2, obtained from the envelope of the kinetic energy $\overline{E}$, is exponential in time, so we deduce a cooling rate γ_c by an exponential fit. The dependence of this rate on the particle number N is presented in Fig. 4, for the detuning Δ_c that optimizes this rate (see discussion below). However, we first remark that the cooling rate γ_c scales with $\ln N$ [see Fig. 4(a)], leading to an increased cooling rate for larger systems. This cooperative enhancement of the cooling, and the detuning Δ_c that optimizes this rate, are given by the following expressions, obtained by numerical fit:

$$\gamma_c \approx \omega_{\text{rec}} \left(\frac{\Omega_0}{\Gamma}\right)^2 [0.4 \ln N - 0.3], \tag{9}$$

$$\frac{\Delta_c}{\Gamma} \approx 0.14 - 0.12 \ln N. \tag{10}$$

We remind that in the present setup there is no external damping force such as fluid friction for scatterers maintained in fluids [7]. Furthermore, in the case of transverse OB, the pump laser confines the particles only along the chain, and have no direct role on the dynamics along that direction: Only interparticle optical forces contribute here.

In Fig. 4(c) we observe a maximum cooling rate very close to resonance, nevertheless the steady state is also determined

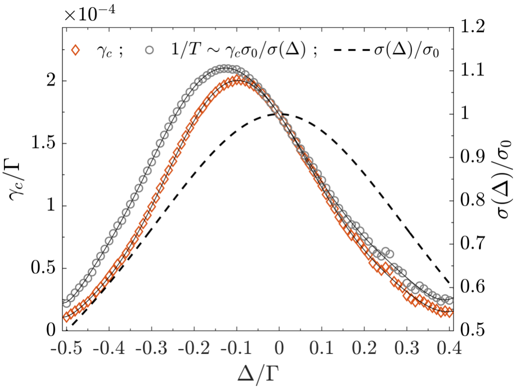

FIG. 5. Cooling rate γ_c/Γ, scattering cross section σ, and inverse temperature $1/T$ for a chain of $N = 7$ atoms and as a function of the detuning of the pump light Δ.

by the spontaneous emission rate, which is also maximum at resonance. Indeed resonant light corresponds to a maximum scattering cross section $\sigma(\Delta) = \sigma_0/(1 + 4\Delta^2/\Gamma^2)$, with $\sigma_0 = 4\pi/k^2$ the resonant scattering atom cross section. The equilibrium temperature resulting from the cooling and the stochastic heating is obtained using a Langevin equation, and scales as $T \propto \sigma(\Delta)/\gamma_c(\Delta)$ (see Sec. IV). As can be observed in Fig. 5, despite the increased spontaneous emission, the equilibrium temperature is predicted to be lowest very close to resonance. The cooling thus appears to rely on the radiation pressure force rather than on the dipolar one.

This makes the cooling mechanism for large ($N \geqslant 3$) optically bound atomic chains quite different from other cooling mechanisms. In the case of an optically bound pair of atoms [18,19], the scaling on the cooling rate was similar to the one obtained for Doppler cooling: Cooling is achieved for negative detuning, ideally for $\Delta \approx -\Gamma/2$, whereas positive detuning is associated with heating [see Fig. 4(c)]. For $N \geqslant 3$ atoms in an OB configuration, the cooling not only appears most efficient very close to resonance, and even scales differently from the $N = 2$ case: It reaches a maximum ~20 times higher for $N = 3$ than the maximum reached for a pair of atoms. Only for larger numbers does the optimal pump frequency start to deviate from the atomic resonance [$\Delta_c \approx \Gamma/4$ for $N = 20$; see Fig. 4(c)]. The present situation is at odds from the cooling by diffuse light reported for atoms trapped in a reflecting cylinder [28–30], where the cooling was achieved in a fully disordered system, and was optimal off resonance ($\Delta \approx -3\Gamma$).

A hint on the origin of this peculiar behavior, as compared to a pair of atoms, can be found in the evolution of the atomic dipoles. Indeed a close analysis of the dynamics shows that for $N \geqslant 3$, differently than for $N = 2$, the dipoles do not evolve synchronously (see Fig. 6). One observes that the dipoles present substantial differences in their oscillations, both in terms of amplitude and oscillations maxima.

This lack of synchronization of the dipoles has strong consequences on the macroscopic dynamics, as revealed by comparing the full dynamics of Eqs. (1) and (2) to a synchronized ansatz, obtained by substituting in Eq. (2) the values of the dipole amplitudes β_j by their average $\overline{\beta} = (1/N)\sum_j \beta_j$.

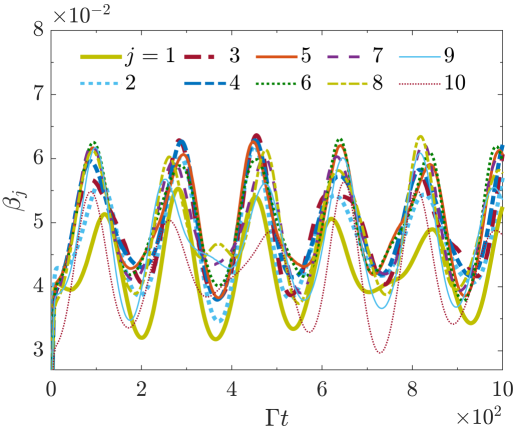

FIG. 6. Evolution of the dipole amplitude β_j over time, for a chain of $N = 10$ atoms. Simulation realized for a detuning $\Delta = -0.3\Gamma$ and a pump strength $\Omega = 0.1\Gamma$. The atomic chain was here initialized with atoms separated by λ, with a tilt of 0.03λ toward positive z of four atoms ($j = 1,\ 3,\ 8,\ 10$): This breaking of symmetry allows one to visualize the distinct dynamics of the 10 dipoles.

As shown in Fig. 7(a), close to resonance the synchronized dynamics presents a heating trend, whereas the full coupled dynamics exhibits a damping of the kinetic energy over time. The systematic comparison presented in Fig. 7(b) confirms that using the synchronized ansatz, a chain of $N = 3$ atoms displays the features of Doppler cooling (we checked that larger chains present a similar behavior, up to a shift in the detuning that optimizes the cooling): Cooling is achieved only for negative detuning, and is maximal for $\Delta \approx -\Gamma/2$, whereas resonant light strongly heats the system. Differently, the $N \geqslant 3$ coupled dipole dynamics obtained from Eqs. (1) and (2) exhibits a cooling which is maximum at resonance, but also significantly larger than for the synchronized case. Unfortunately, the asynchronous nature of this dynamics makes it very challenging to analyze it in more details, as one would need to deal with N internal and N external coupled degrees of freedom. Hence, despite the apparent complexity that the system dynamics presents, it is quite remarkable that this lack of synchronization results in a cooling rate much larger than the one encountered for synchronous dipoles.

IV. IMPACT OF THE SPONTANEOUS EMISSION AND VELOCITY CAPTURE RANGE

Let us now discuss in more detail the effect of heating due to spontaneous emission on the trapping. Considering that this process is dominated by the trapping beam Ω_0, the rate of kinetic energy induced by spontaneous emission is

$$\left(\frac{\delta E}{\delta t}\right)_{\mathrm{SE}} = \frac{\hbar\omega_r\Gamma}{3}\frac{\Omega_0^2}{\Gamma^2 + 4\Delta^2}, \tag{11}$$

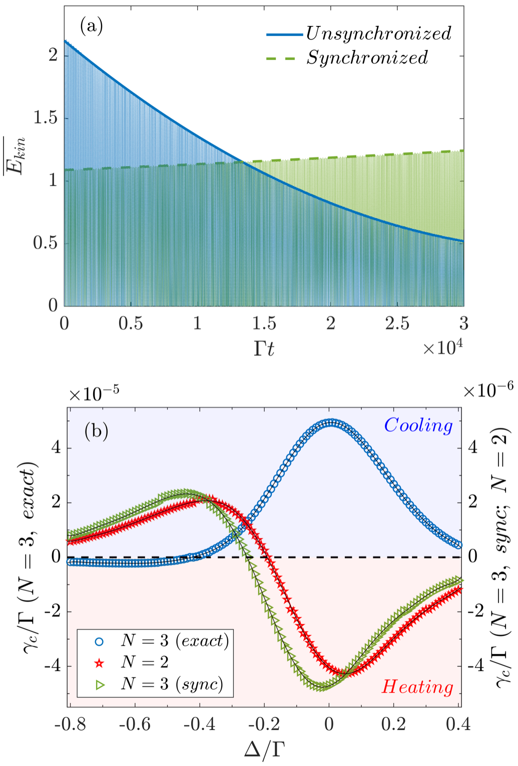

FIG. 7. (a) Dynamics of the kinetic energy for $N = 3$ atoms, comparing the full dipole dynamics of Eqs. (1) and (2) with the synchronized obtained from the synchronization ansatz. Simulations realized with the detuning of optimal cooling for the exact case, $\Delta \approx 0.01\Gamma$. (b) Cooling or heating rate γ_c/Γ for $N = 3$ atoms, for the full dynamics ("exact") and imposing synchronized dipoles ("sync"), and for $N = 2$ (the two dipoles spontaneously synchronize). The cooling or heating rate has been calculated using the evolution of the envelope of the kinetic energy until it reaches the 90%/110% of its initial value.

where the factor 1/3 comes from the fact that the atomic recoil is distributed over the three spatial directions. Due to its oscillating nature [see Fig. 3(a)], the potential minimum is the opposite of its maximum (as the potential is here defined to be zero at large distances), so the heating has to overcome a barrier twice larger than the minimum potential, $\Delta U = 2|U_{\min}|$, where $U_{\min}$ is provided by Eq. (7).

Considering the exponential decay of the kinetic energy over time observed in the simulations, it is reasonable to include the cooperative cooling as a linear damping force, which leads to the following equation for the kinetic energy:

$$\frac{dE}{dt} = -\gamma_c E + \left(\frac{\delta E}{\delta t}\right)_{\mathrm{SE}}, \tag{12}$$

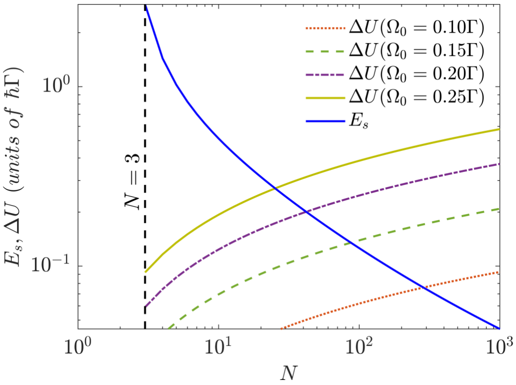

FIG. 8. Steady-state energy E_s obtained from the Langevin equation and potential barrier ΔU, as a function of the number of particles and for different pump strength Ω/Γ.

where γ_c is given by Eq. (9). The steady-state energy is thus given by

$$E_s = \frac{1}{\gamma_c}\left(\frac{\delta E}{\delta t}\right)_{\mathrm{SE}} \tag{13}$$

$$\approx \frac{0.83}{\ln N - 0.8}\frac{\hbar\Gamma}{1 + 4(\Delta_c/\Gamma)^2}. \tag{14}$$

Stability is achieved when $E_s < \Delta U$. For instance, for $\Omega_0/\Gamma = 0.2$ stability should be reached for $N \geqslant 40$ (see Fig. 8). While increasing pump strength suggests that a lower number of atoms is necessary to reach stability, it actually challenges the validity of the linear optics approximation [31], just as in the case of Doppler cooling.

In a similar way, we can estimate the velocity capture range Δv, assuming that the initial kinetic energy must be smaller than the potential barrier for the atoms to become trapped: $(m/2)(\Delta v)^2 < 2|U_{\min}|$. Using Eq. (7), we obtain

$$k\Delta v < 2.4\sqrt{(\omega_r/\Gamma)\ln N}\,\Omega_0. \tag{15}$$

For example, for ^{87}Rb atoms on the D2 line ($5^2S_{1/2} \rightarrow 5^2P_{3/2}$ transition) one has that $\omega_r/\Gamma \sim 6 \times 10^{-4}$, allowing one to attain $k\Delta v/\Gamma \sim 0.06\sqrt{\ln N}(\Omega_0/\Gamma)$. This can be compared to the values for Doppler cooling in optical molasses, $k\Delta v/\Gamma \sim 1$, and for Sisyphus cooling, $k\Delta v/\Gamma \sim \sqrt{\omega_r/\Delta_0}(\Omega_0/\Gamma)$ [32]: The present cooperative cooling mechanism thus shares a scaling closer to Sisyphus cooling although, as discussed earlier, it is more efficient close to resonance. Finally, we point out that since the potential is self-generated by the atoms, this value is a simple estimation of the order of magnitude of the capture velocity, and a detailed study of the microscopic dynamics is necessary to obtain a precise value.

V. CONCLUSIONS AND PERSPECTIVES

In conclusion, we have here shown that one-dimensional chains of cold atoms present a cooling mechanism which grows logarithmically with the system size. It relies on the presence of a resonance, and is thus absent from dielectric scatterers. Differently from other cooling mechanisms of cold atoms, the atomic chains are here most efficiently cooled very close to resonance, despite the strong spontaneous emission. A promising consequence is that chains of a few dozens of cold atoms could become stable thanks to this internal mechanism, without an additional stabilizing mechanism such as optical molasses. Such a self-organization mechanism could be probed, for example, using techniques inspired from Bragg scattering [33].

This cooperative cooling mechanism, here discussed in the context of a purely one-dimensional system, may be even more promising for two-dimensional systems. Indeed, the $1/r$ term of the dipole-dipole interaction leads to a scaling as $\ln N$ in one dimension, but in two-dimensional systems the same argument will lead to a scaling as $\sqrt{N}$. Indeed, in a 2D lattice of atoms of edge $\sqrt{N}$, the cooperativity parameter for an atom at site (i, j) scales as $\sum_{l,m=1}^{\sqrt{N}} 1/\sqrt{(l-i)^2+(m-j)^2} \sim \sqrt{N}$. The OB forces are then expected to overcome in a more efficient way the fluctuations due to spontaneous emission, making two-dimensional self-generated lattices even more robust. One may also consider manipulating the balance between the OB potential and the spontaneous emission by taking advantage of the more complex internal structure of the atoms, using an electromagnetically induced transparency configuration [34,35].

Finally, the self-cooling effect observed in our chain of atoms, connected by the exchanged photons scattered off the transverse driving fields, presents some analogies to collective cavity cooling in a high-finesse optical resonator [36]. These cavity self-organization effects have been suggested and studied theoretically by different groups in the 2000s [37,38] and experimentally by Black *et al.* [39] and, later, by Brennecke *et al.* [40]. Similarly, the atoms self-organize and cool into a self-generated potential with λ spacing, built from the field scattered from a transverse drive. The main difference with free space scattering is that the cavity pre-selects a single mode of the electromagnetic field, in addition to strongly recycling the photons in some cases. More recently, it was suggested [41] that a single, strongly populated mode can spontaneously emerge also in free space from cooperative scattering by the atoms, which presents some analogies with the synchronization issue observed in the present work. An important difference of our work is that addressing all vacuum modes leads to a more complex system, for which the analogy with a single-mode approach remains to be demonstrated. Furthermore, we have observed that the adiabatic approximation, which could be used to simplify drastically the system by suppressing the fast time scale, has important consequences on the long-term stability of the atomic chain. In this context, the present work can be considered another step toward bridging the gap between free space and cavity-based self-organization of cold atoms.

ACKNOWLEDGMENTS

We thank Robin Kaiser and Carlos E. Maximo for fruitful discussions. This work was performed in the framework of the European Training Network ColOpt, which is funded by the European Union (EU) Horizon 2020 program under the Marie Sklodowska-Curie action, Grant Agreement No. 721465. R.B. benefited from grants from São Paulo Research Foundation (FAPESP) (Grants No. 18/01447-2, No. 18/15554-5, and No. 19/12842-2) and from the National Council for Scientific and Technological Development (CNPq) Grants No. 302981/2017-9 and No. 409946/2018-4.

---

[1] A. Ashkin, Phys. Rev. Lett. **24**, 156 (1970).
[2] A. Ashkin, J. M. Dziedzic, J. E. Bjorkholm, and S. Chu, Opt. Lett. **11**, 288 (1986).
[3] S. Chu, L. Hollberg, J. E. Bjorkholm, A. Cable, and A. Ashkin, Phys. Rev. Lett. **55**, 48 (1985).
[4] T. Hänsch and A. Schawlow, Opt. Commun. **13**, 68 (1975).
[5] A. Ashkin and J. Dziedzic, Science **235**, 1517 (1987).
[6] T. Thirunamachandran, Mol. Phys. **40**, 393 (1980).
[7] M. M. Burns, J.-M. Fournier, and J. A. Golovchenko, Phys. Rev. Lett. **63**, 1233 (1989).
[8] K. Dholakia and P. Zemánek, Rev. Mod. Phys. **82**, 1767 (2010).
[9] Z. Yan, S. K. Gray, and N. F. Scherer, Nat. Commun. **5**, 3751 (2014).
[10] M. Guillon, O. Moine, and B. Stout, Phys. Rev. Lett. **96**, 143902 (2006).
[11] V. Karásek, T. Čižmár, O. Brzobohatý, P. Zemánek, V. Garcés-Chávez, and K. Dholakia, Phys. Rev. Lett. **101**, 143601 (2008).
[12] V. Karásek, O. Brzobohatý, and P. Zemánek, J. Opt. A: Pure Appl. Opt. **11**, 034009 (2009).
[13] L. C. D. Romero, J. Rodríguez, and D. L. Andrews, Opt. Commun. **281**, 865 (2008).
[14] L. D. Romero and D. L. Andrews, in *Complex Light and Optical Forces IV*, edited by E. J. Galvez, D. L. Andrews, and J. Glückstad (SPIE, Bellingham, 2010).
[15] M. Guillon, Opt. Express **14**, 3045 (2006).
[16] J. Rodríguez, L. C. D. Romero, and D. L. Andrews, Phys. Rev. A **78**, 043805 (2008).
[17] K. A. Forbes, D. S. Bradshaw, and D. L. Andrews, Nanophotonics **9**, 1 (2020).
[18] C. E. Máximo, R. Bachelard, and R. Kaiser, Phys. Rev. A **97**, 043845 (2018).
[19] A. T. Gisbert, N. Piovella, and R. Bachelard, Phys. Rev. A **99**, 013619 (2019).
[20] R. H. Lehmberg, Phys. Rev. A **2**, 883 (1970).
[21] E. M. Purcell and C. R. Pennypacker, Astrophys. J. **186**, 705 (1973).
[22] B. T. Draine, Astrophys. J. **333**, 848 (1988).
[23] A. Görlitz, J. M. Vogels, A. E. Leanhardt, C. Raman, T. L. Gustavson, J. R. Abo-Shaeer, A. P. Chikkatur, S. Gupta, S. Inouye, T. Rosenband, and W. Ketterle, Phys. Rev. Lett. **87**, 130402 (2001).

[24] B. Paredes, A. Widera, V. Murg, O. Mandel, S. Fölling, I. Cirac, G. V. Shlyapnikov, T. W. Hänsch, and I. Bloch, Nature (London) **429**, 277 (2004).
[25] A. Glicenstein, G. Ferioli, N. Sibalic, L. Brossard, I. Ferrier-Barbut, and A. Browaeys, Phys. Rev. Lett. **124**, 253602 (2020).
[26] A. A. Svidzinsky, J.-T. Chang, and M. O. Scully, Phys. Rev. A **81**, 053821 (2010).
[27] F. Cottier, R. Kaiser, and R. Bachelard, Phys. Rev. A **98**, 013622 (2018).
[28] E. Guillot, P.-E. Pottie, and N. Dimarcq, Opt. Lett. **26**, 1639 (2001).
[29] H.-D. Cheng, W.-Z. Zhang, H.-Y. Ma, L. Liu, and Y.-Z. Wang, Phys. Rev. A **79**, 023407 (2009).
[30] L. Xiao, X. Wang, W. Zhang, H. Cheng, L. Liu, and Y. Wang, Chin. Opt. Lett. **8**, 253 (2010).
[31] L. A. Williamson and J. Ruostekoski, Phys. Rev. Research **2**, 023273 (2020).
[32] J. Dalibard and C. Cohen-Tannoudji, J. Opt. Soc. Am. B **6**, 2023 (1989).
[33] C. von Cube, S. Slama, M. Kohler, C. Zimmermann, and P. Courteille, Fortschr. Phys. **54**, 726 (2006).
[34] O. Kocharovskaya and Y. I. Khanin, Zh. Eksp. Teor. Fiz **90**, 1610 (1986) [JETP **63**, 945 (1986)].
[35] G. Morigi, J. Eschner, and C. H. Keitel, Phys. Rev. Lett. **85**, 4458 (2000).
[36] H. Ritsch, P. Domokos, F. Brennecke, and T. Esslinger, Rev. Mod. Phys. **85**, 553 (2013).
[37] P. Domokos and H. Ritsch, Phys. Rev. Lett. **89**, 253003 (2002).
[38] S. B. Jäger, S. Schütz, and G. Morigi, Phys. Rev. A **94**, 023807 (2016).
[39] A. T. Black, H. W. Chan, and V. Vuletić, Phys. Rev. Lett. **91**, 203001 (2003).
[40] F. Brennecke, S. Ritter, T. Donner, and T. Esslinger, Science **322**, 235 (2008).
[41] S. Ostermann, F. Piazza, and H. Ritsch, Phys. Rev. X **6**, 021026 (2016).

Appendices

Several topics exposed throughout this doctoral thesis need further explanation or derivation, so they are expanded using this chapter. They are presented in the following order:

A) Derivation of the coupled dipole equations (CDE) used in optical binding to study the dynamics of the internal vibration of atoms.

B) The analytical derivation of the vectorial model used to track the path of each individual atom in a cold atomic cloud, provided it is irradiated by a laser beam with a defined polarization vector.

C) The cooling mechanism of the optical binding effect can be considered as a first order correction of the adiabatic solution. The equations of motion for the solution that lays beyond this approximation is derived.

D) The hypothetical case in which the dipoles of the atoms in an optically bound string would be in sync is compared to the actual non-synchronized dynamics of the system.

E) The OB cooling mechanism is shown to be a linear dissipative effect with the velocity of a particle. The optical effect can be combined with other cooling methods, such as optical molasses.

A Coupled dipole equations

The current appendix is introduced to help any reader to understand how the coupled dipole equations, announced in Eq. (3.5), are derived. Obviously, the derivation also includes the origin of the kernel describing the light-mediated dipole-dipole interaction, presented in Eq. (3.2). The whole appendix is a mere extract of the 4th chapter [210] from the 2nd volume of the *annual review of cold atoms and molecules* from 2014 [211]. The only modification performed is related to reference to another section of the original source [210]; it has been eliminated and rephrased to avoid any unnecessary misunderstanding. This small fragment, in order to keep the originality of the essay, is written in italics for an easier identification on this very page.

Quoting...

A.I Scalar microscopic theory

Model

Here a model that describes the interaction of a collection of static two-level atoms with a scalar wave is presented. It accounts for the fact that each atom is affected by the radiation of all the other atoms and so it describes multiple scattering and collective effects. This model has been used to predict several features of collectivity in disordered clouds, such as the modification of the radiation pressure force [118], Mie scattering and resonances [117, 225] or the collective Lamb shift [207]. While the model is formally the same for ordered atoms, as first discussed in Ref. [226], the scattering properties of optical lattices are very different.

The atomic cloud is described as a system of two-level (g and e) atoms, with resonant frequency ω_a and position $\mathbf{r}_j$, which are driven by a uniform laser beam with electric field amplitude E_0, frequency ω_0 and wave vector $\mathbf{k}_0 = (\omega_0/c)\hat{\mathbf{e}}_z$. The atom-laser interaction is described by the Hamiltonian:

$$\begin{aligned}\hat{H} &= \frac{\hbar\Omega_0}{2}\sum_{j=1}^{N}\left[\hat{\sigma}_j e^{i(\Delta_0 t-\mathbf{k}_0\cdot\mathbf{r}_j)}+\text{h.c.}\right] \\ &+ \hbar\sum_{j=1}^{N}\sum_{\mathbf{k}} g_k\left(\hat{\sigma}_j e^{-i\omega_a t}+\hat{\sigma}_j^{\dagger}e^{i\omega_a t}\right)\left[\hat{a}_{\mathbf{k}}^{\dagger}e^{i(\omega_k t-\mathbf{k}\cdot\mathbf{r}_j)}+\hat{a}_{\mathbf{k}}e^{-i(\omega_k t-\mathbf{k}\cdot\mathbf{r}_j)}\right],\end{aligned} \tag{A.1}$$

where $\Omega_0 = dE_0/\hbar$ is the Rabi frequency of the incident laser field and $\Delta_0 = \omega_0 - \omega_a$ is the detuning between the laser and the atomic transition. *For simplicity only scalar light and the two-level atom model is considered.*

In (A.1), $\hat{\sigma}_j = |g_j\rangle\langle e_j|$ is the lowering operator for the jth atom, $\hat{a}_{\mathbf{k}}$ is the photon annihilation operator and $g_k = (d^2\omega_a^2/2\hbar\epsilon_0\omega_k V_\nu)^{1/2}$ is the single-photon Rabi frequency, where d is the electric-dipole transition matrix element and V_ν is the photon volume. The special case of a low-intensity laser, where a single photon from mode $\mathbf{k}$ can be assumed to be present in the system, was extensively investigated in Refs. [114, 122, 227]. In this case the system (atoms+photons) is described by a state of the form [205]:

$$\begin{aligned} |\Psi\rangle &= \alpha(t)|g_1\dots g_N\rangle|0\rangle_{\mathbf{k}} + e^{-i\Delta_0 t}\sum_{j=1}^{N}\beta_j(t)|g_1\dots e_j\dots g_N\rangle|0\rangle_{\mathbf{k}} \\ &+ \sum_{\mathbf{k}}\gamma_{\mathbf{k}}(t)|g_1\dots g_N\rangle|1\rangle_{\mathbf{k}} + \sum_{\mathbf{k}}\sum_{j\neq m}\epsilon_{j,m,\mathbf{k}}(t)|g_1\dots e_j\dots e_m\dots g_N\rangle|1\rangle_{\mathbf{k}}. \end{aligned} \tag{A.2}$$

The first term in (A.2) corresponds to the initial ground state without photons, the second term is the sum over the states where a single atom has been excited by the classical field, and the third term corresponds to the atoms that returned to the ground state having emitted a photon in the mode **k**. Hence, the square modulus of α, β_j and $\gamma_{\mathbf{k}}$ represent respectively the probability that the is no photon in the system and no excited atom, the probability that atom j is excited (and no photon), and the probability to have a photon in mode **k** (and all atoms in the ground state). Finally, $|\epsilon_{j,m,\mathbf{k}}|^2$ describes the probability of having two excited atoms and one virtual photon in mode **k** with 'negative' energy. This last term of (A.2) is due to the counter-rotating terms in the Hamiltonian (A.1) and disappears when the rotating wave approximation is made. The scattering process using the latter approximation was studied in several references [77, 118, 228–230], but the importance of counter-rotating terms during the relaxation process was pointed out in Ref. [231] .

The dynamics of each component of the state (A.2) are deduced from the Schrödinger equation:

$$\frac{\partial|\Psi(t)\rangle}{\partial t} = -\frac{i}{\hbar}\hat{H}|\Psi(t)\rangle. \tag{A.3}$$

Hence, the Hamiltonian (A.1) leads to the following set of differential equations:

$$\dot{\alpha}(t) = -\frac{i}{2}\Omega_0 e^{i\Delta_0 t}\sum_{j=1}^{N}\beta_j(t)e^{-i\mathbf{k}_0\cdot\mathbf{r}_j}\ , \tag{A.4}$$

$$\begin{aligned} \dot{\beta}_j(t) =& i\Delta_0\beta_j - \frac{i}{2}\Omega_0\alpha(t)e^{-i\Delta_0 t+i\mathbf{k}_0\cdot\mathbf{r}_j} - i\sum_{\mathbf{k}} g_k\gamma_{\mathbf{k}}(t)e^{-i(\omega_k-\omega_0)t+i\mathbf{k}\cdot\mathbf{r}_j} \\ & - i\sum_{\mathbf{k}} g_k e^{-i(\omega_k+\omega_a-\Delta_0)t}\sum_{m\neq j}\epsilon_{j,m,\mathbf{k}}e^{i\mathbf{k}\cdot\mathbf{r}_j}\ , \end{aligned} \tag{A.5}$$

$$\dot{\gamma}_{\mathbf{k}}(t) = -ig_k e^{i(\omega_k-\omega_0)t}\sum_{j=1}^{N}\beta_j(t)e^{-i\mathbf{k}\cdot\mathbf{r}_j}\ . \tag{A.6}$$

$$\dot{\epsilon}_{j,m,\mathbf{k}}(t) = -ig_k e^{i(\omega_k+\omega_a-\Delta_0)t}\left[e^{-i\mathbf{k}\cdot\mathbf{r}_j}\beta_m + e^{-i\mathbf{k}\cdot\mathbf{r}_m}\beta_j\right]. \tag{A.7}$$

Then integrating Eqs. (A.6) and (A.7) over time with $\gamma_{\mathbf{k}}(0) = 0$ and $\epsilon_{j,m,\mathbf{k}}(0) = 0$ and substituting them in to (A.5), we obtain N coupled equations describing the dynamics of the atomic dipoles:

$$\begin{aligned}\dot{\beta}_j(t) =& i\Delta_0\beta_j - \tfrac{i}{2}\Omega_0\alpha e^{i\mathbf{k}_0\cdot\mathbf{r}_j} \\ & - \sum_{\mathbf{k}} g_k^2 \sum_{m=1}^{N} e^{i\mathbf{k}\cdot(\mathbf{r}_j-\mathbf{r}_m)} \int_0^t e^{-i(\omega_k-\omega_0)(t-t')}\beta_m(t')dt' \end{aligned} \tag{A.8}$$

$$\begin{aligned} & - \sum_{\mathbf{k}} g_k^2 \int_0^t dt' e^{i(\Delta_0-\omega_k-\omega_a)(t-t')} \\ & \times \left[\sum_{m\neq j} e^{-i\mathbf{k}\cdot(\mathbf{r}_j-\mathbf{r}_m)}\beta_m(t') + (N-1)\beta_j(t')\right]. \end{aligned} \tag{A.9}$$

The interaction with the vacuum field yields diagonal terms with $m = j$ whose real part corresponds to the single-atom decay term and imaginary part to the self-energy shift, and off-diagonal terms with $m \neq j$ which correspond to the atom-atom interaction mediated by the photon. By separating the two contributions, we can write:

$$\begin{aligned}\dot{\beta}_j(t) =& i\Delta_0\beta_j - \tfrac{i}{2}\Omega_0\alpha e^{i\mathbf{k}_0\cdot\mathbf{r}_j} \\ & - \sum_{\mathbf{k}} g_k^2 \int_0^t d\tau \left[e^{-i(\omega_k-\omega_0)\tau} + e^{i(\Delta_0-\omega_k-\omega_a)\tau}(N-1)\right]\beta_j(t-\tau) \\ & - \sum_{\mathbf{k}} g_k^2 \sum_{m\neq j} e^{i\mathbf{k}\cdot(\mathbf{r}_j-\mathbf{r}_m)} \\ & \times \int_0^t d\tau \left[e^{-i(\omega_k-\omega_0)\tau} + e^{i(\Delta_0-\omega_k-\omega_a)\tau}\right]\beta_m(t-\tau). \end{aligned} \tag{A.10}$$

We assume a smooth density of modes, so the discrete sum $\sum_{\mathbf{k}}$ can be replaced by the volume integral $[V_\nu/(2\pi)^3]\int d\mathbf{k}$. In the linear regime $\alpha \approx 1$ and in the Markov approximation, valid if the decay time is larger than the photon time-of-flight through the atomic cloud, in the integrals of (A.10) we can replace $\beta_j(t-\tau)$ with $\beta_j(t)$ and extend the upper integration limit to infinity, so that (A.10) is approximated by

$$\begin{aligned}\dot{\beta}_j(t) =& i\Delta_0\beta_j - \tfrac{i}{2}\Omega_0 e^{i\mathbf{k}_0\cdot\mathbf{r}_j} \\ & - \frac{V_\nu}{(2\pi)^3}\int d\mathbf{k} g_k^2 \int_0^\infty d\tau \left[e^{-i(\omega_k-\omega_0)\tau} + e^{-i(\omega_k+2\omega_a-\omega_0)\tau}(N-1)\right]\beta_j(t) \\ & - \frac{V_\nu}{(2\pi)^3}\int d\mathbf{k} g_k^2 \sum_{m\neq j} e^{i\mathbf{k}\cdot(\mathbf{r}_j-\mathbf{r}_m)} \\ & \times \int_0^\infty d\tau \left[e^{-i(\omega_k-\omega_0)\tau} + e^{-i(\omega_k+2\omega_a-\omega_0)\tau}\right]\beta_m(t). \end{aligned} \tag{A.11}$$

The imaginary part of the self-field contribution (third term of the right hand side of (A.11)) consists of the self-energy shift of the atom in the excited state plus the self-energy contribution of the atom in the ground state. The effect is an adjustment to the transition frequency ω_a, which is assumed to already include the shift. It can not be computed realistically using our model, which treats the atoms as point particles, and is disregarded in the present approach. After performing the integration over τ the real part of the self-field contribution yields:

$$\frac{V_\nu}{2\pi}\int_0^\infty dk k^2 g_k^2\left[\delta(\omega_k-\omega_0)+(N-1)\delta(\omega_k+2\omega_a-\omega_0)\right]=\frac{\Gamma}{2}, \tag{A.12}$$

where $\omega_k = ck$ and $\Gamma = d^2\omega_0^3/(2\pi c^3\hbar\epsilon_0)$ is the single-atom *spontaneous* decay rate in the radiation scalar theory. The last term in (A.12) arises from the counter-rotating wave terms of the Hamiltonian (A.1) and does not contribute as it corresponds to a negative photon energy $\omega_k \approx -\omega_a$. Using (A.12) in (A.11) we obtain:

$$\begin{aligned}\dot{\beta}_j(t) = \left(i\Delta_0-\frac{\Gamma}{2}\right)\beta_j - \tfrac{i}{2}\Omega_0 e^{i\mathbf{k}_0\cdot\mathbf{r}_j} - \frac{V_\nu}{(2\pi)^3}\int d\mathbf{k} g_k^2 \sum_{m\neq j} e^{i\mathbf{k}\cdot(\mathbf{r}_j-\mathbf{r}_m)} \\ \times \int_0^\infty d\tau \left[e^{-i(\omega_k-\omega_0)\tau}+e^{-i(\omega_k+2\omega_a-\omega_0)\tau}\right]\beta_m(t).\end{aligned} \tag{A.13}$$

The last term on the right hand side of (A.13) can be calculated as follows:

$$\begin{aligned}&\frac{V_\nu}{(2\pi)^3}\int d\mathbf{k} g_k^2 e^{i\mathbf{k}\cdot(\mathbf{r}_j-\mathbf{r}_m)}\int_0^\infty d\tau\left[e^{-i(\omega_k-\omega_0)\tau}+e^{-i(\omega_k+2\omega_a-\omega_0)\tau}\right] \\ &= \frac{c\Gamma}{\pi k_0}\int_0^\infty d\tau\cos(\omega_0\tau)\int_0^\infty dk k\frac{\sin(kr_{jm})}{kr_{jm}}e^{-ick\tau},\end{aligned} \tag{A.14}$$

where $r_{jm} = |\mathbf{r}_j - \mathbf{r}_m|$ and we assumed $\omega_0 \approx \omega_a$. We use the integral expression

$$\int_0^\infty dk k\frac{\sin(kr)}{kr}e^{-ick\tau} = \frac{1}{2cr}\left[\frac{1}{\tau+r/c-i\epsilon}-\frac{1}{\tau-r/c-i\epsilon}\right]$$

where $\epsilon \to 0^+$. Changing the sign of the integration variable τ in the first term, (A.14) becomes

$$-\frac{\Gamma}{2\pi k_0 r_{jm}}\int_{-\infty}^{\infty}d\tau\frac{\cos(\omega_0\tau)}{\tau-r_{jm}/c+i\epsilon} = \frac{\Gamma}{2}\frac{\exp(ik_0r_{jm})}{ik_0r_{jm}}. \tag{A.15}$$

Finally, the scattering problem reduces to the set of differential equations [125, 207, 230]:

$$\dot{\beta}_j = \left(i\Delta_0-\frac{\Gamma}{2}\right)\beta_j - i\frac{\Omega_0}{2}e^{i\mathbf{k}_0\cdot\mathbf{r}_j} - \frac{\Gamma}{2}\sum_{m\neq j}\frac{\exp(ik_0|\mathbf{r}_j-\mathbf{r}_m|)}{ik_0|\mathbf{r}_j-\mathbf{r}_m|}\beta_m. \tag{A.16}$$

The kernel in the last term of (A.16) has a real component, $-(\Gamma/2)\sum_{m\neq j}\operatorname{sinc}(k_0|\mathbf{r}_j-\mathbf{r}_m|)$, describing the *collective* atomic decay, and an imaginary component, $i(\Gamma/2)\sum_{m\neq j}\cos(k_0|\mathbf{r}_j-\mathbf{r}_m|)/(k_0|\mathbf{r}_j-\mathbf{r}_m|)$, which contains the collective Lamb shift due to short range interactions between atoms induced by the electromagnetic field [124, 125, 232, 233].

In what follows we will focus on the stationary state of (A.16), which reads

$$(2\Delta_0 + i\Gamma)\,\beta_j = \Omega_0 e^{i\mathbf{k}_0\cdot\mathbf{r}_j} - \Gamma \sum_{m\neq j} \frac{\exp(ik_0|\mathbf{r}_j - \mathbf{r}_m|)}{k_0|\mathbf{r}_j - \mathbf{r}_m|}\beta_m. \tag{A.17}$$

Practically, the value of the atomic dipoles β_j in the stationary regime is evaluated numerically by inverting the linear problem (A.17), since it is easily cast in the form $M\vec{\beta} = e^{i\mathbf{k}_0\cdot\vec{\mathbf{r}}}$, where $\vec{\beta}$ and $\vec{\mathbf{r}}$ refer to the vectors of β_j and $\mathbf{r}_j$. From the β_j, the observables described in the next sections are easily calculated.

While we adopted a quantum, single-photon treatment to derive a description of the collective scattering a classical interpretation is also possible. In fact, (A.16) also describes the dynamics of atomic dipoles driven by the *total* electric field, the sum of the incident field and of the field radiated by the other dipoles. Indeed, the last term of ((A.16)) gives the emission of spherical waves by the latter, as described by Huygens principle. Furthermore, model (A.16) has also been derived through another classical approach which treats the two-level atoms as weakly excited classical harmonic oscillators [205, 234].

B Collective Recoil 3D Equations: vectorial model

B.I Multimode collective recoil equations

In the current appendix the simplified CARL scalar model is extended by including the effects of the polarization of the incident and scattered light. The authorship of the analytical derivation found in the whole appendix, has to be attributed to the professor Nicola Piovella. The writer of this PhD thesis has contributed to adjust the text to improve its readability and to solve numerically the final equations of the model.

As usual, the Hamiltonian for N two-level atoms interacting with an external field and all possible vacuum modes is considered. The atoms have a transition frequency ω_a and dipole d, the vacuum modes' wave-vector are $\boldsymbol{k}_k$ and their frequency ω_k, the optical field's counterparts are $\boldsymbol{k}$ and ω_k, with a polarization $\hat{\epsilon}_0$. Thus, the interaction Hamiltonian reads

$$\begin{aligned} H = \sum_{j=1}^{N} \frac{\boldsymbol{p}_j^2}{2m} + \hbar \sum_{j=1}^{N} \sum_{\alpha} \left[\frac{\Omega_{0\alpha}^*}{2} \sigma_{\alpha j}^- e^{i\Delta_0 t - i\boldsymbol{k}_0 \cdot \boldsymbol{r}_j} + \text{h.c.} \right] \\ + \hbar \sum_{j=1}^{N} \sum_{\boldsymbol{k}} \sum_{\hat{\epsilon} \perp \boldsymbol{k}} \sum_{\alpha} g_k \left[\hat{\epsilon}_{\alpha^*} a_{\boldsymbol{k},\hat{\epsilon}}^{\dagger} \sigma_{\alpha j}^- e^{i\Delta_k t - i\boldsymbol{k}\cdot \boldsymbol{r}_j} + \hat{\epsilon}_{\alpha} \sigma_{\alpha j}^+ a_{\boldsymbol{k},\hat{\epsilon}} e^{-i\Delta_k t + i\boldsymbol{k}\cdot \boldsymbol{r}_j} \right], \end{aligned} \tag{B.1}$$

although this time there are a couple of additional sums: one accounting for the two polarization vectors $\hat{\epsilon}^{(1,2)}$ of the vacuum field operator $a_{\boldsymbol{k},\hat{\epsilon}}$ and the other one considering the Cartesian coordinates $\alpha = x, y, z$ of the polarization operators $\sigma_{\alpha j}$. Here $\Omega_{0\alpha} = dE_{0\alpha}/\hbar$ is the Rabi frequency of the laser with polarization $\hat{\epsilon}_0$, with electric field $E_{0\alpha}$ and detuning with the electron transition of $\Delta_0 = \omega_0 - \omega_a$. Moreover, the radiation modes in vacuum are described by $a_{\boldsymbol{k},\hat{\epsilon}}$, have a detuning with the electronic transition of $\Delta_k = \omega_k - \omega_a$ and a coupling constant $g_k = d[\omega_k/(2\hbar\epsilon_0 V_{ph})]^{1/2}$, being V_{ph} the radiation field's quantization volume.

The dynamics of the system is obtained by calculating the Heisenberg picture for the position, momentum and dipole moment operator of each atom, together with the field operator of each mode:

$$\dot{\boldsymbol{r}}_j = \frac{\boldsymbol{p}_j}{m} \tag{B.2}$$

$$\begin{aligned} \dot{\boldsymbol{p}}_j = i\hbar \boldsymbol{k}_0 \sum_{\alpha} \left[\frac{\Omega_{0\alpha}^*}{2} \sigma_{\alpha j} e^{-i\boldsymbol{k}_0 \cdot \boldsymbol{r}_j} - \text{h.c.} \right] \\ + i\hbar \sum_{\boldsymbol{k}} \sum_{\hat{\epsilon}\perp\boldsymbol{k}} \sum_{\alpha \boldsymbol{k} g_k} \left[\hat{\epsilon}_{\alpha^*} a_{\boldsymbol{k},\hat{\epsilon}}^{\dagger} \sigma_{\alpha j} e^{i(\omega_k - \omega_0)t - i\boldsymbol{k}\cdot\boldsymbol{r}_j} - \text{h.c.} \right] \end{aligned} \tag{B.3}$$

$$\dot{\sigma}_{\alpha j} = (i\Delta_0 - \Gamma/2)\sigma_{\alpha j} - i\frac{\Omega_{0\alpha}}{2} e^{i\boldsymbol{k}_0\cdot\boldsymbol{r}_j} - i \sum_{\boldsymbol{k}} \sum_{\hat{\epsilon}\perp\boldsymbol{k}} \hat{\epsilon}_{\alpha} g_k a_{\boldsymbol{k},\hat{\epsilon}} e^{-i(\omega_k - \omega_0)t + i\boldsymbol{k}\cdot\boldsymbol{r}_j} \tag{B.4}$$

$$\dot{a}_{\boldsymbol{k},\hat{\epsilon}} = -ig_k e^{i(\omega_k - \omega_0)t} \sum_{\alpha} \hat{\epsilon}_{\alpha^*} \sum_{j=1}^{N} \sigma_{\alpha j} e^{-i\boldsymbol{k}\cdot\boldsymbol{r}_j}. \tag{B.5}$$

In the latter expression, a term rearrangement has been introduced $\sigma_{\alpha j} = \sigma^-_{\alpha j} e^{i\Delta_0 t}$, the population of the excited state has been neglected (assuming weak field and/or large detuning Δ_0) and the an spontaneous decay term $-(\Gamma/2)\sigma_{\alpha j}$ has been added. By adiabatically eliminating the internal degree of freedom (making $\dot{\sigma}_j \approx 0$ and substituting the resulting σ_j in the other equations) and, assuming $\Delta_0 \gg \Gamma$ to neglect multiple scattering effects, considering the process to be single-scattering process, the equations can be reduced to three and be rewritten as:

$$\dot{\boldsymbol{r}}_j = \frac{\boldsymbol{p}_j}{m} \tag{B.6}$$

$$\dot{\boldsymbol{p}}_j = \frac{i\hbar\Omega_0}{2\Delta_0}\sum_{\alpha}\sum_{\boldsymbol{k}}\sum_{\hat{\epsilon}\perp\boldsymbol{k}} g_k(\boldsymbol{k}_0-\boldsymbol{k})\left[\hat{\epsilon}_\alpha\hat{\epsilon}^*_{0\alpha}A_{\boldsymbol{k},\hat{\epsilon}}e^{-i(\boldsymbol{k}_0-\boldsymbol{k})\cdot\boldsymbol{r}_j} - \hat{\epsilon}^*_\alpha\hat{\epsilon}_{0\alpha}A^\dagger_{\boldsymbol{k},\hat{\epsilon}}e^{i(\boldsymbol{k}_0-\boldsymbol{k})\cdot\boldsymbol{r}_j}\right] \tag{B.7}$$

$$\dot{A}_{\boldsymbol{k},\hat{\epsilon}} = -\frac{ig_k\Omega_0}{2\Delta_0}\sum_{\alpha}\hat{\epsilon}_{0\alpha}\hat{\epsilon}^*_\alpha\sum_{j=1}^{N}e^{i(\boldsymbol{k}_0-\boldsymbol{k})\cdot\boldsymbol{r}_j} - i\delta_k A_{\boldsymbol{k}} \tag{B.8}$$

with the new filed variable redefine as $A_{\boldsymbol{k},\hat{\epsilon}} = a_{\boldsymbol{k},\hat{\epsilon}}e^{-i\delta_k t}$; the detuning between external field and the vacuum modes as $\delta_k = \omega_k - \omega_0$; and assuming $\Omega_{0\alpha} = \Omega_0\hat{\epsilon}_{0\alpha}$.

B.II Collective recoil equations in free space

The idea is to get the external motion of the atoms and, since the internal degree of freedom has already been adiabatically eliminated, the only thing left to do is to couple the radiation field with the atoms motion. Consequently, by integrating Eq.(B.8) assuming the Markov approximation (there is no re-absoprtion from radiated modes) and neglecting the initial constant term $A_{\boldsymbol{k},\hat{\epsilon}}(0)$, the scattered field for the 3D vacuum modes due to Rayleigh scattering can be calculated to

$$A_{\boldsymbol{k},\hat{\epsilon}}(t) = -\frac{ig_k\Omega_0}{2\Delta_0}\sum_{\alpha}\hat{\epsilon}_{0\alpha}\hat{\epsilon}^*_\alpha\sum_{j=1}^{N}e^{i(\boldsymbol{k}_0-\boldsymbol{k})\cdot\boldsymbol{r}_j}\int_0^t e^{-i(\omega_k-\omega_0)\tau}d\tau \tag{B.9}$$

Then, substituting the latter expression in the force equation (B.7), the external motion of the atoms becomes:

$$\dot{\boldsymbol{p}}_j = \hbar\left(\frac{g_{k_0}\Omega_0}{2\Delta_0}\right)^2\frac{V_{ph}}{8\pi^3}\sum_{m\neq j}\Bigg[e^{-i\boldsymbol{k}_0\cdot\boldsymbol{r}_{jm}}\int_0^t d\tau e^{i\omega_0\tau}$$
$$\int d\boldsymbol{k}(\boldsymbol{k}_0-\boldsymbol{k})e^{i\boldsymbol{k}\cdot\boldsymbol{r}_{jm}}e^{-ick\tau}\sum_{\alpha,\beta}\sum_{\hat{\epsilon}\perp\boldsymbol{k}}(\hat{\epsilon}_\alpha\hat{\epsilon}^*_\beta)(\hat{\epsilon}^*_{0\alpha}\hat{\epsilon}_{0\beta}) + \text{h.c.}\Bigg]; \tag{B.10}$$

where the sum over al possible modes $\boldsymbol{k}$ have been transform into an integral and there is a two dumb indexes sum covering the Cartesian axes —one coming from the field equation (α) and the one from the force (β)–.

The expression can be further reduced if the following relation is employed (see Sec. B.IV for demonstration):

$$\sum_{\hat{\epsilon}\perp\boldsymbol{k}}\hat{\epsilon}_\alpha(\hat{\epsilon}_\beta)^* = \delta_{\alpha\beta} - \hat{k}_\alpha\hat{k}_\beta. \tag{B.11}$$

Instead of applying this relation directly to the force, it is introduced in the second integral of Eq. (B.11) (expression's second row) in order to reduce this one. It is done without taking the sum of the projection of the laser polarization onto the axes α and β (i.e., $\sum_{\alpha,\beta}\hat{\epsilon}_{0\alpha}^{*}\hat{\epsilon}_{0\beta}$), because the two sums are independent from each other. Now the calculation proceeds with four steps to derive an expression than can be more suited to be solve numerically.

Firstly, the modes Cartesian variables (k_x, k_y, k_z) are transform into spherical coordinates (k, θ, φ)

$$\begin{aligned}
&\int d\boldsymbol{k}(\boldsymbol{k}_0-\boldsymbol{k})e^{i\boldsymbol{k}\cdot\boldsymbol{r}_{jm}}e^{-ick\tau}(\delta_{\alpha\beta}-\hat{k}_\alpha\hat{k}_\beta)=\\
&=\boldsymbol{k}_0\int_0^{2\pi}d\varphi\int_0^{\pi}d\theta\sin\theta\int_0^{\infty}dkk^2e^{ikr_{jm}\cos\theta}e^{-ick\tau}(\delta_{\alpha\beta}-\hat{k}_\alpha\hat{k}_\beta)\cdots\\
&-\hat{\boldsymbol{r}}_{jm}\int_0^{2\pi}d\varphi\int_0^{\pi}d\theta\sin\theta\cos\theta\int_0^{\infty}dkk^3e^{ikr_{jm}\cos\theta}e^{-ick\tau}(\delta_{\alpha\beta}-\hat{k}_\alpha\hat{k}_\beta)
\end{aligned}\tag{B.12}$$

where $\boldsymbol{r}_{jm}=\boldsymbol{r}_j-\boldsymbol{r}_m$, $r_{jm}=|\boldsymbol{r}_{jm}|$ and $\hat{\boldsymbol{r}}_{jm}=\boldsymbol{r}_{jm}/r_{jm}$. In the integral, the z-axis is chosen pointing along $\boldsymbol{r}_{jm}$, so that θ is the polar angle of $\boldsymbol{k}$ about $\boldsymbol{r}_{jm}$ (for simplicity, is is written θ instead of θ_{jm}).

Secondly, since the dependence on φ is contained only in the polarization factor $\delta_{\alpha\beta}-\hat{k}_\alpha\hat{k}_\beta$, the integration over φ gives (see Sec. B.IV for demonstration)

$$\int_0^{2\pi}d\varphi(\delta_{\alpha\beta}-\hat{k}_\alpha\hat{k}_\beta)=\pi[(1\cos^2\theta)\delta_{\alpha\beta}+(1-3\cos^2\theta)\hat{r}_\alpha\hat{r}_\beta)]\tag{B.13}$$

Also here, for simplicity of notation, $\boldsymbol{r}_{jm}$ is replaced by $\boldsymbol{r}$. As a third step the a new change of variable, $t=\cos\theta$, is applying and the integral becomes:

$$\begin{aligned}
&\int d\boldsymbol{k}\,(\boldsymbol{k}_0-\boldsymbol{k})\,e^{i\boldsymbol{k}\cdot\boldsymbol{r}}e^{-ick\tau}\left(\delta_{\alpha\beta}-\hat{k}_\alpha\hat{k}_\beta\right)=\\
&=\pi\boldsymbol{k}_0\int_0^{\infty}dkk^2e^{-ick\tau}\int_{-1}^{1}dte^{ikrt}\left[(1+t^2)\delta_{\alpha\beta}+(1-3t^2)\hat{r}_\alpha\hat{r}_\beta)\right]\\
&-\pi\hat{\boldsymbol{r}}\int_0^{\infty}dkk^3e^{-ick\tau}\int_{-1}^{1}dtte^{ikrt}\left[(1+t^2)\delta_{\alpha\beta}+(1-3t^2)\hat{r}_\alpha\hat{r}_\beta)\right]
\end{aligned}\tag{B.14}$$

As a third stage, because it can be assumed that $k\approx k_0$, the external field wave-vector k can be replaced by k_0 in the integrals (everywhere except in the exponential terms) and the lower integration limit can be extended to $-\infty$:

$$\begin{aligned}
&\int d\boldsymbol{k}(\boldsymbol{k}_0-\boldsymbol{k})e^{i\boldsymbol{k}\cdot\boldsymbol{r}}e^{-ick\tau}\left(\delta_{\alpha\beta}-\hat{k}_\alpha\hat{k}_\beta\right)=\\
&=\pi k_0^3\int_{-\infty}^{\infty}e^{-ick\tau}dk\int_{-1}^{1}e^{ikrt}(\hat{\boldsymbol{z}}-t\hat{\boldsymbol{r}})\left[\delta_{\alpha\beta}+\hat{r}_\alpha\hat{r}_\beta+t^2(\delta_{\alpha\beta}-3\hat{r}_\alpha\hat{r}_\beta)\right]dt
\end{aligned}\tag{B.15}$$

Lastly, there only some integrals that can be calculated straightforwardly, considering the following definite integrals [235]:

$$\int_{-1}^{1} e^{ixt}dt = +2\left[\frac{\sin x}{x}\right], \tag{B.16}$$

$$\int_{-1}^{1} e^{ixt}dt = -2i\left[\frac{\cos x}{x} - \frac{\sin x}{x^2}\right], \tag{B.17}$$

$$\int_{-1}^{1} t^2 e^{ixt}dt = +2\left[\frac{\sin x}{x} + 2\frac{\cos x}{x^2} - 2\frac{\sin x}{x^3}\right], \tag{B.18}$$

$$\int_{-1}^{1} t^3 e^{ixt}dt = -2i\left[\frac{\cos x}{x} - 3\frac{\sin x}{x^2} - 6\frac{\cos x}{x^3} + 6\frac{\sin x}{x^4}\right]. \tag{B.19}$$

Once these expressions are employed in Eq. (B.15), it is possible to attain the final expression for the integral contained in the force

$$\begin{aligned}
&\int d\boldsymbol{k}(\boldsymbol{k}_0 - \boldsymbol{k})e^{i\boldsymbol{k}\cdot\boldsymbol{r}}e^{-ick\tau}(\delta_{\alpha\beta} - \hat{k}_\alpha\hat{k}_\beta) = \\
&= \frac{4\pi^2 k_0^3}{c}\,\delta(\tau - r/c)\left\{\hat{\boldsymbol{z}}\left[\frac{-i}{k_0 r}(\delta_{\alpha\beta}-\hat{r}_\alpha\hat{r}_\beta) + \left(\frac{1}{(k_0 r)^2} + \frac{i}{(k_0 r)^3}\right)(\delta_{\alpha\beta}-3\hat{r}_\alpha\hat{r}_\beta)\right]\right. \\
&\left. - \hat{\boldsymbol{r}}_{jm}\left[\frac{-i(\delta_{\alpha\beta}-\hat{r}_\alpha\hat{r}_\beta)}{k_0 r} + \frac{2(\delta_{\alpha\beta}-2\hat{r}_\alpha\hat{r}_\beta)}{(k_0 r)^2} + \frac{3i(\delta_{\alpha\beta}-3\hat{r}_\alpha\hat{r}_\beta)}{(k_0 r)^3} - \frac{3(\delta_{\alpha\beta}-3\hat{r}_\alpha\hat{r}_\beta)}{(k_0 r)^4}\right]\right\}.
\end{aligned} \tag{B.20}$$

Concluding, the final expression of the motion equation of the atoms can be obtained, by inserting the new expression for the integral (B.20) into the force Eq. (B.10):

$$\begin{aligned}
\dot{\boldsymbol{p}}_j =&\Gamma\hbar k_0\left(\frac{\Omega_0}{2\Delta_0}\right)^2\sum_{\alpha,\beta}(\hat{\epsilon}^*_{0\alpha}\hat{\epsilon}_{0\beta})\sum_{m\neq j}\big\{\hat{\boldsymbol{z}}\big[(\delta_{\alpha\beta}-\hat{r}_\alpha\hat{r}_\beta)S^1 + (\delta_{\alpha\beta}-3\hat{r}_\alpha\hat{r}_\beta)\big(C^2-S^3\big)\big] \\
&- \hat{\boldsymbol{r}}_{jm}\left[(\delta_{\alpha\beta}-\hat{r}_\alpha\hat{r}_\beta)S^1 + 2(\delta_{\alpha\beta}-2\hat{r}_\alpha\hat{r}_\beta)\,C^2 - 3(\delta_{\alpha\beta}-3\hat{r}\alpha\hat{r}_\beta)\big(S^3+C^4\big)\right]\big\},
\end{aligned} \tag{B.21}$$

where the Euler's formula[1] has been applied and two new change of variables have been used to compact the expression; $S^n = \sin(k_0[r_{jm} - z_{jm}])/(k_0 r_{jm})^n$ and $C^n = \cos(k_0[r_{jm} - z_{jm}])/(k_0 r_{jm})^n$, being the exponent $n = 1, 2, 3, 4$.

The final expression can be re-written into an even more organized form by re-grouping the term with the same interaction range; since its a final expression,

---

[1] $e^{ix} = \cos x + i\sin x$

the changes of variable S^n and C^n have been undone

$$\begin{aligned}\dot{\boldsymbol{p}}_j = \Gamma\hbar k_0\left(\frac{\Omega_0}{2\Delta_0}\right)^2 \sum_{\alpha,\beta}(\hat{\epsilon}^*_{0\alpha}\hat{\epsilon}_{0\beta})\sum_{m\neq j}\Bigg\{&(\hat{\boldsymbol{z}}-\hat{\boldsymbol{r}}_{jm})\,(\delta_{\alpha\beta}-\hat{r}_\alpha\hat{r}_\beta)\,\frac{\sin[k_0(r_{jm}-z_{jm})]}{k_0 r_{jm}}\\ &+[\hat{\boldsymbol{z}}\,(\delta_{\alpha\beta}-3\hat{r}_\alpha\hat{r}_\beta)-2\hat{\boldsymbol{r}}_{jm}\,(\delta_{\alpha\beta}-2\hat{r}_\alpha\hat{r}_\beta)]\,\frac{\cos[k_0(r_{jm}-z_{jm})]}{(k_0 r_{jm})^2}\\ &-(\hat{\boldsymbol{z}}-3\hat{\boldsymbol{r}}_{jm})\,(\delta_{\alpha\beta}-3\hat{r}_\alpha\hat{r}_\beta)\,\frac{\sin[k_0(r_{jm}-z_{jm})]}{(k_0 r_{jm})^3}\\ &+3\hat{\boldsymbol{r}}_{jm}\,(\delta_{\alpha\beta}-3\hat{r}_\alpha\hat{r}_\beta)\,\frac{\cos[k_0(r_{jm}-z_{jm})]}{(k_0 r_{jm})^4}\Bigg\}.\end{aligned} \tag{B.22}$$

Remember that for simplification the unit vector between two atoms have simplified, so in this expression $\hat{r}_\alpha$ and $\hat{r}_\beta$, actually represent $(\hat{r}_{jm})_\alpha$ and $(\hat{r}_{jm})_\beta$, respectively.

B.III Radiation field

The α-component of the scattered radiation field amplitude is described by the next expression:

$$E^\alpha_s(\boldsymbol{r},t) = i\frac{V_{ph}}{(2\pi)^3}e^{i(\boldsymbol{k}_0\cdot\boldsymbol{r}-\omega_0 t)}\sum_{\hat{\epsilon}\perp\boldsymbol{k}}\hat{\epsilon}_\alpha\int_{\Delta\boldsymbol{k}} d\boldsymbol{k}\mathcal{E}_k A_{\boldsymbol{k},\hat{\epsilon}}(t)e^{i(\boldsymbol{k}-\boldsymbol{k}_0)\cdot\boldsymbol{r}}, \tag{B.23}$$

where $\mathcal{E}_k = (\hbar\omega_k/2\epsilon_0 V_{ph})^{1/2}$ is the 'single-photon' electric field. Substituting the radiation field attained in Eq.(B.9), it is possible to obtain

$$E^\alpha_s(\boldsymbol{r},t) = \frac{V_{ph}g_k\mathcal{E}_k\Omega_0}{2(2\pi)^3\Delta_0}e^{-i\omega_0 t}\sum_\beta\hat{\epsilon}_{0\beta}\int_0^t d\tau e^{i\omega_0\tau}\sum_{j=1}^N e^{i\boldsymbol{k}_0\cdot\boldsymbol{r}_j}\int_{\Delta\boldsymbol{k}}d\boldsymbol{k}e^{i\boldsymbol{k}\cdot(\boldsymbol{r}-\boldsymbol{r}_j)-ick\tau}\sum_{\hat{\epsilon}\perp\boldsymbol{k}}\hat{\epsilon}_\alpha\hat{\epsilon}^*_\beta. \tag{B.24}$$

As before, the relation described in the last section of this appendix B.IV and referred in Eq. (B.11), is employed to get rid of the right-most sum

$$E^\alpha_s(\boldsymbol{r},t) = \frac{V_{ph}g_k\mathcal{E}_k\Omega_0}{2(2\pi)^3\Delta_0}e^{-i\omega_0 t}\sum_\beta\hat{\epsilon}_{0\beta}\int_0^t d\tau e^{i\omega_0\tau}\sum_{j=1}^N e^{i\boldsymbol{k}_0\cdot\boldsymbol{r}_j} \tag{B.25}$$

$$\int_{\Delta\boldsymbol{k}}d\boldsymbol{k}e^{i\boldsymbol{k}\cdot(\boldsymbol{r}-\boldsymbol{r}_j)-ick\tau}(\delta_{\alpha\beta}-\hat{k}_\alpha\hat{k}_\beta); \tag{B.26}$$

consequently, the integral is evaluated in polar coordinates, using once again the expression proved in Sec. B.IV and regarded in Eq.(B.13):

$$E^\alpha_s(\boldsymbol{r}) = \frac{V_{ph}g_k\mathcal{E}_k\Omega_0}{8\pi^2\Delta_0}e^{-i\omega_0 t}\sum_\beta\hat{\epsilon}_{0\beta}\int_0^t d\tau e^{i\omega_0\tau}\sum_{j=1}^N e^{i\boldsymbol{k}_0\cdot\boldsymbol{r}_j} \tag{B.27}$$

$$\int_0^\infty dk k^2 e^{-ick\tau}\int_{-1}^1 dt\, e^{ik|\boldsymbol{r}-\boldsymbol{r}_j|}\,[\delta_{\alpha\beta}+\hat{r}_\alpha\hat{r}_\beta+t^2(\,\delta_{\alpha\beta}-3\hat{r}_\alpha\hat{r}_\beta)\,]. \tag{B.28}$$

Evaluating the integral in t (second row) and keeping only the term decreasing as $1/kr$ (far-field approximation), the field can be approximated to

$$E_s^\alpha(\boldsymbol{r},t) = -i\frac{V_{ph} g_{k_0} k_0 \mathcal{E}_k \Omega_0}{2\pi\Delta_0 c r} e^{-i\omega_0 t}\sum_\beta(\delta_{\alpha\beta}-\hat{r}_\alpha \hat{r}_\beta)\hat{\epsilon}_{0\beta}\sum_{j=1}^{N} e^{i\boldsymbol{k}_0\cdot\boldsymbol{r}_j} e^{ik_0|\boldsymbol{r}-\boldsymbol{r}_j|}. \tag{B.29}$$

then, by assuming the far field limit $\boldsymbol{r} \gg \boldsymbol{r}_j$, it is viable to write $|\boldsymbol{r}-\boldsymbol{r}_j| \approx r - \hat{\boldsymbol{r}}\cdot\boldsymbol{r}_j$ where $\hat{\boldsymbol{r}} = \boldsymbol{r}/r$ and the field becomes

$$E_s^\alpha(\boldsymbol{k},t) = \frac{dk_0^2}{4\pi\epsilon_0}\frac{\Omega_0}{2\Delta_0}\frac{e^{i(k_0 r-\omega_0 t)}}{ir}\sum_\beta(\delta_{\alpha\beta}-\hat{r}_\alpha \hat{r}_\beta)\hat{e}_{0\beta}\sum_{j=1}^{N} e^{i(\boldsymbol{k}_0-\boldsymbol{k})\cdot\boldsymbol{r}_j} \tag{B.30}$$

where $\boldsymbol{k} = k_0\hat{\boldsymbol{r}}$ and $\hat{\boldsymbol{e}}_0$ is the polarization unit vector of the pump. The expression of the Rayleigh scattering field in the far-field limit, depending on the geometrical configuration of the scattering particles have been ontained, , like in the scalar case derivation [160] (or appendendix of section 5.2).

Lastly, if the latter equation is considered in its vectorial form, the final radiation fields is:

$$\boldsymbol{E}_s(\boldsymbol{k},t) \approx [\hat{\boldsymbol{r}}\times(\hat{\boldsymbol{r}}\times\hat{\boldsymbol{e}}_0)]\frac{dk_0^2}{4\pi\epsilon_0}\frac{\Omega_0}{2\Delta_0}\frac{e^{(k_0 r-\omega_0 t)}}{ir}\sum_{j=1}^{N} e^{i(\boldsymbol{k}_0-\boldsymbol{k})\cdot\boldsymbol{r}_j}. \tag{B.31}$$

which, in conclusion, renders the scattered intensity spatial distribution in the far-field limit is

$$I_s(\boldsymbol{k}) = I_1 N^2 |M(\boldsymbol{k},t)|^2 sin^2\psi, \tag{B.32}$$

where $I_1 = (\hbar\omega_0\Gamma/8\pi r^2)(\Omega_0/2\Delta_0)^2$ is the single-atom Rayleigh scattering intensity and

$$M(\boldsymbol{k},t) = \frac{1}{N}\sum_{j=1}^{N} e^{i(\boldsymbol{k}_0-\boldsymbol{k})\cdot\boldsymbol{r}_j(t)} \tag{B.33}$$

is the 'optical magnetization', or 'bunching factor'.

Notice that, when defining the scattered intensity there is an additional factor $sin^2\psi$ (coming from $1-cos^2\psi$), when comparing with the scalar model. The angle φ is the angle between the polarization of the pump ($\hat{\epsilon}_0$) and the scattering direction ($\boldsymbol{k}$). It comes from the extra polarization factor derived in the vectorial expression of the field (B.31), i.e., $\hat{\boldsymbol{r}}\times(\hat{\boldsymbol{r}}\times\hat{\boldsymbol{e}}_0)$, where the scattering intensity is suppressed whenever the polarization is parallel to the main scattering direction, or $\psi = 0$.

B.IV Mathematical expressions demonstration

Equation (B.11)

Following the book by Mandel and Wolf [236], a pair of orthonormal, real vectors $\hat{\boldsymbol{e}}^{(1,2)}$ we select such that $\hat{\boldsymbol{k}}\cdot\hat{\boldsymbol{e}}^{(1,2)}$, $\hat{\boldsymbol{e}}^{(1)*}\cdot\hat{\boldsymbol{e}}^{(2)} = 0$ and $\hat{\boldsymbol{e}}^{(1)}\times\hat{\boldsymbol{e}}^{(2)} = \hat{\boldsymbol{k}}$. The unit vectors $\hat{\boldsymbol{k}}$, $\hat{\boldsymbol{e}}^{(1)}$ and $\hat{\boldsymbol{e}}^{(2)}$ form an orthogonal Cartesian basis. In general, since the elliptical polarization is also considered, $\hat{\boldsymbol{e}}^{(1,2)}$ can be complex. However, when real, the components $\hat{e}_\alpha^{(1)}$, $\hat{e}_\alpha^{(2)}$ and $\hat{k}_\alpha$ are the three direction cosines of the α-axis of the basis (with $\alpha = x, y, z$). Resulting from the well-known direction cosines properties, the general orthogonality condition for the cosines of the angle between the α-axis and the β-axis (where $\alpha, \beta = x, y, z$) can be written as

$$\hat{e}_\alpha^{(1)}\hat{e}_\beta^{(1)} + \hat{e}_\alpha^{(2)}\hat{e}_\beta^{(2)} + \hat{k}_\alpha\hat{k}_\beta = \delta_{\alpha\beta}$$

or, rearranging terms, in an equivalent expression as

$$\sum_{s=1,2} \hat{e}_\alpha^{(s)}\hat{e}_\beta^{(s)} = \delta_{\alpha\beta} - \hat{k}_\alpha\hat{k}_\beta, \tag{B.34}$$

where the sum is over the two polarization vectors. In the case of complex polarization vectors, since these can be obtained from an unitary transformation, Eq.(B.34) can be generalized into:

$$\sum_{s=1,2} \hat{e}_\alpha^{(s)}(\hat{e}_\beta^{(s)})^* = \delta_{\alpha\beta} - \hat{k}_\alpha\hat{k}_\beta. \tag{B.35}$$

In order to have an even more general notation to use in the derivations of both sections above, the sum over $\hat{\epsilon} \perp \boldsymbol{k}$ has been added, leaving the final expression stated in Eq.(B.11) as follow:

$$\sum_{\hat{\epsilon}\perp\boldsymbol{k}} \hat{\epsilon}_\alpha(\hat{\epsilon}_\beta)^* = \delta_{\alpha\beta} - \hat{k}_\alpha\hat{k}_\beta. \tag{B.36}$$

Equation (B.13)

The paper by Manassah [237] is followed to achieve the resulting expression when the define integral within the interval $[0, 2\pi]$ is calculated for of $(\delta_{\alpha\beta} - \hat{k}_\alpha\hat{k}_\beta)$ (resulting from the relation from the previous section). Such expression depends on φ (the azimuthal angle between $\hat{\boldsymbol{k}}$ and $\hat{\boldsymbol{r}}$) and $\cos\theta$, being θ the polar angle between $\hat{\boldsymbol{k}}$ and $\hat{\boldsymbol{r}}$. When the polar coordinates are applied to express $\hat{\boldsymbol{k}}$, the z-axis points along $\hat{\boldsymbol{r}}$ and it is possible to write

$$C_{\alpha\beta}(\cos\theta, \hat{r}) = \frac{1}{2\pi}\int_0^{2\pi} d\varphi(\delta_{\alpha\beta} - \hat{k}_\alpha\hat{k}_\beta) = A(\cos\theta)\delta_{\alpha\beta} + B(\cos\theta)\hat{r}_\alpha\hat{r}_\beta \tag{B.37}$$

with A and B to be determined. If the latter expression is considered for a unique α-direction, the first equation to find A and B reads

$$\sum_\alpha C_{\alpha\alpha} = 3A + B = \frac{1}{2\pi}\int_0^{2\pi} d\varphi\left(3 - \sum_\alpha \hat{k}_\alpha^2\right) = \frac{1}{2\pi}\int_0^{2\pi} d\varphi(3-1) = 2 \tag{B.38}$$

since $\sum_\alpha \hat{r}_\alpha^2 = \sum_\alpha \hat{k}_\alpha^2 = 1$. The second equation need it to find the value of the two parameters comes from two different derivations of the same expression:

$$\sum_{\alpha,\beta} C_{\alpha\beta}\hat{r}_\alpha\hat{r}_\beta = \sum_{\alpha,\beta}(A\delta_{\alpha\beta}+B\hat{r}_\alpha\hat{r}_\beta)\hat{r}_\alpha\hat{r}_\beta = A\sum_\alpha \hat{r}_\alpha^2 + B\left(\sum_\alpha \hat{r}_\alpha^2\right)\left(\sum_\beta \hat{r}_\beta^2\right) = A+B, \tag{B.39}$$

$$\sum_{\alpha,\beta} C_{\alpha\beta}\hat{r}_\alpha\hat{r}_\beta = \frac{1}{2\pi}\sum_{\alpha,\beta}\int_0^{2\pi} d\varphi\left(\delta_{\alpha\beta}-\hat{k}_\alpha\hat{k}_\beta\right)\hat{r}_\alpha\hat{r}_\beta = 1-\left(\sum_\alpha \hat{k}_\alpha\hat{r}_\alpha\right)\left(\sum_\beta \hat{k}_\beta\hat{r}_\beta\right) = 1-\cos^2\theta, \tag{B.40}$$

where it has been exploited the fact that $\sum_\alpha \hat{k}_\alpha\hat{r}_\alpha = \hat{\boldsymbol{k}}\cdot\hat{\boldsymbol{r}} = \cos\theta$. Therefore, equating both expressions ((B.39) and (B.40)), the second equation is achieve. Hence, the values of A and B come from the result of the following determined system of two equations and two unknowns:

$$3A + B = 2, \tag{B.41}$$

$$A + B = 1 - \cos^2\theta \tag{B.42}$$

so that

$$A = \frac{1}{2}(1+\cos^2\theta) \tag{B.43}$$

$$B = \frac{1}{2}(1-3\cos^2\theta) \tag{B.44}$$

and giving the final results stated in Eq. (B.13) of Sec. B.II

$$\frac{1}{2\pi}\int_0^{2\pi} d\varphi(\delta_{\alpha\beta}-\hat{k}_\alpha\hat{k}_\beta) = \frac{1}{2}\left[(1+\cos^2\theta)\delta_{\alpha\beta} + (1-3\cos^2\theta)\hat{r}_\alpha\hat{r}_\beta\right]. \tag{B.45}$$

C Beyond the adiabatic case for atoms optically bound in a line

This appendix section develops the necessary equations to represent a one-dimensional chain of atoms, constrained to move along one dimension. Eqs. (C.1), (C.2) and (C.3), refer to the Eqs. (3.6), (3.2) and (3.3), respectivelly, introduced in the third Chapter of this thesis. Once more, the following derivation are the work of Nicola Piovella annd the author of this PhD thesis has contributed to adjust the text to improve its readability and to solve numerically the final equations.

C.I Setup and basic equations

An ensemble of N atoms with atomic transition of linewidth Γ and frequency ω_0 is considered. It is confined along the x axis by two pairs of standing wave along the transverse direction y and z, with wavevector $\boldsymbol{k}$, Rabi frequency $\Omega \ll \Gamma$ and detuned from the atomic transition by $\Delta = \omega - \omega_0$. The resonant dynamics of the atomic dipoles β_j is given by a set of N coupled equations:

$$\dot{\beta}_j = \left(i\Delta - \frac{\Gamma}{2}\right)\beta_j - i\Omega(\mathbf{r}_j) - \frac{\Gamma}{2}\sum_{m\neq j} G_{jm}\beta_m, \tag{C.1}$$

where

$$G_{jm} = \frac{\exp ik\,|z_j - z_m|}{ik|z_j - z_m|}, \tag{C.2}$$

describes the light-mediated interaction between the dipoles. The dynamics of the atoms center of mass couples to that of the dipoles:

$$m\ddot{\boldsymbol{r}}_j = -\hbar\Gamma k^2 \sum_{m\neq j} \Im\left(\partial_{x_j} G_{jm}\beta_j^*\beta_m\right) = -\hbar\Gamma \sum_{m\neq j} \frac{\hat{u}_{jm}}{q_{jm}^2}\Re\left[\left(1 - iq_{jm}\right)e^{iq_{jm}}\beta_j^*\beta_m\right], \tag{C.3}$$

with $q_j = kz_j$, $q_{jm} = k\,|z_j - z_m|$ and

$$\hat{u}_{jm} = \begin{cases} +1 & if \quad z_j > z_m \\ -1 & if \quad z_j < z_m \\ 0 & if \quad z_j = z_m \end{cases} \tag{C.4}$$

The existence of a short-range potential or a cutt-off parameter is assumed (see Sec.2.3), such that atoms can not cross each other. In this way, the ordering imprinted to the initial configuration, with $z_1 < z_2 \; \cdots < z_N$, does not change during the dynamics.

C.II Synchronization ansatz

The atomic dipoles are assumed to be synchronized after a short transient, with

$j = s$ for all $j = 1, \cdots, N$, which reduces Eqs. (C.1) and (C.3) to:

$$\dot{\beta}_s = \left[-\frac{1}{2}\left(1+\gamma_N\right) + i\left(\delta + \frac{1}{2}\omega_N\right)\right]\beta_s - i\frac{\Omega}{\Gamma} \tag{C.5}$$

$$\ddot{q}_j = -\frac{2\omega_r}{\Gamma}\sum_{m\neq j}\hat{u}_{jm}\left(\frac{\sin q_{jm}}{q_{jm}} + \frac{\cos q_{jm}}{q_{jm}^2}\right)|\beta_s|^2 \tag{C.6}$$

where the time t has been scaled the in $1/\Gamma$ units and with

$$\gamma_N = \frac{1}{N}\sum_j\sum_{m\neq j}\frac{\sin q_{jm}}{q_{jm}} \tag{C.7}$$

$$\omega_N = \frac{1}{N}\sum_j\sum_{m\neq j}\frac{\cos q_{jm}}{q_{jm}} \tag{C.8}$$

C.III Non adiabatic approximation and friction term

Defining

$$g(t) = \gamma_N - i\omega_N = \frac{1}{N}\sum_j\sum_{m\neq j}\frac{e^{iq_{jm}}}{q_{jm}} \tag{C.9}$$

and following the approximation and derivations exposed in the appendix of the annexed paper in Sec. 5.1, it can we written that the dipole moment is

$$\beta(t) \approx -i\frac{2\Omega}{\Gamma}\frac{1}{-2i\delta + g(t)]}\left\{1 + \frac{2\dot{g}(t)}{[1-2i\delta+g(t)]^2}\right\}. \tag{C.10}$$

where

$$\dot{g}(t) = \frac{1}{N}\sum_j\sum_{m\neq j}\left[\left(\frac{\cos q_{jm}}{q_{jm}} - \frac{\sin q_{jm}}{q_{jm}^2}\right) + i\left(\frac{\sin q_{jm}}{q_{jm}} + \frac{\cos q_{jm}}{q_{jm}^2}\right)\right]\dot{q}_{jm} \tag{C.11}$$

being $\dot{q}_{jm} = \dot{q}_j - \dot{q}_m$. Considering $\dot{q}_{jm}$ at the first order, the following equation for the dynamics of each of the N atoms in a line can be obtained:

$$\ddot{q}_j = -\varepsilon^2\left(1+\lambda_N\right)\sum_{m\neq j} w(q_{jm})\hat{u}_{jm} \tag{C.12}$$

with the function w and the friction coefficient λ_N defined as

$$w(q_{jm}) = \frac{1}{D_N}\left(\frac{\sin(q_{jm})}{q_{jm}} + \frac{\cos(q_{jm})}{q_{jm}}^2\right), \tag{C.13}$$

$$\lambda_N = \frac{1}{N}\frac{4}{D_N}\sum_j\sum_{m\neq j}\left\{\frac{\cos(q_{jm})}{q_{jm}} - \frac{\sin(q_{jm})}{q_{jm}^2} - 2w(q_{jm})\left(1+\gamma_N\right)\left(2\delta+\omega_N\right)\right\}, \tag{C.14}$$

where

$$D_N = \left(2\delta+\omega_N\right)^2 + \left(1+\gamma_N\right)^2 \tag{C.15}$$

D Forcing dipoles synchronism in an atomic string

The dynamic behaviour of a cold molecule ($N = 2$) formed by the effect of the optical binding is completely different from that observed in a larger system ($N \geq 3$). The cause has been reduced to the unsynchronized oscillation of the dipoles that form the chains, as shown in Fig 3.4 of Sec. 3.4.1. For that reason, the current appendix studies how the one-dimensional system of a chain of atoms optically bound, introduced in 3.3.2, would behave if all of its dipoles were completely synchronized in a single oscillation.

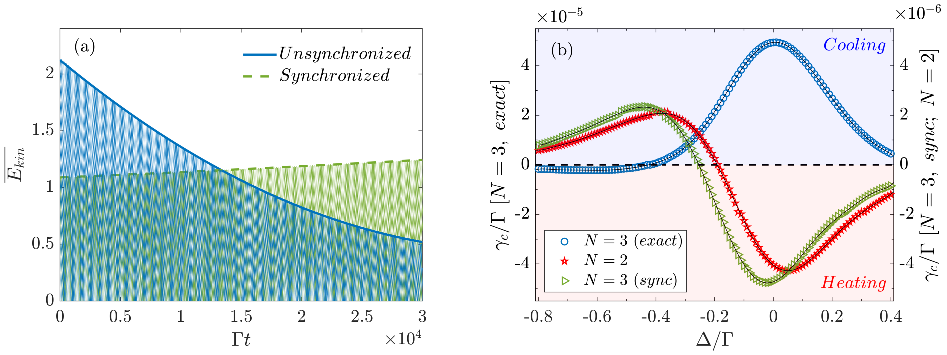

Figure D.1: (a) Shows the dynamics of kinetic energy for $N = 3$ atoms, comparing the exact dipole dynamics obtained from Eqs.((3.7)) and ((3.4)) with the evolution obtained from the synchronization ansatz. Simulations realized with the optimal detuning for the exact case, $\Delta \approx 0.01\Gamma$. (b) Exposes the cooling/heating rate γ_c/Γ for $N = 3$ atoms for the exact dynamics ('exact') and its comparison with the synchronized dipoles ansatz ('sync'). The same rate for the exact solution of a system with two atoms $N = 2$, which presents a single naturally synchronized dipole, it is also included in (b). The cooling/heating rate has been calculated using the evolution of the kinetic energy envelope until it reaches 90/110% of its initial value.

The closest example to an array of two atoms is studied in Fig. D.1(a), where the evolution of the kinetic energy of a chain of a three atoms is analysed. The panel compares the results of the exact equations of motion (Eqs. 3.14 and 3.15) and the results calculated from a synchronized dipole ansatz. This synchronism is achieved by calculating the mean value of the dipole of all the atoms in each iteration step, subsequently assigning this value to each of the dipoles in the system. The artificially synchronized configuration, used in Fig. D.1(a), shows a heating trend close to resonance, while the dynamics of the fully coupled system evolves in the opposite way, with a cooling mechanism. When these two cases are studied for a range of detuning, with their comparison displayed in Fig. D.1(b) together with an additional curve for a two-atom chain, some observations can be made:

- The ansatz with the three dipoles $N = 3$ synchronized in a single oscillation, seems to behave as the case of two atoms, i.e., like Doopler cooling. Note that in such a mechanism, the resonant light generates a heating process, and the cooling phenomenon is achieved only by negative detuning, the maximum cooling being $\Delta \approx -\Gamma/2$.

- The ansatz follows the same trend traced by the two-atom system, where the dipoles spontaneously synchronize, and this behavior extends to larger chains of atoms. The only difference for larger chains is that the optimal detuning value undergoes a shift towards negative values and is slightly stronger with each atom added to the system. Analyzing the ansatz for larger systems, both the change and the cooling improvement with increasing N are not as strong as in the exact dynamics, shown in Fig. 3.15 in second segment of Sec. 3.5.2.
- Oppositely, the results obtained for the $N = 3$ chains from Eqs. Eqs. 3.14 and 3.15, display the inverse trend: with a slight heating for negative detuning and a cooling maximum closer to resonance, which is twice as large as for the one obtained in the ansatz.

The asynchronism of the dipole for OB systems with more than two atoms ($N \geq 3$), makes it very difficult to solve analytically such systems, instead simulations need to be run to solve then numerically. It means dealing with N coupled external and N internal degrees of freedom, which makes the complexity of the problem scale to equations of N^2 equations. However, despite the apparent more complex dynamics of the 1D chain, it is quite extraordinary that precisely this lack of synchronization translates into a higher cooling rate than that obtained for synchronized systems.

E Collective cooling linear behaviour

The current appendix reviews the response of the one-dimensional array if the cooling rate (γ), which occurs naturally due to the optical binding effect, when an additional artificial damping mechanism is added to the system. This trick will allow you to understand if the addition of an extra cooling mechanism alters the conditions of the spontaneously occurring one. The imposed damping is introduced into the general force that describes the external motion of the atoms, as a viscous force term; is proportional to velocity as $-\zeta v$, so it contributes to the final solution as $exp(-\zeta t)$. The equation of motion with this additional term reads as follows:

$$m\ddot{\mathbf{r}}_j = -\hbar\Gamma \sum_{m\neq j} \Im\left[\nabla_{\mathbf{r}_j} G_{jm}\beta_j^*\beta_m\right] - \zeta\dot{q}_j. \tag{E.1}$$

The first RHS term can be simplified for a system that can only move in one direction. Therefore, the equation can be expressed in a simpler analytical form, where the gradient has been calculated. The new expression for the external motion of atoms reads

$$\ddot{r}_j = -\varepsilon_c^2 \sum_{m\neq j} \frac{\hat{u}_{jm}}{r_{jm}^2}\mathrm{Re}\left[(1-ir_{jm})e^{ir_{jm}}\beta_j^*\beta_m\right] - \zeta\dot{q}_j, \tag{E.2}$$

where the position and time have been changed to $r_j = k_0 r_j$ and $t = \Gamma t$, respectively, and the epsilon represents $\varepsilon_c = \sqrt{2\omega_r/\Gamma}$, as in equation (3.15) in the main text. There are other variables that have been modified or redefined, such as: the distance between the atoms $q_j m = |\boldsymbol{q}_j - \boldsymbol{q}_j|$, the kernel of the dipole-dipole interaction $G_{jm} = exp(ir_{jm}) = ir_{jm}$, and the unit vector of the distance between atoms $\boldsymbol{u}_{jm} = \boldsymbol{q}_{jm}/q_{jm}$.

To facilitate the readability of this manuscript, the couple dipole equations, expressed in Eq. 3.14, are here rephrased

$$\dot{\beta}_j = \left(i\delta - \frac{1}{2}\right)\beta_j - i\frac{\Omega}{\Gamma} - \frac{1}{2}\sum_{m\neq j} G_{jm}\beta_m, \tag{E.3}$$

After all, to get the dynamics of the systems, both the internal and external degrees of freedom are coupled in Eqs. (E.2) and (E.3).

The points obtained for the maximum cooling rate for several 1D-chains ($1 \leq N \leq 30$) in the Fig.3.16 (on page 105), are reproduced in Fig. E.1 using a black trace of asterisks located for the lowest values of γ_N/Γ. These results are first translated manually twice: once adding a constant of $\zeta_b = 1e-4$, represented by the center trace of blue asterisks, and a second time $\zeta_r = 2e-4$, depicted with the upper trace of red asterisks). Then, the solution of the system is obtained by solving both Eq. (E.2) and Eq. (E.3) numerically, representing the ζ_b solution with blue squares and the ζ_r case with red diamonds.

By examining Fig. E.1,small discrepancies can be detected between the translation of the collective damping (coloured asterisk) and its numerical solution (diamonds and squares) can be detected. Disagreements are especially evident for

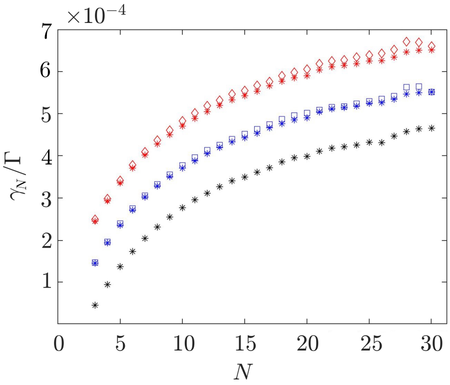

Figure E.1: The circular markers of Fig. 3.16 are represented again employing black asterisks. These latter markers may differ slightly from those used in the quoted figure of Chapter 3, because a different final kinetic energy was fixed. In addition, with red and blue asterisks two manual linear translation from this black tendency of $\zeta_r = 1e - 4$ and $\zeta_b = 2e - 4$ are respectively represented. Both diamonds (red) and square (blue) are obtained by calculating Eqs.(E.2) and (E.3).

larger chains, making points with larger N less accurate with the expected value (blue and red asterisks). Such inaccuracies are due to the way of calculating the cooling rates, which are obtained by extracting the envelope of the oscillating kinetic energy, as described in Secs. 3.4 and 3.5 in the Chapter 3. Despite this error, the asterisks in red and blue, mere translation of the curve represented by black asterisks, coincide quite well with the numerical solution of the system when it is represented numerically using the equations of motion described in the current appendix. Consequently, it can be stated that when an artificial damping is added to the collective cooling, the final total cooling rate is the linear sum of both cooling rates. This statement allows the cooperative cooling described in Sec. 3.5 to be treated as independent cumulative exponential cooling, opening the possibility of using an additional friction mechanism, such as an optical molasses, to control the heating produced by the spontaneous emission.

References

This doctoral thesis has a total of 237 different references, mostly referring to scientific articles published in peer-reviewed journals, but also to books, websites and other doctoral theses. Most of the references are scientific papers that have a *digital object identifier* or *doi*, which is a persistent identifier or handle used to uniquely distinguish digital objects, standardized by the *International Organization for Standardization*. The alphanumeric code that follows the word marked “doi:” from each of these scientific articles has been hyperlinked to the website of the journal that published the essay. Each entry in the chapter that does not have *doi*, because it is a book, website, or other thesis, has also been hyperlinked using the word “link”; whenever it was possible to identify the digital link (all entries without *doi* except one).

[1] R. Bonifacio and L. De Salvo Souza. Collective atomic recoil laser (carl) optical gain without inversion by collective atomic recoil and self-bunching of two-level atoms. *Nuclear Instruments and Methods in Physics Research*, 341(1–3):360–362, March 1994. doi:10.1016/0168-9002(94)90382-4.

[2] Michael M. Burns, Jean-Marc Fournier, and Jene A. Golovchenko. Optical binding. *Physical Review Letters*, 63(12):1233–1236, September 1989. doi:10.1103/physrevlett.63.1233.

[3] N. Bohr Dr. phil. I. on the constitution of atoms and molecules. *The London, Edinburgh, and Dublin Philosophical Magazine and Journal of Science*, 26 (151):1–25, July 1913. doi:10.1080/14786441308634955.

[4] Louis de Broglie. *Recherches sur la théorie des quanta ("Research on Quantum Theory")*. PhD thesis, University of Paris, 1924. (Link).

[5] Claude Cohen-Tannoudji, Jacques Dupont-Roc, and Gilbert Grynberg. *Atom-photon interactions: basic processes and applications*. Wiley-VCH, 1998. ISBN 0471293369. (Link).

[6] John William Strutt Baron Rayleigh. *The theory of sound*. Macmillan and co., 1877. ISBN 9780521784498. (Link).

[7] Gustav Mie. Beiträge zur optik trüber medien, speziell kolloidaler metallösungen. *Annalen der Physik*, 25(3):377–445, 1908. doi:10.1002/andp.19083300302.

[8] H. C. van de Hulst. *Light Scattering by Small Particles*. New York (John Wiley and Sons), London (Chapman and Hall), 1958. ISBN 0486642283. (Link).

[9] Sir Chandrasekhara Venkata Raman. *Molecular diffraction of light*. Univiversity of Calcutta, 1922. ISBN 1341146316. (Link).

[10] Arthur H. Compton. A quantum theory of the scattering of x-rays by light elements. *Physical Review*, 21(5):483–502, May 1923. doi:doi.org/10.1103/PhysRev.21.483.

[11] Sir Joseph John Thomson. *Conduction of electricity through gases*. Cambridge, University Press, 1903. ISBN 1933998490. (Link).

[12] Léon Brillouin. Diffusion de la lumière et des rayons x par un corps transparent homogène. *Annales de Physique*, 9(17):88–122, 1922. doi:10.1051/anphys/192209170088.

[13] The department of physics at the Ohio State University website. Cold atom physics. (Link); Accessed: March 2020.

[14] T.W. Hänsch and A.L. Schawlow. Cooling of gases by laser radiation. *Optics Communications*, 13(1):68–69, January 1975. doi:10.1016/0030-4018(75)90159-5.

[15] D. J. Wineland and H. Dehmelt. Proposed 10^{14} $\delta\nu < \nu$ laser fluorescence spectroscopy on Tl^+ mono-ion oscillator III (sideband cooling). *Bulletin of the American Physical Society*, 20:637, 1975. (Link not available).

[16] W. Phillips and H. Metcalf. Laser deceleration of an atomic beam. *Physical Review Letters*, 48(9):596–599, March 1982. doi:10.1103/PhysRevLett.48.596.

[17] Johannes Kepler. *De cometis libelli tres.* Apergeri, Andreæ, 1619. (Link).

[18] James Clerk Maxwell. On physical lines of force. *The London, Edinburgh, and Dublin Philosophical Magazine and Journal of Science*, 25(4):four–part paper, March 1861. doi:10.1080/14786431003659180. Digitalized original papers (Link 1); original doucment retyped with links to original papers (Link 2).

[19] Peter Lebedew. Untersuchungen über die druckkräfte des lichtes ("studies on the pressure forces of light"). *Annalen der Physik*, 311(11):433–458, January 1901. doi:10.1002/andp.19013111102.

[20] E. F. Nichols and G. F. Hul. The pressure due to radiation. *Proceedings of the American Academy of Arts and Sciences*, 38(20):559–599, January 1903. doi:10.2307/20021808. Also published by (IOP) in The Astrophysical Journal 17(5) - June 1903 and by the American Physical Society (APS), in Physical Review 17(2):91–104, August 1903.

[21] Christian Doppler. Über das farbige licht der doppelsterne und einiger anderer gestirne des himmels - "on the coloured light of the binary stars and some other stars of the heavens". *independently distributed*, 1842. (Link).

[22] Harold J. Metcalf and Peter van der Straten. *Laser cooling and trapping.* Springer Science+Business Media New York, 1999. ISBN 0387987282. (Link).

[23] C. J. Foot. *Atomic Physics.* Oxford university press, 2005. ISBN 0198506961. (Link).

[24] Daniel Adam Steck. Rubidium 85 D Line Data. available online at http://steck.us/alkalidata (revision 2.2.1, 21 November 2019).

[25] S. Chu, L. Hollberg, J. E. Bjorkholm, A. Cable, and A. Ashkin. Three-dimensional viscous confinement and cooling of atoms by resonance radiation pressure. *Physical Review Letters*, 55(1):48–51, July 1985. doi:10.1103/physrevlett.55.48.

[26] D. Sesko, C. G. Fan, and C. E. Wieman. Production of a cold atomic vapor using diode-laser cooling. *Journal of the Optical Society of America B*, 5(6): 1225–1227, June 1988. doi:10.1364/JOSAB.5.001225.

[27] Paul D. Lett, Richard N. Watts, Christoph I. Westbrook, William D. Phillips, Phillip L. Gould, and Harold J. Metcalf. Observation of atoms laser cooled below the doppler limit. *Physical Review Letters*, 61(2):169–172, July 1988. doi:10.1103/PhysRevLett.61.169.

[28] Y. Shevy, D. S. Weiss, and S. Chu. *in Proceedings of the Conference on Spin Polarized Quantum Systems, S S. Stringari, Dipartimento di fisica, Torino, 20-24 June 1988.* World Scientific Pub Co Inc, 1988. ISBN 9971508788. (Link).

[29] Y. Shevy, D. S. Weiss, P. J. Ungar, and Steven Chu. Bimodal speed distributions in laser-cooled atoms. *Physical Review Letters*, 62(10):1118–1121, March 1989. doi:10.1103/PhysRevLett.62.1118.

[30] A. Aspect, E. Arimondo, R. Kaiser, N. Vansteenkiste, and C. Cohen-Tannoudji. Laser cooling below the one-photon recoil energy by velocity-selective coherent population trapping. *Physical Review Letters*, 61(7):826–829, August 1988. doi:10.1103/PhysRevLett.61.826.

[31] J. Dalibard, C. Salomon, A. Aspect, E. Arimondo, R. Kaiser, N. Vansteenkiste, and C. Cohen-Tannoudji. *New Schemes in Laser Cooling, in Proceedings of the 11th International Conferences on Atomic Physics, Gilbert Grynberg and J. C. Gay and S. Haroche, Paris, 4-8 July 1988*. World Scientific Pub Co Inc, 1989. ISBN 9971506386. (Link).

[32] A. Aspect, E. Arimondo, R. Kaiser, N. Vansteenkiste, J. Dalibard, C. Salomon, and C. Cohen-Tannoudji. Laser cooling below the doppler and recoil limits. In *Quantum Electronics and Laser Science Conference*. Optical Society of America, 1989.

[33] C Salomon, J Dalibard, W. D Phillips, A Clairon, and S Guellati. Laser cooling of cesium atoms below 3 μk. *Europhysics Letters (EPL)*, 12(8):683–688, August 1990. doi:10.1209/0295-5075/12/8/003.

[34] P. D. Lett, W. D. Phillips, S. L. Rolston, C. E. Tanner, R. N. Watts, and C. I. Westbrook. Optical molasses. *Journal of the Optical Society of America B*, 6(11):2084–2107, November 1989. doi:10.1364/JOSAB.6.002084.

[35] W. Neuhauser, M. Hohenstatt, P. Toschek, and H. Dehmelt. Optical-sideband cooling of visible atom cloud confined in parabolic well. *Physical Review Letters*, 41(4):233–236, July 1978. doi:10.1103/PhysRevLett.41.233.

[36] F. Diedrich, J. C. Bergquist, Wayne M. Itano, and D. J. Wineland. Laser cooling to the zero-point energy of motion. *Physical Review Letters*, 62(4):403–406, January 1989. doi:10.1103/PhysRevLett.62.403.

[37] M. R. Williams, M. J. Bellanca, L. Liu, C. Xie, W. F. Buell, T. H. Bergeman, and H. J. Metcalf. Atom cooling in one dimension with high-intensity laser light. *Physical Review A*, 57(1):401–411, January 1998. doi:10.1103/PhysRevA.57.401.

[38] Erling Riis, David S. Weiss, Kathryn A. Moler, and Steven Chu. Atom funnel for the production of a slow, high-density atomic beam. *Physical Review Letters*, 64(14):1658–1661, April 1990. doi:10.1103/PhysRevLett.64.1658.

[39] Alain Aspect, Nathalie Vansteenkiste, Robin Kaiser, Helmut Haberland, and Martin Karrais. Preparation of a pure intense beam of metastable helium by laser cooling. *Chemical Physics*, 145(12):307–315, August 1990. doi:10.1016/0301-0104(90)89122-7.

[40] Thad Walker, David Sesko, and Carl Wieman. Collective behavior of optically trapped neutral atoms. *Physical Review Letters*, 64(4):408–411, January 1990. doi:10.1103/PhysRevLett.64.408.

[41] D. J. Wineland, R. E. Drullinger, and F. L Walls. Radiation-pressure cooling of bound resonant absorbers. *Physical Review Letters*, 40(25):1639–1642, June 1978. doi:10.1103/PhysRevLett.40.1639.

[42] E. L. Raab, Steven Chu M. Prentiss, Alex Cable, and D. E. Pritchard. Trapping of neutral sodium atoms with radiation pressure. *Physical Review Letters*, 59(23):2631–2634, December 1987. doi:10.1103/PhysRevLett.59.2631.

[43] J. J. McClelland, A. V. Steele, and B. Lnuffman. Bright focused ion beam sources based on laser-cooled atoms. *Applied Physics Reviews*, 3(1):011302, March 2016. doi:10.1063/1.4944491.

[44] Walter Gerlach and Otto Stern. Der experimentelle nachweis der richtungsquantelung im magnetfeld. *Zeitschrift für Physik*, 9(1):349–352, December 1922. doi:10.1007/BF01326983.

[45] K. Kowalskia, V. Cao Long, K. Dinh Xuan, M. Głódź, B. Nguyen Huy, and J. Szonert. Magneto-optical trap: Fundamentals and realization. *Computational methods in science and technology*, Special Issue(2):115–129, September 2010. doi:10.12921/cmst.2010.SI.02.115-129.

[46] M. Weidemüller, T. Esslinger, M. A. Ol'shanii, A. Hemmerich, and Th. W. Hänsch. A novel scheme for efficient cooling below the photon recoil limit. *Europhysics Letters*, 27(2):109–114, July 1994. doi:10.1209/0295-5075/27/2/006/pdf.

[47] J. Dalibard and C. Cohen-Tannoudji. Dressed-atom approach to atomic motion in laser light: the dipole force revisited. *Journal of the Optical Society of America B*, 2(11):1707–1720, November 1985. doi:10.1364/JOSAB.2.001707.

[48] Naoto Masuhara, John M. Doyle, Jon C. Sandberg, Daniel Kleppner, , and Thomas J. Greytak. Evaporative cooling of spin-polarized atomic hydrogen. *Physical Review Letters*, 61(8):935–938, August 1988. doi:10.1103/PhysRevLett.61.935.

[49] Claude Cohen-Tannoudji. Manipulating atoms with photons. pages 166–190. Nobel prize lecture, December 1997. (Nobel Lecture Link).

[50] William D. Phillips. Laser cooling and trapping of neutral atoms. pages 199–237. Nobel prize lecture, December 1997. (Nobel Lecture Link).

[51] Steven Chu. The manipulation of neutral particles. pages 122–158. Nobel prize lecture, December 1997. (Nobel Lecture Link).

[52] Eric Cornell and Carl Wieman. Bose-einstein condensation in a dilute gas; the first 70 years and some recent experiments. pages 77–108. Nobel prize lecture, December 2001. (Nobel Lecture Link).

[53] Wolfgang Ketterle. When atoms behave as waves: Bose-einstein condensation and the atom laser. pages 118–154. Nobel prize lecture, December 2001. (Nobel Lecture Link).

[54] J. Dalibard and C. Cohen-Tannoudji. Laser cooling below the doppler limit by polarization gradients: simple theoretical models. *Journal of the Optical Society of America B*, 6(11):2023–2045, November 1989. doi:10.1364/JOSAB.6.002023.

[55] S. Chu, D. S. Weiss, Y. Shevy, and P. J. Ungar. *in Proceedings of the 11th International Conferences on Atomic Physics, Gilbert Grynberg and J. C. Gay and S. Haroche, Paris, 4-8 July 1988.* World Scientific Pub Co Inc, 1989. ISBN 9971506386. (Link).

[56] A. Aspect, J. Dalibard, A. Heidmann, C. Salomon, and C. Cohen-Tannoudji. Cooling atoms with stimulated emission. *Physical Review Letters*, 57(14):1688–1691, October 1986. doi:10.1103/PhysRevLett.57.1688.

[57] D. Boiron, C. Triché, D. R. Meacher, P. Verkerk, and G. Grynberg. Three-dimensional cooling of cesium atoms in four-beam gray optical molasses. *Physical Review A*, 52(5):R3425–R3428, November 1995. doi:10.1103/PhysRevA.52.R3425.

[58] A. Hemmerich, M. Weidemüller, T. Esslinger, C. Zimmermann, and T. Hänsch. Trapping atoms in a dark optical lattice. *Physical Review Letters*, 75(1):37–40, July 1995. doi:10.1103/PhysRevLett.75.37.

[59] Wolfgang Ketterle and David E. Pritchard. Atom cooling by time-dependent potentials. *Physical Review A*, 46(7):4051–4054, October 1992. doi:10.1103/PhysRevA.46.4051.

[60] K.B. Davis, M.O. Mewes, and W Ketterle. An analytical model for evaporative cooling of atoms. *Applied Physics B*, 60(2):155–159, February 1995. doi:10.1007/BF01135857.

[61] K. B. Davis, M. O. Mewes, M. R. Andrews, N. J. van Druten, D. S. Durfee, D. M. Kurn, and W. Ketterle. Bose-einstein condensation in a gas of sodium atoms. *Physical Review Letters*, 75(22):3969–3973, November 1995. doi:10.1103/PhysRevLett.75.3969.

[62] Mark Kasevich and Steven Chu. Laser cooling below a photon recoil with three-level atoms. *Physical Review Letters*, 69(12):1741–1744, September 1992. doi:10.1103/PhysRevLett.69.1741.

[63] NASA Jet Propulsion Laboratory California Institute of Technology (NASA/JPL-Caltech). Cold atom laboratory chills atoms to new lows. (Link); accessed: April 2020.

[64] Peter Horak, Gerald Hechenblaikner, Klaus M. Gheri, Herwig Stecher, and Helmut Ritsch. Cavity-induced atom cooling in the strong coupling regime. *Physical Review Letters*, 79(25):4974–4977, December 1997. doi:10.1103/PhysRevLett.79.4974.

[65] Serge Haroche and Daniel Kleppner. Cavity quantum electrodynamics. *Physics Today*, 42(1):24–30, January 1988. doi:10.1063/1.881201.

[66] Paul R. Berman and J. H. Eberly. Cavity quantum electrodynamics. *American Journal of Physics*, 64(2):189–190, February 1996. doi:10.1119/1.18423.

[67] Vladan Vuletić and Steven Chu. Laser cooling of atoms, ions, or molecules by coherent scattering. *Physical Review Letters*, 84(17):3787–3790, April 2000. doi:10.1103/PhysRevLett.84.3787.

[68] Peter Domokos and Helmut Ritsch. Mechanical effects of light in optical resonators. *Journal of the Optical Society of America B*, 20(5):1098–1130, May 2003. doi:10.1364/JOSAB.20.001098.

[69] Stefano Zippilli, Giovanna Morigi, and Helmut Ritsch. Suppression of bragg scattering by collective interference of spatially ordered atoms with a high-q cavity mode. *Physical Review Letters*, 93(12):123002, September 2004. doi:10.1103/PhysRevLett.93.123002.

[70] Stefano Zippilli, Giovanna Morigi, and Helmut Ritsch. Collective effects in the dynamics of driven atoms in a high-q resonator. *The European Physical Journal D - Atomic, Molecular, Optical and Plasma Physics*, 31(3):507–518, December 2004. doi:10.1140/epjd/e2004-00137-8.

[71] Helmut Ritsch, Peter Domokos, Ferdinand Brennecke, and Tilman Esslinger. Cold atoms in cavity-generated dynamical optical potentials. *Reviews of Modern Physics*, 85(2):553–601, April 2013. doi:10.1103/RevModPhys.85.553.

[72] Andrei A. Fotiadi and Patrice Mégret. Cooperative light scattering effects in optical fibers, lasers, and amplifiers. In *Optical Fiber Communication Conference/National Fiber Optic Engineers Conference 2011*, page OMO6. The Optical Society (OSA), March 2011. doi:10.1364/OFC.2011.OMO6.

[73] R. H. Dicke. Coherence in spontaneous radiation processes. *Physical Reveiw*, 93(1):99–100, January 1954. doi:10.1103/PhysRev.93.99.

[74] J. T. Mendonça and R. Kaiser. Photon bubbles in ultracold matter. *Physical Review Letters*, 108(033001):1–5, January 2012. doi:10.1103/PhysRevLett.108.033001.

[75] W. Guerin, M.T. Rouabah, and R. Kaiser. Light interacting with atomic ensembles: collective, cooperative and mesoscopic effects. *Journal of Modern Optics*, pages 1–13, August 2016. doi:10.1080/09500340.2016.1215564.

[76] Deutsches Elektronen-Synchrotron (DESY) internet site. Cooperative effects. (Link); Accessed: March 2020.

[77] T. Bienaimé, S. Bux, E. Lucioni, Ph.W. Courteille, N. Piovella, and R. Kaiser. Observation of a cooperative radiation force in the presence of disorder. *Physical Review Letters*, 104(18):183602, may 2010. doi:10.1103/PhysRevLett.104.183602.

[78] J. M. Raimond, P. Goy, M. Gross, C. Fabre, , and S. Haroche. Collective absorption of blackbody radiation by rydberg atoms in a cavity: An experiment on bose statistics and brownian motion. *Physical Review Letters*, 49 (2):117–120, July 1982. doi:10.1103/PhysRevLett.49.117.

[79] Juha Javanainen. Optical signatures of a tightly confined bose condensate. *Physical Review Letters*, 72(15):2375–2378, April 1994. doi:10.1103/PhysRevLett.72.2375.

[80] N. Skribanowitz, I. P. Herman, J. C. MacGillivray, and M. S. Feld. Observation of dicke superradiance in optically pumped hf gas. *Physical Review Letters*, 30(8):309–312, February 1973. doi:10.1103/PhysRevLett.30.309.

[81] M. Gross, C. Fabre, P. Pillet, and S. Haroche. Observation of near-infrared dicke superradiance on cascading transitions in atomic sodium. *Physical Review Letters*, 36(17):1035–1038, April 1976. doi:10.1103/PhysRevLett.36.1035.

[82] Michelle O. Araújo, Ivor Krešić, Robin Kaiser, and William Guerin. Superradiance in a large and dilute cloud of cold atoms in the linear-optics regime. *Physical Review Letters*, 117(7), August 2016. doi:10.1103/physrevlett.117.073002.

[83] Tom Bienaimé, Nicola Piovella, and Robin Kaiser. Controlled dicke subradiance from a large cloud of two-level systems. *Physical Review Letters*, 108 (12):123602, March 2012. doi:10.1103/physrevlett.108.123602.

[84] M. Gross and S. Haroche. Superradiance: An essay on the theory of collective spontaneous emission. *Physics Reports*, 93(5):301–396, December 1982. doi:10.1016/0370-1573(82)90102-8.

[85] E. Tesio, G. R. M. Robb, T. Ackemann, W. J. Firth, and G.-L. Oppo. Spontaneous optomechanical pattern formation in cold atoms. *Physical Review A*, 86(3):031801, September 2012. doi:10.1103/PhysRevA.86.031801.

[86] Joel A. Greenberg and Daniel J. Gauthier. Steady-state, cavityless, multimode superradiance in a cold vapor. *Physical Review A*, 86(1):013823, July 2012. doi:10.1103/PhysRevA.86.013823.

[87] E. Tesio, G. R. M. Robb, G.-L. Oppo, P. M. Gomes, T. Ackemann, G. Labeyrie, R. Kaiser, and W. J. Firth. Self-organization in cold atomic gases: a synchronization perspective. *Philosophical transactions of the royal society A*, 372(2027):20140002, October 2014. doi:10.1098/rsta.2014.0002.

[88] Peter Domokos and Helmut Ritsch. Collective cooling and self-organization of atoms in a cavity. *Physical Review Letters*, 89(25):253003, December 2002. doi:10.1103/PhysRevLett.89.253003.

[89] Hilton W. Chan, Adam T. Black, and Vladan Vuletić. Observation of collective-emission-induced cooling of atoms in an optical cavity. *Physical Review Letters*, 90(6):063003, February 2003. doi:10.1103/PhysRevLett.90.063003.

[90] Mahdi Hosseini, Yiheng Duan, Kristin M. Beck, Yu-Ting Chen, and Vladan Vuletić. Cavity cooling of many atoms. *Physical Review Letters*, 118(18): 183601, May 2017. doi:10.1103/PhysRevLett.118.183601.

[91] K. Baumann, R. Mottl, F. Brennecke, and T. Esslinger. Exploring symmetry breaking at the dicke quantum phase transition. *Physical Review Letters*, 107 (14):140402, September 2011. doi:10.1103/PhysRevLett.107.140402.

[92] Yong-Chang Zhang, Valentin Walther, and Thomas Pohl. Long-range interactions and symmetry breaking in quantum gases through optical feedback. *Physical Review Letters*, 121(7):073604, August 2018. doi:10.1103/PhysRevLett.121.073604.

[93] G. Labeyrie, E. Tesio, P. M. Gomes, G.-L. Oppo, W. J. Firth, G. R. M. Robb, A. S. Arnold, R. Kaiser, and T. Ackemann. Optomechanical self-structuring in a cold atomic gas. *Nature Photonics*, 8(4):321–325, March 2014. doi:10.1038/nphoton.2014.52.

[94] G. R. M. Robb, E. Tesio, G.-L. Oppo, W. J. Firth, T. Ackemann, and R. Bonifacio. Quantum threshold for optomechanical self-structuring in a bose-einstein condensate. *Physical Review Letters*, 114(17):173903, May 2015. doi:10.1103/PhysRevLett.114.173903.

[95] Bonnie L Schmittberger and Daniel J Gauthier. Spontaneous emergence of free-space optical and atomic patterns. *New Journal of Physics*, 18(10): 103021, October 2016. doi:10.1088/1367-2630/18/10/103021.

[96] Tobias Grießer and Helmut Ritsch. Light-induced crystallization of cold atoms in a 1d optical trap. *Physical Review Letters*, 111(5):055702, August 2013. doi:10.1103/PhysRevLett.111.055702.

[97] M. M. Cola, D. Bigerni, and N. Piovella. Recoil-induced subradiance in an ultracold atomic gas. *Physical Review A*, 79(5):053622, May 2009. doi:10.1103/PhysRevA.79.053622.

[98] D. Pavolini, A. Crubellier, P. Pillet, L. Cabaret, and S. Liberman. Experimental evidence for subradiance. *Physical Review Letters*, 54:1917–1920, April 1985. doi:10.1103/PhysRevLett.54.1917.

[99] William Guerin, Michelle O. Araújo, and Robin Kaiser. Subradiance in a large cloud of cold atoms. *Physical Review Letters*, 116(8):083601, February 2016. doi:10.1103/PhysRevLett.116.083601.

[100] William Guerin and Robin Kaiser. Population of collective modes in light scattering by many atoms. *Physical Review A*, 95(5), May 2017. doi:10.1103/physreva.95.053865.

[101] R. Bonifacio and L. A. Lugiato. Cooperative radiation processes in two-level systems: Superfluorescence. *Physical Review A*, 11(5):1507–1521, May 1975. doi:10.1103/PhysRevA.11.1507.

[102] R. Bonifacio and L. A. Lugiato. Cooperative radiation processes in two-level systems: Superfluorescence. ii. *Physical Review A*, 12(2):587–598, August 1975. doi:10.1103/PhysRevA.12.587.

[103] P. W. Anderson. Absence of diffusion in certain random lattices. *Physical Review*, 109(5):1492–1505, March 1958. doi:10.1103/physrev.109.1492.

[104] D. S. Wiersma, P. Bartolini, A. Lagendijk, and R. Righini. Localization of light in a disordered medium. *Nature*, 390(6661):671–673, December 1997. doi:10.1038/37757.

[105] Martin Störzer, Peter Gross, Christof M. Aegerter, and Georg Maret. Observation of the critical regime near anderson localization of light. *Physical Review Letters*, 96(6):063904, February 2006. doi:10.1103/PhysRevLett.96.063904.

[106] Philip W. Anderson. The question of classical localization a theory of white paint? *Philosophical Magazine B*, 52(3):505–509, March 1985. doi:10.1080/13642818508240619.

[107] T. Sperling, W. Bührer, C. M. Aegerter, and G. Maret. Direct determination of the transition to localization of light in three dimensions. *Nature Photonics*, 7(1):48–52, December 2012. doi:10.1038/nphoton.2012.313.

[108] T Sperling, L Schertel, M Ackermann, G J Aubry, C M Aegerter, and G Maret. Can 3D light localization be reached in 'white paint' ? *New Journal of Physics*, 18(1):013039, January 2016. doi:10.1088/1367-2630/18/1/013039.

[109] S. E. Skipetrov and I. M. Sokolov. Absence of anderson localization of light in a random ensemble of point scatterers. *Physical Review Letters*, 112(2): 023905, January 2014. doi:10.1103/physrevlett.112.023905.

[110] L. Bellando, A. Gero, E. Akkermans, and R. Kaiser. Cooperative effects and disorder: A scaling analysis of the spectrum of the effective atomic hamiltonian. *Physical Review A*, 90(6):063822, December 2014. doi:10.1103/physreva.90.063822.

[111] Yasuo Kuga and Akira Ishimaru. Retroreflectance from a dense distribution of spherical particles. *Journal of the Optical Society of America A*, 1(8):831, August 1984. doi:10.1364/JOSAA.1.000831.

[112] Meint P. van Albada and Ad Lagendijk. Observation of weak localization of light in a random medium. *Physical Review Letters*, 55:2692–2695, Dec 1985. doi:10.1103/PhysRevLett.55.2692.

[113] G. Labeyrie, F. de Tomasi, J.-C. Bernard, C. A. Müller, C. Miniatura, and R. Kaiser. Coherent backscattering of light by cold atoms. *Physical Review Letters*, 83(25):5266–5269, December 1999. doi:10.1103/physrevlett.83.5266.

[114] M.O. Scully, E. Fry, C.H.R. Ooi, and K. Wodkiewicz. Directed spontaneous emission from an extended ensemble of n atoms: Timing is everything. *Physical Review Letters*, 96(1):010501, January 2006. doi:10.1103/PhysRevLett.96.010501.

[115] M. O. Scully. Correlated spontaneous emission on the volga. *Laser Physics*, 17(5):635–646, May 2007. doi:10.1134/S1054660X07050064.

[116] Rafael A. de Oliveira, Milrian S. Mendes, Weliton S. Martins, Pablo L. Saldanha, José W. R. Tabosa, and Daniel Felinto. Single-photon superradiance in cold atoms. *Physical Review A*, 90(2), August 2014. doi:10.1103/physreva.90.023848.

[117] H. Bender, C. Stehle, S. Slama, R. Kaiser, N. Piovella, C. Zimmermann, and Ph. W. Courteille. Observation of cooperative mie scattering from an ultracold atomic cloud. *Physical Review A*, 82(1):011404, July 2010. doi:10.1103/PhysRevA.82.011404.

[118] Ph. W. Courteille, S. Bux, E. Lucioni, K. Lauber, T. Bienaimé, R. Kaiser, and N. Piovella. Modification of radiation pressure due to cooperative scattering of light. *he European Physical Journal D*, 58(1):69–73, may 2010. doi:10.1140/epjd/e2010-00095-6.

[119] S. Bux, E. Lucioni, H. Bender, T. Bienaimé, K. Lauber, C. Stehle, C. Zimmermann, S. Slama, Ph.W. Courteille, N. Piovella, and R. Kaiser. Cooperative scattering by cold atoms. *Journal of Modern Optics*, 57(19):1841–1848, November 2010. doi:10.1080/09500340.2010.503011.

[120] Willis E. Lamb and Robert C. Retherford. Fine structure of the hydrogen atom by a microwave method. *Physical Review*, 72:241–243, August 1947. doi:10.1103/PhysRev.72.241.

[121] Claude Cohen-Tannoudji. Fine structure of the hydrogen atom. pages 286–295. Nobel prize lecture, December 1955. (Nobel Lecture Link).

[122] R. Friedberg, S. R. Hartmann, and J. T. Manassah. Frequency shifts in emission and absorption by resonant systems ot two-level atoms. *Physics Reports*, 7(3):101–179, March 1973. doi:10.1016/0370-1573(73)90001-X.

[123] R. Friedberg and J. T. Manassah. Effects of including the counterrotating term and virtual photons on the eigenfunctions and eigenvalues of a scalar photon collective emission theory. *Physics Letters A*, 372(14):2514–2521, March 2008. doi:10.1016/j.physleta.2007.11.064.

[124] R. Röhlsberger, K. Schlage, B. Sahoo, S. Couet, and R. Rüffer. Collective lamb shift in single-photon superradiance. *Science*, 328(5983):1248–1251, June 2010. doi:10.1126/science.1187770.

[125] Marlan O.Scully. Collective lamb shift in single photon dicke superradiance. *Physical Review Letters*, 102(143601), January 2009. doi:10.1103/PhysRevLett.102.143601.

[126] Paul Adrien Maurice Dirac. The quantum theory of the electron. *Proceedings of the Royal Society A*, 117(778):610–624, February 1928. doi:10.1098/rspa.1928.0023.

[127] R. Bonifacio, L. De Salvo, L. M. Narducci, and E. J. D'Angelo. Exponential gain and self-bunching in a collective atomic recoil laser. *Physical Review A*, 50(2):1716–1724, August 1994. doi:10.1103/PhysRevA.50.1716.

[128] R. Bonifacio and L. De Salvo. Collective resonant compton scattering by two-level particles. *Optics Communications*, 115(5–6):505–510, April 1995. doi:10.1016/0030-4018(95)00011-V.

[129] John M. J. Madey. Stimulated emission of bremsstrahlung in a periodic magnetic field. *AIP Journal of Applied Physics*, 42(5):1906–1913, April 1971. doi:10.1063/1.1660466.

[130] R. Bonifacio and F. Casagrande. Instabilities and quantum initiation in the free-electron laser. *Optics Communications*, 50(4):251–255, June 1984. doi:10.1016/0030-4018(84)90327-4.

[131] R. Bonifacio, C. Pellegrini, and L. M. Narducci. Collective instabilities and high-gain regime in a free electron laser. *Optics Communications*, 50(6): 373–378, July 1984. doi:10.1016/0030-4018(84)90105-6.

[132] Rodolfo Bonifacio and Federico Casagrande. Classical and quantum treatment of amplifier and superradiant free-electron laser dynamics. *Journal of the Optical Society of America B*, 2(1):250–258, September 1985. doi:10.1364/JOSAB.2.000250.

[133] S. Inouye, A. P. Chikkatur, D. M. Stamper-Kurn, J. Stenger, D. E. Pritchard, and W. Ketterle. Superradiant rayleigh scattering from a bose-einstein condensate. *Science*, 285(5427):571–574, July 1999. doi:10.1126/science.285.5427.571.

[134] P. R. Hemmer, N. P. Bigelow, D. P. Katz, M. S. Shahriar, L. DeSalvo, and R. Bonifacio. Self-organization, broken symmetry, and lasing in an atomic vapor: The interdependence of gratings and gain. *Physical Review Letters*, 77(8):1468–1471, August 1996. doi:10.1103/PhysRevLett.77.1468.

[135] J.-Y. Courtois, G. Grynberg, B. Lounis, and P. Verkerk. Recoil-induced resonances in cesium: An atomic analog to the free-electron laser. *Physical Review Letters*, 72(19):3017–3020, May 1994. doi:10.1103/PhysRevLett.72.3017.

[136] J. Guo, P. R. Berman, B. Dubetsky, and G. Grynberg. Recoil-induced resonances in nonlinear spectroscopy. *Physical Review A*, 46(3):1426–1437, August 1992. doi:10.1103/PhysRevA.46.1426.

[137] J. Guo and P. R. Berman. Recoil-induced resonances in pump-probe spectroscopy including effects of level degeneracy. *Physical Review A*, 47(5):4128–4142, May 1993. doi:10.1103/PhysRevA.47.4128.

[138] B. Dubetsky and P. R. Berman. Soft x-ray amplification via resonant backward scattering from relativistic particle beams. *Physical Review Letters*, 74 (16):3149–3152, April 1995. doi:10.1103/PhysRevLett.74.3149.

[139] D. Kruse, C. von Cube, C. Zimmermann, and Ph. W. Courteille. Observation of lasing mediated by collective atomic recoil. *Physical Review Letters*, 91(18): 183601, October 2003. doi:10.1103/PhysRevLett.91.183601.

[140] P. R. Berman. Comparison of recoil-induced resonances and the collective atomic recoil laser. *Physical Review A*, 59(1):585–596, January 1999. doi:10.1103/PhysRevA.59.585.

[141] G. L. Lippi, G. P. Barozzi, S. Barbay, and J. R. Tredicce. Spontaneous generation of a longitudinal atomic density grating in sodium vapor. *Physical Review Letters*, 76(14):2452–2455, April 1996. doi:10.1103/PhysRevLett.76.2452.

[142] D. Kruse, M. Ruder, J. Benhelm, C. von Cube, C. Zimmermann, Ph. W. Courteille, Th. Elsässer, B. Nagorny, and A. Hemmerich. Cold atoms in a high-q ring cavity. *Physical Review A*, 67(5):051802, May 2003. doi:10.1103/PhysRevA.67.051802.

[143] C. von Cube, S. Slama, D. Kruse, C. Zimmermann, Ph. W. Courteille, G. R. M. Robb, N. Piovella, and R. Bonifacio. Self-synchronization and dissipation-induced threshold in collective atomic recoil lasing. *Physical Review Letters*, 93(8):083601, August 2004. doi:10.1103/PhysRevLett.93.083601.

[144] J. Javaloyes, M. Perrin, and A Politi. Collective atomic recoil laser as a synchronization transition. *Physical Review E*, 78(1):011108, July 2008. doi:10.1103/PhysRevE.78.011108.

[145] Yoshiki Kuramoto. Cooperative dynamics of oscillator community: A study based on lattice of rings. *Progress of Theoretical Physics Supplement*, 79: 223–240, February 1984. doi:10.1143/PTPS.79.223.

[146] Ph. W. Courteille, C. von Cube, B. Deh, D. Kruse, A. Ludewig, S. Slama, and C. Zimmermann. The collective atomic recoil laser. *(AIP) Conference Procedings*, 770(1):135–143, May 2005. doi:10.1063/1.1928848.

[147] S. Slama, S. Bux, G. Krenz, C. Zimmermann, and Ph. W. Courteille. Superradiant rayleigh scattering and collective atomic recoil lasing in a ring cavity. *Physical Review Letters*, 98(5), February 2007. doi:10.1103/physrevlett.98.053603.

[148] Sebastian Slama, Gordon Krenz, Simone Bux, Claus Zimmermann, and Philippe W. Courteille. Cavity-enhanced superradiant rayleigh scattering with ultracold and bose-einstein condensed atoms. *Physical Review A*, 75(6): 063620, June 2007. doi:10.1103/PhysRevA.75.063620.

[149] M. G. Moore and P. Meystre. Effects of atomic diffraction on the collective atomic recoil laser. *Physical Review A*, 58(4):3248–3258, October 1998. doi:10.1103/PhysRevA.58.3248.

[150] M. G. Moore and P. Meystre. Theory of superradiant scattering of laser light from bose-einstein condensates. *Physical Review Letters*, 83(25):5202–5205, December 1999. doi:10.1103/PhysRevLett.83.5202.

[151] N. Piovella, R. Bonifacio, B. W. J. McNeil, and G. R. M. Robb. Superradiant light scattering and grating formation in cold atomic vapours. *Optics Communications*, 187(1–3):165–170, January 2001. doi:10.1016/S0030-4018(00)01106-8.

[152] N. Piovella, M. Gatelli, and R. Bonifacio. Quantum effects in the collective light scattering by coherent atomic recoil in a bose–einstein condensate. *Optics Communications*, 194(1–3):167–173, July 2001. doi:10.1016/S0030-4018(01)01293-7.

[153] R Bonifacio, M. M Cola, N Piovella, and G. R. M Robb. A quantum model for collective recoil lasing. *Europhysics Letters (EPL)*, 69(1):55–60, January 2005. doi:10.1209/epl/i2004-10308-1.

[154] N. Piovella. Two-dimensional quantum theory of collective light scattering from bose–einstein condensates. *Laser Physics*, 13(4):611–618, 2003.

[155] N. Piovella, M. Cola, and R. Bonifacio. Quantum fluctuations and entanglement in the collective atomic recoil laser using a bose-einstein condensate. *Physical Review A*, 67(1):013817, January 2003. doi:10.1103/PhysRevA.67.013817.

[156] R. Bonifacio, N. Piovella, G. R. M. Robb, and M. M. Cola. Propagation effects in the quantum description of collective recoil lasing. *Optics Communications*, 252(4–6):381–396, August 2005. doi:10.1016/j.optcom.2005.04.037.

[157] G. R. M. Robb, N. Piovella, A. Ferraro, R. Bonifacio, Ph. W. Courteille, and C. Zimmermann. Collective atomic recoil lasing including friction and diffusion effects. *Physical Review A*, 69(4):041403, April 2004. doi:10.1103/PhysRevA.69.041403.

[158] D. Schmidt, H. Tomczyk, S. Slama, and C. Zimmermann. Dynamical instability of a bose-einstein condensate in an optical ring resonator. *Physical Review Letters*, 112(11):115302, March 2014. doi:10.1103/PhysRevLett.112.115302.

[159] H. Tomczyk, D. Schmidt, C. Georges, S. Slama, and C. Zimmermann. Stability diagram of the collective atomic recoil laser with thermal atoms. *Physical Review A*, 91(6):063837, June 2015. doi:10.1103/PhysRevA.91.063837.

[160] R. Ayllon, J. T. Mendonça, A. T. Gisbert, N. Piovella, and G. R. M. Robb. Multimode collective scattering of light in free space by a cold atomic gas. *Physical Review A*, 100(2):023630, August 2019. doi:10.1103/PhysRevA.100.023630.

[161] Johannes Diderik van der Waals. *Over de Continuiteit van den Gas- en Vloeistoftoestand (on the continuity of the gas and liquid state)*. PhD thesis, Leiden University, 1873. (Link).

[162] James Cleark Maxwell. O ver de contimiiteit van den gas- en vloeistofioc-stand academisch proefschrift (about the contimacy of the gas and liquid condition academic thesis). *Nature*, 10(259):477–480, October 1874. doi:10.1038/010477a0.

[163] Johannes Diderik van der Waals. The equation of state for gases and liquids. Nobel prize lecture, 1910. Nobel Lecture.

[164] Philip McCord Morse. Diatomic molecules according to the wave mechanics. ii. vibrational levels. *Physical Review*, 34(1):57–64, July 1929. doi:10.1103/PhysRev.34.57.

[165] John Edward Lennard-Jones. On the determination of molecular fields. —ii. from the equation of state of a gas. *Proceedings of the Royal Society A*, 106 (706):463–477, October 1924. doi:10.1098/rspa.1924.0082.

[166] Adolf Kratzer. Die ultraroten rotationsspektren der halogenwasserstoffe (the ultra red rotation spectra of the hydrogen halide). *Zeitschrift für Physik*, 3 (5):289–307, September 1920. doi:10.1007/BF01327754.

[167] Teik-Cheng Lim. Long range relationship between morse and lennard–jones potential energy functions. *Molecular Physics*, 105(8):1013–1018, December 2007. doi:10.1080/00268970701261449.

[168] Teik-Cheng Lim. The relationship between lennard-jones (12-6) and morse potential functions. *Zeitschrift für Naturforschung A*, 58(11):615–617, June 2014. doi:10.1515/zna-2003-1104.

[169] H. C. Plummer. On the problem of distribution in globular star clusters: (plate 8.). *Monthly Notices of the Royal Astronomical Society*, 71(5):460–470, March 1911. doi:https://doi.org/10.1093/mnras/71.5.460.

[170] Herwig Dejonghe. A completely analytical family of anisotropic plummer models. *Monthly Notices of the Royal Astronomical Society*, 224(1):13–39, January 1987. doi:10.1093/mnras/224.1.13.

[171] M. Baes and H. Dejonghe. The hernquist model revisited: Completely analytical anisotropic dynamical models. *Astronomy and Atrophysics (A&A)*, 393(2):485–497, October 2002. doi:10.1051/0004-6361:20021064.

[172] J. Barnes and P. Hut. A hierarchical o(n log n) force-calculation algorithm. *Nature*, 324(6096):446–449, July 1986. doi:10.1038/324446a0.

[173] Loup Verlet. Computer "experiments" on classical fluids. i. thermodynamical properties of lennard-jones molecules. *Physical Review*, 159(1):98–103, July 1967. doi:10.1103/PhysRev.159.98.

[174] Binbin Li. Error propagation of verlet algorithm. (Link), September 2014.

[175] M. Hofmann, G. Rünger, P. Gibbon, and R. Speck. Parallel sorting algorithms for optimizing particle simulations. In *2010 IEEE International Conference On Cluster Computing Workshops and Posters (CLUSTER WORKSHOPS)*, pages 1–8, 2010. doi:10.1109/CLUSTERWKSP.2010.5613105. ISBN Information: 978-1-4244-8397-6.

[176] Richard Feynman, Robert Leighton, and Matt Sands. *The Feynman Lectures on Physics*. Addison–Wesley, 1964. ISBN 0201021153. (Link).

[177] R. W. Hockney and J. W. Eastwood. *Computer Simulation Using Particles*. Taylor & Francis, 1988. ISBN 0852743920.

[178] Several contributing authors (Link). Frequently Asked Questions of DifferentialEquations.jl. Accessed: July 2020.

[179] Nisha Chandramoorthy and Jerry Chun-Ping Wang. Jamd : Julia-accelerated molecular dynamics. pages 1–10. Semantic Scholar, 2015. Corpus ID: 52972603. (Link).

[180] Several contributing authors (Link with list). Dynamical, hamiltonian, and 2nd order ode solvers. (Link); accessed: July 2020.

[181] MATLAB. *version 9.6.0.1335978 (R2019a)*. The MathWorks Inc., Natick, Massachusetts, 2010. (Link).

[182] Christopher Rackauckas and Qing Nie. Differentialequations. jl–a performant and feature-rich ecosystem for solving differential equations in julia. *Journal of Open Research Software*, 5(1), 2017. doi:10.5334/jors.151.

[183] Dominik Schneble, Yoshio Torii, Micah Boyd, Erik W. Streed, David E. Pritchard, and Wolfgang Ketterle. The onset of matter-wave amplification in a superradiant bose-einstein condensate. *Science*, 300(5618):475–478, April 2003. doi:10.1126/science.1083171.

[184] S. Giovanazzi, D. O'Dell, and G. Kurizki. Density modulations of bose-einstein condensates via laser-induced interactions. *Physical Review Letters*, 88(13):130402, March 2002. doi:10.1103/PhysRevLett.88.130402.

[185] Noam Matzliah, Hagai Edri, Asif Sinay, Roee Ozeri, and Nir Davidson. Observation of optomechanical strain in a cold atomic cloud. *Physical Review Letters*, 119(16), October 2017. doi:10.1103/physrevlett.119.163201.

[186] T. Thirunamachandran. Intermolecular interactions in the presence of an intense radiation field. *Molecular Physics*, 40(2):393–399, June 1980. doi:10.1080/00268978000101561.

[187] A Ashkin and J. Dziedzic. Optical trapping and manipulation of viruses and bacteria. *Science*, 235(4795):1517–1520, March 1987. doi:10.1126/science.3547653.

[188] A. Ashkin. Acceleration and trapping of particles by radiation pressure. *Physical Review Letters*, 24(4):156–159, January 1970. doi:10.1103/physrevlett.24.156.

[189] A. Ashkin, J. M. Dziedzic, J. E. Bjorkholm, and Steven Chu. Observation of a single-beam gradient force optical trap for dielectric particles. *Optics Letters*, 11(5):288, May 1986. doi:10.1364/ol.11.000288.

[190] M. M. Burns, J.-M. Fournier, and J. A. Golovchenko. Optical matter: Crystallization and binding in intense optical fields. *Science*, 249(4970):749–754, August 1990. doi:10.1126/science.249.4970.749.

[191] Marc Guillon, Olivier Moine, and Brian Stout. Longitudinal optical binding of high optical contrast microdroplets in air. *Physical Review Letters*, 96(14): 143902, April 2006. doi:10.1103/physrevlett.96.143902.

[192] Marc Guillon, Olivier Moine, , and Brian Stout. Erratum: Longitudinal optical binding of high optical contrast microdroplets in air [phys. rev. lett. 96, 143902 (2006)]. *Physical Review Letters*, 99(7):079901, August 2007. doi:10.1103/PhysRevLett.99.079901.

[193] Shiyang Liu and Ji-tong Yu. Comment on "longitudinal optical binding of high optical contrast microdroplets in air". *Physical Review Letters*, 100(19): 199403, May 2008. doi:10.1103/physrevlett.100.199403.

[194] P. C. Chaumet and M. Nieto-Vesperinas. Optical binding of particles with or without the presence of a flat dielectric surface. *Physical Review B*, 64(3): 035422, June 2001. doi:10.1103/PhysRevB.64.035422.

[195] Justo Rodríguez, Luciana C. Dávila Romero, and David L. Andrews. Optical binding in nanoparticle assembly: Potential energy landscapes. *Physical Review A*, 78(4), October 2008. doi:10.1103/physreva.78.043805.

[196] Kayn A. Forbes, David S. Bradshaw, and David L. Andrews. Optical binding of nanoparticles. *Nanophotonics*, 9(1):1–17, November 2019. doi:10.1515/nanoph-2019-0361.

[197] M. C. Frawley, I. Gusachenko, V. G. Truong, M. Sergides, and S. Nic Chormaic. Selective particle trapping and optical binding in the evanescent field of an optical nanofiber. *Optics Express*, 22(13):16322–16334, June 2014. doi:10.1364/OE.22.016322.

[198] Jack Ng, Z. F. Lin, C. T. Chan, and Ping Sheng. Photonic clusters formed by dielectric microspheres: Numerical simulations. *Physical Review B*, 72(8), August 2005. doi:10.1103/physrevb.72.085130.

[199] V. Karásek, T. Čižmár, O. Brzobohatý, P. Zemánek, V. Garcés-Chávez, and K. Dholakia. Long-range one-dimensional longitudinal optical binding. *Physical Review Letters*, 101(14):143601, October 2008. doi:10.1103/physrevlett.101.143601.

[200] S. A. Tatarkova, A. E. Carruthers, and K. Dholakia. One-dimensional optically bound arrays of microscopic particles. *Physical Review Letters*, 89(28): 283901, December 2002. doi:10.1103/PhysRevLett.89.283901.

[201] J. M. Taylor and G. D. Love. Optical binding mechanisms: a conceptual model for gaussian beam traps. *Optics Express*, 17(17):15381–15389, August 2009. doi:10.1364/OE.17.015381.

[202] Wolfgang Singer, Manfred Frick, Stefan Bernet, and Monika Ritsch-Marte. Self-organized array of regularly spaced microbeads in a fiber-optical trap. *Journal of the Optical Society of America B*, 20(7):1568, July 2003. doi:10.1364/JOSAB.20.001568.

[203] Gustav Kirchhoff. Ueber das verhältniss zwischen dem emissionsvermögen und dem absorptionsvermögen der körper für wärme und licht ("about the relationship between the emissivity and the absorption capacity of the body for heat and light"). *Annalen der Physik*, 185(2):275–301, 1860. doi:10.1002/andp.18601850205.

[204] C. E. Máximo, R. Bachelard, and R. Kaiser. cold atoms. *Physical Review A*, 97(4), April 2018. doi:10.1103/physreva.97.043845.

[205] Anatoly A. Svidzinsky, Jun-Tao Chang, and Marlan O. Scully. Cooperative spontaneous emission of n atoms: Many-body eigenstates, the effect of virtual lamb shift processes, and analogy with radiation of n classical oscillators. *Physical Review A*, 81(5):053821, May 2010. doi:10.1103/PhysRevA.81.053821.

[206] R. H. Lehmberg. Radiation from an N-atom system. I. General formalism. *Physical Review A*, 2:883–888, Sep 1970. doi:10.1103/PhysRevA.2.883.

[207] T. Bienaimé, M. Petruzzo, D. Bigerni, N. Piovella, and R. Kaiser. Atom and photon measurement in cooperative scattering by cold atoms. *Journal of Modern Optics*, 58(21):1942–1950, July 2011. doi:10.1080/09500340.2011.594911.

[208] T. Bienaimé, R. Bachelard, N. Piovella, and R. Kaiser. Cooperativity in light scattering by cold atoms. *Fortschritte der Physik*, 61(2-3):377–392, February 2013. doi:10.1002/prop.201200089.

[209] Florent Cottier, Robin Kaiser, and Romain Bachelard. Role of disorder in super- and subradiance of cold atomic clouds. *Physical Review A*, 98(1): 013622, July 2018. doi:10.1103/physreva.98.013622.

[210] Marina Samoylova, Nicola Piovella, Michael Holynski, Philippe Wilhelm Courteille, and Romain Bachelard. *One-dimensional Photonic Band Gaps in Optical Lattices*, chapter Chapter 4, pages 193–249. doi:10.1142/9789814590174_0004.

[211] Kirk Madison, Kai Bongs, Lincoln D Carr, Ana Maria Rey, and Hui Zhai. *Annual Review of Cold Atoms and Molecules*. World Scientific, 2014. doi:10.1142/9100.

[212] F. Schreck, L. Khaykovich, K. L. Corwin, G. Ferrari, T. Bourdel, J. Cubizolles, and C. Salomon. Quasipure bose-einstein condensate immersed in a fermi sea. *Physical Review Letters*, 87(8):080403, August 2001. doi:10.1103/PhysRevLett.87.080403.

[213] A. Görlitz, J. M. Vogels, A. E. Leanhardt, C. Raman, T. L. Gustavson, J. R. Abo-Shaeer, A. P. Chikkatur, S. Inouye S. Gupta, T. Rosenbanda, , and W. Ketterle. Realization of bose-einstein condensates in lower dimensions. *Physical Review Letters*, 87(13):130402, September 2001. doi:10.1103/PhysRevLett.87.130402.

[214] Belén Paredes, Artur Widera, Valentin Murg, Olaf Mandel, Simon Fölling, Ignacio Cirac, Gora V. Shlyapnikov, Theodor W. Hänsch, and Immanuel Bloch. Tonks–girardeau gas of ultracold atoms in an optical lattice. *Nature*, 429(6989):277–281, May 2004. doi:10.1038/nature02530.

[215] Antoine Glicenstein, Giovanni Ferioli, Nikola Šibalić, Ludovic Brossard, Igor Ferrier-Barbut, and Antoine Browaeys. Collective shift in resonant light scattering by a one-dimensional atomic chain. *Physical Review Letters*, 124(25): 253602, Jun 2020. doi:10.1103/PhysRevLett.124.253602.

[216] Angel T. Gisbert, Nicola Piovella, and Romain Bachelard. Stochastic heating and self-induced cooling in optically bound pairs of atoms. *Physical Review A*, 99(1):013619, January 2019. doi:10.1103/PhysRevA.99.013619.

[217] Angel T. Gisbert, Nicola Piovella, and Romain Bachelard. Cooperative cooling in a one-dimensional chain of optically bound cold atoms. *Physical Review A*, 102(1):013312, July 2020. doi:10.1103/PhysRevA.102.013312.

[218] Simon B. Jäger, Stefan Schütz, and Giovanna Morigi. Mean-field theory of atomic self-organization in optical cavities. *Physical Review A*, 94(2):023807, August 2016. doi:10.1103/PhysRevA.94.023807.

[219] Adam T. Black, Hilton W. Chan, and Vladan Vuletić. Observation of collective friction forces due to spatial self-organization of atoms: From rayleigh to bragg scattering. *Physical Review Letters*, 91(20):203001, November 2003. doi:10.1103/PhysRevLett.91.203001.

[220] Ferdinand Brennecke, Stephan Ritter, Tobias Donner, and Tilman Esslinger. Cavity optomechanics with a bose-einstein condensate. *Science*, 322(5899): 235–238, October 2008. doi:10.1126/science.1163218.

[221] C. von Cube, S. Slama, M. Kohler, C. Zimmermann, and Ph.W. Courteille. Creating and probing long-range order in atomic clouds. *Fortschritte der Physik / Progress of Physics*, 54(8–10):726–745, August 2006. doi:10.1002/prop.200610307.

[222] S. Ostermann, F. Piazza, and H. Ritsch. Spontaneous crystallization of light and ultracold atoms. *Physical Review X*, 6(2):021026, May 2016. doi:10.1103/PhysRevX.6.021026.

[223] O.A. Kocharovskaya and Ya. I. Khanin. Population trapping and coherent bleaching of a three-level medium by a periodic train of ultrashort pulses. *Journal of Experimental and Theoretical Physics (JETP)*, 63(5):945, May 1986. (Link).

[224] Giovanna Morigi, Jürgen Eschner, and Christoph H. Keitel. Ground state laser cooling using electromagnetically induced transparency. *Physical Review Letters*, 85(21):4458–4461, November 2000. doi:10.1103/physrevlett.85.4458.

[225] R. Bachelard, Ph.W. Courteille, R. Kaiser, and N. Piovella. Resonances in mie scattering by an inhomogeneous atomic cloud. *Europhys. Lett.*, 97:14004, 2012.

[226] M. Samoylova, N. Piovella, R. Bachelard, and Ph. W. Courteille. Microscopic theory of photonic band gaps in optical lattices. *Optics Communications*, 312: 94–98, February 2014. doi:10.1016/j.optcom.2013.09.016.

[227] Anatoly A. Svidzinsky, Jun-Tao Chang, and Marlan O. Scully. Dynamical evolution of correlated spontaneous emission of a single photon from a uniformly excited cloud of n atoms. *Physical Review Letters*, 100(16):160504, April 2008. doi:10.1103/PhysRevLett.100.160504.

[228] I E Mazets and G Kurizki. Multiatom cooperative emission following single-photon absorption: Dicke-state dynamics. *Journal of Physics B: Atomic, Molecular and Optical Physics*, 40(6):F105–F112, March 2007. doi:10.1088/0953-4075/40/6/f01.

[229] S E Skipetrov and A Goetschy. Eigenvalue distributions of large euclidean random matrices for waves in random media. *Journal of Physics A: Mathematical and Theoretical*, 44(6):065102, January 2011. doi:10.1088/1751-8113/44/6/065102.

[230] R. Bachelard, N. Piovella, and Ph. W. Courteille. Cooperative scattering and radiation pressure force in dense atomic clouds. *Physical Review A*, 84(1): 013821, July 2011. doi:10.1103/PhysRevA.84.013821.

[231] Jamal T. Manassah. Comparison of the cooperative emission profile from a spherical distribution of two-level atoms resulting from the choice of the interaction kernel. *Physical Review A*, 85:015801, Jan 2012. doi:10.1103/PhysRevA.85.015801.

[232] Marlan O. Scully and Anatoly A. Svidzinsky. The lamb shift—yesterday, today, and tomorrow. *Science*, 328(5983):1239–1241, 2010. ISSN 0036-8075. doi:10.1126/science.1190737.

[233] J. Keaveney, A. Sargsyan, U. Krohn, I. G. Hughes, D. Sarkisyan, and C. S. Adams. Cooperative lamb shift in an atomic vapor layer of nanometer thickness. *Physical Review Letters*, 108(17):173601, April 2012. doi:10.1103/PhysRevLett.108.173601.

[234] Sudhakar Prasad and Roy J. Glauber. Coherent radiation by a spherical medium of resonant atoms. *Physical Review A*, 82(6):063805, December 2010. doi:10.1103/PhysRevA.82.063805.

[235] Murray R. Spiegel, Seymour Lipschutz, and John Liu. *Mathematical Handbook of Formulas and Tables*. McGraw Hill, 2017. ISBN 9781260010541. Any of the five editions (Link 5th edition).

[236] Leonard Mandel and Emil Wolf. *Optical Coherence and Quantum Optics*. Cambridge University Press, 1995. ISBN 9781139644105. doi:10.1017/CBO9781139644105.

[237] Jamal T. Manassah. Cooperative radiation from atoms in different geometries: decay rate and frequency shift. *Advances in Optics and Photonics*, 4 (2):108–156, June 2012. doi:10.1364/AOP.4.000108.